Modélisation multi-échelle de l'endommagement et de l'émission acoustique dans les roches

Anca Dobrovat

UNIVERSITÉ DE GRENOBLE

THÈSE

Pour obtenir le grade de

DOCTEUR DE L'UNIVERSITÉ DE GRENOBLE

Spécialité : **Matériaux, Mécanique, Génie Civil, Électrochimie**
Arrêté ministériel : 7 août 2006

Présentée par

Anca - Madalina DOBROVAT

Thèse dirigée par **Cristian DASCALU** et
codirigée par **Stephen HALL**

préparée au sein du **Laboratoire 3SR**
dans **l'École Doctorale IMEP2**

Modélisation multi-échelle de l'endommagement et de l'émission acoustique dans les roches

Thèse soutenue publiquement le **27 mai 2011**,
devant le jury composé de :

M. Carlo CALLARI
Professeur, Università del Molise, Rapporteur
M. Michael KENDALL
Professeur, University of Bristol, Rapporteur
M. Gioacchino VIGGIANI
Professeur, Université de Grenoble, Président
M. Bertrand FRANÇOIS
Professeur, Université Libre de Bruxelles, Membre
M. Angelo SIMONE
Assistant Professor, Delft University of Technology, Membre
M. Cristian DASCALU
Professeur, Université de Grenoble, Membre
M. Stephen HALL
Chargé de Recherche, CNRS, Membre

1 Acknoledgements

My gratitude goes to Prof. Cristian Dascalu for the opportunity of doing my PhD under his constant supervision during 3 and $\frac{1}{2}$ years I spent in the Lab 3SR from Grenoble. All the discussions, the constant support and (sometimes more than) weekly meetings were very helpful to the development of my knowledge.

Special thanks to my co-superviser, Prof. Stephen Hall (Steve), for his constant support especially in difficult moments, for weekly meetings, daily discussions and permanent "monitoring". Thank you for allowing me to discover very interesting domains completely unknown before, such as AE events, micro-seismicity, etc. and also new places (Stavanger - Norway or Barcelona - Spain).

Prof. Victor Tigoiu and Prof. Sanda Cleja-Tigoiu are without any doubts the guardian angels of my "professional life". "Domnule profesor, nu am cuvinte sa va multumesc pentru tot binele facut din momentul in care v-am cunoscut in facultate, culminand cu oportunitatea de a studia in Franta!".

Prof. Angelo Simone and Prof. Bertrand François - without your help and friendship I would still be a PhD student!

Many thanks to Prof. Kendall and Prof. Callari for reviewing this manuscript and for all the short discusions after the defence. I cannot go further without mentioning Prof. Cino Viggiani (Meusieur le Professeur) for all the K-fet discussions and good advice I received.

Next in rank are my parents: "Multumesc Mama si Tata pentru tot ce ati facut pentru ca eu sa ajung pana aici!"

And since I talk about family, it is the time to say "Merçi pour tout!" to my french mom, Danièle and to my french "family (heart relatives)" Martine, Nadine, Mounette, Boris, Claudie and Ives, Françoise and Claude.

And to finish with close foreigner friends: "Multumesc din inima, Gabi, pentru ca te-ai ocupat de mine tot timpul!"; Hola (Don) Marquitos - muchas gracias para todo (musica, comida, amistad)!; Dear Roxana and Rebecca, when I will go to USA and specially to Chicago or San Francisco, be sure that I will come to see you!; Ola, thanks for standing me in the good and bad moods! Thank you also for the coffee machine from Torino-still working and goooood coffee! Cross fingers for you!; Fab - you know that I owe you big time for all you have done for me for my thesis defence!; Nando - thank you for everything. Thanks to you, Prof. Kendall recieved the manuscript of my thesis!; Jeremy, "Merci pour ton aide et pour les discusions et pour ton amitié." Many thanks to all from the lab: Eddy (thanks from behalf of my computer - remember "Frogs" and thanks also for Mozart and Bethoveen and motorbike),Rémi - thanks for the informatic support, Hana, Erika (veeery good cakes at the K-fet), Kryzstof, Eva, Lam, Michal (at 11h30 we go to Epicea!), Matias (good initiative with Wednesday Cinema), Khadi, Hassan and Debo be brave, you are at the beggining!

Thank you for all the administrative support in France! I would have been lost without Carole (Mme. Reverdit) and Sheherezade (Mme. Mezener).

Back to Romania, I cannot forget my best friend, Laura (Thank you and take care, sis!), or Valentin or Maria (See you soon in Bucharest! Thanks for standing me all this decades!). Also special thaughts for my friends and collegues from Colegiul National "Gheorghe Lazar" ("the informaticians": d-na Simona Popa, Oana, Cami) or from Liceul Teoretic "Eugen Lovinescu" Bucuresti who always encouraged and helped me.

Abstract

Multi-scale modeling of damage and acoustic emission in rocks

Accurate modeling of failure of geomaterials is the key to the success of a diverse range of engineering challenges including the topic of CO_2 sequestration, nuclear waste disposal and hydrocarbon production plus civil engineering projects for tunnels or excavations. The aim of this thesis is to develop macroscopic damage evolution laws based on explicit descriptions of fracture at the micro-scale level which can be successfully employed to describe long term damage behavior of geologic storage sites. The approach taken is based on homogenization through asymptotic developments combined with micro-crack propagation energy analysis which leads to an explicit quantification of the acoustic emission (AE) energy associated with damage. Proposed damage models are capable of modeling the degradation of elastic moduli due to the micro-crack evolution. This representation allows the modeling of wave propagation in a medium with evolving damage.

Two types of damage models will be considered: time independent and time dependent. Time independent damage models capable of describing progressive micro-cracking propagation (i.e. quasi-brittle type damage law) are considered. In the case of time-dependent damage models, the evolution of the micro-crack length during propagation is described through a sub-critical criterion and mixed mode propagation by branching. Using the time dependent damage model including rotational micro-cracks, simulations will be made at three levels: laboratory, tunnel and reservoir scales.

Keywords: micro-cracks, asymptotic homogenization, damage, geomaterials, quasi-brittle behaviour, sub-critic, time effects, micro-cracks' kinking, rocks, acoustic emissions

Résumé

Modélisation multi-échelle de l'endommagement et de l'émission acoustique dans les roches

La modélisation de la rupture des géo-matériaux constitue un important défi pour les applications telles que la séquestration du CO_2, le stockage de déchets nucléaires, la production des hydrocarbures ainsi que les projets de génie civil concernant les tunnels ou les excavations.

L'objectif de cette thèse est de développer des lois d'évolution macroscopiques d'endommagement à partir des descriptions explicites de la rupture à l'échelle microscopique en vue de la modélisation du comportement d'endommagement à long terme des sites de stockage géologique.

L'approche adoptée est basée sur l'homogénéisation par développements asymptotiques et la description énergétique de la propagation des micro-fissures, qui permettent l'obtention des lois d'endommagement et conduisent à une quantification explicite de l'énergie de l'émission acoustique associée à la rupture. Les modèles obtenus sont capables de prédire la dégradation des modules d'élasticité en raison de l'évolution des micro-fissures. Cette représentation permet de modéliser la propagation des ondes dans un milieu à endommagement évolutif.

Deux types de modèles d'endommagement seront proposés: indépendants de temps et dépendants de temps. Les modèles dépendants de temps décrivent l'évolution progressive quasi-fragile de la micro-fissuration. Dans les modèles dépendants de temps, l'évolution des micro-fissures est décrite à travers un critère sous-critique et la propagation mixte, par branchement. En utilisant le modèle dépendant de temps, des simulations seront faites à trois niveaux: du laboratoire, du tunnel et du réservoir.

Mots clés: micro-fissures, homogénéisation asymptotique, endommagement, géo-matériaux, comportement quasi-fragile, sous-critique, effets de temps, branchement des micro-fissures, roches, emission acoustique

Contents

List of Figures

2 Notations

E - Young modulus
ν - Poisson's ratio
$\mathbf{x}$ - macroscopic system of coordinates
$\mathbf{y}$ - microscopic system of coordinates
ε - material's internal length represented by the size of a periodicity cell (elementary cell); equivalent to the size between centers of two neighboring micro-cracks
$\boldsymbol{\sigma}^{\varepsilon}$ - stress tensor of the initial heterogeneous body (before homogenization)
$\mathbf{u}^{\varepsilon}$ - displacement field of the initial heterogeneous body (before homogenization)
$e_{\mathbf{x}}$ - small strain tensor with respect to the macroscopic variable.
$Y = [0,1] \times [0,1]$ - unit cell (microscopic level)
$2a$ - length of a micro-crack in the elementary cell
θ - orientation of a micro-crack in the elementary cell
d - length of a crack in the unit cell; it varies between 0 (for virgin material) and $1/[\max(|\cos(\theta)|; |\sin(\theta)|)]$ (for a micro-crack that completely cross the cell)
d^* - normalized damage variable (projection of d on the sides of the unit cell). In case of vertical and horizontal micro-cracks, $d = d^*$
θ_0 - initial micro-crack orientation in the unit (and elementary) cell
d_0 - initial micro-crack length in the unit cell
$\mathbf{N}$ - unit normal vector to the crack
$\mathbf{T}$ - unit tangent vector to the crack
$[\,\cdot\,]$ - jump across the crack faces
$\xi(\mathbf{y})$ - *characteristic functions* representing elementary deformation modes of the unit cell
$\langle\cdot\rangle$ - mean value operator
λ and μ - Lamé constants
C_{ijkl} - effective elastic coefficients
$\mathcal{G}^{\varepsilon}$ - energy release rate at the crack tip
$\mathcal{G}_f$ - critical fracture energy
$\mathcal{G}_c$ - maximum of $\mathcal{G}_f$
τ_s - shear stress (used in this thesis only in the case of wing-type micro-cracks)
μ_f - friction coefficient (used in this thesis only in the case of wing-type micro-cracks)
ϕ - angle made by the inclined crack with the horizontal axis (in the case of wing-type micro-cracks)
ϕ_P - diameter of a pore in the elementary cell
a_P - diameter of a pore in the unit cell
I^{ε} - the central part of the vertical equivalent crack, which replace the sliding crack.
cf - size of the fracture process zone around a crack tip
d^{ε} - a squared plane crack side length in a 3D unit volume
Y_d - damage energy release rate (in this thesis only in the 3D case)
τ_0 - characteristic time (see [126])
$K_{I,II}$ - stress intensity factors at the tips of a straight micro-crack
$K^*_{I,II}$ - stress intensity factors at the tips of the kinks
K_0 - limit value of the mode I stress intensity factor
n - Charles' law exponent
ε_{eq} - energy release rate in the case of linear coefficients
dl - length of a kink

ϕ_{max} - kinking angle between the existing crack and the incrementally propagated crack.
λ' - mode mixity factor used for computing ϕ_{max}
$F(\phi_{max})$ - 2×2 Leblond matrix of 20 - degree polynomials
$d\theta$ - increment of the orientation of a micro-crack
TC - (Trajectory Corrector) - parameter used in the kinked-crack damage model which giva a correct trajectory of the equivalent micro-crack
AE - acoustic emissions
v_{Ph} - horizontal P-wave velocity
$v_{Ph}0$ - horizontal P-wave velocity at the beggining of the simulation
v_{Pv} - vertical P-wave velocity
v_{Pv0} - vertical P-wave velocity at the beggining of the simulation

3 General introduction

3.1 Objectives

Accurate modeling of inelasticity and failure of geomaterials is the key to the success of a diverse range of engineering challenges including the topic of CO_2 sequestration, nuclear waste disposal and hydrocarbon production plus civil engineering projects for tunnels or excavations. However, the geomaterials are notoriously difficult to model due to the complexity of the micro-structure, heterogeneities and anisotropy at all scales. Particular characteristics of geomaterials are their pressure sensitive properties, non-linearity and localized deformation phenomena, which can occur across the scales, e.g., grain-scale cracking to lithospheric faults. Localization of damage, in particular, can be critical factor in determining the success or failure of an engineering project. For example, localized failure will lead to large changes in strength and permeability that could cause borehole failure and leakage from hydrocarbon or CO_2 reservoirs.

Another key aspect in project development in civil engineering (tunnels, foundations, ...), geological storage of radioactive waste or CO_2 and oil production field is monitoring of the actual processes in play. Such monitoring generally requires the use of geophysical techniques such as seismic/acoustic imaging. Such monitoring is however only of real benefit if it can be linked back to the modeling and thus engineering development plan. *Therefore links are required between the geophysical monitoring techniques and the geomechanical simulations.*

Two main areas of application are of interest in this work, subsurface reservoir engineering (hydrocarbon production and CO_2 sequestration) and underground geologic storage of nuclear waste. In geological storage of CO_2, storage reservoirs are formations of porous rocks in the deep subsurface with an overlying impermeable barrier (cap-rock seal). A critical issue is to understand how the seal rock responds to CO_2 injection into the reservoir and so to prevent catastrophic failures, which could result in costly damage to well-bores/facilities and dangerous large-scale leakage of carbon dioxide in the atmosphere. It should be noted that similar challenges exist in the domain of oil and gas production. Nuclear waste requires sophisticated treatment followed by a long-term management strategy involving storage. The basic concept of the long term management of geologic waste disposal, is to locate a large, stable geologic formation and use mining technology to drill a shaft 500-1000 meters below the surface where rooms or vaults can be excavated for disposal of high-level radioactive waste. Perpetual management and monitoring of these sites is required for safety reasons. Even very low container leakage and radionuclide migration rates must be taken into account. Therefore interest in understanding the excavation-induced disturbance to the rock mass around tunnels has increased. This thesis concentrates on the development of modeling of damage evolution and its links to monitoring techniques involving elastic (seismic and ultrasonic) waves. This integration of geophysics and geomechanics approach targets two key research areas:

- microscopic and macroscopic processes governing rock behavior and the evolution of the constitutive properties;

- the connection between "geomechanical" and "geophysical" properties of rocks and associated phenomena plus their modeling.

More specifically, the objective of this thesis is to develop macroscopic damage evolution laws based on explicit descriptions of the micro-scale level which can be successfully employed to describe long term damage behavior of geologic storage sites. One element of major importance in this work is the change-of-scale procedure, in other words: homogenization. The approach taken is based on asymptotic developments of displacement and stress fields combined with micro-crack propagation energy analysis which leads to an explicit quantification of the acoustic emission (AE) energy associated with damage. Proposed damage models will be capable of modeling the degradation of elastic moduli due to the micro-crack evolution. This representation will allow the modeling of wave propagation in a medium with evolving damage starting from fracture events. This will allow comparison with AE laboratory tests or with micro-seismic (reservoir or tunnel scale) data and also seismic or ultrasonic velocity imaging. Future extensions of the models could be made to include hydro-mechanic effects. The consequence will be that on a rational basis, an intelligent in-situ alert system using AE (or micro-seismicity) could be developed, since AE are able to give an alert sign when fracture phenomena are activated leading to a change in permeability and therefore to a possible leakage of stored CO_2 or radioactive waste.

In the following we present an overview of the main issues connected to the thesis objectives. Section 3.2 gives a wider description of the modeling approach taken and Section 3.3 introduces the context and motivation of choosing this specific modeling approach. The scientific background is presented in Sections 3.4 - 3.6. Section 3.4 makes a short review of the possible approaches to address the challenges discussed and highlights that the only way is to consider a damage mechanics framework. Section 3.5 introduce the damage mechanics modeling principles in two parts: in the beginning fracture mechanics is introduced and then the difference between damage and fracture mechanics is underlined. We choose the category of models which connects microscopic analysis with macroscopic behavior. Therefore, we construct our model independent of the external factors, by the use of a homogenization technique through asymptotic developments. In Section 3.6 an overview of the homogenization techniques is given, and asymptotic developments techniques were best suited to the post challenge in terms of viability and simplicity. This chapter finishes with the structure of the thesis (Section 3.7).

3.2 Modeling approach taken

Continuum damage mechanics (CDM) framework has been considered to be the best choice in geomechanical modeling of elastic properties and failure. The degradation of elastic moduli occurs through a damage variable for which evolution laws are postulated. From the point of view of the construction procedure, one can classify the damage models in: macroscopic models (usually phenomenologically based) and micro-mechanical approaches. In recent years, considerable efforts have been made to establish a link be-

tween micro-structural fracture phenomena and the corresponding macroscopic behaviors (see for instance Nemat-Nasser and Hori ([112]) for a review). The majority of the works devoted to this subject treat the case of non-evolving cracks or the micro-mechanical analysis for stationary cracks supplemented by phenomenological assumptions on the evolving damage.

In this thesis, we consider a procedure to obtain micro-mechanical damage models for solids, in which the damage evolution laws are completely deduced from a micro-structural analysis. This procedure was initially developed by Dascalu and co-workers ([36], [37], [38], [39], [17],[56]). Two directions have been followed: development of time-independent ([36], [37], [38], [17]) and of time-dependent damage models ([38], [39], [56]). The basic upscaling procedure is a combination of periodic homogenization based on asymptotic developments (e.g., Bakhvalov and Panasenko ([7])) and energy analysis of fracture. This rigorous mathematical method has been previously employed, for elastic bodies with non-propagating micro-cracks, for instance in Leguillon and Sanchez-Palencia ([96]) or in Terada and Kikuchi ([139]). The purpose is to deduce damage evolution laws completely given by homogenization, without supplementary phenomenological assumption. The key is given by microscopic energy analysis, performed on a finite-size cell, which leads, through homogenization, to a macroscopic evolution equation for damage. In this equation a micro-crack length appears as a damage variable and the cell size as a material length parameter. This parameter is introduced through the damage evolution law, as a consequence of the microscopic balance energy and a Griffith type propagation criterion for micro-cracks.

In the case of time independent damage models, Dascalu et al. ([36], [37], [17]), only considered brittle-type damage and the macroscopic implementation only permitted four discrete micro-crack orientations, which, once chosen, were maintained during whole simulation (no micro-crack rotation was allowed). In this thesis several development directions of this approach will be followed. At the microscopic level, in the case of straight micro-cracks, more orientations will be considered and a spatial interpolation procedure will make possible a full description of any distribution of micro-cracks giving the length and inclination angle with respect to x-axis. Wing-type micro-cracks will also be considered. A new time independent damage model capable of describing progressive micro-cracking propagation will be deduced (quasi-brittle type damage law) adding realism to the model since experimental observations indicate that rocks show a more gradual fracture behavior. An extension to three-dimensions will be also given.

The second type of damage models considered in this thesis corresponds to a time-dependent class. The evolution of the micro-crack length during propagation is described through a sub-critical criterion, that is a criterion considering crack propagation for energy lower than the critical limit of fracture. First step in the development of such models is the implementation of a simplified time-dependent damage model in which the stiffness of the solid is governed by linear coefficients that depend on the elastic properties of the solid matrix and on micro-cracks lengths. Second step is to replace the linear coefficients with the homogenized ones previously computed for a straight crack. The propagation occurs in the fixed direction given by the orientation of the crack. This model was previously developed by Dascalu ([38]), but only the macroscopic local level was taken into account. Global macroscopic implementation is the contribution of this thesis. The third step was the consideration of rotating micro-cracks time-dependent damage models, initially

developed by François and Dascalu ([56]) the main objective was the development of a complex two-scale time-dependent damage model capable to take into account both a crack propagation and its change of orientation. The orientation of the crack growth is governed by the maximum energy release rate at the crack tips and the introduction of an equivalent straight crack. The passage from micro-scale to macro-scale is done through an asymptotic homogenization approach. Extensions to the model are given in this thesis. Initially, stress intensity factors (SIF) for straight micro-cracks were computed with the help of path-independent integral method in [56]. In this thesis displacement correlation method is used for computation of SIFs and comparison between the two methods was made. At the macroscopic local level we agreed with the criteria for the equivalent crack from [56] in the case of opened micro-cracks, but, in the case of compressive micro-cracks, previous criteria was not enough. We give a new way of replacing the kinked crack with an equivalent straight one. All the consideration of rotating micro-cracks damage model were made at the level of en elementary cell (macroscopic local level). Global macroscopic implementation is entirely our contribution.

For both time-independent and time-dependent class of damage models the energy analysis is performed on a periodicity cell of finite-size containing a micro-crack. Different crack orientations are allowed through a numerical procedure developed for comparison and choice between elementary homogenized solutions, corresponding to different trajectories. The homogenized coefficients (and in the case of time-dependent rotating micro-cracks damage models also the stress intensity factors) are computed for every micro-crack orientation and length and an incremental computational scheme is considered in which, at every step, the damage law corresponding to different trajectories is solved. There are two possible choices in solving geomechanical problems: either the most important crack length is chosen and its orientation is maintained during all subsequent steps, or, like in the case of micro-crack rotation, at each step, a kinking angle is computed, but since homogenization procedure is developed in the case of straight micro-cracks, the kinked crack is replaced with an equivalent straight one.

The models are currently formulated for quite general crack-face conditions, including frictionless contact. At the macroscopic level, the switch between the homogenized behaviors corresponding to crack opening or closure is carried out numerically. Different local micro-crack orientations provided by the damage law lead to induced anisotropy and heterogeneity in the global response of the specimen. The model also allows for different fracture energies, in tension and compression.

This model allows future extensions to include the effect of fluid/gas pressure using hydraulic fracture approach (Garagash and Detournay [62], Zhang et al. ([153])), a unilateral hydro-mechanical damage model being obtained which can be used to give even more realistically solution for further simulations.

3.3 Context and motivation

This thesis is motivated by the need to understand damage evolution around subsurface geologic disposal sites. In the following we provide the context of this work in terms of the CO2 sequestration and nuclear waste disposal challenges.

3.3.1 Carbon capture and storage

There are two major reasons for the CO_2 to be captured and stored: climate change and enhanced oil recovery.

On one hand, climate changes have been observed in direct correlation with the industrialization from the last century. Nowadays this gas represents about 385 parts per million (ppm) which is $\approx 0.3\%$ of the atmosphere. Approximately one third of all CO_2 emissions is due to human activity and comes from fossil fuels used for generating electricity. A variety of other industrial processes also emit large amounts of carbon emission, for example oil refineries, cement works and iron and steel production. These emissions could be reduced substantially without major changes to the basic process, by capturing and storing the carbon dioxide.

On the other hand, CO_2 injection become very important in the last decades in the oil industry. In the same manner as water injection, CO_2 is injected back into he reservoir, usually to increase pressure and thereby stimulate production. Water or liquefied carbon dioxide is injected, in the first phase, to support pressure of the reservoir (also known as voidage replacement) and, in the second phase, to sweep or displace oil from the reservoir, and push it towards a well. Normally only 30 % of the oil in a reservoir can be extracted, but water or carbon dioxide injection increases that percentage (known as the recovery factor) and maintains the production rate of a reservoir over a longer period of time.

Once captured, in order to avoid reaching the atmosphere, CO_2 can be stored securely in geological reservoirs in the same way as oil and gas have been stored for millions of years. Many reservoirs, suitable for storage, have been identified under the earth's surface and in the oceans. [1] In the following, two case studies will be given: Weyburn field in Saskatchewan, Canada and Sleipner field in the North Sea.

Weyburn Carbon Dioxide Sequestration Project ([144])

Weyburn oil field in Saskatchewan, Canada, was discovered about fifty years ago. Since September 2000, CO_2 has been transported from the Dakota Gasification Plant in North Dakota through a 320 km pipeline and injected into this field. The impact of the CO_2 injection was major since it is estimated that by 2035, 155 million gross barrels of incremental oil will be recovered.

In October 2005, CO_2 injection began also at the adjacent Midale oilfield, and an additional 45 - 60 millions barrels of oil are expected to be recovered during 30 years.

Concerning both Weyburn and Midale commercial oilfields a significant monitoring project is in place. This project is the largest, full - scale, in-the-field scientific study ever conducted in involving carbon dioxide storage. The goal of this project is to enhance the knowledge and understanding of the underground sequestration of CO_2 associated with EOR (Enhanced Oil Recovery) and the objectives can be classified in 5 themes:

- Geologic integrity - selection of suitable sites for CO_2 geologic storage in terms of seal integrity.

[1] When describing CO_2 in geological formations and oceans, the term **storage** is used. **Sequestration** refers only to the terrestrial storage of CO_2.

- Wellbore integrity - development of a list of remediation activities that could be applied; tests for establishing pressure and mobile fluids to look for CO_2 migration out of zone.
- Storage monitoring methods - characterization of the accuracy of monitoring technologies for quantitatively predicting the location and volume-in-place of CO_2 and determine from the four-dimensional (4-D) seismic program interpretation results if multi-year programs are appropriate for ongoing monitoring and verification.
- Risk assessment and storage mechanisms - all relevant storage and leakage mechanisms should be modeled and studied, with risk levels determined for various operations scenarios.
- Data validation and management.

This thesis has implications for all of these 5 themes.

Sleipner Carbon Dioxide Sequestration Project ([132])

Whilst $C0_2$ injection has been carried out for many years to enhanced oil production, the Sleipner CO_2 sequestration project was the first example of underground geologic storage of CO_2 for climate change reasons.

Sleipner field is one of the largest natural gas producers in the North Sea. The natural gas produced from this field contains about 9 % CO_2, but the required export specifications imply that it needs to be reduced to a maximum of 2.5 %. This equates to an extraction of nearly 1 million tonnes CO_2 / year. In order not to let CO_2 in the atmosphere, Statoil adopted a saline aquifer storage strategy for the Sleipner West field. Natural gas production from the field started in 1996, with CO_2 injected, following a four stage compression system, into the Utsira aquifer formation, which is a 200 - 250 meters thick massive sandstone formation located at a depth of 800 - 1000 meters beneath the seabed.

The reduction of CO_2 level from 9 % to about 2.5 % is achieved by stripping the CO_2 from the gas stream using large absorption towers and amine scrubbing technology. Then, by flash regeneration, was separated out, the CO_2 is transported to the Sleipner A platform for injection into the Utsira aquifer. The presence and movement of the carbon dioxide in the Utsira formation is monitored by examination of 3D seismic data.

3.3.2 Radioactive waste disposal

The term "radioactive waste" defines a waste product containing radioactive material. Usually it is the product of a nuclear process such as nuclear fission, but also industries which are not directly connected to the nuclear power industry may produce radioactive waste.

Radioactivity diminishes over time, so in principle the waste needs to be isolated for a period of time until it no longer poses a hazard. But "time" notion covers a very big interval, from hours to years for some common medical or industrial radioactive wastes, or

thousands of years for high-level wastes from nuclear power plants and nuclear weapons reprocessing.

As a general rule, short-lived waste (mainly non-fuel materials from reactors) is buried in shallow repositories, while long-lived waste (from fuel and fuel-reprocessing) is deposited in deep underground facilities.

Nuclear waste requires sophisticated treatment and management to successfully isolate it from interacting with the biosphere. This usually necessitates treatment, followed by a long-term management strategy involving storage, disposal or transformation of the waste into a non-toxic form. The basic concept of the long term management of geologic waste disposal, is to locate a large, stable geologic formation and use mining technology to drill a shaft 500-1000 meters below the surface where rooms or vaults can be excavated for disposal of high-level radioactive waste. The goal is to permanently isolate nuclear waste from the human environment. Various organizations examine the feasibility of deep geological disposal of radioactive waste and stability of tunnels which would be created to store such waste materials. Perpetual management and monitoring of these sites is required for safety reasons. Because some radioactive species have half-lives (the time it takes for any radionuclide to lose half of its radioactivity) longer than one million years, even very low container leakage and radionuclide migration rates must be taken into account. Therefore interest in understanding the excavation-induced disturbance to the rock mass around tunnels has increased. This has involved significant research efforts in modeling, monitoring and in-situ testing.

3.3.3 Monitoring geomechanical processes

Monitoring of subsurface processes, such as CO_2 sequestration, fluid extraction (e.g., oil and gas production) or tunnel drilling, requires remote sensing techniques. The most used of these remote techniques is "seismic imaging", a geophysical technique involving measurements of elastic wave propagation through the imaged body, but also acoustic emission and micro-seismic monitoring (i.e., the listening for small earthquakes that occur due to deformation and associated cracking of the rocks) are equally used. This can be carried out at any scale - from the scale of a laboratory sample to the scale of the earth. The modeling approach presented in this thesis considers the evolution of elastic properties and thus provides a means to link geomehanical modeling to seismic monitoring. Consequently, for context, the basics of seismic monitoring are outlined in the following.

Elastic waves (a term which includes sound, ultrasonic and seismic waves) are "mechanical disturbances that propagate through a material" ([55]) and can be used to assess, in a non-destructive fashion, the evolution of elastic properties, e.g., as a result of deformation. The term elastic is used here since the waves propagate without causing any permanent deformation. We usually denote by "acoustic waves" or "sound waves" the elastic waves in air and water. These terms are often used about elastic waves in rocks too.

Fjaer et al. ([55]) describe the propagation of waves and gave also the mathematical deduction of the propagation velocity. The waves propagate from point to point with a velocity defined by the elastic properties of the medium and the density. Therefore if damage occurs that results in changes in the elastic properties, this will effect the elastic-

wave propagation velocity, which might be measurable. The velocities can be anisotropic due to fabric or the evolution of anisotropic damage. Elastic waves can be used for monitoring damage with *passive* (waves propagating from acoustic emissions or micro-seismic sources due to the development of damage) or *active* sources. "Passive" refers to the use of the waves propagating from acoustic emissions or micro-seismic sources due to the development of damage. "Active" source methods use explosions to produce waves that propagate through the rock mass and so to characterize the properties of the medium through which the wave pass (e.g., Hall and Kendall ([72])). Passive source data, associated with hydrocarbon production, can be used in a similar way, but in addition the characteristics of the "event" that produced the waves can be analyzed (e.g., Teanby et al. ([137])). Both passive and active methods are of significant interest but the former is becoming increasingly attractive due to the desire to monitor injection/production processes continuously.

Elastic wave and acoustic-emission/micro-seismic assessment and monitoring of damage can be performed at all scales and in the following a few examples at laboratory, tunnel excavation and reservoir scales are provided.

- laboratory scale - In laboratory rock mechanics acoustic emissions and irreversible changes in ultrasonic velocities with loading are commonly measured. These effects are linked to damage evolution. An advanced example is given by Charalampidou et al. ([29]) in a study of the development of compaction bands in triaxial compression on a sandstone. In this work acoustic emission recordings allowed mapping of active deformation sites during loading (see Figure 3.1), characterization of the event mechanisms was also carried out. Furthermore, in this work ultrasonic tomography was used to characterize the localized deformation zones (after testing) as zones of localized damage (zones of reduced elastic wave propagation velocity, Figure 3.2).

  Another suggestive example of monitoring at laboratory scale can be found in Nguyen ([113]). A two notched Tuff of Naple specimen was solicited under uniaxial compression loading. Between the two notched a damage localization zone occurs which is pointed out with the help of P-wave velocity measurements.

  Figure 3.3 shows the evolutions of 6 P-waves normalized velocities. The velocities along three trajectories, denoted by "group 2" (5-7 ; 8-6 ; 9-6) pass through a zone between the two notched of the specimen, meanwhile, the other three waves, denoted by "group 1" (9-12, 9-10, 11-10), do not pass the mentioned zone. It is observed that at the beginning all the 6 velocities diminish just a little at the beginning of the test. After about 300 seconds, the curves separate in two groups: wave velocity measured for the trajectory of group 1 rapidly decrease, meanwhile group 2 velocity diminish much slowly. The decrease of wave velocity for group two, which pass the zone between the two notches, clearly indicate an increase in a density of micro-cracks in that zone, in other words, localized damage is present. In the last phase of the test, which corresponds also to the softening process occurring, important drops in velocity measured four group 1, meanwhile, in group 2 velocities remain almost constant.

  One reason leading to the choice of this example is that it is perfect to show both localized strain and localized damage (which) is indicated by ultrasonic velocity reduction. Figure 3.3 showed the evolution of six P-waves, among which three

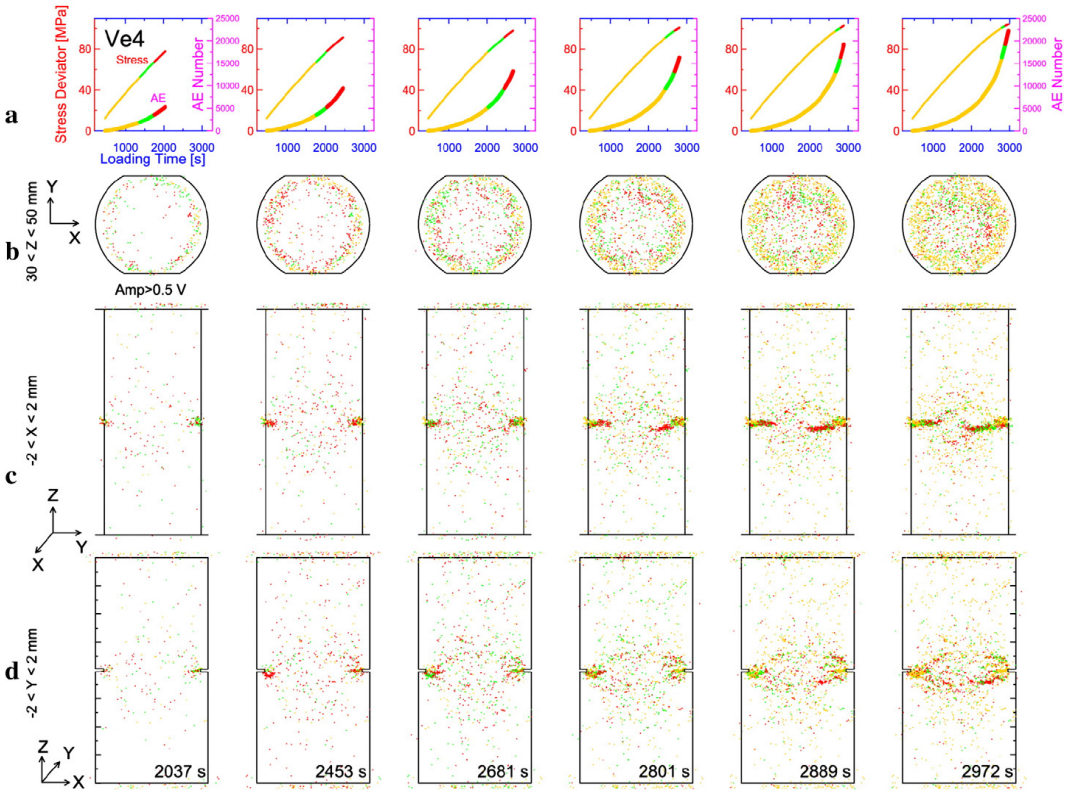

Figure 3.1: (a) Stress deviator and number of AE events as functions of time for seven time steps. In red, the events that nucleated at the last time increment are represented, in green - the events of the previous time increment and the history of all previous events is shown in yellow; (b)-(d) show maps of AE event locations for the same time step, represented in the three 2D orthogonal projections. (image from [29]).

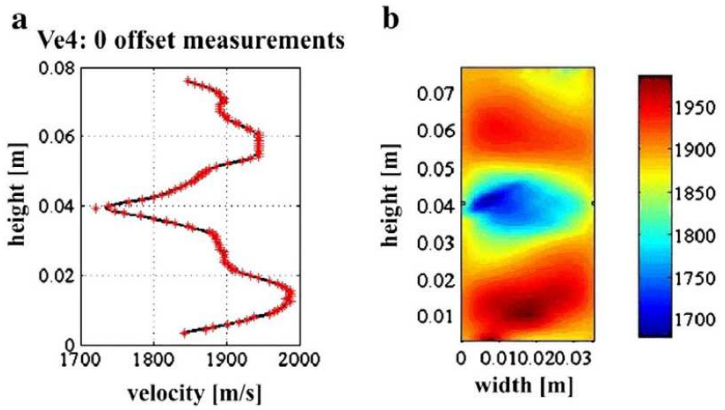

Figure 3.2: Velocity profile of zero-offset measurements (a) and velocity field using UT (b); (image from [29]). The smallest velocity values are in the most damaged zone

trajectories decreased rapidly clearly indicating an increase in a density of micro-cracks. Figure 3.4 shows maximum shear strain maps corresponding to the times

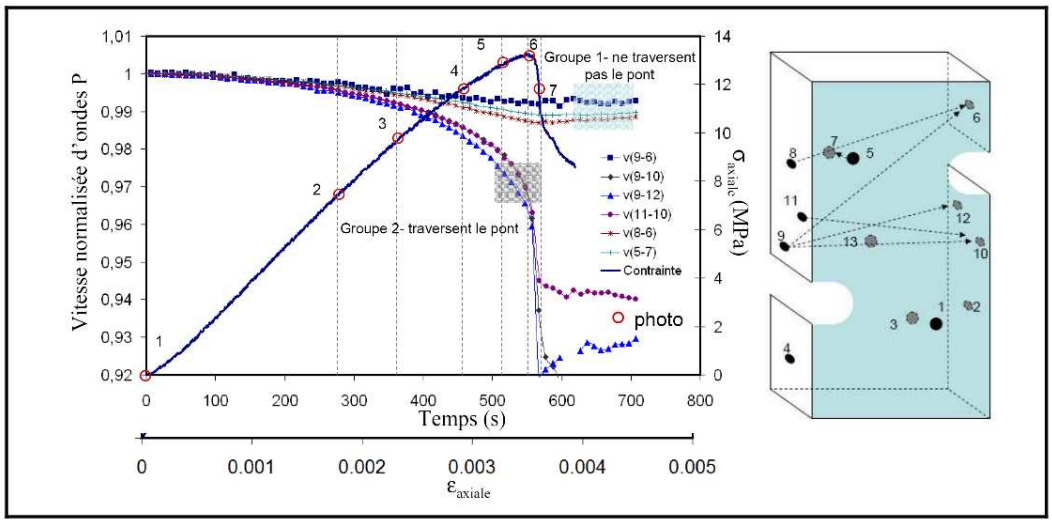

Figure 3.3: P-waves propagation velocity evolution. On the right part of the figure position of the captors and waves trajectories used to measure velocity. On the left part, normalized velocities measured for different couples of captors-emitters (image from [113])

.

1-7 represented with red circles on the global stress-strain curve of previous figure. Strain localization process is more pronounced between times 4-7 (Photos: 4-5, 5-6, 6-7) and perfectly match the decrease in ultrasonic velocities.

- tunnel excavation level - Acoustic emissions and ultrasonic wave propagation can provide complementary methods of assessing damage around tunnel excavations in the so-called excavation-disturbed zone investigation (EDZ). The near-field EDZ, less than one tunnel radius from the tunnel perimeter, may be expected to include significant brittle deformation, meanwhile, the far-field EDZ may expect to be dominated by the effects caused by redistribution of the stress field.

  Using AE and ultrasonic techniques to study these tunnels, Falls & Young ([50]) were able to examine the nature of the EDZ around tunnels in granitic material at approximately 420 m depth. The studies have been undertaken at both the Atomic Energy of Canada Limited (AECL) Underground Research Laboratory (URL) and at the Swedish Nuclear Fuel Waste Management Company (SKB) Hard Rock Laboratory (HRL). AE monitoring during excavation showed that some activity occurred in the sidewall regions, but the spatial density of AE hypocenters increased toward the regions in the floor and roof of the tunnel where breakout notches formed. This sidewall activity was clustered primarily within 0.5 m of the tunnel wall. AE monitoring in the floor of the tunnel showed that small numbers of AE continued to occur in the notch region in the floor of the tunnel over 2 years after excavation was completed.

  Meglis et al. ([103]) used detailed ultrasonic velocity measurements within at 1-m deep shell around the tunnel at URL to determine the variation of velocity in situ, and from this to infer the relative distribution of excavation induced crack damage. Ultrasonic measurements were used because at the frequency of 1MHz waves are

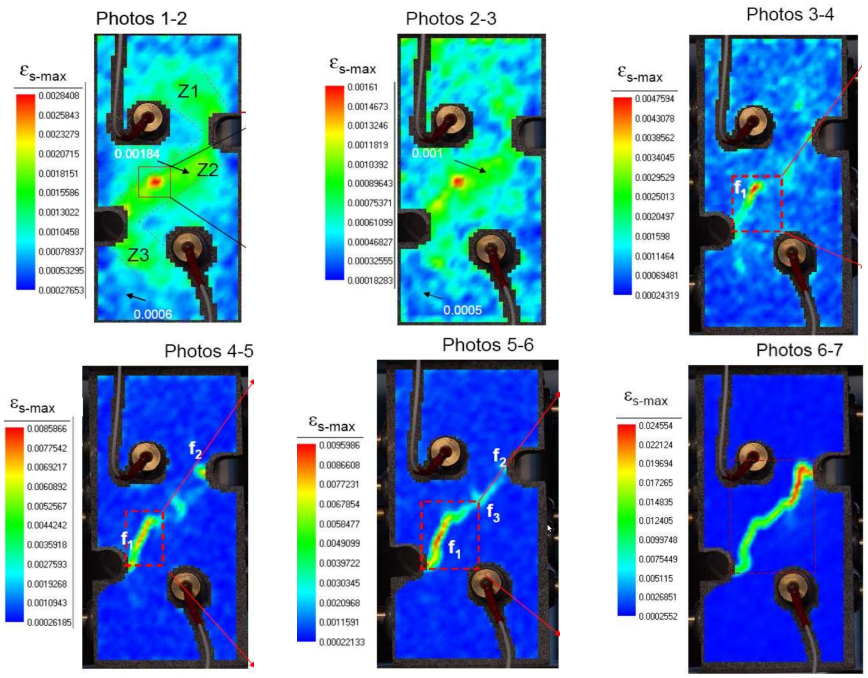

Figure 3.4: Six maximum shear strain maps obtained with DIC corresponding to the times 1-7 represented with red circles on the global stress-strain curve in Figure 3.3 (images from [113])

.

highly sensitive to cracks in order of a few mm, approximately the grain size of the rock. Compressional (P) wave velocity reflects both the degree of micro-crack damage and any preferred orientation of crack planes within the imaged region. The conclusion was that the micro-crack damage is more concentrated in the material immediately adjacent to the tunnel, although in the sidewall region it extends more deeply into the rock.

- reservoir level - Damage is one of the causes of changes in seismic properties around producing hydrocarbon reservoirs (including aspects of seismic anisotropy and travel-time). These changes, have been observed in many locations around the world. For instance in the Valhall field in the Norwegian North Sea observations have been made of seismic anisotropy and travel-time differences due to velocity changes (see Barkved et al. ([9]), Hall ([73]),Van Gestel et al. ([142])). These changes are associated with subsidence and compaction caused by hydrocarbon production and fluid injection which is also observed in other places around the world e.g. Wilmington, Lost Hills and Belridge in California (see Fielding et al. ([54])), Lake Maracaibo in Venezuela etc.

  Exploitation of both seismic anisotropy and micro-seismic data is thus of significant interest in reservoir surveillance during production of hydrocarbons or sequestration of CO_2. Temporal changes of a reservoir properties during its production (such as saturation and pressure), mainly based on changes in seismic reflection amplitudes, can be identified and even characterized using seismic imaging, since high-resolution

3D images of the subsurface can be provided.

Hall ([73]) presented a methodology for 7D warping which has the potential to address the full 3D time-lapse deformation including lateral or shear deformation and anisotropy development.The methodology is presented with reference to time-lapse seismic analysis of heterogeneous 3D vector displacements associated with compaction and subsidence.

[9] and [142] summarize the acquisition, processing and automated work-flow established to produce time-lapse analysis displays and maps within weeks after final shot of a LoFS ("life of field seismic project") survey taking place at Valhall Field, Norway. The LoFS system, which is the world's largest permanently installed seismic array, is designed to monitor the production and water injection at Valhall. The integration of the data from the LoFS is explained. Barkved et al. ([9]) draw the attention to the fact that understanding the overburden deformation in detail is driven, on one hand, by the potential impact on drilling stability and long term well integrity (previously mentioned by [93]) but, on the other hand, also by the potential of using these observations to indirectly define the reservoir dynamic and static properties in better detail.

The use of the LoFS data to reduce the risk of drilling a crestal well to provide pressure support for existing producers in the area or to predict the pressures regimes encountered when drilling a horizontal well, is mentioned ([142]). Strong time-lapse seismic responses from subsequent LoFS surveys were observed in the toe of the well. They were related to depletion from nearby wells and were used to guide pressure estimation along the well. When the first significant pressure drop was confirmed, drilling was stopped. Further drilling would most likely have resulted in possible loss of the well.

In addition to seismic imaging, micro-seismic data are being increasingly used to monitor subsurface operations; these data can indicate the areas of active deformation and also information on changing stress fields. (Hall ([74]) provides an overview and references for these different geomechanical effects on seismic data).

In summary, damage is the principal mechanism leading to the degradation of elastic properties and seismic/acoustic emission associated with deformation from laboratory to reservoir scale. Both hydrocarbon reservoir engineering and nuclear waste disposal have significant risk associated with the damage induced by fluid production or tunnel excavation, respectively. Therefore perpetual management and monitoring is considered for safety reasons and monitoring techniques improved very much in the last decades. However, to have an intelligent in-situ alert system using seismic/ultrasonic imaging and acoustic emissions (or micro-seismicity), damage models capable of modeling the degradation of elastic moduli due to micro-crack evolution and quantification of associated acoustic emission energy should be available. The models proposed in this thesis will allow the modeling of wave propagation in an evolving damaged medium and acoustic/micro-seismic events, therefore a comparison with acoustic emissions in laboratory tests or micro-seismic databases (from monitoring at large scales - i.e fluid injection/extraction in the oil reservoir, tunnel excavation ...) will be possible.

3.4 Geomechanical modeling of elastic properties and their evolution

As outlined in the previous section, exploitation of both seismic anisotropy and micro-seismic data has been shown to be very successful for monitoring geomechanical evolution from a laboratory scale to subsurface reservoirs. However, to fully exploit such observations requires simulation models that can be used to predict, and match, the changes (take, for instance, the example of an oil reservoir where the CO_2 injection process needs to be accurately simulated in order to avoid mechanical changes/failures that may be costly).

Commonly used geomechanical constitutive models (e.g., elasto-plasticity approaches) do not generally account for rock property evolution and thus cannot be used to predict any changes in the measurable elastic properties. Anisotropy and evolving elastic properties are often neglected due to the difficulty and uncertainty in their parametrization and also in their experimental characterization. However, several approaches were dedicated to this subject but they are incomplete or too simplified. For instance, Pietruszczak et al. ([122]) considered a constitutive model including intrinsic anisotropy due to sedimentary fabrics, but does not evolve with loading. Gajo et al. ([60]) provided a model that considers anisotropy and elastic property evolution through elasto-plastic coupling.

A better alternative is the use of continuum damage mechanics (CDM). More detail is given on CDM in Section 3.5.2. Various models have been proposed that provide predictions of the evolution of elastic properties as a result of micro-crack evolution, but often the models describe just isotropic damage evolution if the effects of evolving elastic properties and anisotropy are considered, the descriptive models are not well developed (approaches are generally phenomenological or highly idealized and do not explicitly describe the micro-structure and its evolution). For example, Conil et al ([33]) presented a poro-plastic damage model for clay rocks, which includes damage-induced evolution of anisotropic elastic properties (decoupled from the plasticity), but the microstructure is not considered. More recently multi-scale approaches have been proposed in which the grain-scale stress-strain problem is solved explicitly at the appropriate scale using either DEM or FEM approaches, for each integration point in the model (e.g. Espinosa et al. ([49])), then, it is incorporated back into the full-scale FEM model. In those cases, the macroscopic constitutive model is just replaced by a numerical representation of the underlying grain-scale mechanics ([58], [115]).

In the approach to damage modeling that will be adopted in this thesis, micro-scale evolution of damage (micro-cracking) is explicitly modeled, as previously explained in the "modeling approach" section (4). A direct output from this model is the degradation of elastic properties and the development of elastic anisotropy. Furthermore, the evolution of the micro-crack damage is based on an energy dissipation approach such that the energy release with damage evolution, which may be related to acoustic emission energy of micro-seismic events, is another direct product.

3.5 Introduction to fracture and damage mechanics

In this section, a short introduction of fracture and damage mechanics principles is given. First are introduced concepts as "fracture energy", "energy release rate","elementary modes of rupture". Then, the passage to damage mechanics is made, the two keywords being "macroscopic damage models" and "micro-mechanical approaches".

3.5.1 Brittle fracture mechanics

The base of modern mechanics of brittle failure was put at the beginning of XX^{th} century (e.g., [67]). Considering the propagation of a preexisting crack in a glass, in 1920, Griffith affirmed that a crack in a brittle material propagates when the elastic energy released with the increase of the crack is bigger than the necessary energy to create a new surface. This concept is based on the first law of thermodynamics and on the stress analysis, initially developed by Inglis ([86]). Griffith theory has two major benefits: allows the estimation of the resistance of a brittle solid and gives a relation between material resistance to fracture and the length of the preexisting defect in solid.

The notion of "energy release rate" (G), which corresponds to the total energy released on unit crack length propagation, was introduced. G depends on the material, on the loading conditions and on the initial crack length. The propagation criterion was then given by the following formulation:

$$G < G_c \quad \text{- no propagation,} \tag{1}$$
$$G = G_c \quad \text{- propagation possible.} \tag{2}$$

where G_c is a critical value of G which corresponds to the the stress level needed for fracture propagation.

In 1957, Irwin introduced three fundamental "modes" of cracking (Figure 3.5) which have since played a very important role in the analysis of crack propagation mechanisms . In terms of movement of crack surfaces, the crack modes are classified in the following manner:

- mode I (opening): crack surfaces open in two opposite directions perpendicular to the crack plane. The propagation occurs in the plane of the crack.
- mode II (translational sliding): crack surfaces move in the same plane but perpendicular to the crack front. Shearing direction is parallel to the crack propagation plane.
- mode III (rotational sliding): crack surfaces moves in shear in the same plane and with a parallel direction to the crack front and perpendicular to the propagation direction.

A crack is considered to be propagating in mixed mode if more than one of the fundamental modes are present simultaneously.

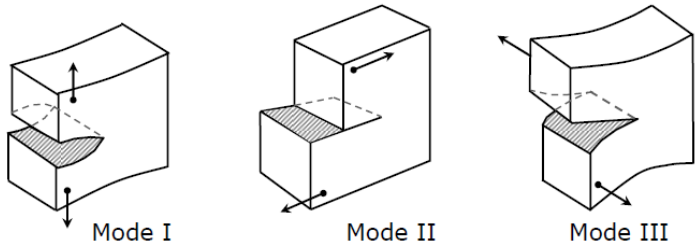

Figure 3.5: The three main modes of crack propagation [89]

.

About the same period, Irwin ([89]) made another great contribution to the understanding of crack propagation by proposing the concept of the "stress intensity factor" (K). He affirmed that a crack propagates if the singular stress distribution characterized by a critical "strength" K in the vicinity of the crack is reached. Material parameters that control crack propagation are "fracture toughness" (K_c) or critical energy value (G_c).

Energy based as well as stress intensity approach became fundamental in linear elastic fracture mechanics (LEFM).

3.5.2 Modeling principles of damage mechanics

Several sources of heterogeneities can be found at the microscopic scale (cracks, pores, grain boundaries, ...) serving as stress concentrators and leading to the formation of micro-cracks, the consequence being that the macroscopic mechanical behavior is affected. However it is impossible to consider a large number of cracks in the construction of a constitutive model. A more efficient method is to determine a mechanically equivalent homogeneous material at the macro-scale, having relatively similar properties to the heterogeneous medium.

Damage mechanics studies the evolution of a large number of small cracks by adopting an overall point of view, through a macroscopic continuous damage variable. Kachanov [90] introduced for the first time a continuous damage variable in the fracture framework, motivated by the results of a metal creep test in unidimensional loading conditions. In the 70's continuum damage mechanics theory developed very much and it was very useful in the thermodynamics case of irreversible process to show the progressive degradation of a material.

In general terms, Lemaitre et Chaboche ([97], [27]) defined damage as "progressive deterioration of material cohesion under the action of monotonic or repeated solicitations leading to the fracture of representative volume". In other words, damage corresponds to the appearance and evolution of new surfaces of non-adherence (e.g. micro-cracks at the small scale) and implies a loss in material resistance.

From the point of view of the construction procedure, one can classify the damage models in: macroscopic models and micro-mechanical approaches. The behavior of macroscopic models is described with the help of phenomenological ore highly idealized assumptions (see for instance Carol et al. ([26]), Chaboche ([28]), Dragon and Mroz ([46]),

Voyiadjis and Park ([143]) ...). In recent years, research focused on the development of macroscopic modeling starting from considerations of micro-mechanical analysis of a cracked medium through homogenization procedures. In that way, the micro-mechanical arguments, may lead to a better understanding of the phenomena observed at the macroscopic level (see the works of Dormieux and Kondo ([41, 45, 43, 44]), Andrieux et al. ([3]), Dartois et al. ([35]), Lene ([98]), Nemat-Nasser and Horii ([110]), Zhu et al. ([154]), Dascalu et co-workers ([36], [37], [38], [39], [17],[56]) ...).

However, this solution is not simple and one of the problems encountered when we trying to analyze the behavior of structures based on small specimens at laboratory level, is the scale effect (more precisely the microscopic size effect on the structure resistance). Mechanical performances of the real structures are not necessarily identical to those of laboratory specimens, therefore, the passage to structure scale needs to take into account scale effects. Another challenge it may appear is related to non-uniqueness of the solution and mesh-dependence, therefore solutions to overcome this problem need to be searched (one solution can be, for instance, time-dependence to be taken into account in the modeling approach).

In this thesis, an approach starting at the micro-scale is considered. Extensions on the previous models of Dascalu et al. ([36], [37], [38], [39], [17],[56]) will be developed, therefore an approach starting at the micro-scale is considered. Macroscopic behavior will be described using damage laws completely deduced from the micro-structure analysis without any kind of phenomenological assumptions or idealizations of the model.

3.6 Introduction to homogenization methods

An approach by homogenization is used in the present work, the behavior of the macroscopic structure being deduced from the properties of the material at the micro-scale (one example is the description of a filtration process in a porous rigid solid through a two-scale analytical approach found in [6]). Given L the macroscopic characteristic dimension, and l a characteristic length of heterogeneities, the homogenization method is possible if and only if $\frac{l}{L} << 1$. The choice of the representative elementary volume (REV) length is the subject of various discussions, (see for instance Dormieux [45]); the REV needs to be small with respect to the macroscopic structure, but it also needs to be able to consider enough heterogeneities.

Most analytical or semi-analytical homogenization methods are based on the computation of the homogenized (effective) coefficients using various methods shortly summarized below:

- based on averaging theory. This is the simplest homogenization method and consists of the computation of global properties of a heterogeneous material using the averaging technique on each composant weighted by its volume. This method is used and/or enriched by different researchers, such as Eshelby ([48]) or Mori and Tanaka ([107]).

- "self-consistent" method developed by Hill ([76]) or Christensen and Lo ([31]). In this case, global properties of the material are obtained by analytical solving of a boundary value problem on a micro-structure composed of a first phase of constituting the matrix and a second phase of a spherical or ellipsoidal inclusion. This homogenization technique works very well in the case of linear problems, but much more difficult in non-linear cases, even if interesting results were obtained by Guery ([69]) using an elasto-plastic damage model on Callovo-Oxfordian argilites, or, in more general works of Dormieux and Kondo ([41, 45, 43, 44]);

- asymptotic developments based method of displacement and stress fields with respect to a natural material length defined as the ratio between heterogeneities length and macroscopic characteristic length (Benssousan et al. [13], Sanchez-Palencia [127], Bakhvalov and Panasenko [7]).

Besides analytical homogenization methods, one can find also numerical improvements (Guedes and Kikuchi [68], Terada and Kikuchi [138], Ghosh et al. [64]). The weak point of a purely numerical homogenization technique is the computational time. Indeed, in this process, for each time increment, in each macroscopic integration (Gauss) point, a full computation on the micro-structure is necessary.

An upscaling procedure which is a combination of periodic homogenization based on asymptotic developments and energy analysis of fracture, previously developed by Dascalu et co-workers will be enriched in this thesis.

3.7 Structure of thesis

The structure of this thesis, involving this introductory chapter, four main chapters and conclusions, is briefly presented below:

- Chapter 4 - the multi-scale damage modeling method is briefly shown and previously made development are underlined. This thesis enriches results found in ([36], [37], [17]), in the case of time-independent damage models, and found in ([38], [39], [56]), for the time-dependent damage models. Key words/phrases of this chapter will be: "homogenization by asymptotic developments", "locally periodical distribution of micro-cracks", "change of scale procedure", "elementary cell", "unit cell", "homogenized coefficients", "energy analysis and deduction of damage evolution laws".

- Chapter 5 - dedicated to time independent extensions. Dascalu et al. ([36], [37], [17]) considered only brittle-type damage law and the macroscopic implementation permitted four discrete micro-crack orientations, which, once chosen, were maintained during whole simulation (no micro-crack rotation was allowed). In the beginning of the chapter, the numerical method for computing the effective elasticity of a micro-fractured medium is presented. At the microscopic level, in the case of straight micro-cracks, more orientations will be considered and a spatial interpolation procedure (which will be given in the next chapter when rotation of micro-cracks is

considered) will make possible a full description of any distribution of micro-cracks giving the length and inclination angle with respect to x-axis. Our first extension will be the introduction of a wing-type micro-crack mechanism. Second developement is given by the introduction of a damage evolution law for micro-cracks emerging from pores. Previously deduced brittle-type damage law was used to characterize macroscopic behavior of a body containing a periodic distribution of wing-type micro-cracks or of "pore-type" micro-cracks. Third development presented in our thesis is given by quasi-brittle type damage laws in both two- and three-dimensional space. In the 2D case, a distribution of periodic (square) cells containing vertical micro-cracks have been considered and, in 3D, plane squared micro-cracks in periodic volumes were taken. Key words/phrases of this chapter will be: "brittle/quasi-brittle type damage law", "wing-crack", "size effect", "fracture process zone", "snap-back", "stable/unstable micro-crack propagation".

- Chapter 6 - dedicated to time-dependent damage laws. An alternative solution to avoid the snap-back problems encountered at the macroscopic local level (which induce difficulties also at the global level) using time independent damage models was to consider a time-dependent model. Moreover, time-dependency solves mesh dependency previously encountered and provides a model able to predict phenomena like creep and relaxation associated with damage.

  The evolution of the micro-crack length during propagation is described through a sub-critical criterion governed by Charles' law. First, a simplified damage model using linear effective coefficients was deduced mostly for theoretical purposes (comparisons between analytical and numerical results for a simple problem in order for the law to be correctly implemented). Once the method was verified using the simple linear coefficients model, developments were made with a model considering propagating micro-cracks with a single, fixed orientation. Homogenized coefficients previously computed in the frame of the up-scaling procedure were used instead of linear coefficients and intrinsic anisotropy due to preference of the orientation was naturally captured. This model was previously developed by Dascalu and François ([38]), but only the macroscopic local level was taken into account. Global macroscopic implementation is the contribution of this thesis.

  Propagation in a fixed direction is not enough to simulate real processes, therefore, a more complex damage law considering rotating micro-cracks was deduced. This model was partially developed by François and Dascalu ([56]). Their main objective was the development of a complex two-scale time-dependent damage model capable to take into account both a crack propagation and its orientation. Propagation and trajectory of micro-cracks were controlled by the stress intensity factors, therefore, before introducing the damage law, a short section is dedicated to $K_{I,II}$ for straight micro-cracks. A path-independent integral method was used for the computation of SIF in [56]. In this thesis displacement correlation method is considered and comparison between the two methods is made. At the macroscopic local level we adopted the criteria for the equivalent crack from [56] in the case of opened micro-cracks, but, in the case of compressive micro-cracks, previous criteria was not enough. We give a new way of replacing the kinked crack with an equivalent straight one. Previously, all the consideration of rotating micro-cracks damage

model were made at the level of en elementary cell (macroscopic local level). Global macroscopic implementation is entirely our contribution. Key words/phrases of this chapter: "time-dependency", "Charles' law", "kinked cracks", "SIF", "rotating micro-cracks", "equivalent straight micro-cracks", "TC (trajectory corrector).

- Chapter 7 - Using the time dependent damage model including rotational micro-cracks, simulations were made at three levels: laboratory, tunnel and reservoir scales. A specific two notched geometry is used in a uniaxial compression laboratory test in the first part of the chapter with results being compared to ones obtained experimentally in [113]. Next, a simple simulation of a tunnel excavation was made, with the influence of the initial micro-crack orientation on fracture zone orientations being discussed. At the reservoir scale, oil production/CO_2 injection processes were represented through the simulation of an overburden of a reservoir under displacement imposed subsidence conditions, the specificity of this numerical application being given by the modeling of micro-seismic events and changes in seismic properties including anisotropy. Key words/phrases: "laboratory tests", "tunnel/reservoir scale", "nuclear waste disposal", "CO_2 sequestration", "overburden", "compaction/subsidence", "wave propagation", "acoustic events", "P-wave anisotropy".

The thesis finishes with a conclusions section, where we underline that our objective was achieved: a two-scale damage model where the macroscopic behavior is totally described by the micro-scopic analysis (macroscopic time dependent damage law is fully deduced on the base of homogenized coefficients and stress intensity factors computed at the micro-scopic level). This damage model takes into account all the possibilities considering micro-cracks evolving both in length and in orientation the consequence being the possibility of modeling micro-seismic events so linking "geophysics" and "geomechanics".

4 Multiscale modeling of damage

Contents

In continuum damage models, micro-cracking is represented as a degradation of elastic moduli through damage variables. In general, this has been achieved by supplementing the micro-mechanical analysis for stationary cracks by phenomenological assumptions on the evolution of damage. In recent years, many researchers have made considerable efforts to establish a link between micro-structural fracture phenomena and the corresponding macroscopic behaviors (see for instance Nemat-Nasser and Hori ([112]) for a review). Even if contributions to this topic are quite extensive, the majority of the works treat the case of non-evolving cracks, or the micro-mechanical analysis for stationary cracks supplemented by phenomenological assumptions on the evolving damage. Of course, there are exceptions and among the researchers which take into account micro-crack evolution one can cite: Andrieux et al. ([3]), Prat and Bazant ([123]), Caiazzo and Constanzo ([21]) or Pénse et al. ([121]).

Consideration of a large number of cracks in the material increases modeling difficulty. One alternative is to determine of a mechanically equivalent homogeneous material at the macro-scale, having relatively similar properties to the heterogeneous medium. Increase of efficiency in the construction of a constitutive model is given by approximation of the initial distribution of micro-cracks with a periodic one, for which the distance between two adjacent micro-cracks plays the role of an internal length.

Dascalu and co-workers ([36], [37], [38], [39], [17],[56]) proposed a new procedure to obtain micro-mechanical damage models using an upscaling procedure - a combination of periodic homogenization based on asymptotic developments (e.g., Bakhvalov and Panasenko ([7])) and micro-fracture energy analysis. Damage evolution laws are completely deduced from microstructural analysis by homogenization, without any kind of phenomenological assumption. The key to this approach is microscopic energy analysis, performed on a finite-size cell, which leads, through homogenization, to a macroscopic evolution equation for damage. In this equation a normalized micro-crack length appears as a damage variable and the cell size as a material length parameter.

The model of Dascalu et al. ([36], [37], [38], [39], [17],[56]) was formulated for quite general crack-face conditions, including frictionless contact. At the macroscopic level, the switch between the homogenized behaviors corresponding to crack opening or closure was carried out numerically. The model also allowed for different fracture energies

in tension and compression and damage irreversibility was assured by looking only for growing length solutions. The model could also describe failure initiation when the initial state is an undamaged one. Only time independent damage models were developed. A brittle-type damage law was considered, therefore, under progressive loading, a material directly passed from the undamaged (virgin) to completely damaged state. Macroscopic implementation was incomplete since only four discrete micro-crack orientation were taken (straight cracks orientated at 0°, 45°, 90° and 135° with respect to x-axis) and the trajectory of crack propagation was chosen in the first step and maintained during whole simulation.

In this thesis the following extensions of the previous models will be considered:

- any distribution of micro-cracks will be fully described by length and orientation; this will be achieved in two steps:
  - more micro-crack orientations will be considered;
  - all the discrete orientations will be spatially interpolated.
- time independent damage model class will be enriched by taking a quasi-brittle type damage law leading to progressive micro-cracking propagation (adding realism to the model since experimental observations indicate that rocks show a more gradual fracture behaviour);
- an extension to three-dimensional damage models will be also given;
- a new class of damage models will be developed: time-dependent models which help to regularize some of the limitations occuring with the time independent class (e.g. mesh dependency, macro-scopic snap-back ...). We will pass from an energy-based to a stress intensity factor - based propagation criterion. A time dependent damage model which allows rotation of micro-cracks will be set following the developments from [56].

4.1 The model problem

Consider a two-dimensional isotropic elastic medium containing a locally periodic distribution of micro-cracks. Each crack is straight with a length $2a$ and an orientation of angle θ with respect to the x_1 direction (abscissa of the referential system considered at the macro-scale). The length $2a$ and the orientation θ are assumed to vary smoothly everywhere in the elastic body. The length ε represents the size of the periodicity cell as well as the distance between two neighboring micro-cracks (Fig. 4.1).

Let $\mathcal{B}$ be the whole body, which consists of a bounded domain of $\Re^2$, containing $\mathcal{N}$ micro-cracks $\mathcal{C}_n, n = 1, \ldots, \mathcal{N}$. The solid part is defined as $\mathcal{B}_s = \mathcal{B} \backslash \mathcal{C}$, where $\mathcal{C} = \cup_{n=1}^{\mathcal{N}} \mathcal{C}_n$.

In the solid part $\mathcal{B}_s$, we have the equilibrium equation

$$\frac{\partial \boldsymbol{\sigma}_{ij}^{\varepsilon}}{\partial x_j} = 0, \tag{3}$$

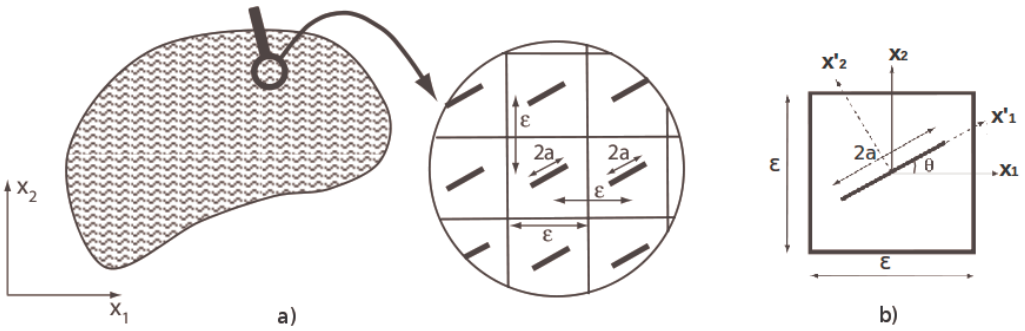

Figure 4.1: (a) Fissured medium with locally periodic microstructure. (b) Elementary cell containing one crack. ($2a$ = length of the micro-crack; ε = distance between two neighboring micro-cracks; θ = orientation of the micro-crack with respect to the x_1 axis.) (image from [56])

and the constitutive relations for the linear elasticity

$$\boldsymbol{\sigma}_{ij}^{\varepsilon} = a_{ijkl} e_{xkl}(\mathbf{u}^{\varepsilon}), \tag{4}$$

where $\mathbf{u}^{\epsilon}$ and $\boldsymbol{\sigma}^{\epsilon}$ are the displacement and the stress fields. e_{xij} is the small strain tensor defined by

$$e_{xij} = \frac{1}{2}\left(\frac{\partial u_i}{\partial x_j} + \frac{\partial u_j}{\partial x_i}\right), \tag{5}$$

and a_{ijkl} are the elastic coefficients of the solid part, which can be generally anisotropic; for an isotropic medium a_{ijkl} are given by

$$a_{ijkl} = \lambda \delta_{ij}\delta_{kl} + \mu(\delta_{ik}\delta_{jl} + \delta_{il}\delta_{jk}), \tag{6}$$

with λ and μ the Lamé coefficients.

On the crack faces we consider two possible conditions:
- traction free opening,

$$\boldsymbol{\sigma}^{\varepsilon}\mathbf{N} = 0 \quad , \quad [\mathbf{u}^{\varepsilon} \cdot \mathbf{N}] > 0; \tag{7}$$

- contact without friction,

$$[\boldsymbol{\sigma}^{\varepsilon}\mathbf{N}] = 0 \ , \ \mathbf{N} \cdot \boldsymbol{\sigma}^{\varepsilon}\mathbf{N} < 0 \ , \ \mathbf{T} \cdot \boldsymbol{\sigma}^{\varepsilon}\mathbf{N} = 0 \ , \ [\mathbf{u}^{\varepsilon} \cdot \mathbf{N}] = 0. \tag{8}$$

Here $\mathbf{N}$ is the unit normal vector, $\mathbf{T}$ is the unit tangent vector to the crack and $[\ \cdot\ ]$ denotes the jump across the crack faces.

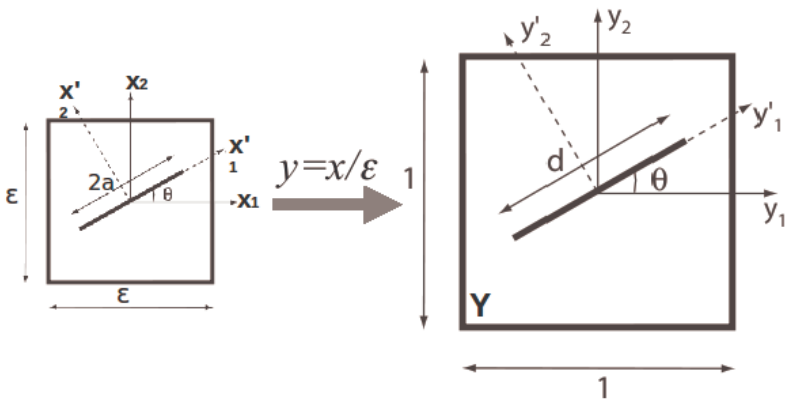

Figure 4.2: Rescaling of the unit cell to the microstructural period of the material.

4.2 Homogenization by asymptotic developments

We define a square unit cell with sides of length 1 denoted by $Y = [0,1] \times [0,1]$. The unit cell Y contains a crack CY of length d given by

$$d = \frac{2a}{\varepsilon}.$$

The damage variable d introduced here may vary between 0 (for virgin material) and $1/[\max(|\cos(\theta)|; |\sin(\theta)|)]$ (for a micro-crack that completely crosses the cell). The solid part of the unit cell is $Y_s = Y \backslash CY$.

From this unit cell containing a single micro-crack, through rescaling by a small parameter ε, the locally periodic microstructure can be constructed (Fig. 4.2). In this way εY is the natural microscopic length scale. The homogenization method requires a separation of scales. This imposes that the microscopic length $\mathbf{y}$ must be much smaller than the macroscopic length $\mathbf{x}$. The introduction of the two scales implies, for the total derivative with respect to $\mathbf{x}$,

$$\frac{d}{dx_i} = \frac{\partial}{\partial x_i} + \frac{1}{\varepsilon}\frac{\partial}{\partial y_i}.$$

Following the homogenization method by asymptotic developments (e.g. Leguillon D. and Sanchez-Palencia E. ([96]); Bakhvalov N. and Panasenko G., ([7])) the expansions of $\mathbf{u}^\varepsilon$ and $\boldsymbol{\sigma}^\varepsilon$ can be given in the form

$$\mathbf{u}^\varepsilon(\mathbf{x},t) = \mathbf{u}^{(0)}(\mathbf{x},\mathbf{y},t) + \varepsilon\mathbf{u}^{(1)}(\mathbf{x},\mathbf{y},t) + \varepsilon^2\mathbf{u}^{(2)}(\mathbf{x},\mathbf{y},t) + \ldots, \tag{9}$$

$$\boldsymbol{\sigma}^\varepsilon(\mathbf{x},t) = \frac{1}{\varepsilon}\boldsymbol{\sigma}^{(-1)}(\mathbf{x},\mathbf{y},t) + \boldsymbol{\sigma}^{(0)}(\mathbf{x},\mathbf{y},t) + \varepsilon\boldsymbol{\sigma}^{(1)}(\mathbf{x},\mathbf{y},t) + \ldots, \tag{10}$$

where $\mathbf{u}^{(i)}(\mathbf{x},\mathbf{y},t), \boldsymbol{\sigma}^{(i)}(\mathbf{x},\mathbf{y},t),\ \mathbf{x} \in \mathcal{B}_s,\ \mathbf{y} \in Y$ are smooth functions and Y-periodic in $\mathbf{y}$ (See Fig. 4.3).

Substituting the expansion (9) and (10) into (3), we get for different orders of ε,

$$\frac{\partial \boldsymbol{\sigma}_{ij}^{(-1)}}{\partial y_j} = 0, \quad \frac{\partial \boldsymbol{\sigma}_{ij}^{(-1)}}{\partial x_j} + \frac{\partial \boldsymbol{\sigma}_{ij}^{(0)}}{\partial y_j} = 0, \quad \frac{\partial \boldsymbol{\sigma}_{ij}^{(0)}}{\partial x_j} + \frac{\partial \boldsymbol{\sigma}_{ij}^{(1)}}{\partial y_j} = 0. \tag{11}$$

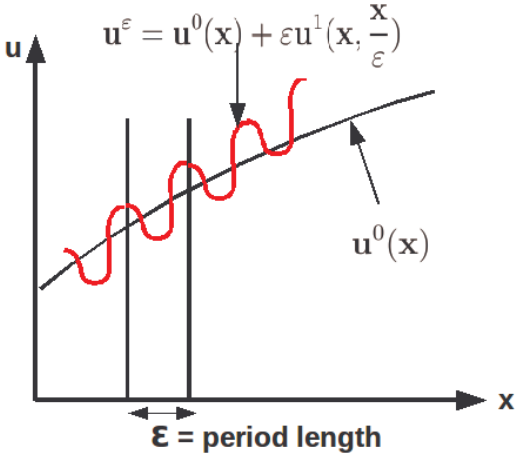

Figure 4.3: Homogenization by asymptotic development

From those relations we can deduce

$$\begin{aligned}
\boldsymbol{\sigma}_{ij}^{(-1)} &= a_{ijkl} e_{ykl}(\mathbf{u}^{(0)}), \\
\boldsymbol{\sigma}_{ij}^{(0)} &= a_{ijkl}(e_{xkl}(\mathbf{u}^{(0)}) + e_{ykl}(\mathbf{u}^{(1)})), \\
\boldsymbol{\sigma}_{ij}^{(1)} &= a_{ijkl}(e_{xkl}(\mathbf{u}^{(1)}) + e_{ykl}(\mathbf{u}^{(2)})),
\end{aligned} \tag{12}$$

and the boundary conditions

$$\boldsymbol{\sigma}_{ij}^{(-1)} N_j = 0, \quad \boldsymbol{\sigma}_{ij}^{(0)} N_j = 0, \quad \boldsymbol{\sigma}_{ij}^{(1)} N_j = 0, \qquad \text{on} \quad CY. \tag{13}$$

Bringing together 9 - 13, if the order of ε is 0, we get the boundary-value problem, for $\mathbf{u}^{(0)}$

$$\frac{\partial}{\partial y_j}\left(a_{ijkl} e_{ykl}(\mathbf{u}^{(0)})\right) = 0, \qquad \text{in} \quad Y_s \tag{14}$$

$$\left(a_{ijkl} e_{ykl}(\mathbf{u}^{(0)})\right) N_j = 0, \qquad \text{on} \quad CY. \tag{15}$$

Moreover, $\mathbf{u}^{(0)} = \mathbf{u}^{(0)}(\mathbf{x}, t)$ is independent of $\mathbf{y}$, such that it represents the *macroscopic displacement field*.

The first approximation boundary-value problem is given to the first order in ε,

$$\frac{\partial}{\partial y_j}\left(a_{ijkl} e_{ykl}(\mathbf{u}^{(1)})\right) = 0, \qquad \text{in} \quad Y_s, \tag{16}$$

$$a_{ijkl} e_{ykl}(\mathbf{u}^{(1)}) N_j = -a_{ijkl} e_{xkl}(\mathbf{u}^{(0)}) N_j, \qquad \text{on} \quad CY. \tag{17}$$

In each regime (opening (+) or contacting (-) of the micro-crack) the first order perturbation, $\mathbf{u}^{(1)}$, can be given in the form

$$\mathbf{u}_{\pm}^{(1)}(\mathbf{x}, \mathbf{y}, t) = \xi_{\pm}^{pq}(\mathbf{y}) e_{xpq}(\mathbf{u}^{(0)})(\mathbf{x}, t), \tag{18}$$

where $\xi(\mathbf{y})$ are the *characteristic functions* representing elementary deformation modes of the unit cell ([7], [96]).

The difference between the microscopic states of contact and opening are obtained from the orientation of the force vector, deduced from the force-type source term of Eq. (17), with respect to the crack line. In the space of macroscopic deformations, these two states induce a separation of the space $\mathbf{R}$ of deformations $e_{x11}, e_{x12}, e_{x22}$ into two subregions $\mathbf{R}^{\pm}$ defined by

$$\mathbf{R}^{\pm} = \left\{ \mathbf{e_x} | \quad N_i a_{ijkl} e_{xkl}(\mathbf{u}^{(0)}) N_j \gtrless 0 \right\}. \tag{19}$$

The relations (16)-(17) are equivalent to the cell problem

$$\frac{\partial}{\partial y_j} \left(a_{ijkl} e_{ykl}(\xi_{\pm}^{pq}) \right) = 0, \qquad \text{in} \quad Y_s, \tag{20}$$

$$a_{ijkh} e_{ykh}(\xi_{\pm}^{pq}) N_j = -a_{ijpq} N_j, \qquad \text{on} \quad CY, \tag{21}$$

for every p and q and with periodicity conditions on the cell boundary.

In the following the *mean value operator* is employed; this is defined by

$$\langle \cdot \rangle = \frac{1}{|Y|} \int_{Y_s} \cdot \, dy, \tag{22}$$

where $|Y|$ is the measure of Y.

By applying the mean value operator, we get

$$\frac{\partial}{\partial x_j} \langle \boldsymbol{\sigma}_{ij}^{(0)} \rangle = 0 \tag{23}$$

and

$$\Sigma_{ij}^{(0)} \equiv \langle \boldsymbol{\sigma}_{ij}^{(0)} \rangle = C_{ijkl} e_{xkl}(\mathbf{u}^{(0)}), \tag{24}$$

where

$$C_{ijkl}^{\pm}(d, \theta) = \frac{1}{|Y|} \int_{Y_s} \left(a_{ijkl} + a_{ijmn} e_{ymn}(\xi_{\pm}^{kl}) \right) \, dy \tag{25}$$

are the effective homogenized coefficients. The effective coefficients are symmetric in i, j, k and l (see [17] for proof).

Putting together the Eqs. (23) and (24), the homogenized or averaged equation of equilibrium is given as

$$\frac{\partial}{\partial x_j} \left(C_{ijkl} e_{xkl}(\mathbf{u}^{(0)}) \right) = 0. \tag{26}$$

4.3 Energy analysis

In this subsection the damage law based on the micromechanical energy balance in an elementary volume containing one evolving micro-crack is deduced. Initially the trajectory of the propagation is considered to be regular and known. For a symmetric propagation

of the crack with respect to its center, the micro-crack evolution is completely described by the variation of its length.
In the following we will analyze the energy balance during crack evolution for general boundary conditions on the crack lips. We consider the general relation:

$$[\boldsymbol{\sigma}^{(0)}\mathbf{N}] = 0. \tag{27}$$

The derivation of damage law follows the two propositions given below.

Proposition 1: Under the continuity conditions (27), the energy balance during the evolution of the micro-crack, has the following form,

$$\frac{d}{dt}\int_{Y_s}\frac{1}{2}a_{ijkl}e_{ykl}(\mathbf{u}^{(1)})e_{yij}(\mathbf{u}^{(1)})dy + \mathcal{G}_y\dot{d} = \int_{CY} a_{ijkl}e_{ykl}(\mathbf{u}^{(1)})N_j[\dot{u}_i^{(1)}]ds_y, \tag{28}$$

with

$$\mathcal{G}_y = \lim_{r\to 0}\int_{\Gamma Y_r}\mathbf{e}\cdot\mathbf{b}(\mathbf{u}^{(1)})\mathbf{n}\; ds_y, \tag{29}$$

where

$$\begin{aligned} b_{ij}(\mathbf{u}^{(1)}) &= U(\mathbf{u}^{(1)})\delta_{ij} - \boldsymbol{\sigma}_{ik}(\mathbf{u}^{(1)})\frac{\partial u_k^{(1)}}{\partial y_j}, \\ U(\mathbf{u}^{(1)}) &= \frac{1}{2}a_{ijkl}e_{ykl}(\mathbf{u}^{(1)})e_{yij}(\mathbf{u}^{(1)}), \\ \boldsymbol{\sigma}_{ik}(\mathbf{u}^{(1)}) &= a_{iklm}e_{ylm}(\mathbf{u}^{(1)}). \end{aligned} \tag{30}$$

ΓY_r represents a circle of an infinitesimal radius, r, surrounding the crack tip.
Proposition 2: With $[\boldsymbol{\sigma}_{ij}^{(0)}N_j] = 0$ on the crack lips CY of evolving length $d(t)$ and fixed orientation θ, we have

$$\frac{1}{2}\dot{d}\frac{dC_{ijkl}}{dd}e_{xkl}(\mathbf{u}^{(0)})e_{xij}(\mathbf{u}^{(0)}) + \mathcal{G}_y\dot{d} + \frac{d}{dt}\int_{CY}\frac{1}{2}\boldsymbol{\sigma}_{ij}^{(0)}N_j[\mathbf{u}_i^{(1)}]ds_y - \int_{CY}\boldsymbol{\sigma}_{ij}^{(0)}N_j[\dot{\mathbf{u}}_i^{(1)}]ds_y = 0. \tag{31}$$

Proposition 1 and *Proposition 2* are two intermediate key results fundamental in the deduction process of the damage evolution law.

4.4 Damage evolution law

Starting with relation (31) and using the properties of the homogenized solution plus the relation between the energy release rate at different scales, the damage law can be deduced.
First, the integrals in (31) can be expressed in terms of the characteristic functions ξ_i^{pq},

$$\begin{aligned} &\frac{d}{dt}\int_{CY}\frac{1}{2}\boldsymbol{\sigma}_{ij}^{(0)}N_j[u_i^{(1)}]ds_y = \\ &\dot{d}\frac{d}{dd}\left(\frac{1}{2}\int_{CY}a_{ijkl}\left(\delta_{mk}\delta_{nl} + e_{ykl}(\xi^{mn})\right)N_j[\xi_i^{pq}]ds_y\right)e_{xmn}(\mathbf{u}^{(0)})e_{xpq}(\mathbf{u}^{(0)}) + \\ &\int_{CY}a_{ijkl}\left(\delta_{mk}\delta_{nl} + e_{ykl}(\xi^{mn})\right)N_j[\xi_i^{pq}]ds_y e_{xmn}(\mathbf{u}^{(0)})e_{xpq}(\dot{\mathbf{u}}^{(0)}), \end{aligned} \tag{32}$$

and

$$\int_{CY} \boldsymbol{\sigma}_{ij}^{(0)} N_j[\dot{u}_i^{(1)}] ds_y =$$

$$\int_{CY} a_{ijkl} \left(\delta_{mk}\delta_{nl} + e_{ykl}(\xi^{mn})\right) N_j[\xi_i^{pq}] ds_y \; e_{xmn}(\mathbf{u}^{(0)}) e_{xpq}(\dot{\mathbf{u}}^{(0)}) +$$

$$\int_{CY} a_{ijkl} \left(\delta_{mk}\delta_{nl} + e_{ykl}(\xi^{mn})\right) N_j[\dot{\xi}_i^{pq}] ds_y e_{xmn}(\mathbf{u}^{(0)}) e_{xpq}(\mathbf{u}^{(0)}). \tag{33}$$

Substituting these relations into (31), we obtain

$$\dot{d} \left(\frac{1}{2} \frac{dC_{ijkl}}{dd} e_{xkl}(\mathbf{u}^{(0)}) e_{xij}(\mathbf{u}^{(0)}) + \mathcal{G}_y + \right.$$

$$\frac{d}{dd} \left(\frac{1}{2} \int_{CY} a_{ijkl} (\delta_{mk}\delta_{nl} + e_{ykl}(\xi^{mn})) N_j[\xi_i^{pq}] ds_y \right) e_{xmn}(\mathbf{u}^{(0)}) e_{xpq}(\mathbf{u}^{(0)})) -$$

$$\left. \int_{CY} a_{ijkl} \left(\delta_{mk}\delta_{nl} + e_{ykl}(\xi^{mn})\right) N_j \left[\frac{d\xi_i^{pq}}{dd} \right] ds_y e_{xmn}(\mathbf{u}^{(0)}) e_{xpq}(\mathbf{u}^{(0)}) \right) = 0. \tag{34}$$

For crack evolution a Griffith-type energy criterion is considered, such that propagation occurs only when the energy release rate at the crack tip $\mathcal{G}^\varepsilon$ reaches the critical energy threshold $\mathcal{G}_f$,

$$\mathcal{G}^\varepsilon = \mathcal{G}_f. \tag{35}$$

$\mathcal{G}_f$ may be a function of the crack length and velocity.

The energy release rate is given as:

$$\mathcal{G}^\varepsilon = \lim_{r \to 0} \int_{\Gamma_r} \mathbf{e} \cdot \mathbf{b}(\mathbf{u}^\varepsilon) \mathbf{n} \; ds, \tag{36}$$

where Γ_r is a circle of an infinitesimal radius surrounding the crack tip, $\mathbf{e}$ is the unit vector in the propagation direction and

$$b_{ij}(\mathbf{u}^\varepsilon) = \frac{1}{2} a_{mnkl} e_{xkl}(\mathbf{u}^\varepsilon) e_{xmn}(\mathbf{u}^\varepsilon) \delta_{ij} - \boldsymbol{\sigma}_{jk}^\varepsilon u_{k,i}^\varepsilon \tag{37}$$

is the Eshelby configurational stress tensor.

Thus, it can be shown that $\mathcal{G}_y$ can be expressed with $\mathcal{G}^\varepsilon$ and, if a propagation criterion (35) is used in the relation giving the energy balance, a damage law is obtained under the form

$$\dot{d} \left(\frac{1}{2} \frac{dC_{ijkl}}{dd} e_{xkl}(\mathbf{u}^{(0)}) e_{xij}(\mathbf{u}^{(0)}) + \frac{\mathcal{G}_f}{\varepsilon} + I_{mnpq} e_{xmn}(\mathbf{u}^{(0)}) e_{xpq}(\mathbf{u}^{(0)}) \right) = 0, \tag{38}$$

where

$$I_{mnpq} = \frac{d}{dd} \left(\frac{1}{2} \int_{CY} a_{ijkl} (\delta_{mk}\delta_{nl} + e_{ykl}(\xi^{mn})) N_j[\xi_i^{pq}] ds_y \right) -$$

$$\int_{CY} a_{ijkl} \left(\delta_{mk}\delta_{nl} + e_{ykl}(\xi^{mn})\right) N_j \left[\frac{d\xi_i^{pq}}{dd} \right] ds_y, \tag{39}$$

and G_f represents the critical fracture energy which can be given by a constitutive function.

Remarks:

- In the relation (38), we used the symmetry property of integrals I_{ijkl} in i and j, k and l, but also the symmetry with respect to pair (i,j) and (k,l). This property is valid under the same hypothesis as that of the symmetry of C_{ijkl} and can be proven in a similar manner (see [17]).

- Equation (38) is totally expressed in terms of the homogenized solution $\mathbf{u}^{(0)}$. The effective coefficients (25) and the integrals (39) can be a priori computed using the solution on the unit cell for different length and orientations of the crack.

- In this thesis the case of frictionless unilateral contact and opening conditions on micro-cracks are taken into account. This implies that integrals I_{ijkl} are vanishing.

In (38), we used the relation between the energy release rate with respect to each scale ([17]),

$$\mathcal{G}^{\varepsilon} = \varepsilon \, \mathcal{G}_y. \tag{40}$$

This relation allows the introduction of the microstructural length parameter ε in the damage law.

To summarize, the problem to be solved can be defined in terms of the "homogenized equilibrium equation" (Eq. 26) and "the damage law" plus the "irreversibility condition" as given below:

- Homogenized equilibrium equation:

$$\frac{\partial}{\partial x_j}(C_{ijkl} e_{xkl}(\mathbf{u}^{(0)})) = 0, \tag{41}$$

- The damage law (under Kuhn - Tucker loading - unloading form):

$$\begin{aligned} &\frac{dd}{dt} \geq 0, \qquad -\frac{1}{2}\frac{dC_{ijkl}(d)}{dd} e_{xkl}(\mathbf{u}^{(0)}) e_{xij}(\mathbf{u}^{(0)}) \leq \frac{G_f}{\varepsilon}, \\ &\left(\frac{1}{2}\frac{dC_{ijkl}(d)}{dd} e_{xkl}(\mathbf{u}^{(0)}) e_{xij}(\mathbf{u}^{(0)}) + \frac{G_f}{\varepsilon}\right) \dot{d} = 0. \end{aligned} \tag{42}$$

In the equation (42) $\frac{dd}{dt} \geq 0$ expresses the irreversibility condition.

4.5 Summary

In this chapter, the starting point for the developments of this thesis have been introduced. This starting point is the previous development by Dascalu and co-workers ([36], [37], [17]) in the framework of time-independence. The theory on which these developments are based was shortly outlined. Section 4.1 introduced the model problem and Section 4.2 described the change-of-scale procedure through asymptotic developments of displacement and stress fields. Energy analysis at the level of a periodicity cell was shortly presented in Section 4.3 and the general damage law under Kuhn - Tucker loading-unloading form was given in Section 4.4.

Before the developments to be presented in this thesis, the model of Dascalu et al., only cosidered time independent damage models with brittle-type damage and the macroscopic implementation only permitted four discrete micro-crack orientations, which, once chosen, was maintained during whole simulation (no micro-crack rotation was allowed). In this thesis several development directions of this approach were followed. At the microscopic level, in the case of straight micro-cracks, more orientations will be used and wing-type mechanics (in particular) and kinked-type micro-cracks (in general) will be considered. A new time independent damage model capable of describing progressive micro-cracking propagation will be deduced (quasi-brittle type damage law) and an extension to three-dimensions will be also given.

Finally, time-dependence concept will be introduced both to overcome some limitation arising in the case of the time independent damage models (mesh independency, snap-back behavior, ...) but also for the capacity of this models to describe time effects due to damage (for instance creep or relaxation). We will pass from an energy-based to a stress intensity factor - based propagation criterion. A time dependent damage model which allows rotation of micro-cracks will be set.

5 Time independent damage models

Contents

The present chapter is dedicated to time independent damage models in which the classical criteria of crack propagation, such as the Griffith criterion [67] is used. The chapter begins with the implementation of the microscopic level (characteristic functions and homogenized coefficients), detailed in Section 5.1. Brittle type of crack propagation will be considered in the case of wing-type micro-cracks in Section 5.2. Quasi-brittle type of crack propagation in two- and three-dimensional spaces will be considered (Sections 5.5 and 5.6).

In all the 2D models further developed in this chapter, vertical cracks are taken, meanwhile, for the 3D extension, square, horizontal plane cracks are considered. We consider an isotropic elastic material with the Young's modulus E = 2 GPa. Poisson's ratio $\nu = 0.3$ in general, but in the case of wing-type or "pore-type" cracks, to add more realism, $\nu = 0.1$. The critical threshold of the fracture energy $G_{cr} = 100\ J/m^2$ and the length of the elementary cell ε = 1e-5 m.

5.1 Numerical implementation of the micro-structure

The aim of this thesis is to implement two-scales damage models in the Finite Element software FEAP ([136]). We start at the microscopic level by computing the characteristic function and the homogenized coefficients. In some cases, microstructure was implemented also in the Matlab code, therefore results could be compared.

Computation of the characteristic functions ξ^{ij}

The first step in the development of any damage model, at the microscopic scale, the characteristic functions ξ^{ij} are computed by solving the elementary boundary-value problems (20) and (21) presented in the theoretical part. Iso-parametric 3-node-triangles were used and ξ^{ij} were computed in traction and in compression. The periodicity condition was implemented and, in the case of compression, several algorithms (Penalty method, Augmented Penalty method based on Uzawa algorithm) have been tried, the best being considered Lagrange Multipliers Method.

Fig. 5.1 shows the schematic representation of the basic deformation modes of a unit cell containing one vertical micro-cracks, under tension conditions. The purpose is to check the crack opening and the effect of periodicity on the unit cell. The periodicity is clear in figure 5.1 *b*) which corresponds to ξ^{12}. In the 5.1 *a*), corresponding to ξ^{11}, or 5.1 *c*), corresponding to ξ^{22}, the periodicity condition is less evident due to equal but opposite forces applied on the crack lips. This aspect combined with the periodicity conditions leads to zero displacement on the exterior boundaries.

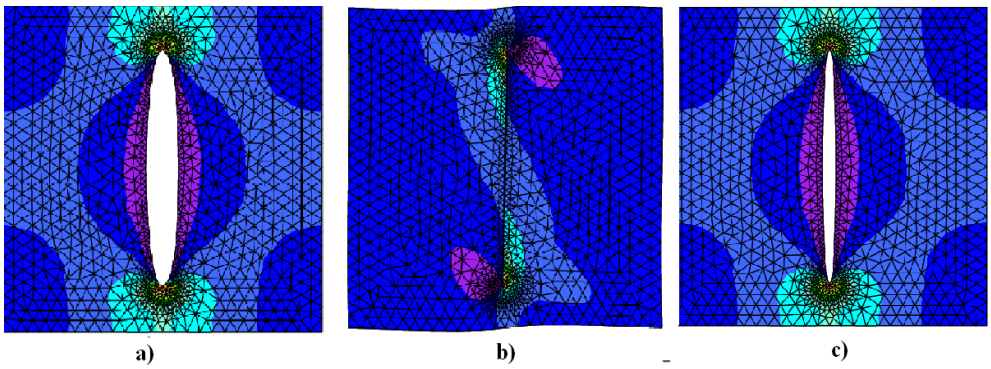

Figure 5.1: Schematic view of the basic deformation modes which corresponds to the characteristic functions: a) ξ^{11} , b) ξ^{12} and c) ξ^{22}

Homogenized coefficients - interpolation for a fixed orientation

The analytical form of $C^{\pm}_{ijkl}(d,\theta)$ is given, in the previous section, by Eq. 25. d is the damage variable, θ is the orientation of the micro-crack. The couple (d, θ) and $\pm$ establish the state of the crack (open or close).

Any damage model implies that the effective tensor is known at each moment. In other words it is necessary to have the values of the effective coefficients for each length

d and each orientation θ. This goal has been achieved in the following manner:
Step 1: - 13 orientation have been chosen in the interval of $[0°, 180°]$ (θ = 15°, 30°, 45°, ...);
Step 2: - 11 discrete micro-crack lengths have been taken into account for each orientation ($[0.0; 0.05; 0.1; 0.2; 0.3; 0.4; 0.5; 0.6; 0.7; 0.8; 0.9; 0.95]$);
Step 3: - 2 micro-crack states have been considered (tension and compression).
Step 4: - for each orientation of the micro-crack, interpolation on interval $[O, 1]$ of the computed values of homogenized coefficients in each particular d has been made.

There is a fifth step (surface interpolation on interval $[0°, 180°]$*) to be taken, but it will be detailed in the next chapter, when kinking micro-crack concept will be introduced.*

It must be reminded that the homogenized coefficients are computed for each of the 3 elementary deformation modes. Given the symmetry in indexes ([17]) only 6 values are necessary to be computed: C_{1111}, C_{1211}, C_{2211} (from the problem $\xi^{\mathbf{11}}$), C_{1212} (from $\xi^{\mathbf{12}}$) and, respectively C_{2122}, C_{2222} (from $\xi^{\mathbf{22}}$). Step 1 - 3 imply the creation of a large database of effective coefficients (6 (coefficients) x 13 (orientations) x 11 (micro-crack lengths) x 2 (micro - crack states)). This goal was achieved using Finite Element program FEAP developed at Berkeley University ([136]) and the results were verified also with COMSOL code ([32]).

Figure 5.2 presents the interpolation procedure of C_{1111} in a case of a vertical crack for all d between 0 (virgin cell) and 1 (completely crossed cell by micro-crack). The blue line corresponds to a 9 degree polynomial which interpolate the best all the discrete values (red disks). Several tests have been made to obtain a good interpolation for each micro-crack. Two aspects needed to be considered in order to define the best interpolation scheme

- The interpolation should give the minimum fitting error (e.g. defined by least square fitting);
- Derivatives should be smooth and decrease continuously.

If one of the two conditions is not respected, numerical errors are introduced into the subsequent modeling.

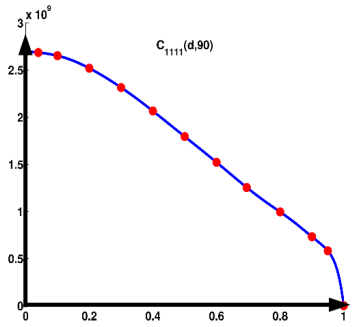

Figure 5.2: Exemplification of the interpolation procedure in the case of $C^{p}_{1111}(d, 90°)$.

In Figure 5.3 the effective response ($C_{ijkl}(d, 0)$) of a tensile case is given. The homogenized coefficients are represented as functions of the damage variable d. The presence of

the micro-cracks leads to induced anisotropy, the resulting effective elastic response being orthotropic. We note the non-linear dependence of the homogenized coefficients on the damage variable d. With an horizontal crack line, the loss of rigidity with the damage variable increases is maximum when the unit cell is loaded in the vertical direction (22), i.e. perpendicular to the crack (coefficients C_{2222} and C_{1122}) while the rigidity is much less affected when loaded in the horizontal direction (11), i.e. parallel to the crack (coefficient C_{1111}). This is characteristic of the damage-induced anisotropy observed at the macroscopic scale.
For d = 1 corresponding to a unit cell completely crossed by the micro-crack, the residual value of C_{2222} and C_{1122} is not zero because the micro-crack tips are assumed to remain in contact, even for fully damaged state. It produces a residual rigidity of the unit cell.

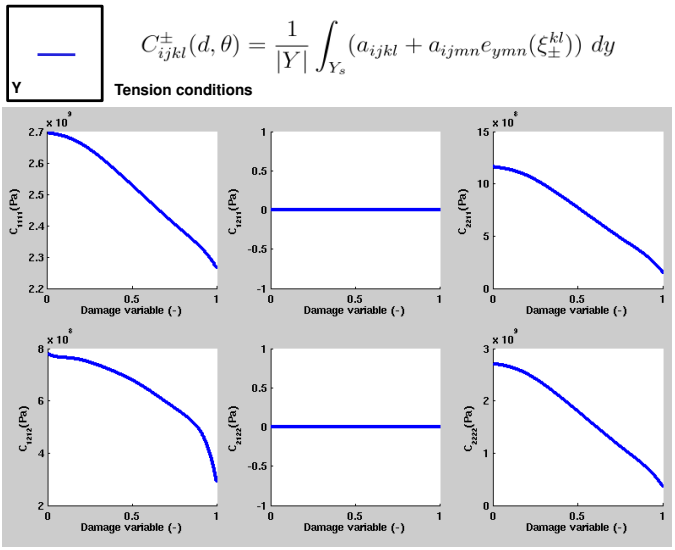

Figure 5.3: Homogenized coefficients for horizontal crack orientation for elastic parameters E = 2 GPa a and $\nu = 0.3$ in tension case

In the end of this part, Figure 5.4 presents an example of the polynomial expressions of each of the 12 coefficients (6 in tensile mode and 6 in compressive mode) $C_{ijkl}(d,\theta)$ obtained by linear interpolation between the polynomial curves for the interpolation. The isotropic matrix is characterized by the Young modulus $E = 2GPa$ and the Poisson ratio $\nu = 0.3$. The presence of micro-cracks induces anisotropy in the effective behavior.

The micro-structure is completely described by the characteristic functions and by the homogenized coefficients. The next step of the modeling is to use C_{ijkl} in the elementary cell (of length ε) tests in order to characterize the local macroscopic behaviour, and, in the end, global macroscopic simulations are run.

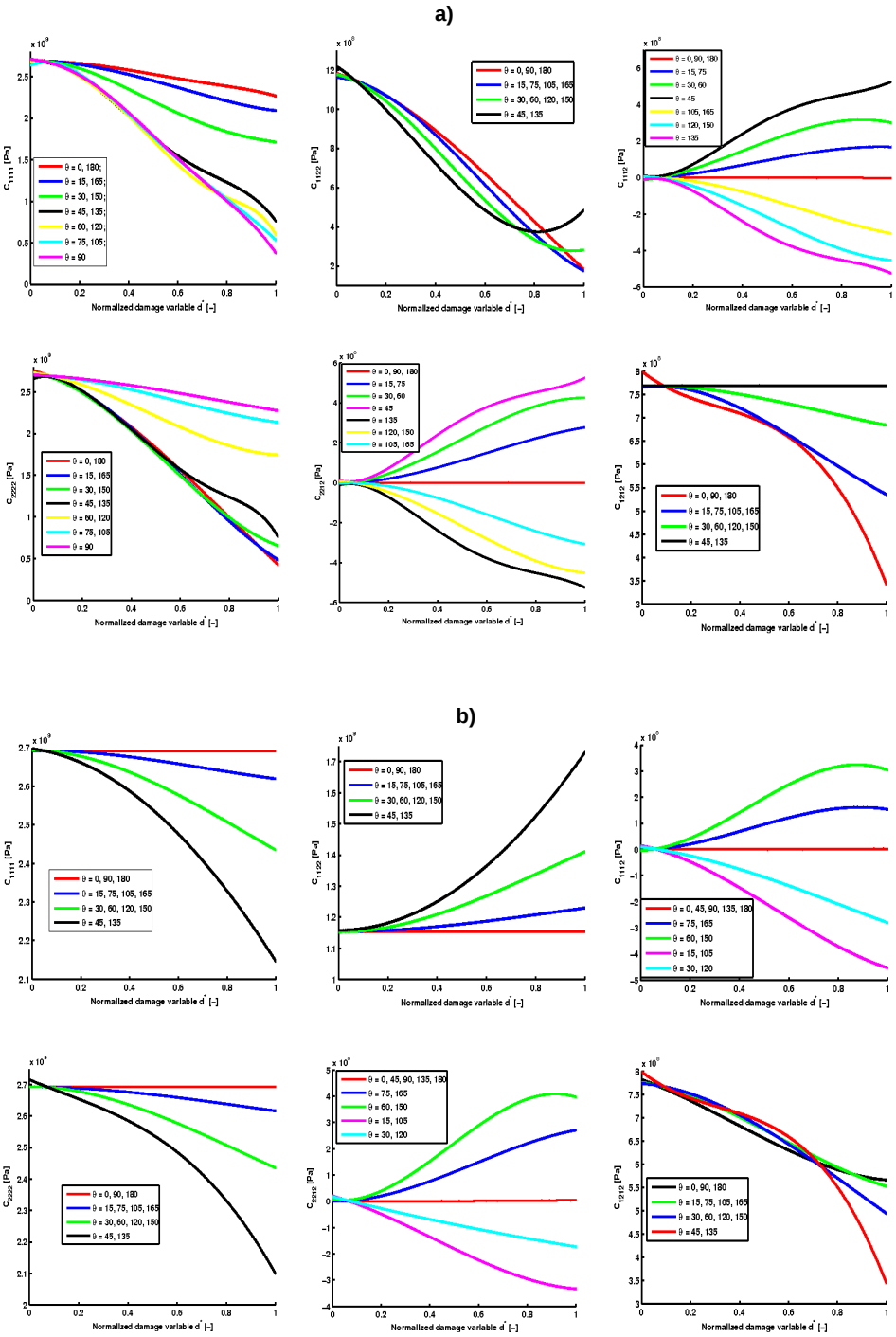

Figure 5.4: Evolution of the homogenized coefficients with respect to the normalized damage variable d^* and the crack orientation θ: a) Opening conditions of the crack lips and b) Contact conditions of the crack lips.

5.2 Damage law for wing - type cracks

In this section we develop a new two-scale damage model for the wing-type micro-mechanisms of compression fracture. This damage model is obtained by extending the two-scale homogenization by asymptotic developments method described in Chapter 4. The new approach is illustrated in the case of brittle damage for a uniaxial splitting test. The X-FEM method is used for the numerical modeling of the macro-crack initiation and growth.

At the local level the size dependency of the critical energy (i.e. the energy of damage initiation) on the elementary cell length ε is underlined by proving the Hall-Petch rule.

The outline of the section is as follows: Subsection 5.2.2 is dedicated to the theory of our model and it has four subsections:
1) the presentation of the problem statement;
2) the homogenization approach;
3) the homogenized elastic coefficients;
4) the damage law.
Subsection 5.2.5 starts with a small introduction about the tests we run meanwhile subsubsection 5.2.6 presents the microscopic approach and 5.2.7 the macroscopic study. The section finishes with discussions.

5.2.1 Background

Bobet ([19]) classified the type of cracks which can occur during tests (Figure 5.5). First, tensile crack (usually mode I) appears at the tip of the notch and propagates on a curvilinear trajectory. These cracks propagates in a stable manner and tends to align to the maximum principal compressive stress. In the literature, different names were given to them: "Tensile Fractures" - Lajtai ([94]); "Branch Cracks" - Brace and Bombolakis ([20]); "Primary Cracks" - Ingraffea and Heuze ([87]); "Primary Forward Tensile Cracks (PFTCs)" par Huang et al. ([82]); "wing cracks" - Shen et al. ([129]), Li et al. ([100]), Bobet ([19]).

After an additional loading, new cracks, generally called "Secondary Cracks" appear. They are often described as shear cracks (or shear zones). They start at the end of the notch and can have two possible directions:
(1) coplanar to the preexisting crack, or
(2) on the same inclination as the wing but in opposite direction.
In literature they are cited as: "Inclined, Normal Shear Fractures and Shear Zone" - Lajtai ([94]; "Secondary Cracks" - Ingraffea and Heuze ([87]), Li et al. ([100]); "Forward and Backward Shear Belts (FSBs and BSBs)" - Huang et al. ([82]).

Several models have been developed to describe the mechanism leading to the wing-crack propagation in the quasi-static case. The first characterization of this mechanism is found in the work of Brace and Bombolakis ([20]). Since then, many researchers studied and modeled them (Hoek and Bienawski ([78]), Horii and Nemat-Nasser ([80], [79]),

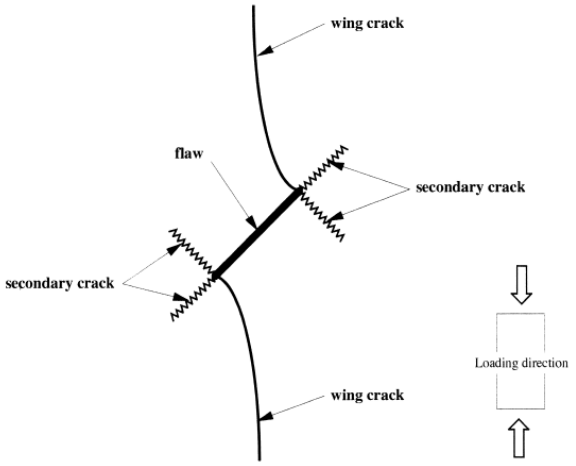

Figure 5.5: Classification of the commonly observed crack in a rock specimen with pre-existing notch ([19]).

Fanella and Krajcinovic ([51]), ...). The experiments showed that the cracks start at the tips of a pre-existing flaw and propagate as the load increases, with the tendency of alignment with the direction of the principal compressive stress, making a "wing".

Other researchers investigate the wing-type crack and the brittle failure in solids using the continuum theory (also called interaction field theory, IFT) for short- and long-term behavior of hard rock under compression. One of these approaches was made by Miura et al. ([106]) who considered the mechanisms of crack growth of IFT and a uniform stress state in order to give a simple way of predicting the creep failure of rocks in compression. Since a uniform stress state is assumed, the continuum theory (IFT) is reduced to an evolution problem of two interacting cracks.

Recently, the previous models were extended to take into account dynamic effects. Nemat-Nasser and Deng ([111]) considered an array of interacting and dynamically growing wing crack to estimate the rate-dependent dynamic damage evolution in brittle solid. The effect of strain rate is included through the dependence of dynamic stress intensity factor (SIF) on the speed of the crack growth. Huang et al.([83], [84]) proposed an approach that combines damage theory with dynamic growth of the wing cracks, in order to model the dynamic fracture process of rock specimens subjected to high strain rate uniaxial compressive loading. Their model assumed dilute pre-existing crack distributions with no interaction, but Paliwal et al. ([119]) tried to overcome this inconvenience and developed a methodology based on a complex variable approach to obtain an approximate local effective stress field as a manifestation of micro-crack interactions.

Our model, which will be presented in the following, focuses on a single wing-type crack and, by the use of the homogenization through asymptotic developments method previously presented, starting from the micro-scale study, we model the macroscopic behavior.

5.2.2 Damage model

In Chapter 4 the two-scale homogenization through asymptotic developments method for straight micro-cracks has been described. In this section we consider a particular case of a 2D isotropic elastic medium containing wing type micro-cracks. As before, the distribution is assumed to be locally periodic and each micro-crack (composed by a main inclined crack with two branches) is considered in one periodicity cell of length ε (Fig. 5.6). The length ε also represents the distance between centers of two neighbor micro-cracks.

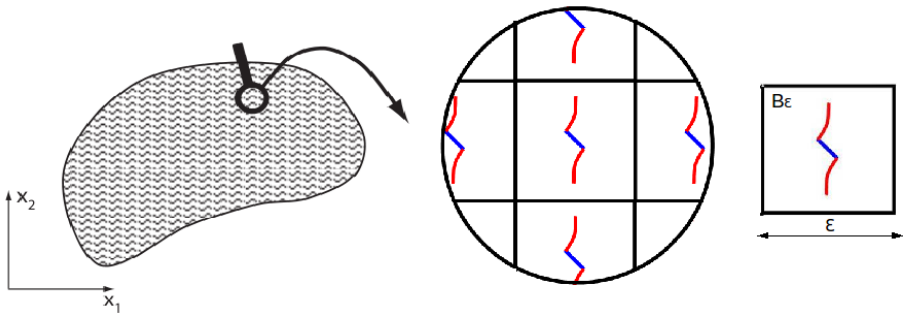

Figure 5.6: Fissured medium with locally periodic micro-structure containing wing-type micro-cracks.

Starting from the initial model of Brace et al. ([20]), many researchers proposed models for the wing-type crack. These models have in common the fact that the extension of the branches is controlled by the shear of the initial inclined crack. We adopt here the model of Fanella and Krajcinovic ([51]) and we implement their idea in our framework of homogenization through asymptotic developments. In the model we assume a the sliding crack of length $2a$ (Fig. 5.7). Using a Coulomb type criterion, the shear stress denoted by τ_s reduced by the presence of the friction, is given by ([51]):

$$\tau_s = (\sigma^\varepsilon_{11} - \sigma^\varepsilon_{22})\frac{sin(2\phi)}{2} - \mu_f(\sigma^\varepsilon_{11}\cos^2(\phi) + \sigma^\varepsilon_{22}\sin^2(\phi)), \tag{43}$$

where μ_f is the friction coefficient, ϕ is the angle made by the inclined crack with the horizontal axis and $\boldsymbol{\sigma}^\varepsilon$ is the stress field (Eq. 3).

The shear on the crack induces a traction zone at the crack tips, the consequence being the appearance of branches (wings) that progressively align to the maximum loading direction.

Following Fanella and Krajcinovic ([51]) we replace the sliding crack and the branches by an equivalent vertical crack. On the central part of the equivalent crack I^ε, of length $2a\alpha\sin\phi$, we apply a concentrated pressure $P(e_x(\mathbf{u}^\varepsilon))$ on the normal direction (Fig. 5.7 (b)). The value of the pressure $P(e_x(\mathbf{u}^\varepsilon))$ is given by the relation below:

$$P(e_x(\mathbf{u}^\varepsilon)) = \begin{cases} 2\int_0^{a\alpha\sin\phi} \frac{\tau_s}{\alpha}\cot\phi dx, & e_{x22}(\mathbf{u}^\varepsilon) \neq \mathbf{0}, \\ 0, & e_{x22}(\mathbf{u}^\varepsilon) = \mathbf{0}. \end{cases} \tag{44}$$

We considered $\mu_f = 0.3$, $\phi = 45$ degrees and $\alpha = 0.25$. The correction factor α was introduced by the authors of [51] in order to recover the correct stress intensity factor for wing cracks as obtained in the numerical study of Horii and Nemat-Nasser ([80]).

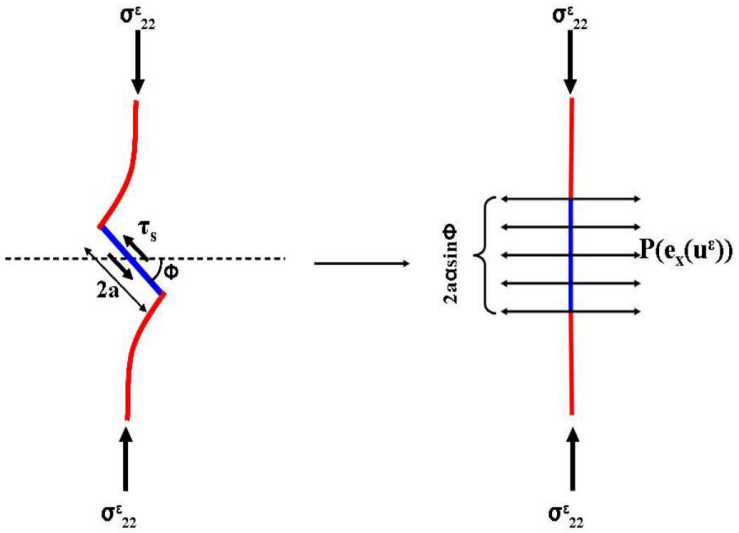

Figure 5.7: Micro-crack model under compression: a) sliding crack model; b) Vertical equivalent model.

Let $\mathcal{B}$ denote the initial heterogeneous medium represented by a bounded two-dimensional domain with a smooth external boundary, $\mathcal{C}$ the union of all the micro-cracks inside $\mathcal{B}$, $\mathcal{B}_s$ the solid part of $\mathcal{B}$. Let remind that the central part of the vertical equivalent crack, which replace the sliding cracks, is denoted I^ε.

Like in Section 4, in $\mathcal{B}_s$ we have the equilibrium equations and the elasticity law (Eq. 3).

On the central part of the crack I^ε the concentrated pressure $P(e_x(u^\varepsilon))$ is acting, due to the replacement of the original sliding crack. The rest of the crack boundaries are traction-free:

$$\sigma^\varepsilon \mathbf{N} = 0 \text{ on } \mathcal{C} \text{ - } I^\varepsilon \tag{45}$$

$$\sigma^\varepsilon \mathbf{N} = P(e_x(\mathbf{u}^\varepsilon)) \text{ on } I^\varepsilon \tag{46}$$

We denote by $\mathbf{N}$ the normal unit vector on the crack faces.

5.2.3 Homogenization by asymptotic developments

Similar to the case of straight micro-cracks, we assume that we can reproduce the locally periodic microstructure of the body through a unit cell $Y = [0,1] \times [0,1]$, by rescaling with the small parameter ε. In this way the period of the material is εY, as in Fig. 5.8. The two distinct scales are represented by the variables $\mathbf{x}$ and $\mathbf{y} = \frac{\mathbf{x}}{\varepsilon}$ defined previously. In the unit cell Y, we denote the lips of the two cracks by CY, the central part which replace the sliding crack by I and the solid part by Y_s. We introduce the normalized damage parameter $\frac{d^\varepsilon}{\varepsilon}$ representing the scaled distance between the two crack tips in the cell.

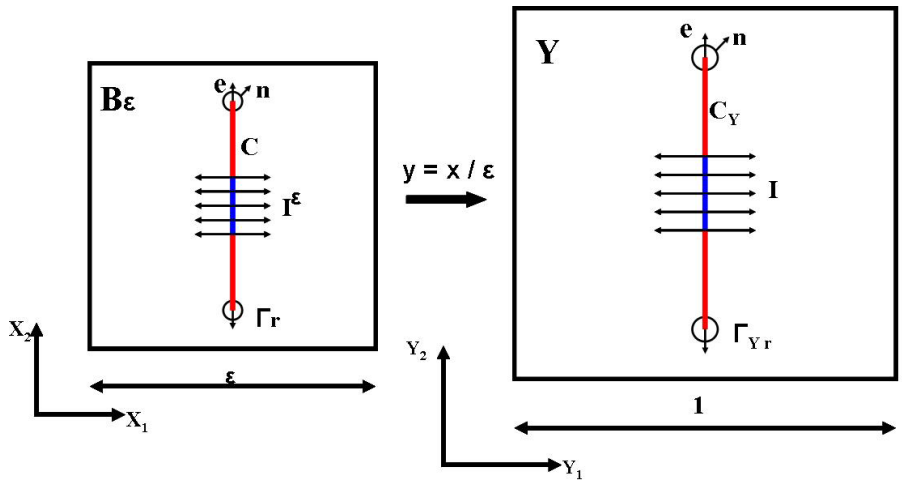

Figure 5.8: Material period and the unit cell.

Following the method of asymptotic homogenization and using the expansion of $\mathbf{u}^\varepsilon$ and $\boldsymbol{\sigma}^\varepsilon$ (Eq. 9 - 10) into Eq. 3 and the boundary conditions (45), we obtain the boundary value problems for the different orders of ε, formulated on the unit cell Y.

As for the case of straight micro-cracks, we prove that $\mathbf{u}^{(0)} = \mathbf{u}^{(0)}(\mathbf{x}, t)$ being a trully macroscopic displacement field.

For a given $e_x(\mathbf{u}^{(0)})$ corresponding to a compression loading ($e_{x22}(\mathbf{u}^{(0)}) < 0$), the boundary-value problem for the first microscopic correction $\mathbf{u}^{(1)}$ is deduced as:

$$\frac{\partial}{\partial y_j}(a_{ijkl}e_{ykl}(\mathbf{u}^{(1)})) = 0 \qquad \text{in } Y_s, \tag{47}$$

$$a_{ijkl}(e_{ykl}(\mathbf{u}^{(1)}) + e_{xkl}(\mathbf{u}^{(0)}))n_j = 0 \text{ on } CY^{\pm}\text{–I}^{\pm}, \tag{48}$$

$$a_{ijkl}(e_{ykl}(\mathbf{u}^{(1)}) + e_{xkl}(\mathbf{u}^{(0)}))n_j = -P(e_x(u^{(0)}))n_i \text{ on I}^{\pm}. \tag{49}$$

where $\pm$ denote the values on the two faces of the micro-cracks.

The microscopic correction $\mathbf{u}^{(1)}$ has a linear dependence of the *macroscopic deformations* $e_{xpq}(\mathbf{u}^{(0)})$:

$$\mathbf{u}^{(1)} = \xi^{11}e_{x11}(\mathbf{u}^{(0)}) + 2\xi^{12}e_{x12}(\mathbf{u}^{(0)}) - \xi^{22}e_{x22}(\mathbf{u}^{(0)}). \tag{50}$$

The characteristic functions $\boldsymbol{\xi}^{pq}(\mathbf{y}, d, a)$ are elementary solutions of (47-49), for a given length of the crack and for particular macroscopic deformations having the only non-vanishing component $e_{x11} = 1$ or $e_{x12} = 1$ or $e_{x22} = -1$, respectively. As before, $\boldsymbol{\xi}^{22}(\mathbf{y}, d, a)$ corresponds to a compressive macroscopic deformation applied to the unit cell through the internal boundary conditions (49).

By applying the mean value operator to the boundary value problem corresponding to the 1^{st}-order of ε, we can deduce the homogenized equilibrium equation (Eq. 23) and the effective elastic law (Eq. 24) where $C_{ijkl}(d, a)$ are the effective homogenized coefficients. The general formula is given by Eq. (25), except for the homogenized coefficients corresponding to $\boldsymbol{\xi}^{22}$ given by: $C_{1122} =< a_{1122} - a_{1111}e_{y11}(\xi^{22}) - a_{1122}e_{y22}(\xi^{22}) >$ and $C_{2222} =< a_{2222} - a_{1111}e_{y11}(\xi^{22}) - a_{1122}e_{y22}(\xi^{22}) >$.

5.2.4 The damage law

In the previous section (4), the damage law was deduced in the form:

$$\dot{d}(\frac{1}{2}\frac{dC_{ijkl}}{dd}e_{xkl}(\mathbf{u}^{(0)})e_{xij}(\mathbf{u}^{(0)}) + \frac{\mathcal{G}_c}{\varepsilon} + I_{mnpq}e_{xmn}(\mathbf{u}^{(0)})e_{xpq}(\mathbf{u}^{(0)})) = 0 \tag{51}$$

where

$$I_{mnpq} = \frac{d}{dd}\left(\frac{1}{2}\int_{CY} a_{ijkl}(\delta_{mk}\delta_{nl} + e_{ykl}(\xi^{mn}))N_j[\xi_i^{pq}]ds_y\right) - \int_{CY} a_{ijkl}\left(\delta_{mk}\delta_{nl} + e_{ykl}(\xi^{mn})\right)N_j\left[\frac{d\xi_i{}^{pq}}{dd}\right]ds_y \tag{52}$$

Usually, the integrals $I_{mnpq}(d)$ are computed on the entire crack lips ([37]), but in our specific case, are computed only on the central part, I. The non null integrals entering the damage laws are given by

$$I_{22pq}(\xi^{22}) = \frac{d}{dd}(\frac{1}{2}\int_I P^{22}n_j[\xi_i^{pq}]dS_y). \tag{53}$$

where

$$P^{22} = 2\int_0^{a\alpha\sin\phi}\frac{\mu + 0.3(\lambda+\mu)}{\alpha}\cot\phi dx. \tag{54}$$

In the previous formula $\lambda = \frac{\nu E}{(1+\nu)(1-2\nu)}$ and $\mu = \frac{E}{2(1+\nu)}$, with E = Young modulus and ν = Poisson ratio.

5.2.5 Numerical implementation - size effects

In this section we give numerical results we obtained using the homogenization by asymptotic developments technique on the special case of wing-type cracks. Elastic isotropic material described by Young's modulus $E = 2GPa$ and Poisson's ratio $\nu = 0.1$ was used.

Starting from the elementary deformation modes, we compute the homogenized coefficients which are functions of the damage parameter, d. For the computation of C_{ijkl} and I_{ijkl} we used the finite element program FEAP, developed by the Berkeley University [136]. For the homogenized coefficients we used triangular finite elements with three Gauss points for the displacements. The modeling of the wing-type micro-cracks demands the computation of C_{ij11}, in tension, for ξ^{11}, and those corresponding to the $\boldsymbol{\xi}^{22}$ (C_{ij22}) in compression. For these coefficients we used Lagrange Multipliers method for the contact between the crack faces.

In Fig. 5.9 we represent the homogenized coefficients and I_{2222}. Nonlinear dependence of the homogenized coefficients on the damage variable d is observed as well as the anisotropy in the effective response, induced by the presence of the micro-crack.

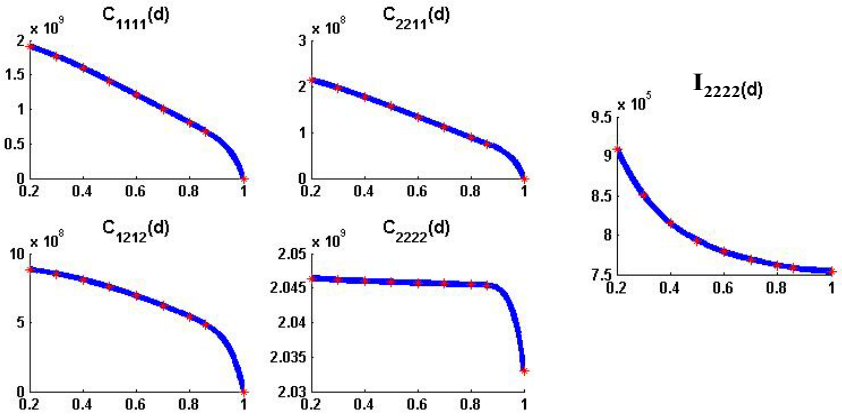

Figure 5.9: Left)Homogenized coefficients; Right) The integral I_{2222} of the jumps over the crack faces

5.2.6 Local macroscopic behavior

Using the numerical implementation previously done for the standard crack model, some elementary damage tests have been simulated. The most significant result at the local macroscopic level is the size dependence of the damage yield stress on the microscopic cell size ε shown in Fig.5.10 (a). For each value of ε, the uniaxial tests were controlled through the applied deformation e_{x22}. We note that for smaller cell sizes we have higher thresholds of damage initiation.

In Fig. 5.10 (b), the critical macroscopic stress Σ_{22} is represented for different microscopic lengths ε which shows the linear dependence of the damage yield stress on $\varepsilon^{-\frac{1}{2}}$. This prove a size effect of the Hall-Petch type.

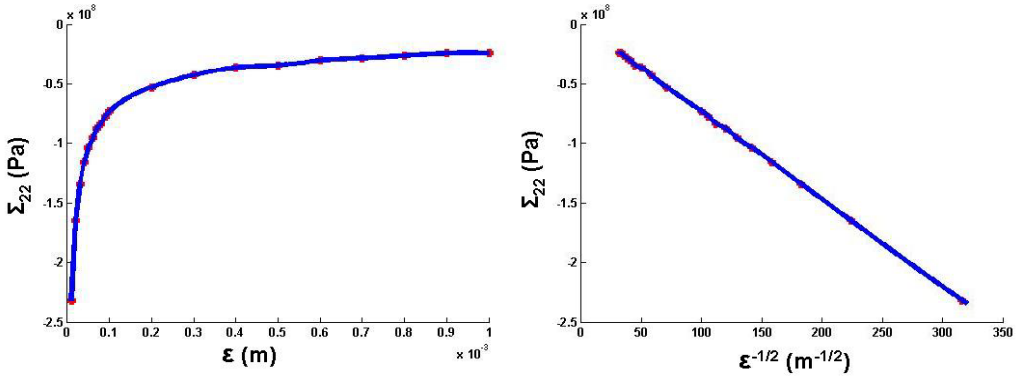

Figure 5.10: a) Size effect - dependency of the critical stress Σ_{22} on the macro-parameter ε; b) The Hall-Petch relation

5.2.7 Global macroscopic behavior

At the macroscopic global level an axial splitting test was performed. Axial splitting failure begins when a primary crack undergoes sliding, creating wing-type cracks at the tips of the primary crack. The failure occurs when a series of cracks extend and finally link together and split the material.
The geometry and the material parameters are shown in Fig. 5.11. A vertical displacement u_2 is applied uniformly on the top boundary, while the bottom boundary is fixed on the y-direction. We considered a specimen with the height of 0.1 m and the width half of the height (0.05 m). The computation were made on a uniform mesh with 9 x 21 elements, and the cell size $\varepsilon = 1e-3$ m. The material parameters were kept from the micro-scale analysis (Young's modulus = 2 GPa and Poisson's ratio = 0.1).

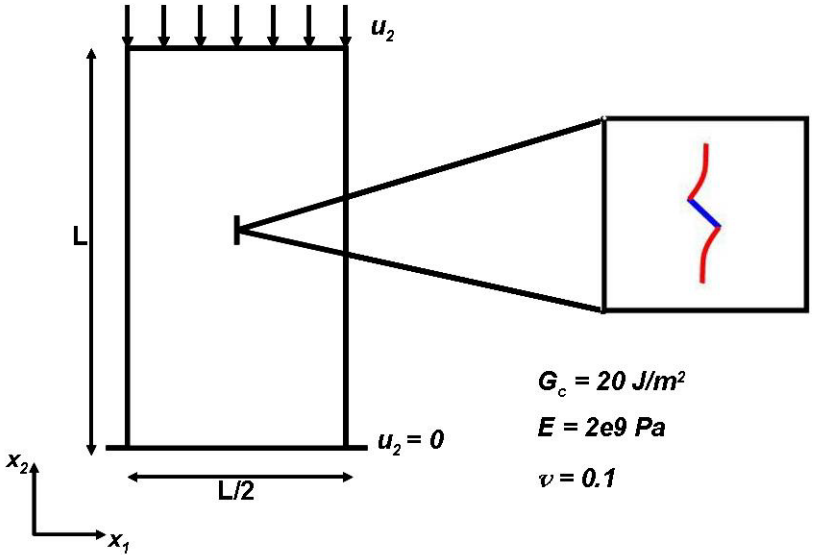

Figure 5.11: Geometry and material parameters used in the axial splitting test

In the test we run at the macroscopic level, usually we have difficulties when the damage parameter d is close to 1 because the assumption of the periodicity may not be verified anymore. In order to avoid that, we have used the extended finite element technique (XFEM) to introduce a displacement discontinuity. In that way the standard finite element approximation is enriched by Heaviside type discontinuities in the direction of the micro-crack found in the integration point of the element: (see Fig. 5.12)

$$u^h(x) = \sum_{i \in E_I} u_i N_i(x) + \sum_{j \in E_J} a_j N_j(x) H(x) \tag{55}$$

where the first term is the standard interpolation with E_I the set of all the nodes of the mesh, while the second term represents the discontinuous enrichments with $E_J \subset E_I$ the set of nodes that belong to elements in which discontinuities are introduced (see Fig. 5.12). Here H(x) is a generalized Heaviside function, taking the value +1 on one side and -1 on the other side of the line of discontinuity.

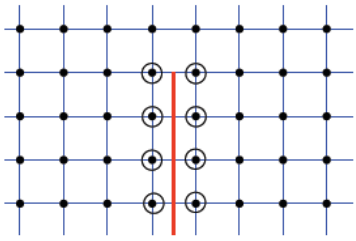

Figure 5.12: Enriched nodes progressively introduced in damaged elements through the XFEM technique

The modeled experiment consists in progressive compressing uniaxial loading in the y-direction. In Figure 5.13 we represent the horizontal global stress over the specimen vs. the applied displacement. We denote by (a) - (d) initiation and growth of the macro-fracture until failure. In the model a symmetrical propagation with respect to the horizontal axis is assumed. From a certain critical value, we observe the rapid propagation of the crack.

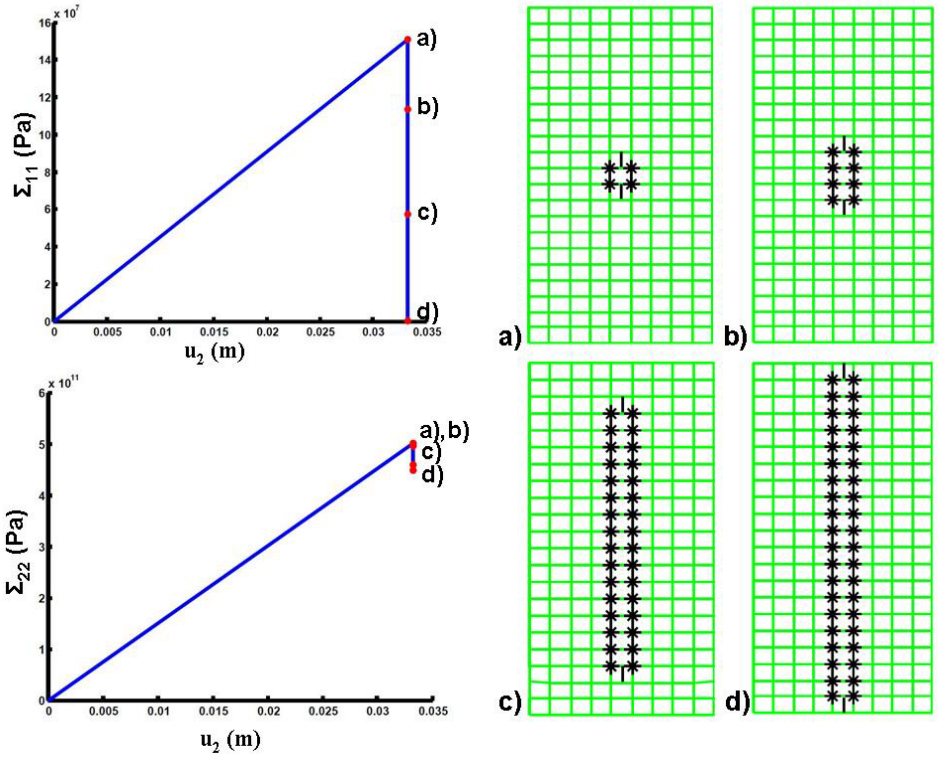

Figure 5.13: Axial splitting test. Horizontal global stress over the specimen vs. the applied displacement, with points corresponding to initiation (a) and growth (b,c,d) of the splitting macro-crack.

5.2.8 Summary and discussions

A micro-mechanical damage model deduced with homogenization by asymptotic developments technique in the case of the wing-type cracks was developed. Micro-cracks equivalence procedure is the one given by Fanella and Krajcinovich, but used in the homogenization framework. At the microscopic level the critical energy (i.e. the energy of damage initiation) is underlined by proving the Hall-Petch relation, connecting the size dependency and the yield stress. At the macroscopic level a uniaxial test in compression was performed to show the fracture of a specimen starting from a wing type crack which is growing and propagating along the stress direction.

5.3 Damage law for microcrack emerging from pores

5.3.1 Introduction

Experimental observations show that, in brittle specimens under uniaxial compression, macroscopic cracks nucleate and grow in the direction parallel to that of the axial loading. At the origin of such macroscopic crack formation are small-scale heterogenities, like wing cracks or pore-like flaws. Under compression loading, such micro-heterogeneities lead to tensile micro-crack formation, growth and coalescence to macroscopic cracks.

Since the origin of this particular type of failure is a micromechanical one, the proper way to describe these phenomena is a multiscale approach. In this section, we study the macroscopic compression-induced splitting failure in brittle materials based on a two-scale damage model that accounts for micro-crack nucleation and growth from pre-existing small-size pores, like grain boundary cavities.

Previously, Dascalu and co-workers ([37], [38], [39], [56]) proposed a damage model for straight micro-cracks based on a change of scale linking the microscopic energy dissipated by the micro-fracture and the macroscopic energy release rate. A material length characterizing the size of the micro-structure was present in the deduced damage equations, therefore the model was able to describe size effects.

In this section we propose a model which considers the complex case of small-scale geometry with cracks propagating from pores and evolving symmetrically with respect to them in the direction of the loading. The damage evolution laws are deduced based on the method developed in [37], [38], [39], [56] and taking into account the porous microstructure ([5], [102]). The pore size is considered as a parameter of the model and the damage variable is defined as the normalized length of the flaw composed by the pore and the two symmetric micro-cracks connected with it (Fig.5.14).

We illustrate the capacity of the deduced damage model to predict axial splitting failure by the numerical simulation of an axial compression test. Extended finite elements (XFEM) are used for the numerical treatment of the nucleation and growth of macro-cracks, as the result of micro-fracture evolution. The influence of the porosity and the micro-structural size of the material on the macroscopic response will also be emphasized.

5.3.2 The model problem

Consider a two-dimensional isotropic elastic medium containing a large number of small pores and micro-cracks developed from pores. The distribution is assumed to be locally periodic, so that one can locally find a periodicity cell, of length ε, containing one pore with two symmetric cracks (see Fig.5.14). The length ε, also representing the mutual distance between centers of neighbor pores, is a characteristic size of the micro-structure. The two cracks are assumed to be straight and of total length $d^\varepsilon - \phi_P$, where ϕ_P is the diameter of the pore.

We consider the initial heterogeneous porous medium represented by a bounded two-dimensional domain $\mathcal{B}$ with a smooth external boundary. In the solid part we have the equilibrium equations

$$\frac{\partial \sigma_{ij}^\varepsilon}{\partial x_j} = 0, \qquad \sigma_{ij}^\varepsilon = a_{ijkl} e_{xkl}(\mathbf{u}^\varepsilon), \tag{56}$$

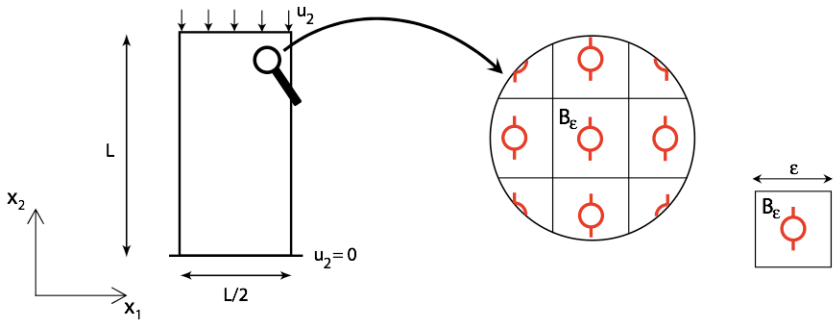

Figure 5.14: Fissured porous medium with locally periodic microstructure.

where $\mathbf{u}^\varepsilon$ and $\boldsymbol{\sigma}^\varepsilon$ are the displacement and the stress fields, a_{ijkl} are the elasticity coefficients and where we denoted the strain tensor $e_{xij}(\mathbf{u}^\varepsilon) = \frac{1}{2}(\frac{\partial u_i^\varepsilon}{\partial x_j} + \frac{\partial u_j^\varepsilon}{\partial x_i})$ with respect to x coordinates. We assume that the boundaries of the cracks and of the pores are traction-free :

$$\boldsymbol{\sigma}^\varepsilon \mathbf{N} = 0 \tag{57}$$

where $\mathbf{N}$ is the unit normal vector.

5.4 Homogenization by asymptotic developments

Local periodicity is assumed, that is around each point one can find a small neighborhood in which the microstructure is periodically distributed, with periods of size ε (see Fig.5.14). Such a distribution can be reproduced from the unit cell $Y = [0,1] \times [0,1]$ by rescaling with the small parameter ε so that the period of the material is εY, as in Fig. 5.15. The parameter ε, which is assumed to be small enough with respect to the characteristic dimensions of the whole body, is the microscopic length scale. This condition allow us to distinguish between microscopic and macroscopic variations. The two distinct scales are represented by the variables $\mathbf{x}$, which are referred to as *macroscopic variables* and the variables $\mathbf{y} = \mathbf{x}/\varepsilon$, referred to as *microscopic variables*.

In the unit cell Y, we denote the union of the two cracks by CY, the pore boundary by CP and the solid part by Y_s. We introduce the damage parameter $d = d^\varepsilon/\varepsilon$, representing the scaled distance between the two crack tips in the cell, and the scaled diameter of the pore $a_P = \phi_P/\varepsilon$. For a given pore diameter a_P, the time evolution of the damage variable d describes the symmetric micro-crack propagation. This evolution will make the object of the next section, here we consider only a spatial distribution $d = d(\mathbf{x})$ of "frozen" micro-crack lengths, at a given instant of time t.

According to the method of asymptotic homogenization (e.g. [13],[96]), we look for expansion of $\mathbf{u}^\varepsilon$ and $\boldsymbol{\sigma}^\varepsilon$ in the form given by (58) and (59):

$$\mathbf{u}^\varepsilon(\mathbf{x},t) = \mathbf{u}^{(0)}(\mathbf{x},\mathbf{y},t) + \varepsilon\mathbf{u}^{(1)}(\mathbf{x},\mathbf{y},t) + \varepsilon^2\mathbf{u}^{(2)}(\mathbf{x},\mathbf{y},t) + \varepsilon^3\mathbf{u}^{(3)}(\mathbf{x},\mathbf{y},t) + \dots \tag{58}$$

$$\boldsymbol{\sigma}^\varepsilon(\mathbf{x},t) = \frac{1}{\varepsilon}\boldsymbol{\sigma}^{(-1)}(\mathbf{x},\mathbf{y},t) + \boldsymbol{\sigma}^{(0)}(\mathbf{x},\mathbf{y},t) + \varepsilon\boldsymbol{\sigma}^{(1)}(\mathbf{x},\mathbf{y},t)\dots \tag{59}$$

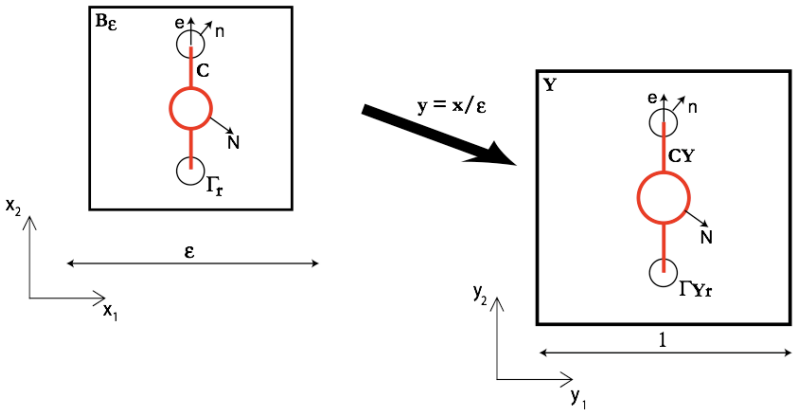

Figure 5.15: Material period and the unit cell.

where $\mathbf{u}^{(i)}(\mathbf{x},\mathbf{y},t), \boldsymbol{\sigma}^{(i)}(\mathbf{x},\mathbf{y},t),\ \mathbf{x}\in\mathcal{B}_s,\ \mathbf{y}\in Y$ are smooth functions and Y-periodic in $\mathbf{y}$.

Substituting the expansions into the eq. (56) and the boundary conditions (57) we obtain boundary value problems for the different orders of ε, formulated on the unit cell Y. It can be shown (e.g. [96]) that the function $\mathbf{u}^{(0)} = \mathbf{u}^{(0)}(\mathbf{x},t)$ is independent of $\mathbf{y}$ variable, representing the *macroscopic displacement* field.

For given $e_x(\mathbf{u}^{(0)})$ in the case of open traction-free cracks, we deduce the following boundary-value problem for the displacement field $\mathbf{u}^{(1)}$:

$$\frac{\partial}{\partial y_j}\left(a_{ijkl}e_{ykl}(\mathbf{u}^{(1)})\right) = 0, \qquad \text{in } \ Y_s \tag{60}$$

$$a_{ijkl}e_{ykl}(\mathbf{u}^{(1)})N_j = -a_{ijkl}e_{xkl}(\mathbf{u}^{(0)})N_j, \qquad \text{on } \ CY^{\pm}\cup CP \tag{61}$$

and with periodicity conditions on the external boundary of the cell. In the last relation $CY^{\pm}$ denote the two faces of the micro-cracks.

The microscopic correction $\mathbf{u}^{(1)}$ has a linear dependence of the *macroscopic deformations* $e_{xpq}(\mathbf{u}^{(0)})$:

$$\mathbf{u}^{(1)} = \xi^{11}e_{x11}(\mathbf{u}^{(0)}) + 2\xi^{12}e_{x12}(\mathbf{u}^{(0)}) - \xi^{22}e_{x22}(\mathbf{u}^{(0)}) \tag{62}$$

The characteristic functions $\boldsymbol{\xi}^{pq}(\mathbf{y},d,a_P)$ are elementary solutions of (60-61), for a given length of the crack, for a given size of the pore and for particular macroscopic deformations having the only non-vanishing component $e_{x11}=1$ or $e_{x12}=1$ or $e_{x22}=-1$, respectively. Remark that $\boldsymbol{\xi}^{22}(\mathbf{y},d,a_P)$ corresponds to a compressive macroscopic deformation applied to the unit cell through the internal boundary conditions (61).

Consider the mean value operator $\langle\cdot\rangle = \frac{1}{|Y|}\int_{Y_s}\cdot\, dy$, where $|Y|$ is the measure of Y. By applying the mean value operator to the boundary value problem corresponding to the 1^{st}-order of ε, we can deduce (e.g. [96]) the homogenized equilibrium equation

$$\frac{\partial}{\partial x_j}\Sigma^{(0)}_{ij} = 0 \tag{63}$$

where $\Sigma^{(0)}_{ij} = \langle\sigma^{(0)}_{ij}\rangle = \langle a_{ijkl}(e_{xkl}(\mathbf{u}^{(0)}) + e_{ykl}(\mathbf{u}^{(1)}))\rangle$ is the *macroscopic stress*.

The effective elastic law is obtained as

$$\Sigma_{ij}^{(0)} = C_{ijkl}(d, a_P) e_{xkl}(\mathbf{u}^{(0)}), \tag{64}$$

where $C_{ijkl}(d, a_P)$ are the homogenized coefficients given generally by the formula

$$C_{ijkl}(d, a_P) = \frac{1}{|Y|} \int_{Y_s} (a_{ijkl} + a_{ijmn} e_{ymn}(\xi^{kl}))\ dy \tag{65}$$

except for the coefficients calculated computed with $\boldsymbol{\xi}^{22}$ which are given by : $C_{1122} =< a_{1122} - a_{1111} e_{y11}(\xi^{22}) - a_{1122} e_{y22}(\xi^{22}) >$ and $C_{2222} =< a_{2222} - a_{1111} e_{y11}(\xi^{22}) - a_{1122} e_{y22}(\xi^{22}) >$.

These formulae allow for the computation of the homogenized coefficients as functions of the damage variable.

5.4.1 The damage law

For the modeling of the evolution of damage we adopt a quasi-static description, in which the previous equilibrium problem should be completed with damage evolution equations. In this section we remind the main steps to be followed in obtaining the damage equation through the homogenization of the microscopic balance of energy for propagating micro-cracks. For the details of the procedure the reader is reffered to [37], [38].

For the initial heterogeneous problem, the *fracture energy release rate* during crack extension can be expressed as

$$\mathcal{G}_\varepsilon = \lim_{D_\epsilon \to O} \int_{\partial D_\varepsilon} \mathbf{e} \cdot \mathbf{b}(\mathbf{u}^\varepsilon) \mathbf{n}\ ds \tag{66}$$

where D_ε is a disk of infinitesimal radius, surrounding the crack tip O, with $\mathbf{n}$ the outward normal to the disk D_ϵ, $\mathbf{e}$ is the unit vector in the propagation direction (see Fig. 5.15) and $b_{ij}(\mathbf{u}^\varepsilon) = \frac{1}{2} a_{mnkl} e_{xkl}(\mathbf{u}^\varepsilon) e_{xmn}(\mathbf{u}^\varepsilon) \delta_{ij} - \sigma_{jk}^\varepsilon u_{k,i}^\varepsilon$ is the Eshelby configurational stress tensor.

The propagation of each micro-crack in the elastic body is governed by the following laws:

$$\mathcal{G}_\varepsilon \leq \mathcal{G}_f\ ;\ \dot{d}^\varepsilon \geq 0\ ;\ \dot{d}^\varepsilon (\mathcal{G}_\varepsilon - \mathcal{G}_f) = 0 \tag{67}$$

where a superimposed dot denotes time derivative and $\mathcal{G}_f$ is the critical fracture energy of the material. These relations should be completed with the reduced dissipation inequality:

$$\mathcal{D}_f \equiv \mathcal{G}_\varepsilon \dot{d}^\varepsilon \geq 0 \tag{68}$$

Assuming the symmetric extension of micro-cracks, from (60)-(61) and the periodicity conditions we deduce ([37], [38]) for $\dot{d} \neq 0$, the global balance of energy on the unit cell :

$$\frac{\mathcal{G}_\varepsilon}{\varepsilon} = -\frac{1}{2} \frac{dC_{ijkl}(d, a_P)}{dd} e_{xkl}(\mathbf{u}^{(0)}) e_{xij}(\mathbf{u}^{(0)}) \tag{69}$$

where the right member $Y_d \equiv -\frac{1}{2} \frac{dC_{ijkl}(d, a_P)}{dd} e_{xkl}(\mathbf{u}^{(0)}) e_{xij}(\mathbf{u}^{(0)})$ is the *damage energy release rate*. We note that this relation is entirely deduced from microstructural assumptions,

without any assumptions on the scaling of energy. This scaling with ε is naturally appearing in the derivation of the damage equation (69). For evolving damage, the previous relation shows that the microstructural length ε makes the link between the surface energy dissipated during micro-crack propagation and damage energy dissipated per unit volume. This energy scaling property will assure the presence of the internal length ε in the damage law.

Using (69) from the micro-crack evolution laws (67) we deduce the *damage laws :*

$$Y_d \leq \frac{\mathcal{G}_f}{\varepsilon} \ ; \ \dot{d} \geq 0 \ ; \ \dot{d}(Y_d - \frac{\mathcal{G}_f}{\varepsilon}) = 0 \tag{70}$$

$$\mathcal{D}_d \equiv Y_d \dot{d} \geq 0 \tag{71}$$

These relations are coupled with the equilibrium equation (63). For brittle damage, $\mathcal{G}_f$ is a constant. Generally, it may depend on the crack length d and its velocity $\dot{d}$. The last relation in (70) represents the damage criterion.

5.4.2 Numerical implementation - size effects

In this section we give numerical results for the case of cracks emerging from pores. We consider that the elastic matrix is isotropic, of Young's modulus $E = 2\ GPa$ and Poisson's ratio $\nu = 0.1$. The normalized pore diameter is taken $a_P = 0.2$. The fracture energy was taken $\mathcal{G}_f = 20 J/m^2$.

In section 5.4 formulae for the computation of the homogenized coefficients starting from the elementary deformation modes were deduced. For the numerical implementation of the effective coefficients we used the finite element program FEAP, developed by Berkeley University ([136]). Triangular finite elements with three Gauss points for the displacements were used. Computation technique has two steps: first, one needs to compute finite element solutions for the characteristic functions on unit cells containing micro-cracks of different lengths; then polynomial interpolation to construct the functions $C_{ijkl}(d, a_P)$ of the variable d is used.

In Fig. 5.16 we represented the homogenized coefficients vs. the damage variable d. We note that the presence of micro-cracks induces an anisotropic effective response and that the homogenized coefficients depend nonlinearly on the damage variable.

Since the damage evolution law was obtained from a brittle micro-fracture criterion, our model predicts brittle damage. For an increasing vertical compressive loading, starting from an undamaged state $d = a_P$, the macroscopic stress do not induce damage until it reaches a critical value Σ_{22} for which the complete failure of the cell occurs in a brittle way. In Fig. 5.17, we plotted the critical failure stress as a function of the micro-structural size ε. The two curves correspond to two different normalized pore sizes $a_P = 0.2$ and $a_P = 0.3$. The fracture energy is taken $\mathcal{G}_f = 20 J/m^2$ while the elasticity coefficients are the same as in the previous section. We remark that the failure compressive stress increases for smaller inter-distances between pores, for proportional pore sizes, and for smaller pore diameters when the mutual distance between centers is fixed. These results clearly shows the influence of the micro-structural parameters: the distance between centers of two neighbor pores ε and the pore size $a_P \cdot \varepsilon$ on the effective elasto-damage response.

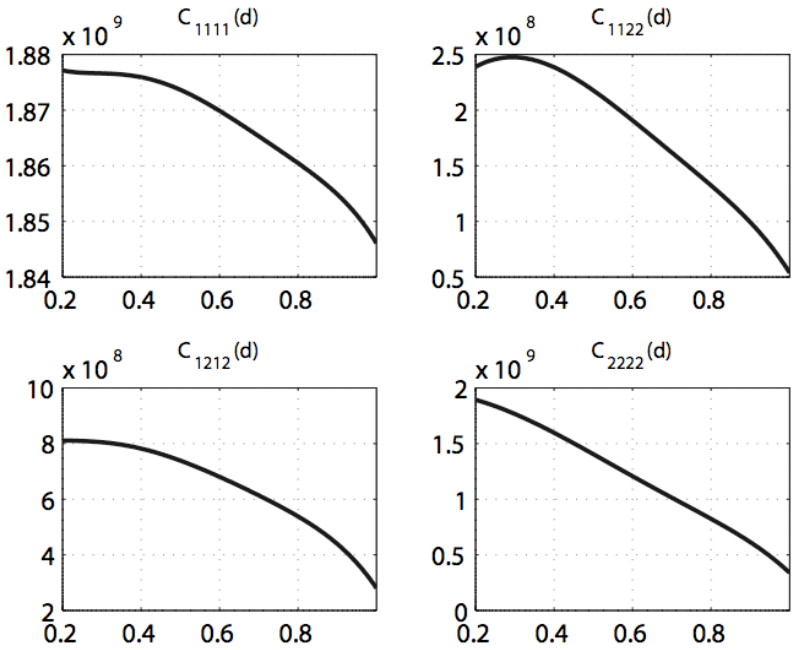

Figure 5.16: Homogenized coefficients vs. damage variable d.

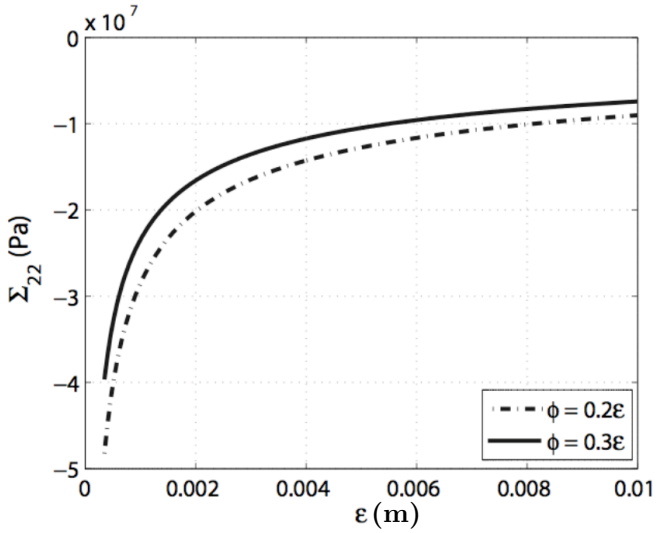

Figure 5.17: Size effects: critical failure stress Σ_{22} vs. microscopic size ε, for pore diameters $0.2 \cdot \varepsilon$ and $0.3 \cdot \varepsilon$

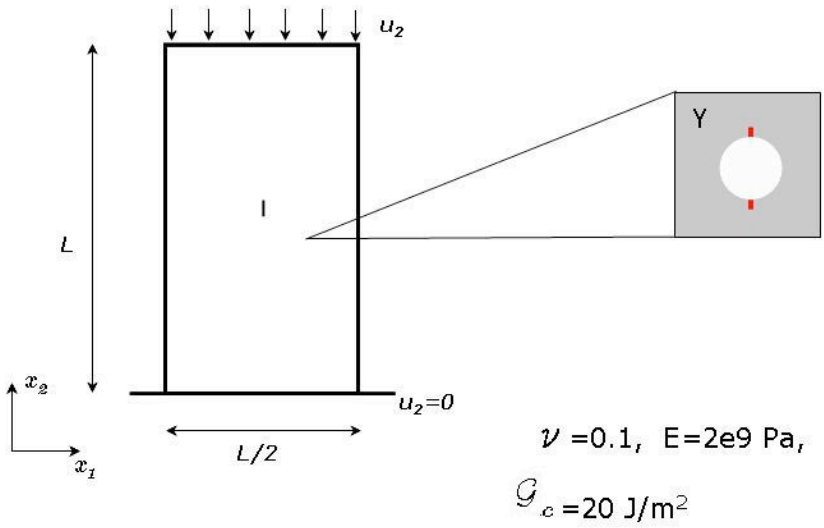

Figure 5.18: Axial splitting test for a porous material specimen.

5.4.3 Axial splitting test

In this section we use the damage model described previously to simulate the axial splitting failure under compression loading. An initial micro-heterogeneity is assumed by considering a macroscopic point in which $d > a_P$. Under compressive loading, micro-cracks propagate and coalesce forming a macroscopic crack that nucleate and grows in the specimen. We show that our model is able to describe this multi-scale failure process. The geometry and the parameters of the specimen are shown in Fig. 5.18. A vertical displacement u_2 is applied uniformily on the top boundary, while the bottom boundary is fixed on the y-direction. We considered a specimen with the height of 0.1 m and the width 0.05 m. For the initiation of damage we considered a central element with pre-existing micro-cracks of normalized length d = 0.4 and positioned in the center of the specimen. The computations were made on a uniform mesh with 9 x 21 elements (see Fig. 5.11), with one Gauss point per element. The microscopic size was taken as $\varepsilon = 6e - 4$ m. The other material parameters were kept the same as before ($E = 2GPa$ and $\nu = 0.1$, $\mathcal{G}_f = 20J/m^2$).

For the finite element solution, at a given time/load step, the damage equation is solved in every integration point. When the damage variable d is close to 1, the micro-cracks are coalescing and the periodicity assumption may not be valid anymore. In order to avoid this situation, as in the previous section for the case of wing-type micro-cracks, in elements with $d \geq 0.9$ we introduced a macroscopic discontinuity. To do this, we used the extended finite element technique (XFEM).

Under progressive increase of the displacement applied at the top of the specimen, we first have an overall elastic deformation, then the micro-crack in the central element grows and leads to the nucleation of a macro-cracks. Further, the micro-cracks in neighbor elements on the vertical direction grow at d close to 1 and induce the propagation of a macro-crack. This process is continued up to the total splitting of the specimen. In Fig. 5.19 we represent the global stresses over the specimen vs. the applied displacement. The points corresponding to the nucleation (a) and growth (b,c,d) of the splitting macro-crack.

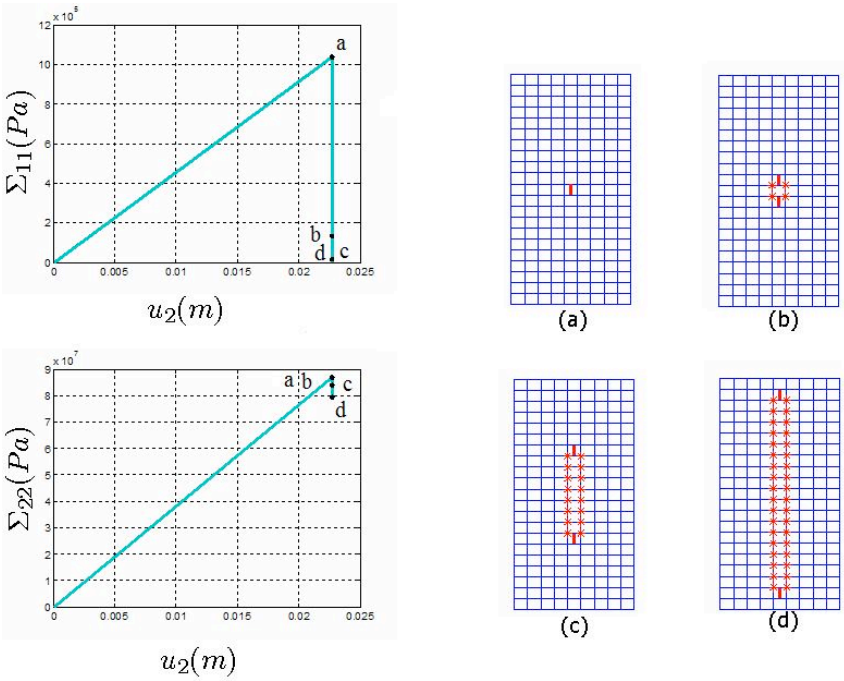

Figure 5.19: Axial splitting test. Global stresses over the specimen vs. the applied displacement, with points corresponding to initiation (a) and growth (b,c,d) of the splitting macro-crack.

The propagation is unstable in the sense that, once started, its evolution can not stopped even for very small loading steps.

This result clearly show the ability of the two-scale model to describe axial splitting failure under compression loadings.

5.4.4 Conclusions

We constructed a two-scale damage model, for locally periodic distribution of micro-cracks and pores, using asymptotic developements homogenization. An elementary period consisted of a pore and two aligned cracks that develope symmetrically from the pore. An energy-based criterion has been considered for micro-cracks and the macroscopic damage equations have been deduced exclusively through the change of scale procedure, without supplementary assumptions at the macroscopic level. The influence of micro-structural parameters, like the mutual distance between centers of neighbor pores and the pore size, on the local macroscopic response has been emphasized. The brittle failure nucleation and growth under axial compression has been simulated with the proposed two-scale model, by using progressive XFEM enrichments for the numerical treatment of evolving macroscopic discontinuities.

5.5 2D quasi-brittle damage model

The previous model is adequate for truly brittle materials, however experimental observations indicate that rocks show a more gradual fracture behavior, i.e. a quasi-brittle response.

In this section we describe an alternative two-scale damage model, in which as the crack grows the resistance of the material increases until a maximum value is achieved. Such a behavior arises due to the development of the fracture process zone (FPZ) ahead of the crack tip. The Fracture Process Zone (Figure 5.20) is defined as a damaged zone around a defect tip, where we can find micro- and meso-cracks (cracks transversing several grains and, eventually, connecting several micro-cracks). The size of the FPZ is given by the distance between the defect tip and the most far micro-crack from this tip.

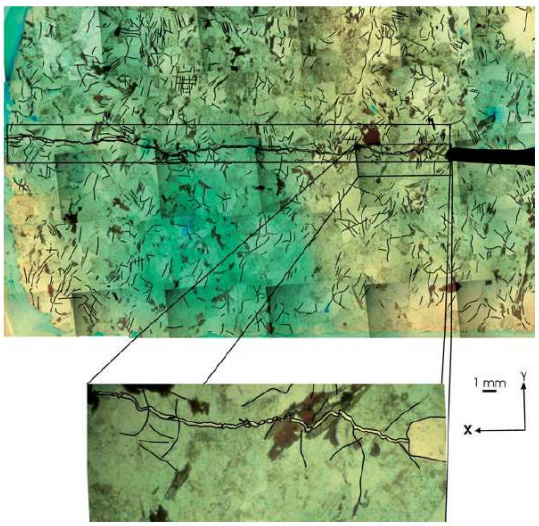

Figure 5.20: Process Zone in Granite of Barre ([109]).

The maximum value of G_f is reached when this process zone is fully developed.

The curve describing the increase in G_f with d is often referred as the R-curve (resistance curve) (see Fig. 5.21). We denote by cf the value of the crack extension at which the R-curve reaches the plateau and by G_c the maximum G at the plateau level. To specify a particular material we have to give particular values for those parameters.

5.5.1 Local macroscopic behavior

The material used in the following numerical computations is the one considered in the previous section: Young's modulus E = 2 GPa, Poisson's ratio $\nu = 0.3$ and the cell length ε = 1e-5 m. The initial part of the R-curve we took in the damage law is $G_f(d) = \frac{G_c 2d}{cf}$ where $G_c = 100\ \frac{J}{m^2}$.

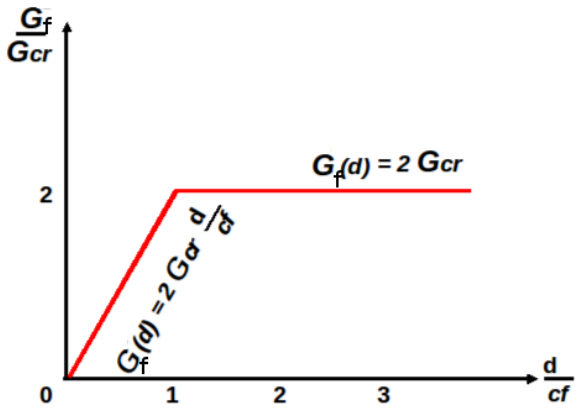

Figure 5.21: Typical R-curve

At the macroscopic scale, for a fully developed damage zone, d, the damage parameter, should be equal to 1. We achieve this goal by the use of a full load-unload phase in the macroscopic strain control. The consequence of the complete phase of load-unload is a snap-back behavior. We load until a critical value for the damage parameter is obtained (in our case 0.74) and then we continue with the unloading procedure that will have as effect the development of the fracture zone until the maximum damage state is achieved. In this way, we realize a path-following procedure (represented in Fig. 5.22) for the stress-strain curve.

Contrary to the brittle-type damage models where we pass directly from a initial non-damaged state (d = 0) to a fully damaged one, in the quasi-brittle case, progressive development of the fracture process zone implicate continuously decreasing values of stiffness until the maximum d is reached.

Figure 5.22 presents the strain-stress curve for 3 different values of the parameter cf. As we can see the initiation point of the fracture is increasing with the decreasing of the critical length cf. In conclusion, we have the latest initialization for the minimum of the critical length. This fact can be explained by the increase $G_f(d) = \frac{G_{cr}2d}{cf}$, which leads to bigger $G_f(d)$ for smaller d with smaller cf.

With the quasi-brittle model it is also possible to describe the generally identified 3 stages of fracture: (I) initiation; (II) stable propagation; (III) unstable propagation to the maximum damage state. The two phases of the propagation are identified using a stability criterion.

$$\frac{dG}{dd} \leq \frac{dR}{dd}, \tag{72}$$

where $R(d) = \frac{2G_{cr}2d\varepsilon}{cf}$.

During snap-back, the micro-fracture propagation is unstable until the maximum level of damage is reached.

It can be clearly seen in Figure 5.23 the two phases of the propagation: blue when the crack appears and starts to propagate in a stable manner and red on the part with snap-back where we observe the unsable propagation up to a maximum level of damage.

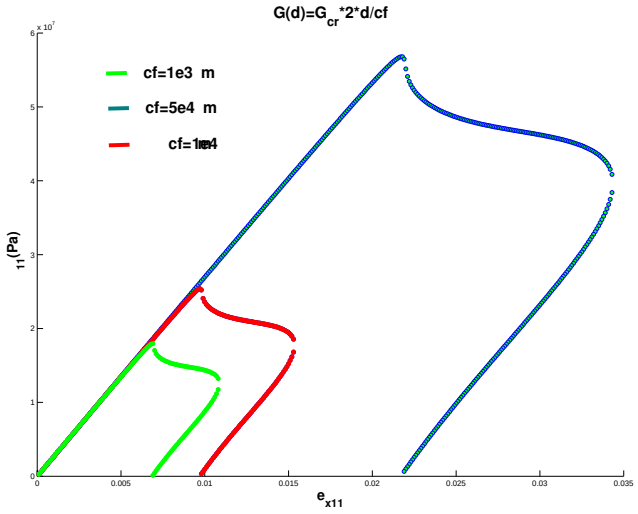

Figure 5.22: Stress-strain curves for the quasi-brittle case: initialization phase for different cf

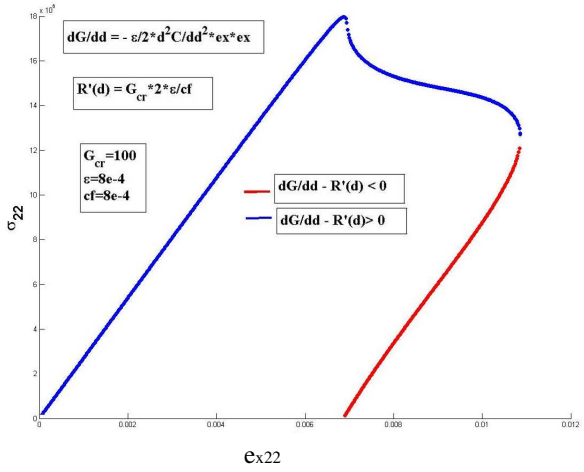

Figure 5.23: Instability for the quasi-brittle case with snap-back (blue for stable propagation, red for unstable propagation)

5.5.2 Summary and discussions

In this section, an alternative two-scale damage model, in which as the crack grows the resistance of the material increases until a maximum value is achieved is considered. The notion of Fracture Process Zone is introduced and the size of FPZ enters into the quasi-brittle type damage law through the variable cf. At the macroscopic local level size effect and instability notions were presented. It was shown that initiation point of the fracture is increasing with the decreasing of the critical length cf (latest initialization occurs for the minimum of the critical length).

Snap-back behavior appears for the first time as a consequence of a complete load-

unload phase in order to have a fully developed damage zone where d, the damage parameter, should be equal to 1.

Using a stability criterion, it was proved that quasi-brittle type damage model was able to show the two phases of the propagation: stable and unstable. Moreover, a direct link was made between snap-back behavior and instability of the crack propagation.

At the macroscopic global level the snap-back behavior leads very difficult, even impossible, a full simulation. In the next section, a 3D extension of the quasi-brittle damage law is proposed. Also there we get the same difficulties connected to snap-back. One way to pass this impediment is to develop time dependent damage models which are capable to regularize the problem. Those models will be addressed in the next Chapter.

5.6 3D extension for the quasi-brittle damage models

In the previous subsection a quasi-brittle type damage law was deduced in the 2D case and exemples were given at macroscopic local level. The present section's aim is at constructing a three-dimensional time independent formulation of a damage model. In order to have clear modeling aspects, several points need to be respected:

- Notion of "3D cracks" is to be given, then, generalities on 3D micro-cracks distributions are to be outlined. The objective is to proove that local periodicity assumption, usually made for the homogenization of heterogenous materials, does not alter the overall behaviour;
- Application of the homogenization procedure in three-dimentional case is to be described (formulation of the initial problem involving an heterogeneuous medium, up-scaling procedure and energy analysis, deduction of damage evolution laws);
- Numerical application at the macroscopic local level tu be run, first in the case of a brittle and last in the case of the quasi-brittle type damage law.

5.6.1 Aspects on the 3D extention

In this subsection a locally periodic distribution of plane micro-cracks is considered, periodicity assumption being usually made for the homogenization of heterogenous materials. Some authors also considered the homogenization for randomly inhomogeneouous materials, as more realistic representations of physical microstructures. For instance, Gambin and Telega [61] considered such a method for the study of the effective properties of elastic solids with random distributions of microcracks. Their analysis led to complicated developments which they estimated as difficult to use for real problems and they concluded by mentioning the periodic case as a possible issue.

5.6.2 Initial 3D problem

Consider a three-dimensional isotropic elastic medium containing a large number of small cracks. A (locally) periodic distribution of micro-cracks is assumed, so as one can locally find a periodicity cell, of length ε, containing one squared plane crack (see Fig. 5.24). The length ε, also representing the mutual distance between centers of neighbor micro-cracks, characterizes the size of the microstructure. At every instant of time, the sides of the squared plane cracks are assumed to be of length $d^{\varepsilon}(t)$.

Penny-shaped cracks are usually considered in order to deduce the effective behavior. Within a particular upscaling procedure, Grechka et al. [66], Sevostianov and Kachanov [128] showed the equivalence between penny-shaped cracks and the irregular shape ones (including also a squared crack) in what concern the effective elasticity of fracture rocks.

Such a result is expected for different homogenization approaches.
The symmetry of the propagation is a standard assumption at the micro-scale. We suppose that the squared crack will extend symmetrically in its own plane. This extension allows for a simple description of the crack front evolution and for a proper comparison with the 2D case.

For a finite value of ε, which is small with respect to the dimension of the macrostructure, we consider asymptotic developments of the mechanical fields with respect to ε. The mathematical formulation of the asymptotic homogenization method involves a suite of periodic structures, indexed over ε, and evaluates the limit, as $\varepsilon \to 0$, of the corresponding solutions of the mechanical problems. It is not our purpose to perform this analysis here, the interested reader being referred to [38].

Let $\mathcal{B}$ denote the initial heterogeneous medium represented by a bounded three-dimensional domain with a smooth external boundary and $\mathcal{C}$ the union of all the microcracks inside $\mathcal{B}$. In the solid part $\mathcal{B}_s = \mathcal{B}\backslash\mathcal{C}$, we have in $\mathcal{B}_s$ the equilibrium equations 3, like in Section 4.

We assume that the cracks are open and traction-free : $\boldsymbol{\sigma}^\varepsilon \mathbf{N} = 0$, where $\mathbf{N}$ is the unit normal vector to the crack faces, as in Fig. 5.24.

For the description of the evolution of damage, the previous equilibrium problem should be completed with damage equations. In subsection 5.6.4, we obtain general damage laws as the result of homogenization of the microscopic balance of energy for propagating micro-cracks.

For the initial problem, the *fracture energy release rate* (e.g. [57]) during crack extension can be expressed as

$$\mathcal{G}^\varepsilon = \lim_{r\to 0} \int_{\Gamma_r} \mathbf{e} \cdot \mathbf{b}(\mathbf{u}^\varepsilon)\mathbf{n}\ ds, \tag{73}$$

where Γ_r is the union of four cylinders of infinitesimal radius r, surrounding the four crack fronts, $\mathbf{e}$ is the unit vector in the propagation direction (see Fig. 5.24), $\mathbf{n}$ defines the outward normal to cylinders Γ_r and $b_{ij}(\mathbf{u}^\varepsilon)$ is the Eshelby configurational stress tensor.

The energy-release rate $\mathcal{G}^\varepsilon$ depends on the crack length $d^\varepsilon(t)$. The crack propagation is described by the following laws:

$$\mathcal{G}_\varepsilon \leq \mathcal{G}_f\ ;\ \dot{d^\varepsilon} \geq 0\ ;\ \dot{d^\varepsilon}(\mathcal{G}^\varepsilon - \mathcal{G}_f) = 0. \tag{74}$$

where $\mathcal{G}_f$ is the critical fracture energy of the material. $\mathcal{G}_f$ may depend on the crack length or the crack velocity [57].

5.6.3 Asymptotic homogenization for bodies with cracks

The locally periodic microstructure is reproduced from the unit cell $Y = [0,1]\times[0,1]\times[0,1]$ by scaling with the small parameter ε so that the period of the material is εY, as in Fig.5.24. The two distinct scales are represented by the *macroscopic variables* $\mathbf{x}$ and the *microscopic variables* $\mathbf{y} = \mathbf{x}/\varepsilon$. In the unit cell Y we denote the crack by CY and solid part by $Y_s = Y\backslash CY$. The size of CY is $d = d^\varepsilon/\varepsilon$. According to the method of asymptotic

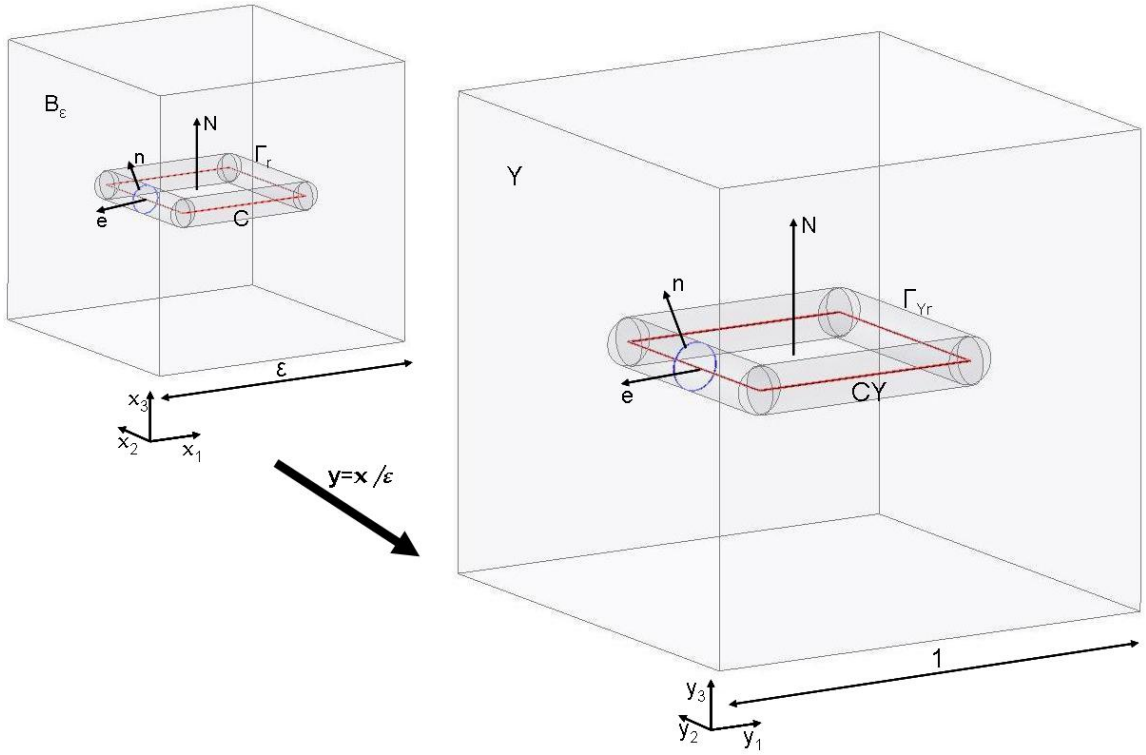

Figure 5.24: Scaling of the local microstructural period to the unit cell.

homogenization (e.g. [96]) and folowing the same path as previously presented in Section 4, we deduce the formula for the effective coefficients $C_{ijkl}(d,0)$ as well as

$$\frac{\partial}{\partial x_j}\Sigma_{ij} = 0.$$

5.6.4 Energy analysis and damage laws

We present in this subsection the homogenization of micro-fracture equations that leads to a general 3D damage model. The particular cases of brittle and quasi-brittle damage will be considered in the next section. To our knowledge, this 3D analysis is here presented for the first time. The micro-mechanical energy analysis on the unit cell is of fundamental importance for our objective: in fact, writing the balance of energy of the unit cell, for evolving microcracks, allows for the obtention of the damage evolution laws without any phenomenological assumption on the macroscopic behavior.

As noted previously, we assume that the micro-cracks are extending symmetrically, in their own plane, so as to remain squared. For such a symmetric propagation, the motion

of the points belonging to the crack front, with respect to the center of the crack, is completely described by the variation of its length.

We saw in the previous chapter that, at the order 0, the traction-free condition gives:

$$\sigma_{ij}^{(0)} N_j = 0. \tag{75}$$

By multiplication of the equation

$$\frac{\partial}{\partial y_j}\left(a_{ijkl} e_{xkl}(\mathbf{u}^{(0)})\right) = 0.$$

with $\dot{u}_i^{(1)}$, integrating over Y_s and use of the periodicity of $\mathbf{u}^{(1)}$ one obtains

$$\int_{CY} a_{ijkl} e_{xkl}(\mathbf{u}^{(0)}) N_j [[\dot{u}_i^{(1)}]] ds_y = \int_{Y_s} a_{ijkl} e_{xkl}(\mathbf{u}^{(0)}) e_{yij}(\dot{\mathbf{u}}^{(1)}) dy. \tag{76}$$

where we denoted by $[[\,\cdot\,]]$ the jump across the crack faces. On the other hand, the second equation in (11) can be written as

$$\frac{\partial}{\partial y_j}\left(a_{ijkl} e_{xkl}(\mathbf{u}^{(0)}) + a_{ijkl} e_{ykl}(\mathbf{u}^{(1)})\right) = 0.$$

Multiplication of this equation by $u_i^{(1)}$, integration on Y_s and use of the continuity condition (75) lead to

$$\int_{CY} \sigma_{ij}^{(0)} N_j [[u_i^{(1)}]] ds_y = \int_{Y_s} (a_{ijkl} e_{xkl}(\mathbf{u}^{(0)}) + a_{ijkl} e_{ykl}(\mathbf{u}^{(1)})) e_{yij}(\mathbf{u}^{(1)}) dy. \tag{77}$$

From (27) we get zero value for the integral on the right. We also have the equality

$$\int_{Y_s} a_{ijkl} e_{ykl}(\mathbf{u}^{(1)}) dy = (C_{ijkl} - a_{ijkl}) e_{xkl}(\mathbf{u}^{(0)}). \tag{78}$$

Indeed, taking into account the linear dependence of $\mathbf{u}^{(1)}$ of the macroscopic deformations (see section 5.6.3), for the right member of (78) we have :

$$\int_{Y_s} a_{ijkl} e_{ykl}(\mathbf{u}^{(1)}) dy = \int_{Y_s} a_{ijkl} e_{ykl}(\boldsymbol{\xi}^{mn}(\mathbf{y})) dy \; e_{xmn}(\mathbf{u}^{(0)}).$$

and by using the expression (25) under the form:

$$C_{ijmn} = a_{ijmn} + \int_{Y_s} a_{ijkl} e_{ykl}(\boldsymbol{\xi}^{mn}(\mathbf{y})) dy.$$

we get (78).

Proposition 1. During the crack propagation, the following energy balance relation holds:

$$\frac{d}{dt}\int_{Y_s} \frac{1}{2} a_{ijkl} e_{ykl}(\mathbf{u}^{(1)}) e_{yij}(\mathbf{u}^{(1)}) dy + \frac{\dot{d}}{2} \mathcal{G}_y = \int_{CY} a_{ijkl} e_{ykl}(\mathbf{u}^{(1)}) N_j [[\dot{u}_i^{(1)}]] ds_y, \tag{79}$$

with

$$\mathcal{G}_y = \lim_{r \to 0} \int_{\Gamma Y_r} \mathbf{e} \cdot \mathbf{b}(\mathbf{u}^{(1)}) \mathbf{n} \; ds_y. \tag{80}$$

where ΓY_r is the union of the four cylinders of infinitesimal radius r, surrounding the crack fronts, $\mathbf{e}$ is the unit vector in the propagation direction (see Fig. 5.24), $\mathbf{n}$ defines the outward normal to the cylinder ΓY_r and $\mathbf{b}(\mathbf{u}^{(1)})$ is the Eshelby configurational stress tensor constructed with the first displacement corrector:

$$\begin{aligned} b_{ij}(\mathbf{u}^{(1)}) &= U(\mathbf{u}^{(1)})\delta_{ij} - \sigma_{ik}(\mathbf{u}^{(1)})u^{(1)}_{k,j}, \\ U(\mathbf{u}^{(1)}) &= \frac{1}{2}a_{ijkl}e_{ykl}(\mathbf{u}^{(1)})e_{yij}(\mathbf{u}^{(1)}), \\ \sigma_{ik}(\mathbf{u}^{(1)}) &= a_{iklm}e_{ylm}(\mathbf{u}^{(1)}). \end{aligned} \tag{81}$$

Proof: Let $Y_r \subset Y$ the domain in the unit cell defined by $Y_r = Y \backslash \{CY_r^+ \cup CY_r^- \cup \Gamma Y_r\}$, where CY_r^+ and CY_r^- are subdomains of the upper and, respectively, lower crack faces interior to the four cylinders. At the limit :

$$\lim_{r\to 0} Y_r = Y_s$$

Multiplication of (16) by $\dot{u}_i^{(1)}$ and integration on Y_r give

$$\int_{Y_r} \frac{d}{dt}\left(\frac{1}{2}a_{ijkl}e_{ykl}(\mathbf{u}^{(1)})e_{yij}(\mathbf{u}^{(1)})\right)dy - \int_{Y_r}\frac{\partial}{\partial y_j}\left(a_{ijkl}e_{ykl}(\mathbf{u}^{(1)})\dot{u}_i^{(1)}\right)dy = 0. \tag{82}$$

By using a transport theorem (see [141], eq. (81.4)) for the first integral we get

$$\int_{Y_r} \frac{d}{dt}\left(\frac{1}{2}a_{ijkl}e_{ykl}(\mathbf{u}^{(1)})e_{yij}(\mathbf{u}^{(1)})\right)dy = \frac{d}{dt}\int_{Y_r}\frac{1}{2}a_{ijkl}e_{ykl}(\mathbf{u}^{(1)})e_{yij}(\mathbf{u}^{(1)})dy + \int_{\Gamma Y_r}\frac{1}{2}a_{ijkl}e_{ykl}(\mathbf{u}^{(1)})e_{yij}(\mathbf{u}^{(1)})\frac{\dot{d}}{2}n_p e_p ds_y.$$

Integrating by parts in the second integral of (82) and using the periodicity of $\mathbf{u}^{(1)}$ on the external boundary and (75) we obtain

$$\int_{Y_r}\frac{\partial}{\partial y_j}\left(a_{ijkl}e_{ykl}(\mathbf{u}^{(1)})\dot{u}_i^{(1)}\right)dy = \int_{CY_r^+} a_{ijkl}e_{ykl}(\mathbf{u}^{(1)})N_j^+[[\dot{u}_i^{(1)}]]ds_y - \int_{\Gamma Y_r} a_{ijkl}e_{ykl}(\mathbf{u}^{(1)})n_j\dot{u}_i^{(1)}ds_y.$$

In this way (82) becomes

$$\begin{aligned} &\frac{d}{dt}\int_{Y_r}\frac{1}{2}a_{ijkl}e_{ykl}(\mathbf{u}^{(1)})e_{yij}(\mathbf{u}^{(1)})dy + \\ &\int_{\Gamma Y_r}\left(\frac{1}{2}a_{ijkl}e_{ykl}(\mathbf{u}^{(1)})e_{yij}(\mathbf{u}^{(1)})\frac{\dot{d}}{2}n_p e_p + a_{ijkl}e_{ykl}(\mathbf{u}^{(1)})n_j\dot{u}_i^{(1)}\right)ds_y - \\ &\int_{CY_r^+} a_{ijkl}e_{ykl}(\mathbf{u}^{(1)})N_j^+[[\dot{u}_i^{(1)}]]ds_y = 0. \end{aligned}$$

Considering the contributions of the four crack fronts, at the limit, for $r \to 0$, we obtain

$$\frac{d}{dt}\int_{Y_s}\frac{1}{2}a_{ijkl}e_{ykl}(\mathbf{u}^{(1)})e_{yij}(\mathbf{u}^{(1)})dy + \frac{\dot{d}}{2}\mathcal{G}_y - \int_{CY} a_{ijkl}e_{ykl}(\mathbf{u}^{(1)})N_j[[\dot{u}_i^{(1)}]]ds_y = 0.$$

which proves the relation (79).

This allows us to formulate the following :

Proposition 2. For an evolving squared crack CY of length d(t), in the unit cell, we have:

$$\frac{1}{2}\dot{d}\frac{dC_{ijkl}}{dd}e_{xkl}(\mathbf{u}^{(0)})e_{xij}(\mathbf{u}^{(0)}) + \frac{\dot{d}}{2}\mathcal{G}_y = 0. \tag{83}$$

Proof. By addition of (76) and (79) and reordering the terms we arrive at:

$$\int_{CY}\left(a_{ijkl}e_{xkl}(\mathbf{u}^{(0)}) + a_{ijkl}e_{ykl}(\mathbf{u}^{(1)})\right)N_j[[\dot{u}_i^{(1)}]]\ ds_y - \frac{\dot{d}}{2}\mathcal{G}_y = \frac{d}{dt}\int_{Y_s}\frac{1}{2}a_{ijkl}e_{ykl}(\mathbf{u}^{(1)})e_{yij}(\mathbf{u}^{(1)})dy + \int_{Y_s}a_{ijkl}e_{xkl}(\mathbf{u}^{(0)})e_{ykl}(\dot{\mathbf{u}}^{(1)})\ dy.$$

Using the above-mentioned transport formula and the fact that $\mathbf{u}^{(0)}$ does not depend on the variable $\mathbf{y}$, the second integral in the right member of the previous relation reads

$$\int_{Y_s}a_{ijkl}e_{xkl}(\mathbf{u}^{(0)})e_{ykl}(\dot{\mathbf{u}}^{(1)})\ dy = \frac{d}{dt}\int_{Y_s}a_{ijkl}e_{xkl}(\mathbf{u}^{(0)})e_{yij}(\mathbf{u}^{(1)})\ dy - \int_{Y_s}a_{ijkl}e_{xkl}(\dot{\mathbf{u}}^{(0)})e_{yij}(\mathbf{u}^{(1)})\ dy,$$

so that

$$\int_{CY}\left(a_{ijkl}e_{xkl}(\mathbf{u}^{(0)}) + a_{ijkl}e_{ykl}(\mathbf{u}^{(1)})\right)N_j[[\dot{u}_i^{(1)}]]\ ds_y - \frac{\dot{d}}{2}\mathcal{G}_y - \frac{1}{2}\frac{d}{dt}\int_{Y_s}a_{ijkl}\left(e_{xkl}(\mathbf{u}^{(0)}) + e_{ykl}(\mathbf{u}^{(1)})\right)e_{yij}(\mathbf{u}^{(1)})dy = \frac{1}{2}\frac{d}{dt}\int_{Y_s}a_{ijkl}e_{xkl}(\mathbf{u}^{(0)})e_{yij}(\mathbf{u}^{(1)})dy - \int_{Y_s}a_{ijkl}e_{xkl}(\dot{\mathbf{u}}^{(0)})e_{yij}(\mathbf{u}^{(1)})\ dy.$$

This equation can be further modified by making use of (77) for the last integral in the left-hand side. We get

$$\int_{CY}\left(a_{ijkl}e_{xkl}(\mathbf{u}^{(0)}) + a_{ijkl}e_{ykl}(\mathbf{u}^{(1)})\right)N_j[[\dot{u}_i^{(1)}]]\ ds_y - \frac{\dot{d}}{2}\mathcal{G}_y - \frac{1}{2}\frac{d}{dt}\int_{CY}\left(a_{ijkl}e_{xkl}(\mathbf{u}^{(0)}) + a_{ijkl}e_{ykl}(\mathbf{u}^{(1)})\right)N_j[[u_i^{(1)}]]\ ds_y = \frac{1}{2}\dot{d}\frac{dC_{ijkl}}{dd}e_{xkl}(\mathbf{u}^{(0)})e_{xij}(\mathbf{u}^{(0)}). \tag{84}$$

Taking into account the traction free condition (75), the integrals on the left side of the equality become zero, so eq. (84) proves the theorem.

Starting from (83) we construct a damage law, using the properties of the homogenized solution and a scaling relation for the energy release rate. Indeed we can prove the relation :

$$\mathcal{G}^{\varepsilon} = \varepsilon^2\ \mathcal{G}_y. \tag{85}$$

For that we use the expression (73) of the initial energy-release rate and the two-scale development (9) of $\mathbf{u}^\varepsilon(\mathbf{x},t)$. The first terms in the developments of $e_{xkl}(\mathbf{u}^\varepsilon)$ and σ^ε_{jk} are:

$$e_{xkl}(\mathbf{u}^\varepsilon) = e_{xkl}(\mathbf{u}^{(0)}) + e_{ykl}(\mathbf{u}^{(1)}),$$
$$\sigma^\varepsilon_{jk} = a_{jkmn}(e_{xmn}(\mathbf{u}^{(0)}) + e_{ymn}(\mathbf{u}^{(1)})).$$

Therefore, the relation (73) becomes:

$$\mathcal{G}^\varepsilon = \lim_{r\to 0}\int_{\Gamma_r} e_i \left(\frac{1}{2}a_{mnkl}\left(e_{xkl}(\mathbf{u}^{(0)}) + e_{ykl}(\mathbf{u}^{(1)})\right)\left(e_{xmn}(\mathbf{u}^{(0)}) + e_{ymn}(\mathbf{u}^{(1)})\right)\delta_{ij} - a_{ikmn}\left(e_{xmn}(\mathbf{u}^{(0)}) + e_{ymn}(\mathbf{u}^{(1)})\right)\left(\frac{\partial u^{(0)}_k}{\partial x_j} + \frac{\partial u^{(1)}_k}{\partial y_j}\right)\right) n_j ds. \tag{86}$$

By change of variables in the integral (86) with $ds = \varepsilon^2 ds_y$ and taking into account the singularity of $\mathbf{u}^{(1)}$ at crack tips (e.g. [57]) we get:

$$\mathcal{G}^\varepsilon = \varepsilon^2 \lim_{r\to 0}\int_{\Gamma Y_r} e_i \left(\frac{1}{2}a_{mnkl}e_{ykl}(\mathbf{u}^{(1)})e_{ymn}(\mathbf{u}^{(1)})\delta_{ij} - a_{ikmn}e_{ymn}(\mathbf{u}^{(1)})\frac{\partial u^{(1)}_k}{\partial y_j}\right) n_j ds_y,$$

which proves that $\mathcal{G}^\varepsilon = \varepsilon^2\ \mathcal{G}_y$.

Denoting by Y_d the damage energy release rate

$$Y_d = -\frac{1}{2}\frac{dC_{ijkl}}{dd}e_{xkl}(\mathbf{u}^{(0)})e_{xij}(\mathbf{u}^{(0)}),$$

and using the proved scaling relation and theorem, we obtain

$$\mathcal{G}^\varepsilon = 2\varepsilon^2 Y_d.$$

With this, the fracture relations stated previously become

$$Y_d \le \frac{\mathcal{G}_f}{2\varepsilon^2}\ ;\ \dot{d} \ge 0\ ;\ \dot{d}(Y_d - \frac{\mathcal{G}_f}{2\varepsilon^2}) = 0. \tag{87}$$

The macroscopic damage relations (87), obtained in Kuhn-Tucker form, are entirely expressed in terms of the homogenized solution $\mathbf{u}^{(0)}$. We remark that the homogenized coefficients, appearing in the expression of the damage energy release rate, can be a priori computed as functions of the damage variable, from the unit cell solutions.

5.6.5 Brittle and quasi-brittle damage - size effects

In this section we consider two particular criteria for micro-cracks - corresponding to brittle and quasi-brittle fracture - and we investigate the corresponding homogenized damage response in a macroscopic point. In these examples, the micro-cracks are considered to be embedded in an elastic isotropic matrix, with Young's modulus E = 2 GPa and Poisson's ratio ν= 0.3.

The damage response is computed for a macroscopic deformation driven loading. The main steps for the numerical computations are:

- Solve the elastic problem for the characteristic functions $\boldsymbol{\xi}^{pq}(\mathbf{y})$, for different normalized crack lengths d.
- Compute the homogenized coefficients $C_{ijkl}(d)$ for different lengths d and perform polynomial interpolation.
- Solve of damage equation of the specific model for the unknown d and for prescribed macroscopic deformation.
- Compute the macroscopic stress Σ_{ij} for given macroscopic deformation

To compute the characteristic functions we used the FEM software Comsol Multiphysics [32]. The periodicity conditions are satisfied using Lagrange Multipliers method. Tetrahedral elements meshes are used and $\boldsymbol{\xi}^{pq}(\mathbf{y})$ are computed for 24 different lengths of the crack. The functions $C_{ijkl}(d)$ are then obtained by interpolation with 15-degree polynomials.

In Fig. 5.25, we present the homogenized coefficients as functions of the damage variable d. We remark the high nonlinearity of the functions $C_{ijkl}(d)$, very different from the linear approximations usually assumed for phenomenological damage models. We also note the induced anisotropy, due to the presence of micro-cracks in the isotropic elastic matrix.

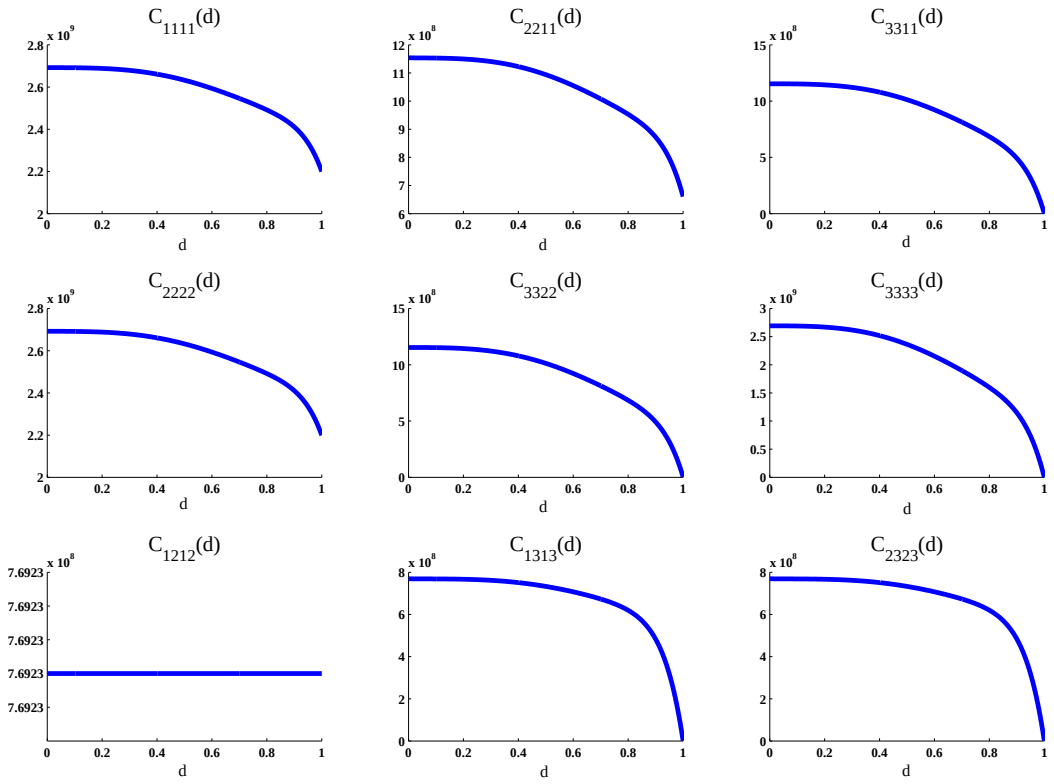

Figure 5.25: Effective coefficients vs. damage variable.

Brittle damage

Our first example concerns the brittle damage behavior. In previous papers [37], [38], we showed that a 2D brittle damage model is obtained through homogenization when a Griffith fracture criterion is assumed for micro-cracks. The critical fracture energy was considered to be a constant, i.e. $\mathcal{G}_f = \mathcal{G}_{cr}$.

In the present case, the damage laws (87) become:

$$Y_d \leq \frac{\mathcal{G}_{cr}}{2\varepsilon^2} \; ; \; \dot{d} \geq 0 \; ; \; \dot{d}(Y_d - \frac{\mathcal{G}_{cr}}{2\varepsilon^2}) = 0. \tag{88}$$

We consider the material parameters : Young's modulus E = 2 GPa, Poisson's ratio ν= 0.3 and the critical fracture energy $\mathcal{G}_{cr} = 20 \; J/m^2$.

For an initially undamaged material, the response predicted by the damage model is an elastic one up to a threshold of damage initiation, when complete failure ($d = 1$) instantaneously occurs. In order to investigate the size effect in the homogenized behavior, we analyze the dependence of the damage yield stress on the microscopic length ε under uniaxial deformation loading. For each value of ε, the test are driven by the applied deformation e_{x33}.

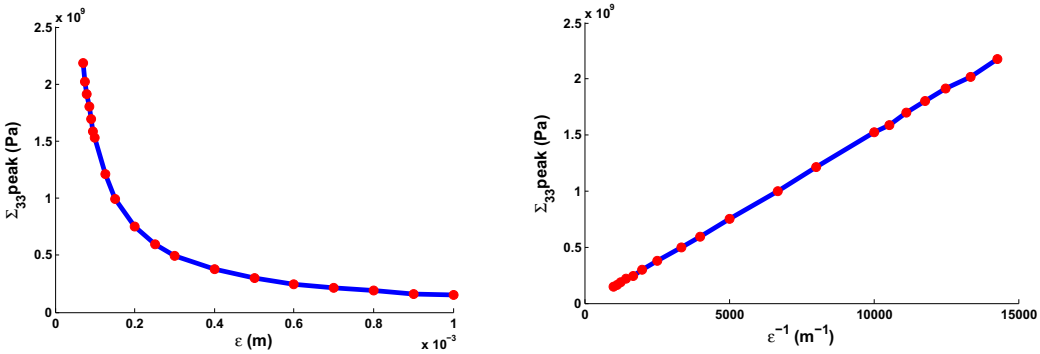

Figure 5.26: Size effects on brittle damage response: the critical stress vs. microstructural length ε and, respectively, ε^{-1}.

The damage yield stress as function of the microscopic length ε is plotted in Fig. 5.26. We remark the linear dependence of the damage yield stress on ε^{-1}. In the 2D case presented in [37], we obtained a $\varepsilon^{-\frac{1}{2}}$ dependence for the damage yield stress. The difference is the result of the 3D geometry of micro-cracks. We note that for smaller cell sizes we have higher thresholds of damage initiation.

Quasi-brittle damage

The second example concerns a more gradual failure behavior: the quasi-brittle damage. To model the quasi-brittle effects, we adopt the point of view of [12], [11] and

consider the equivalent crack in an elastic matrix but which propagation is controlled by a resistance curve. We consider the critical fracture energy given by :

$$\mathcal{G}_f(d^\varepsilon) = \mathcal{G}_{cr}\frac{(d^\varepsilon)^2}{c_f^2}, \tag{89}$$

where c_f could be related to the size of the process zone.
A 2D version of the previous assumption has been adopted in [38], for a two-dimensional quasibrittle damage model. In the present 3D case, the damage laws (87) become:

$$Y_d \leq \frac{\mathcal{G}_{cr}d^2}{2c_f^2} \;;\; \dot{d} \geq 0 \;;\; \dot{d}(Y_d - \frac{\mathcal{G}_{cr}d^2}{2c_f^2}) = 0. \tag{90}$$

We note that the process zone characteristic length c_f is now naturally captured by the damage equations, becoming the material length of the homogenized model.

The model predicts progressive evolution of damage. For a loading controlled by the one-dimensional macroscopic deformation e_{x33}, the elasto-damage response is presented in Fig 5.27. The same material parameters as before have been used for the numerical computations. The three curves, for stress and damage, correspond to different values of the material length c_f, showing micro-structural size effects for the homogenized response. We also note the snap-back behavior that occurs for values of d close to 1. Using the numerical solution, it can be shown that this regime corresponds to unstable propagation of micro-cracks.

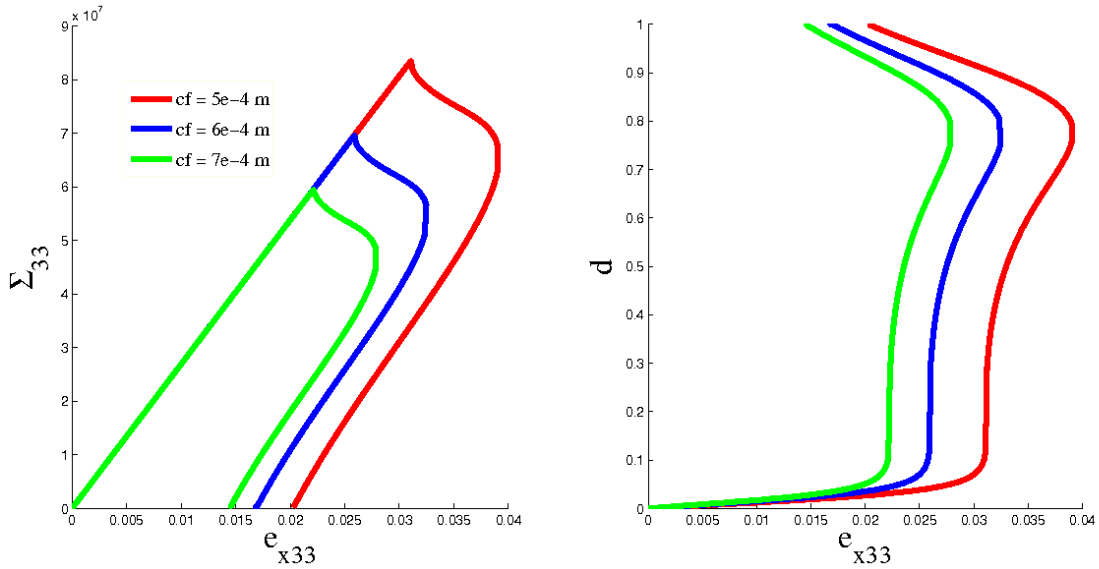

Figure 5.27: Quasi-brittle homogenized response in stress and damage. Influence of the microstructural length.

5.6.6 Summary and discussions

The 3D micro-mechanical elasto-damageable model presented in this subsection is an extension of the 2D one and it was built on the same principles as that one. A locally periodic distributions of squared horizontal micro-cracks was considered. At the microscopic level, an energy-based propagation criterion was considered and the macroscopic damage equations were deduced exclusively through the change of scale procedure. It has been shown that the new damage evolution equations naturally capture microscopic lengths. The presence of such a length in the macroscopic damage law leads to size effects. The predicted size-dependent response of the deduced two-scale model has been illustrated in the particular cases of brittle and, respectively, quasi-brittle materials.

Nevertheless it is more reliable for having overall good responses than the previous so it can be applied for the real cases. The two models are able to describe size effects in both brittle and the quasi-brittle cases. We analyzed the dependence of the damage yield stress on the microscopic length ε under uniaxial deformation loading. We remark in the 3D case the linear dependence of the damage yield stress on ε^{-1} meanwhile in the 2D case we obtained a $\varepsilon^{-\frac{1}{2}}$ dependence. The difference is the result of the 3D geometry of micro-cracks.
Further improvements of the model, like unilateral contact on the crack faces, arbitrary micro-crack orientations, are necessary in order to reproduce complex damage situations.

5.7 Conclusions

This chapter was dedicated to time independent damage models. The chapter begun with the implementation of the microscopic level (characteristic functions and homogenized coefficients). Brittle type of crack propagation was used in the case of wing-type micro-cracks. Quasi-brittle type of crack propagation in two- and three-dimensional spaces was also considered.

Unfortunately, one of the limitations of previously developed damage models, is the difficulty in characterizing global behavior, mainly due to snap-back. Also, even if simulations are not presented in this thesis, in our work, mesh dependency occurred. This undesirable effect was due to the fact that chosen criteria of crack propagation ignores the time effect on the fracture behavior, or the evolution of damage in many materials, such as glasses, rocks, ceramics or ceramic composites, is time-dependent.

6 Rate dependent, kinking - crack damage models

Contents

6.1 Introduction

The previous chapter was dedicated to time independent damage models for which a classical criteria of crack propagation (the Griffith criterion [67]) was used. Both brittle and quasi-brittle type of crack propagation in two- or three-dimensional space were considered. Difficulties in describing global macroscopic behavior have been observed in the case of quasi-brittle type damage models. To overcome effects like snapback, mesh dependency, ..., a new class is considered: time-dependent damage models. In this class, the chosen propagation criteria does not ignore the time-effects on the fracture behavior, therefore it is more appropriate to describe the damage evolution in various materials such as glasses, rocks, ceramics or ceramic composites. The use of time-dependent damage models was imperative not only because the inconveniencies of the previously considered time independent damage models are overcome, but also due to their capability of describing time effects for damage like: creep and relaxation.

An important source of time-dependency is the subcritical propagation of microcracks. The classical criteria of crack propagation (i.e. Griffith [67]), ignore the time effect on the fracture behavior. On the contrary, a subcritical criterion, that is a criterion considering crack propagation for energy lower than the critical limit of fracture, takes into account time effects ([2],[4]). Phenomenological models of time-dependent damage have been proposed in the literature (e.g. [130]).

The main objective of this chapter is the development of a two-scale time-dependent damage model capable to take into account both a crack extension and its change of orientation. Theoretical developments and numerical applications of a time-dependent damage law which is deduced from considerations at the micro-scale with non-planar growth of micro-cracks will be given. The evolution of the micro-crack length during propagation is described through a sub-critical criterion, that is a criterion considering crack propagation for energy lower than the critical limit of fracture, meanwhile the orientation of the crack growth is governed by the maximum energy release rate at the crack tips and the introduction of an equivalent straight crack. The passage from micro-scale to macro-scale is done through an asymptotic homogenization approach.

A first contribution to this model is found in [56]. A development is given in this thesis and to accomplish this, several steps have been done:

- Stress intensity factors (SIF) for straight micro-cracks were computed using displacement correlation method. In [56] SIF have been computed with the help of path-independent integral method. When comparison between the two methods was made, a question on the computation of SIF values for higher normalized micro-crack lengths > 0.9 arised.
- At the macroscopic local level we adopted the previous criteria for the equivalent crack, in the case of the micro-crack development in Mode I or mixed mode. But for the case of pure Mode II, previous criteria suffered modification.
- Global macroscopic implementation of the model was performed in three steps:
  - Implementation of a simplified time-dependent damage model in which the stiffness of the solid is governed by linear coefficients that depend on the elastic properties of the solid matrix and on micro-cracks lengths.
  - Implementation of a time-dependent damage model in which linear coefficients were replaced by homogenized coefficients previously computed for a straight crack and the propagation occurs in the fixed direction given by the orientation of the crack.
  - Macroscopic simulations with the complex time-dependent damage model including kinking micro-cracks.

The chapter is organized as follows: first, extensions of the mathematical formulation for the general model, including the modification of macroscopic equilibrium equations and the sub-critical propagation of cracks, is presented. Then implementation of the three time-dependent damage models previously named will be given in three subsections. In each subsection, in general, the next structure will be followed:

- Particular extension to general damage model, when necessary: the mathematics behind the computations.
- Behavior of a body at local macroscopic scale: Numerical examples.
- Damage behavior at the global macroscopic scale: Numerical examples.

In the case of the damage model for kinking micro-cracks, two subsections will be very important: the first one is dedicated to the surface interpolation for different orientations of homogenized coefficients and the other addresses the computation of the stress intensity factors that are needed to quantify the sub-critical growth of cracks at the tips. The chapter will finish with a short summary where advantages and disadvantages as well as the differences between models will be underlined.

One-dimensional example of a bar, under tensile solicitation will be considered in the case of the first two damage models. Simplified model will use the 1D geometry on theoretic purpose - to compare analytically and numerically obtained uniform solutions, therefore to prove the correctness of the implementation. For the propagation in a fixed

direction, the same test will be considered, but a study on the localization zone will be made.

For a better comparison of the three time-dependent damage models presented in this chapter, at the global macroscopic level the same 2D test in uniaxial tension loading conditions will be simulated. The geometry and boundary conditions are shown in the upper left part of Figure 6.1 (length L = 10 cm and width $L/2$ structure submitted to a displacement controlled loading). Each simulation will be run for a regular mesh of 1275 elements (mesh b) in Figure 6.1). In the case of the time dependent damage models which includes kinked micro-cracks, mesh independency is proven with the help of this 2D tension test. For the model with fixed direction of the propagation, will be sufficient to consider mesh independency at the 1D level.

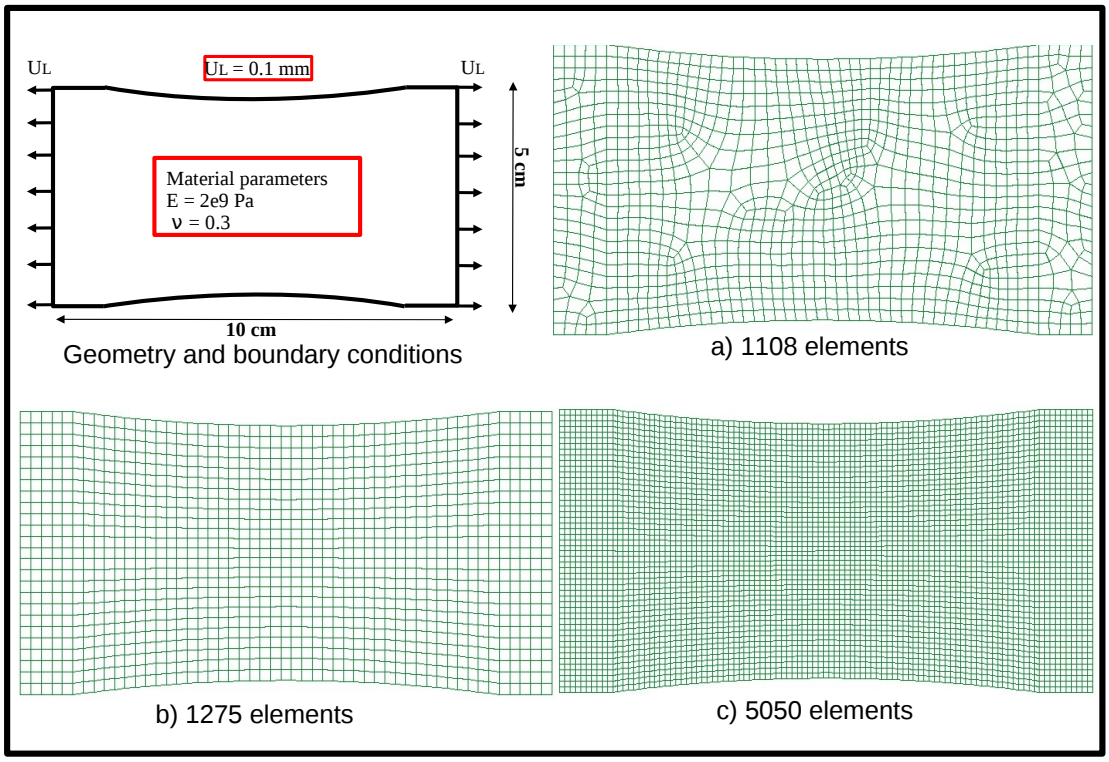

Figure 6.1: Geometry, boundary conditions and the three meshes used in a uniaxial 2D tension simulation.

One of the aspects of major importance treated in the case of time dependency is the unloading process. In the research work we considered two types of unloading: (a) elastic - classical mechanism described by the constance of damage with the decrease of the strain and (b) unloading with the same damage evolution law - damage still propagates under the same criteria as in loading. All the results presented in this thesis are obtained with the second type of unloading.

6.2 Mathematical formulation of the time-dependent model in general form

The main result of Chapter 4 is the general formulation of the damage evolution law (Eq. 42). We remind that G_f represents the critical fracture energy and it can be given by a constitutive function depending on the critical energy threshold $\mathcal{G}_c$ and on the damage parameter d.

In this chapter, time - dependence is achieved by the use of a sub-critical propagation criterion for micro-cracks. In this class of damage models, rate of crack propagation may be expressed with respect to stress intensity factor at the crack tips, under tensile mode, using a power law [30] or an exponential law [145]. The first one will be used in this thesis.

Consider the mode I growth described by a law of the type of that proposed by Charles ([30],[126]):

$$\frac{d(2a)}{dt} = \frac{c_f}{\tau_0}(\frac{K_I}{K_0})^n. \tag{91}$$

K_0 is a limit value of the mode I stress intensity factor K_I and Salganik et al. ([126]) was followed by introducing the size of the process zone c_f and the characteristic time τ_0. For simplicity the sub-critical exponent, n, was taken 2. Later tests have been done with bigger values for this exponent. Using the relation between the stress intensity factor and the energy-release rate we obtain the critical fracture energy:

$$G_f = \frac{\varepsilon \mathcal{G}_c \tau_0}{c_f}\frac{dd}{dt}; \qquad \mathcal{G}_c = \frac{{K_0}^2}{E'}; \qquad E' = \frac{E}{1-\nu^2} \qquad \text{in plane strain conditions.} \tag{92}$$

We assume that K_0, τ_0 and c_f are constant parameters of the sub-critical propagation law, independent on the size ε. In this case, the damage law (Eq. 42) becomes:

$$\frac{dd}{dt}(\frac{1}{2}\frac{dC_{ijkl}}{dd}e_{xkl}(u^{(0)})e_{xij}(u^{(0)}) + \frac{{K_0}^2\tau_0}{c_f E'}\frac{dd}{dt}) = 0. \tag{93}$$

6.3 Simplified model - linear coefficients

6.3.1 Introduction

In this subsection we introduce the time dependent concepts with the help of a simplified model using linear coefficients. The advantage is that this model is easy to understand and to follow, so we easily compute analytically the consistent tangent and the integration in time of the damage propagation. Moreover we will start with the 1D model that was solved both analytically and numerically to verify that results corresponded.

In the considered simplified damage model, linear coefficients $C_{ijkl}(d,\theta) = (1-d)a_{ijkl}$ allow us to reduce the general time-dependent damage evolution law (93) to the following expression:

$$\frac{dd}{dt} = \frac{c_f E'}{{K_0}^2 \tau_0}(\frac{1}{2})a_{ijkl}e_{xkl}(u^{(0)})e_{xij}(u^{(0)}). \tag{94}$$

This model is used primarily for development of the method as the linear model cannot fully represent damage evolution due to its limitations. It cannot distinguish the state of the crack (opened or closed) and it does not give the orientation of the crack. Moreover, the homogenization part is incomplete (the damage evolution law is deduced using the homogenization by asymptotic developments technique, but the effective coefficients are replaced by linear polynomial of damage variable) and, in consequence, information on the microstructure is lost.

6.3.2 Numerical implementation

Linear coefficients simplifies very much the time dependent damage model and no information on the micro-crack orientation is available. The direct consequence is the absence of the intrinsic anisotropy in the effective behavior. So, there is no interest in presenting the local macroscopic behavior. Concerning the macroscopic global behavior, it will be presented in two steps:

- One simple 1D problem is formulated and solved both analytically and numerically using Finite Element Method. Global stress - time curves will be compared and the perfect match of the results will prove the correctness of the numerical implementation.
- 2D uniaxial displacement test controlled in tension will be performed.

Discussion on the damage and strain localization will take place for the 1D simulation. For a better understanding of the method, a numerical algorithm precedes the simulations.

Numerical integration scheme

Fig. 6.2 presents the numerical algorithm used to implement simplified time-dependent damage model using linear coefficients. At each time step $n+1$ we have as input the current deformation tensor e_x^{n+1}. With the help of this tensor we deduce the formula for the energy release rate, denoted ε_{eq}:

$$\varepsilon_{eq} = -\frac{1}{2}a_{ijkl}e_{xij}^{n+1}e_{xkl}^{n+1} \tag{95}$$

It can be noted that it does not depend on the damage parameter d. The damage variable is then updated using the time dependent damage law given by Eq. 94. Having the current deformation tensor e_x^{n+1} and the current value of the damage d_{n+1} the last step to be done is updating the stress tensor Σ_{n+1}.

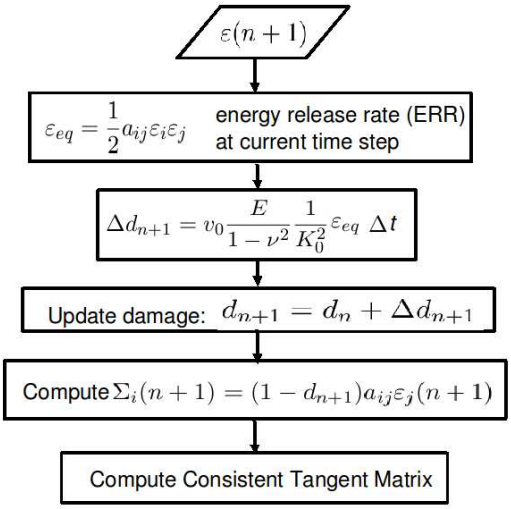

Figure 6.2: Incremental iterative procedure for the time-dependent damage model with linear coefficients

Algorithm for analytical computation of the consistent tangent

To run macroscopic simulations, at every time step, the consistent tangent matrix need to be known. $\frac{\partial \Delta\Sigma}{\partial \Delta\epsilon}$ is computed analytically. Figure 6.3 shows the main terms entering the computation: on the right, energy release rate, followed by the derivative of the actual ERR with respect to actual strain; damage derivative with respect to ERR (easily computed starting from Eq. 94) is the third term and the homogenized coefficients correspond to the last term which enters directly in the computation of the consistent tangent matrix.

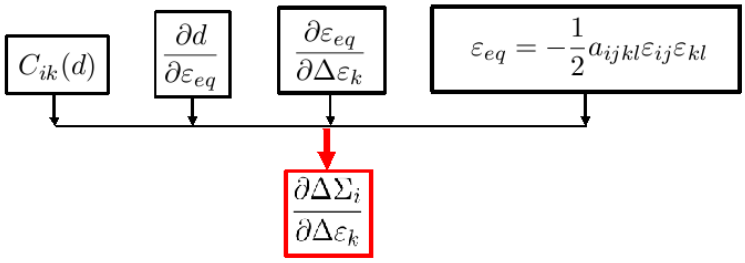

Figure 6.3: Analytical method of computation of the consistent tangent matrix for the time-dependent damage model with linear coefficients

6.3.3 Global macroscopic behavior

1D damage problem

We consider an one-dimensional medium having an elasto-damage behavior, in small deformations. The behavior is that of a solid body occupying the interval $[0, L]$. The end $x = 0$ of the solid is fixed and the displacement applied at the other end is a positive increasing function of time $u_L(t)$. We denote by t the time, Σ the stress and ε_L the uniform strain. The real case of a bar of length L fixed at one side with a progressive load at the other is a good example. The complete description of the 1D problem is given by the following system:

$$\begin{aligned} \sigma = (1-d)E\varepsilon_L, \qquad \varepsilon_L = \frac{u_L(t)}{L}, \\ \frac{d\sigma}{dx} = 0, \\ \frac{dd}{dt} = \frac{cfE'}{{K_0}^2\tau_0}\left(\frac{1}{2}\right)E\varepsilon_L^2. \end{aligned} \tag{96}$$

E is the elastic modulus for the undamaged material and d is the damage variable.

The problem can be solved analytically, a complete description of the solving process in the case of time-dependent damage models been found in [22]. A constant strain loading is considered, therefore

$$\varepsilon_L(t) = \beta t, \quad \beta > 0.$$

Damage at the time t is then given by the formula:

$$d(t) = 1 + \frac{\beta^2}{3}\frac{Ec_f}{2G_c\tau_0}(t^3 - t_0^3)$$

where t_0 is a value of an initial time.

Same problem was solved using the finite element code FEAP ([136]). Two Gauss points "truss" elements with cross section 1 were considered. Comparison between analytical and numerical methods have been made and obtained results matched perfectly (Figure 6.4).

In both numerical and analytical simulations, the following parameters have been considered: $c_f = 8e^{-4}$ m, $\tau_0 = 1e^8$ $\frac{1}{s}$, $G_0 = 100$ $\frac{J}{m}$, $U_L = 0.1$ m and E = 2 GPa.

This simple 1D simulation allows the study of strain and damage evolution. Figure 6.5 shows damage (left) and strain (right) profile along the bar in the last part of the simulation. We consider 6 time steps. A virgin material was initially taken. At the time step t_1 we see the appearance of the localization process. This process is more visible at the time steps t_5 and t_6. In the right part of Figure 6.5 the strain profile is shown. The loading - unloading phase, which is in direct connection with the localization phenomena, occurs. It can be seen that on the right part of the bar the elements have high values of damage which continue to increase with the decrease in strain, meanwhile, in the rest of the bar, the damage and strain increase continuously.

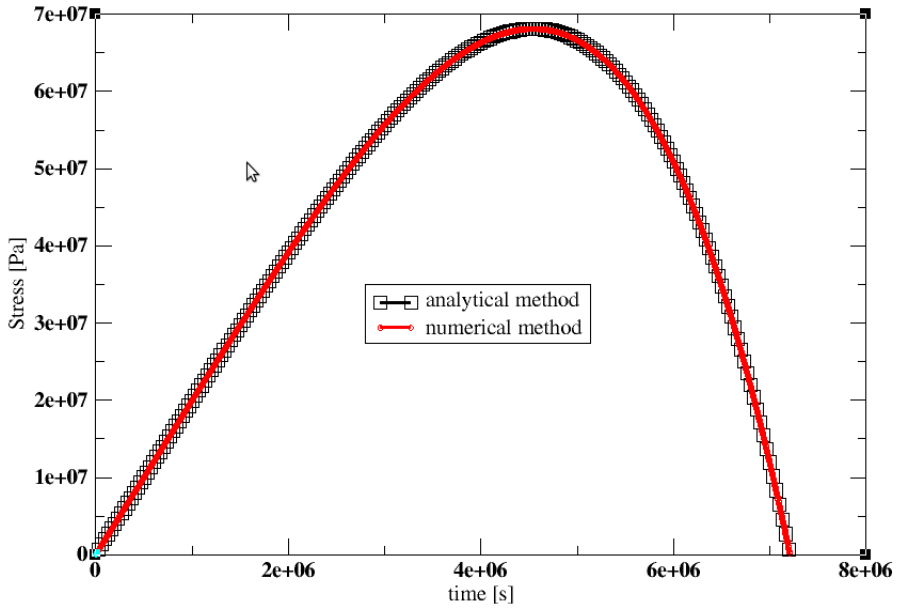

Figure 6.4: Analytic and numeric examples of stress-time curves

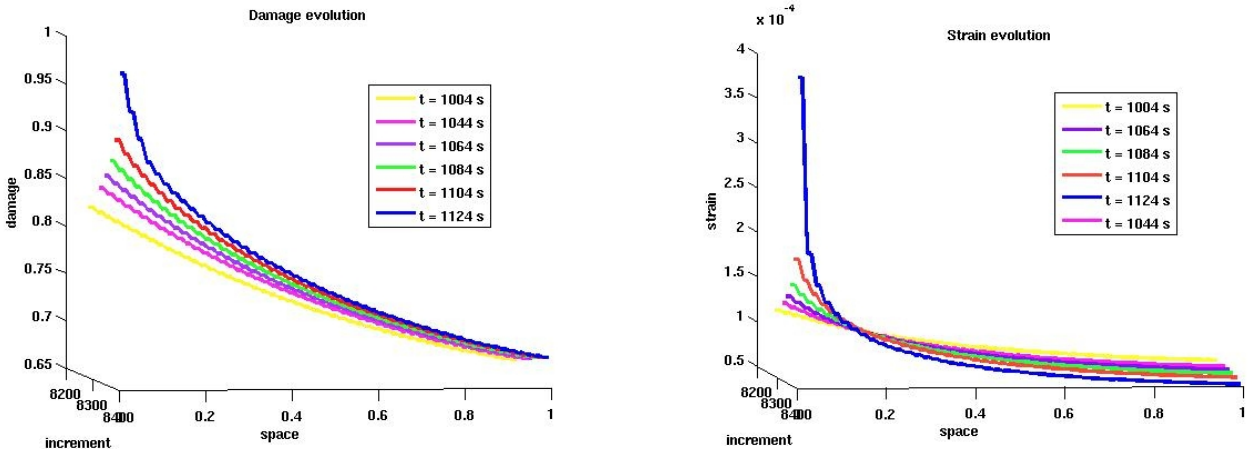

Figure 6.5: Damage and strain profiles along the bar at six time steps from the end of the simulation. Localization phenomena is in progress

2D - uniaxial tension test

After the proof of the correctness of the macroscopic implementation, which has been achieved by the comparison between analytical and numerical solutions for the 1D problem, the 2D simulations are run with the following parameters:

- Parameters used in Charles' law: $K_0 = 2.5e5Pa(m^{\frac{1}{2}})$, $v_0 = 3e-4m/s$, $n = 2$.
- Material parameters: Young modulus $E = 2GPa$, Poisson's coefficient $\nu = 0.3$.
- Deformation speed $\frac{d\varepsilon}{dt}$ = 1e-4 s^{-1} and applied displacement in the x - direction U_L = 0.001 m.

Here we denoted $v_0 = \frac{cf}{\tau_0}$ as a referential velocity of crack propagation.

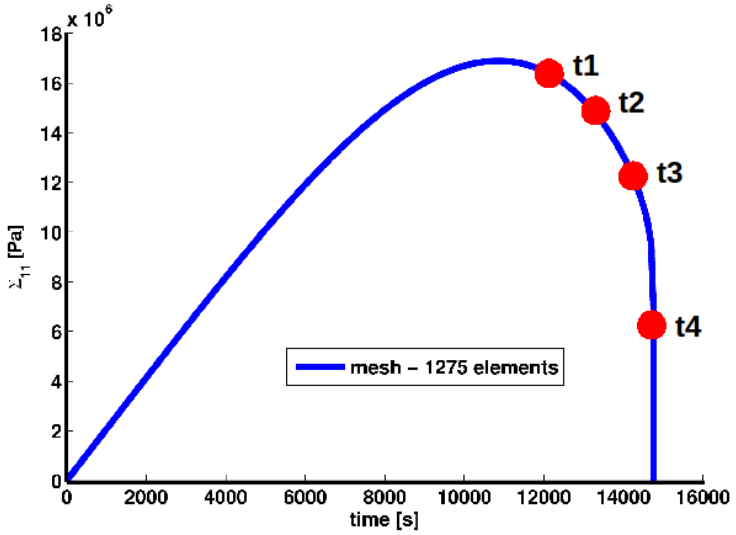

Figure 6.6: Global stress vs time curve from a simulation run with the regular mesh with 1275 elements. With red circles, the four chosen time steps are marked.

In Figure 6.7 localization mechanism is presented through a series of evolution maps at four time steps: on the left, damage distribution; on the right corresponding horizontal (direction of the solicitation) strain along the loading. A damage band begins to form at the time step t_1 = 11828 s and evolves until the complete failure of the specimen (t_4 = 14559 s). A diffused damaged zone in the central part of the specimen is observed. Central part of this zone shows progressive formation of a localization band which starts right after the pick stress value is reached. The damage parameter inside the band reaches its maximum. The formation of this band is clearly visible on the distribution of the horizontal strain.

Figure 6.8 shows localization mechanism through a series of five profiles. The last profile is realized at the time t_1. The elements taken into account are found in the vicinity of the bottom (or top, due to symmetry - the red band from the geometry shown in Figure 6.8) boundary. At step 2 the tendency of the localization appears, but it is more visible

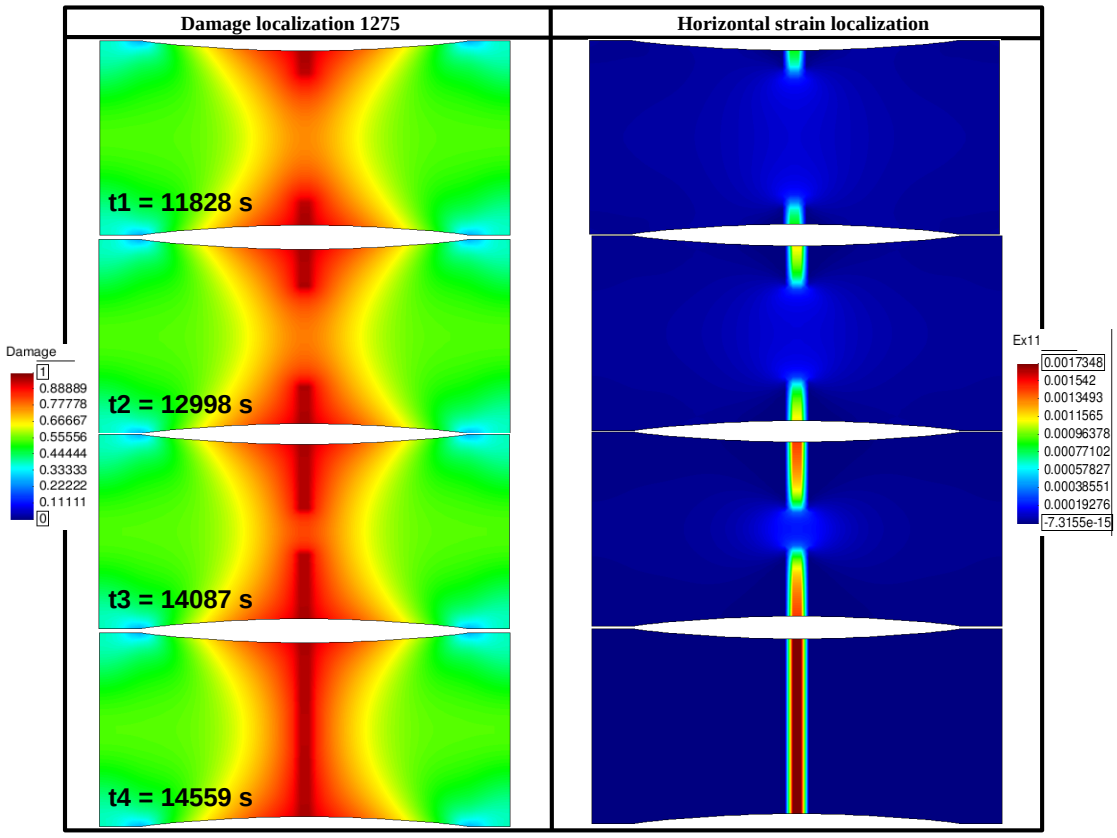

Figure 6.7: Strain evolution for four time steps. On the right of the figure horizontal strain localization perfectly follows damage localization is shown.

at the last steps. In the right part of the figure the Strain profile is shown. Central parts of the damage and strain profiles show increasing values of damage simultaneously with the decrease in strain values. In the rest of the profiles, the damage and strain increase continuously proving the development of localization bands.

6.3.4 Summary

In this section time-dependency concepts are introduced for the first time with the help of a simplified model using linear coefficients. The advantage is that this model was easy to understand and to follow. 1D simulation was run at the beginning and numerical and analytical results have been compared. Then, a 2D simulation was run proving the same tendency of damage and strain localization as observed at the one-dimensional test.

This model is used primarily for development of the method as the linear model cannot fully represent damage evolution due to its limitations (no distinction between opened an closed cracks, no information about the orientation, no information on the microstructure). Nevertheless, its contribution to the development of time-dependent damage modeling is really important. Its simplicity can be seen as a default, as previously said, but also as an advantage since it allows, on one hand, verification of the numerically obtained results with the analytical ones, and on the other hand, progress, since the

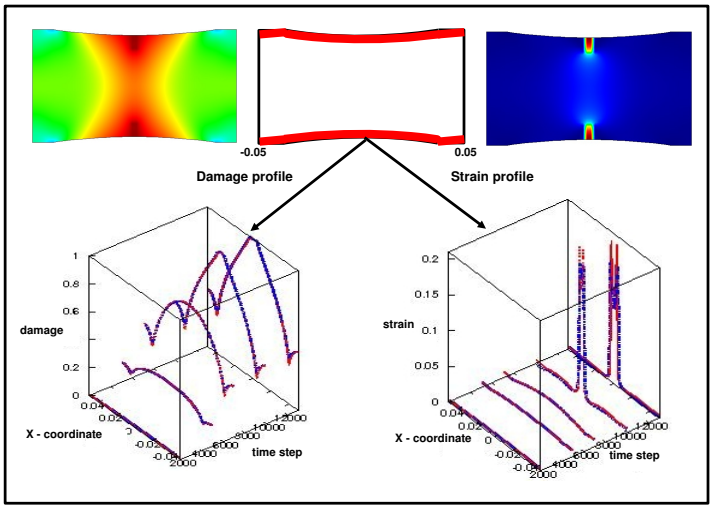

Figure 6.8: Appearance of the localization of the damage and strain bands during the loading.

second model, described by the propagation of the crack in a fixed direction, can be easily deduced, based on the simplified one.

6.4 Homogenized coefficients - propagation in a fixed direction

6.4.1 Introduction

In the following sections, time dependent damage models are deduced using homogenized (effective) coefficients. The starting point is the introduction of a criterion of the damage propagation in one fixed direction. Then micro-crack trajectory at each moment in time will be considered, since damage propagation in a fixed direction is not conform to the reality.

6.4.2 Numerical implementation

Correctness and efficiency of the method will be tested by giving some examples at the local and, respectively, global level. For a better understanding of the method, a numerical algorithm precedes the simulations.

Numerical iteration scheme

A simple procedure to follow in solving the simulations using this time-dependent damage model is illustrated in Fig. 6.9.
At each time step, $n+1$, the current deformation tensor e_x^{n+1} is known. In the first step damage variable is updated using trapezoidal rule which allows computation of the propagation increment Δd_{n+1}. The obtained value Δd_{n+1} is added to the previous micro-crack length leading to the real damage value at the current time step (d_{n+1}). Having the current deformation tensor e_x^{n+1} and the current value of the damage d_{n+1} the last step to be done is to update the stress tensor Σ_{n+1}.

Algorithm for analytical computation of the consistent tangent

To compute the consistent tangent matrix we start from the small strain tensor at the current state. As mentioned in the first part of this section, using trapezoidal rule, the damage parameter at the current time step is deduced. Having $e_x(n+1)$ and d_{n+1} we are able to compute the actual value of the energy release rate at the current (ERR). Knowing the value of ERR, all the other terms entering in the computation of the consistent tangent matrix (shown in Figure 6.10) are easily deduced.

6.4.3 Local macroscopic behavior

In this subsection we show only one theoretical example. Maximum of details on the development at the macroscopic local level on the time-dependent damage model with propagation in a fixed direction (tests on influence of the strain rate or elementary cell size on the damage, dependence on the environmental conditions, or relaxation tests) can

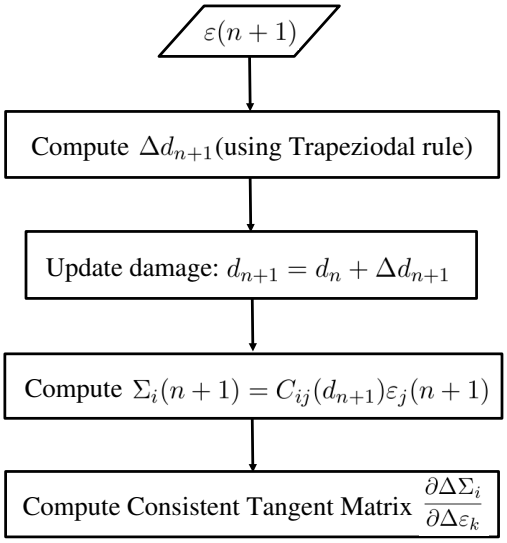

Figure 6.9: Incremental iterative procedure for the Time dependent damage model

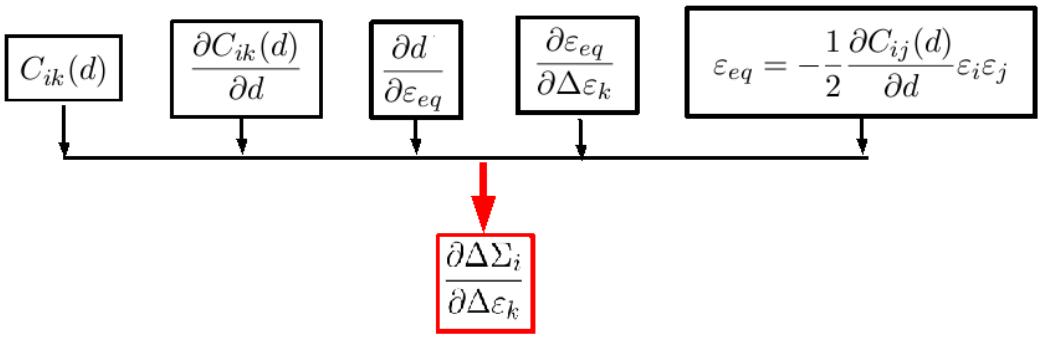

Figure 6.10: Analytical method for computing Consistent Tangent

be found in [117].

The 1D response, in tension, predicted by the elasto-damageable model is represented in Fig. 6.11. The material parameters are captured in the figure. It can be seen that the micro-crack evolution leads to material softening in the macroscopic response.

The effective coefficients used in the damage model corresponds to a horizontal crack. The crack propagates in this fixed direction until the complete failure $d = 1$.

6.4.4 Global macroscopic behavior

Our contribution is the modeling of the macroscopic part of the damage model. As for the previous damage model, one-dimensional test will be presented first, and then, a 2D simulation. The same type of test (displacement controlled tension) as used in the previous section is considered.

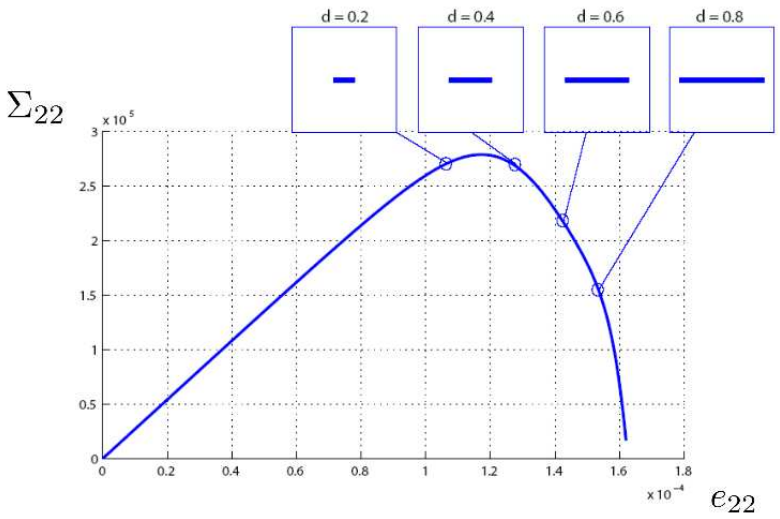

Figure 6.11: 1D response sub-critical homogenized response in tension (image from [38]).

1D damage problem

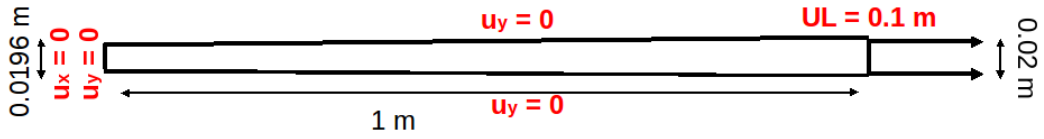

Figure 6.12: Geometry and boundary conditions for the 1D problem.

As in the case of the simplified damage model previously developed, this simple 1D simulation allows the study of the strain and damage evolution. Figure 6.13 shows damage (left) and strain (right) profile along the bar at 8 time steps. At the beginning of the test, a distribution of vertical micro-cracks of normalized length $d = 0.01$ is considered. Time t_1 corresponds to the appearance of the localization process. The process accelerates from time t_4 up to time t_8 which coincide with the complete failure of the bar.

In the right part of Figure 6.13 the strain profile is shown. The loading - unloading process which is in a direct link with the localization phenomena is presented. As in the 1D simulation realized with the simplified damage model presented in the previous section, it can be seen that damage increases continuously along the bar, meanwhile strain values decrease in the right part and increase continuously in the left of the bar.

The question which arises now is: *Which parameters influence the localization zone?*. In order to answer to this question, several simulations have been run and the influence of three parameters was studied. First, a mesh dependency test was run. Four regular meshes have been taken containing 100, 200, 400 and, respectively, 600 elements. Figure 6.14 fully answer to our question: no, the length of the localization band does not depend

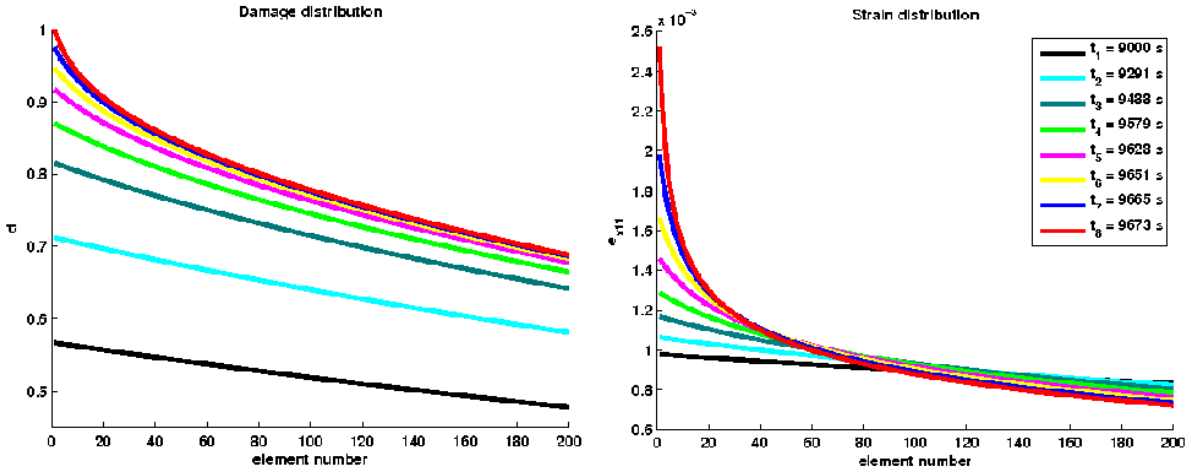

Figure 6.13: Damage and strain profiles along the bar at eight time steps. t_1 corresponds to the beginning of the localization phenomena and t_8 is the end of the simulation when complete failure occurs.

on the chosen mesh. Indeed, in the top part of the figure, with red is represented the localization zone at the last step of the simulation, right before complete failure. The length of the zone is ≈ 0.12 m. Bottom part of the figure presents the damage distribution along the bar at the last time step. No visible differences between the four distributions are encountered.

After proving mesh independence, influence of the initial crack normalized length and of the referential velocity v_0 is shown in Figures 6.15 - 6.16. As for the previous picture, the same structure is employed: at the top, with red, localization zone is depicted, meanwhile damage distribution is at the bottom. It is clear that bigger initial micro-crack length, bigger the localization zone, since, for $d_0 = 0.01$ the zone size is $\approx 0.12m$ and for $d_0 = 0.3$ is $\approx 0.21m$ which give an important difference of about 10 % of the bar. Also the damage distribution shows the increase in this length since at the last time step, the damage along all the bar is bigger for significant d_0.

Six values for v_0 were considered in the test with a significant difference between the biggest and smallest value, in order to assure the pertinence of the results. A very slight decrease in the size of the localization zone with the decrease of the velocity v_0 it can be observed. For the first 3 values, 1e-1 m/s, 1e-2 m/s, 1e-3 m/s the time influence almost vanishes and the obtained length is constant ≈ 0.125 m. For really small values (e.g. 1e-10 m/s,) a small decrease can be seen, the localized zone being of ≈ 0.0105 m. This very small variation compared with the change in v_0, do not allow us to conclude that a real influence of v_0 exists. They are probably due to numerical effects.

2D tension test

As in the section 6.3 the test that will be presented at the macroscopic global level is a 2D tensile displacement controlled test. We remind that geometry and boundary

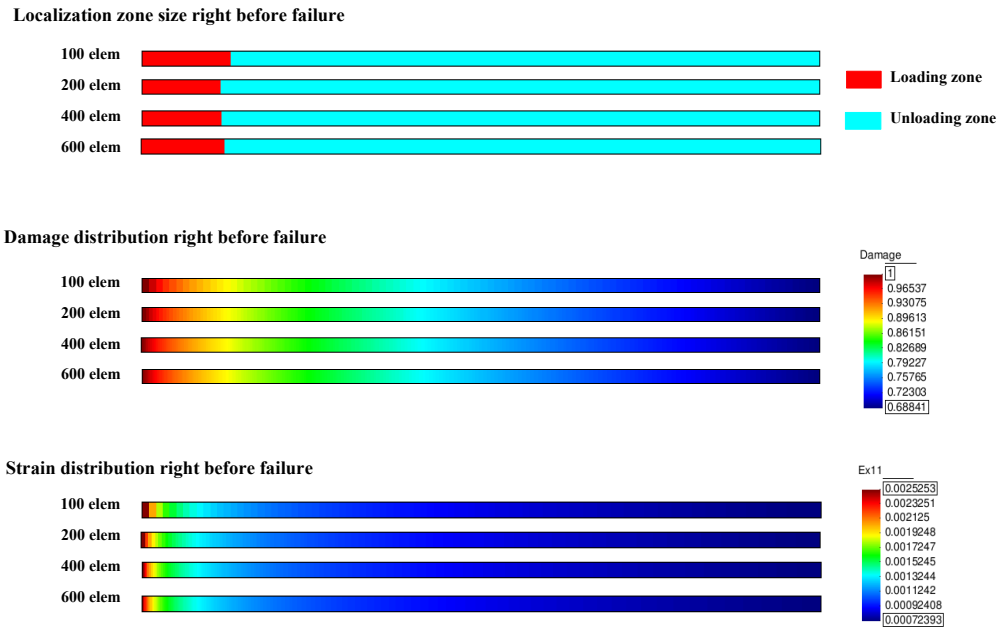

Figure 6.14: Mesh independence.

conditions for this test are given on the upper left part of Figure 6.1. Same parameters as for section 6.3 will be used.

As in the 1D simulation, a result given by the rate dependent model is the localization of the damage, and by consequence, the localization of the deformation (Figure 6.18). All the macroscopic tests were run assuming a locally periodic distribution of vertical cracks. It is well known that, in tension, the cracks tends to alligne perpendicular to the direction of the main loading. In this case, since horizontal displacement is imposed, all the cracks will tend to 90°, proving the pertinence of our choice concerning micro-crack initial orientation.

In the top of the Figure 6.18 the damage and strain distribution are shown for four different time steps represented with red dots on the global horizontal stress - time curve presented in Figure 6.17. It is very clear that a damage band is forming at the time step $t_1 = 15465$ s and evolves until the complete failure of the specimen ($t_4 = 15651$ s). The global curve, as well as the numerical values of t_1 - t_4, presents a rapid propagation up to the complete failure. This rapid behavior was also found in the previous case where the time dependent damage law was based on linear coefficients.

As in the simplified model, we observe a diffused damaged zone (normalized damage variable $d \approx 0.7$) in the central part of the specimen. In the interior of this zone we observe progressive formation of a localization band which starts right after the peak stress value is reached. The normalized damage value inside the band reaches its maximum ($d = 1$). The formation of this band is clearly visible on the distribution of the horizontal strain. In the band zone strain increases with the damage, (red colored middle band), meanwhile,

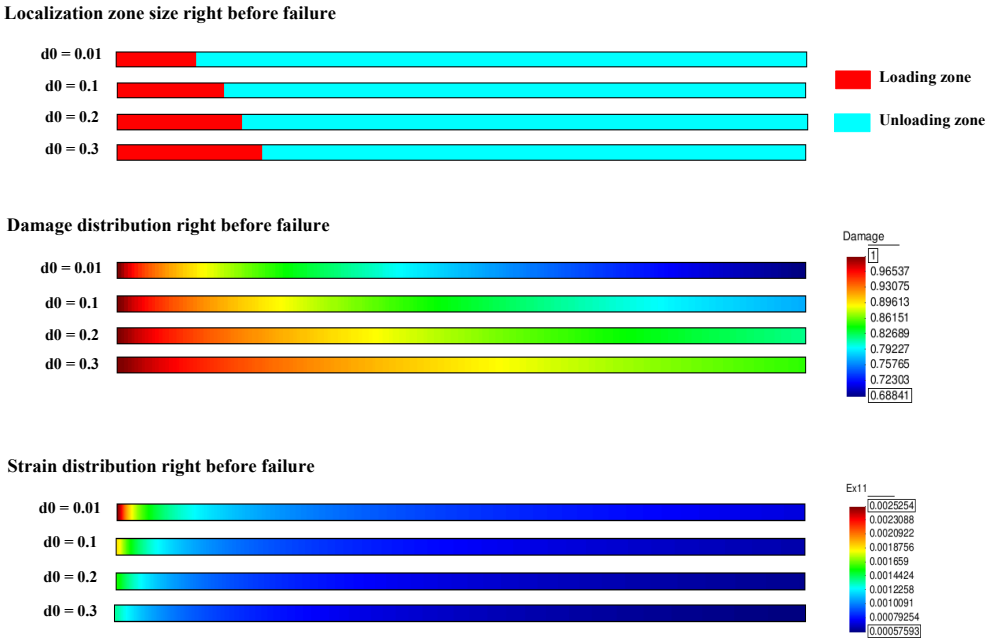

Figure 6.15: Influence of the initial micro-crack length d_0 on the localization zone.

in the rest of the specimen, the strain decrease (to be observed a change in the blue color spectrum: dark blue seen on the strain map at the last time step from figure 6.18 corresponds to the absolute minim from all the loading process).

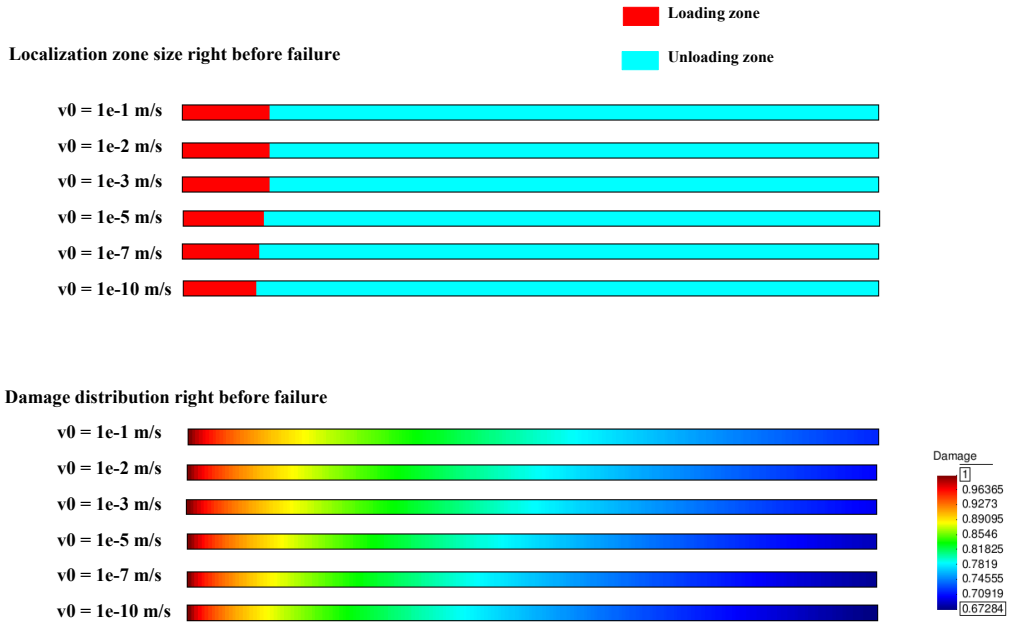

Figure 6.16: Very small influence of specific velocity v_0 on the localization zone.

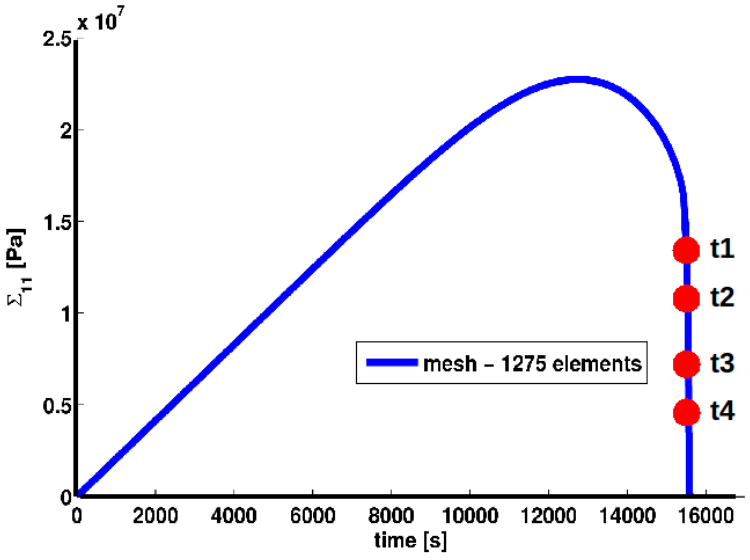

Figure 6.17: Damage evolution (left) and changes in the micro-craks orientation for four time steps.

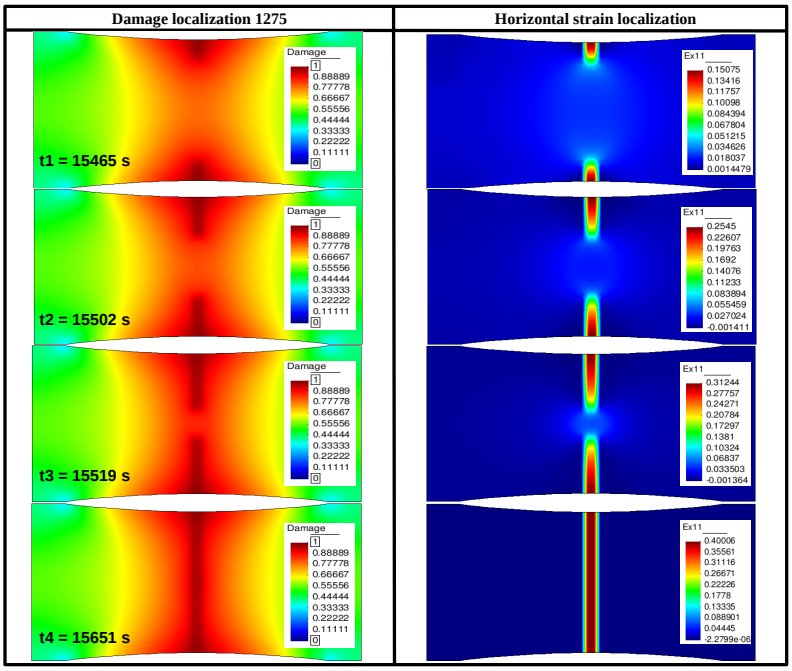

Figure 6.18: Damage and horizontal strain evolution for four time steps. On the right of the figure, horizontal strain localization follows perfectly damage localization.

6.5 Time-dependent damage model with kinking micro-cracks

6.5.1 Introduction

In the previous two time-dependent damage models only criteria for crack extension were introduced. In this section, for the first time, criteria for the evolution of the crack orientations will be used. In the existing damage models the change of orientation of micro-cracks is generally not taken into account. In our model, the crack evolution will be realistically controlled, at the same time, by the speed and by the orientation of the propagation.

A first contribution to the development of this time-dependent damage model is found in [56]. We continued this work on three levels:

- Microscopic level: in [56], Stress Intensity Factors (SIF) have been computed using path-independent integrals method. In this thesis SIF will be deduced using displacement correlation method (6.5.3). A comparison between the two methods will be done. It will be seen that this comparison will lead to a question on the influence of periodicity on the computation of SIF for high values of the normalized crack length.

- Macroscopic local level: the case of micro-cracks under compressive conditions have been developed. The criterion in [56] shows rapid, unrealistic micro-cracks rotations. Some elements of remedy to this problem are proposed in our work.

- Macroscopic global level: implementation in Finite Element code FEAP ([136]) fully represents our contribution. The macroscopic implementation of the previous two time-dependent damage models naturally leaded to the full development of the two-scale time-dependent including micro-cracks kinking damage model that will be presented in this subsection.

In order to give a full description of this model, another two small parts need to be added. Because of the micro-cracks kinking mechanism, first, a discussion on the surface interpolation for the homogenized coefficients is necessary. Then, a full description of the stress intensity factors for straight micro-cracks will be given. In the simulations, it is necessary for SIF to be known for every crack length and orientation, therefore, the same interpolation process as for the homogenized coefficients (an interpolation for a fixed orientation followed by a surface interpolation for all the 13 considered orientations in the interval $[0°, 180°]$) will be given.

6.5.2 Homogenized coefficients - interpolation for different orientations

Theoretical aspects which lead to the computation of the homogenized coefficients have been presented in Chapter 4. The analytical form of $C_{ijkl}(d, \theta)$ was given through Eq. 25, where d is the damage variable and θ is the orientation of the micro-crack. The couple (d, θ) completely characterizes the state of damage at a given macroscopic point. In the previous chapter, interpolation method was discussed in the case of a fixed trajectory of the propagation. Until this moment this procedure was sufficient since all damage models, either time-dependent or time-independent, concerned the crack propagation in a fixed direction chosen from the beginning of the computations. In the following, a criteria for the orientation of the propagation will be proposed, which requires $C_{ijkl}(d, \theta)$ to be known at any value of the rotation angle on interval $[0°, 180°]$. This goal is achieved using a surface linear interpolation (Eq. 97).

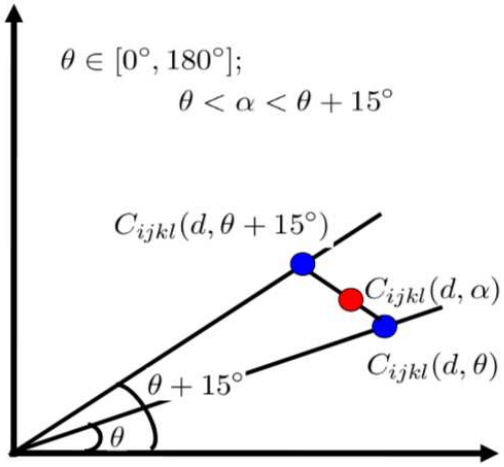

Figure 6.19: Linear spatial interpolation of the effective coefficients.

In Figure 6.19 the interpolation with respect to the rotation angle θ, based on the interpolation in d is performed. We have the polynomial for each discreet orientation $15°, 30°, \ldots$ and we obtain by linear interpolation the values of the coefficients in each angle α between two consecutive values of θ. The formula for obtaining the values of $C_{ijkl}(d, \alpha)$ is deduced as the following

$$C_{ijkl}(d, \alpha) = C_{ijkl}(d, \theta) + \frac{C_{ijkl}(d, \theta + 15°) - C_{ijkl}(d, \theta)}{15}(\alpha - \theta). \tag{97}$$

Remark: The same procedure of interpolation is valid also for the Stress Intensity Factors.

6.5.3 Stress intensity factors for straight micro-cracks

Asymptotic near-tip stress fields

Linear elasticity leads to stress singularities at a sharp crack tip and Williams ([146]) has shown that the asymptotic behavior of stresses, strains and displacements in the vicinity of a crack tip is the same for every crack problem. In particular, the stresses distribution is given universally by

$$\sigma_{ij} = \frac{1}{\sqrt{2\pi r}}(K_I f_{ij}^I(\varphi) + K_{II} f_{ij}^{II}(\varphi) + K_{III} f_{ij}^{III}(\varphi)) \tag{98}$$

with plane polar coordinates r and φ centered at the crack tip. The universals dimensionless functions f_{ij} depend only on the angular coordinate φ. Gdoutos (1993) [63] gave explicitly the form of those functions which led to explicit formula for the stresses and displacements near the tip of a crack given below:

$$\sigma_{11} = \frac{K_I}{\sqrt{2\pi r}} \cos\frac{\varphi}{2}(1 - \sin\frac{\varphi}{2}\sin\frac{3\varphi}{2}) + \frac{K_{II}}{\sqrt{2\pi r}} \sin\frac{\varphi}{2}(-2 - \cos\frac{\varphi}{2}\cos\frac{3\varphi}{2}), \tag{99}$$

$$\sigma_{22} = \frac{K_I}{\sqrt{2\pi r}} \cos\frac{\varphi}{2}(1 + \sin\frac{\varphi}{2}\sin\frac{3\varphi}{2}) + \frac{K_{II}}{\sqrt{2\pi r}} \sin\frac{\varphi}{2}\cos\frac{\varphi}{2}\cos\frac{3\varphi}{2}, \tag{100}$$

$$\sigma_{12} = \frac{K_I}{\sqrt{2\pi r}} \sin\frac{\varphi}{2}\cos\frac{\varphi}{2}\cos\frac{3\varphi}{2} + \frac{K_{II}}{\sqrt{2\pi r}} \cos\frac{\varphi}{2}(1 - \sin\frac{\varphi}{2}\sin\frac{3\varphi}{2}), \tag{101}$$

$$4Gu_1 = \sqrt{\frac{r}{2\pi}}[K_I((2k-1)\cos\frac{\varphi}{2} - \cos\frac{3\varphi}{2}) + K_{II}((2k+3)\sin\frac{\varphi}{2} + \sin\frac{3\varphi}{2})], \tag{102}$$

$$4Gu_2 = \sqrt{\frac{r}{2\pi}}[K_I((2k+1)\sin\frac{\varphi}{2} - \sin\frac{3\varphi}{2}) + K_{II}(-(2k-3)\cos\frac{\varphi}{2} - \cos\frac{3\varphi}{2})]. \tag{103}$$

where $G = \frac{E}{2(1+\nu)}$ is the shear modulus and $k = \begin{cases} \frac{3-\nu}{1+\nu} & \text{for plane stress,} \\ (3-4\nu) & \text{for plane strain.} \end{cases}$

It is obviously that at the crack tip, the stresses are governed by a $1/\sqrt{r}$ singularity. The constants K_I, K_{II} and K_{III} are called *stress intensity factors* and they represents measures for the intensity of the increase of stresses near the crack tip.

Homogenization by asymptotic developments - computation of SIF

All the multi-scale damage models we present in this thesis start by considering a two-dimensional isotropic elastic medium containing a locally periodic distribution of micro-cracks of length $2a$ and orientation θ with respect to the x_1 direction (abscissa of the referential system considered at the macro-scale). Therefore, in the macroscopic problem $K_{I,II}(\mathbf{u}^\varepsilon)$ must be determined. The upscaling procedure ($d = 2a/\varepsilon$, $\mathbf{y} = \mathbf{x}/\varepsilon$ and $\mathbf{y}' = \mathbf{x}'/\varepsilon$, $ds_y = dS/\varepsilon$ and $\mathbf{u}^\varepsilon \simeq \mathbf{u}^{(0)}(\mathbf{x}) + \varepsilon\mathbf{u}^{(1)}(\mathbf{x}, \mathbf{y})$, $\mathbf{u}^{(0)}$ being independent of the microscopic variable $\mathbf{y}$) enables us to express K_I and K_{II} in the macroscopic problem:

$$K_I(\mathbf{u}^\varepsilon) = \sqrt{\varepsilon} K_I(\mathbf{u}^{(1)}) \tag{104}$$

$$K_{II}(\mathbf{u}^{\varepsilon}) = \sqrt{\varepsilon} K_{II}(\mathbf{u}^{(1)}) \tag{105}$$

But, for any macroscopic field $[e_{x11}\ e_{x22}\ e_{x12}]$, the resulting stress intensity factors are determined by the superposition of the stress intensity factors of the elementary deformation modes ($\xi_{\pm}^{11}$, $\xi_{\pm}^{22}$, $\xi_{\pm}^{12}$), as a consequence of (18):

$$K_{I,II}(\mathbf{u}^{(1)}) = \pm(e_{x11} K_{I,II}(\xi_{\pm}^{11}) + e_{x22} K_{I,II}(\xi_{\pm}^{22}) + e_{x12} K_{I,II}(\xi_{\pm}^{12})), \qquad \text{in } \mathbf{R}^{\pm} \tag{106}$$

The distinction between stress intensity factors for opening and closure of micro-cracks is given by the orientation of the force-type vector in the right member of Eq. (17) with respect to crack line (see relation 19).
In conclusion, to obtain the stress intensity factors in the macroscopic problem, $K_{I,II}$ of the elementary deformation modes it is necessary to be determined. In the next lines we will present the methods to achieve this goal.

If a single mode of crack loading (exclusively mode I or exclusively mode II) is taken into account, the non-null stress intensity factor can be deduced from the energy release rate at the crack tips $\mathcal{G}^{\varepsilon}$ (in a plane strain configuration):

$$\mathcal{G}^{\varepsilon} = \frac{1-\nu^2}{E}[K_I^2 + K_{II}^2] \tag{107}$$

under the condition that K_I or K_{II} is null.

Based on micro-mechanical energy balance on a periodicity cell with evolving micro-cracks and assuming a straight micro-crack trajectory and a traction-free opening (Eq. 7) or frictionless contact of the crack lips (Eq. 8), [37] deduced the following energy balance equation entirely expressed in terms of the homogenized solution $\mathbf{u}^{(0)}$, that enables to determine the energy release rate $\mathcal{G}^{\varepsilon}$ for the locally periodic structure:

$$\frac{dd}{dt}\left(\frac{1}{2}\frac{\partial C_{ijkl}(d,\theta)}{\partial d} e_{xkl}(\mathbf{u}^{(0)}) e_{xij}(\mathbf{u}^{(0)}) + \frac{\mathcal{G}^{\varepsilon}}{\varepsilon}\right) = 0 \tag{108}$$

The first term in the parenthesis is the negative of the damage energy release rate. For evolving damage, the previous relation shows that the microstructural length ε makes the link between the surface energy dissipated during micro-crack propagation and damage energy dissipated per unit volume.

However, if mixed modes of crack loading are considered, individual stress intensity factor modes cannot be determined from the energy-release rate and a different technique must be used. Such techniques generally include local computations at the crack tips or use of path-independent integrals that can be computed in term of far-field quantities. Both methods were taken into account and in the next lines we will make a parallel between them.

The first method uses information from a small distance away from the crack tip where the stress field is singular. It is known as *displacement correlation method*. The idea behind it is to extract stress intensity factors from the results of a finite element simulation of a cracked body and to match the asymptotic fields.

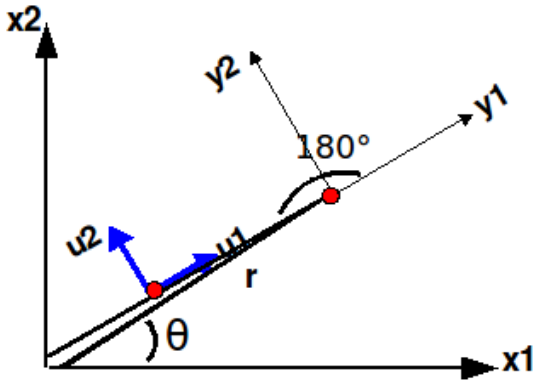

Figure 6.20: Describe of the displacement correlation method

We denote by r the distance between the crack tip and the neighborhood node (Figure 6.20). Equations 103 become:

$$u_1(r,\pi) = -\sqrt{\frac{r}{2\pi}}\frac{4K_{II}}{E'}, \tag{109}$$

$$u_2(r,\pi) = \sqrt{\frac{r}{2\pi}}\frac{4K_I}{E'}. \tag{110}$$

where $E' = \frac{E}{1-\nu^2}$ for the plane strain case.
u_1 and u_2 represents the tangential and, respectively, normal displacement of the node near the crack tip, with respect to the crack system of coordinates. Since in any Finite Element simulation the displacement field is given with respect to x-coordinates, a formula to connect the two displacement fields is necessary to be given. Taking into account the crack orientation given by the angle θ (Figure 6.20), u_1 and u_2 become:

$$u_1(r,\pi) = \cos\theta u_x + \sin\theta u_y, \tag{111}$$

$$u_2(r,\pi) = -\sin\theta u_x + \cos\theta u_y \tag{112}$$

The minus of this method is that in order to have good results special finite elements are needed for the computation of K_I and K_{II}. Moreover, since the formula involves the distance between two nodes, a mesh dependency must be taken into account. To overcome the two minuses of this method several simulations have been run with different type of meshes and the final results were considered those which, from a certain mesh length, do not change drastically the values.

On the other hand, it is true that the use of far-field quantities is very convenient since it can be carried out within a standard finite element code. Starting from the procedure proposed by [91], the expression of stress intensity factors with respect to the L-, M- and [H]-integrals has been given in [56].

K_I and K_{II} were computed for a large number of lengths d and orientations θ of cracks and for the three modes of deformations ($\xi_{\pm}^{11}$, $\xi_{\pm}^{22}$ and $\xi_{\pm}^{12}$) in both states of opening (+) or contact (-) of the crack lips. On the same manner as for the homogenized coefficients we obtain by interpolation the polynomial expressions of $K_I(d^*,\theta)$ and $K_{II}(d^*,\theta)$.
The results given by the two methods were compared. One example is given in Figure

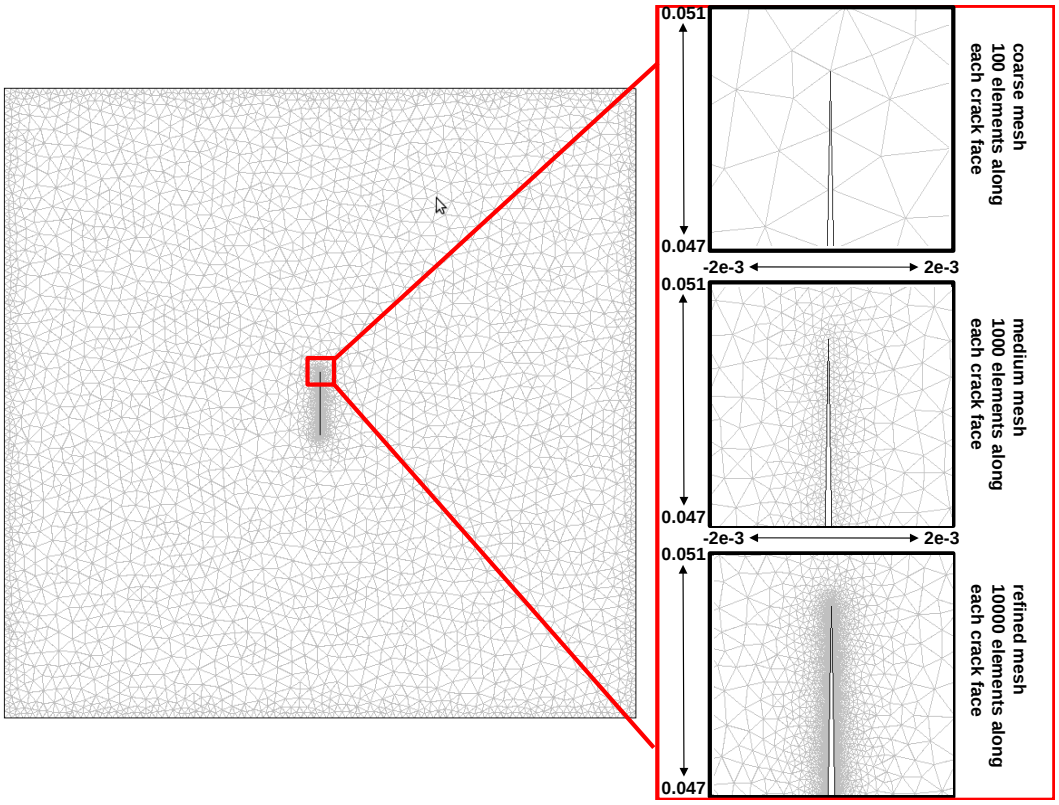

Figure 6.21: Mesh dependency test

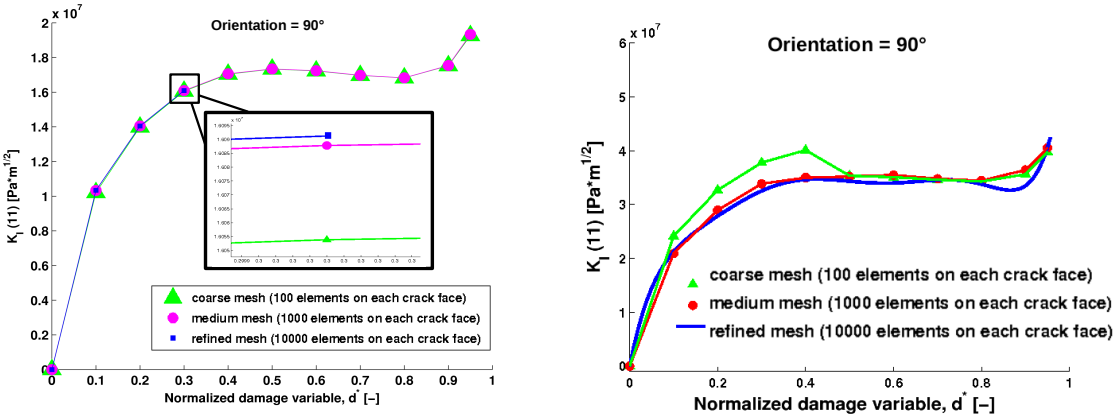

Figure 6.22: Mesh dependency: left - in compression; right - in tension

6.23. Although the computed values are not too far from each other, a question arises: 'What happens for big values of crack length? The values of the stress intensity factors should still increase since we deal with periodicity? Or they should decrease since less energy for the propagation of the crack is necessary?'. Unfortunately we do not have an answer at this moment, so we decided to interpolate using the computed values up to normalized damage variable $d^* = 0.9$ and bigger values will come from the interpolation polynomial.

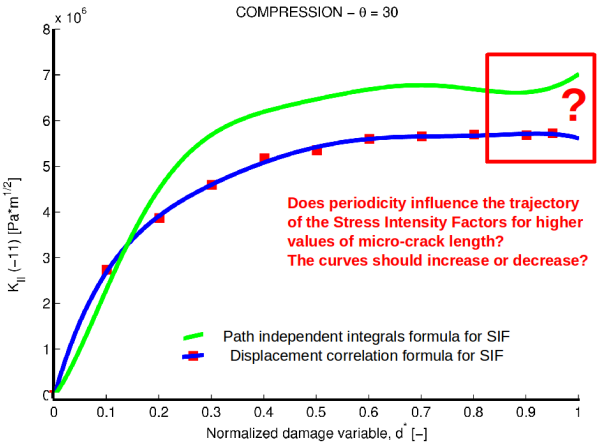

Figure 6.23: Comparison between the two method for computing stress intensity factors

In the end of this section, the results of the evolution of stress intensity factors as a function of normalized damage variable $d^\star$ for different micro-crack orientations θ are presented in Figures 6.24 and 6.25. In the second case, for cracks in contact, $K_I = 0$ for any loading mode of the unit cell. K_{II} is antisymmetric either with respect to $\theta = 90$ (i.e. $K_{II}(d^*, 15) = -K_{II}(d^*, 165)$, $K_{II}(d^*, 30) = -K_{II}(d^*, 150)$; ...) for ξ^{11} and ξ^{22}, either with respect to $\theta = 45$ (i.e. $K_{II}(d^*, 15) = -K_{II}(d^*, 75)$, $K_{II}(d^*, 30) = -K_{II}(d^*, 150)$; ...) for the shear mode. The computations have been performed with the finite element code [32] and displacement correlation method has been used.

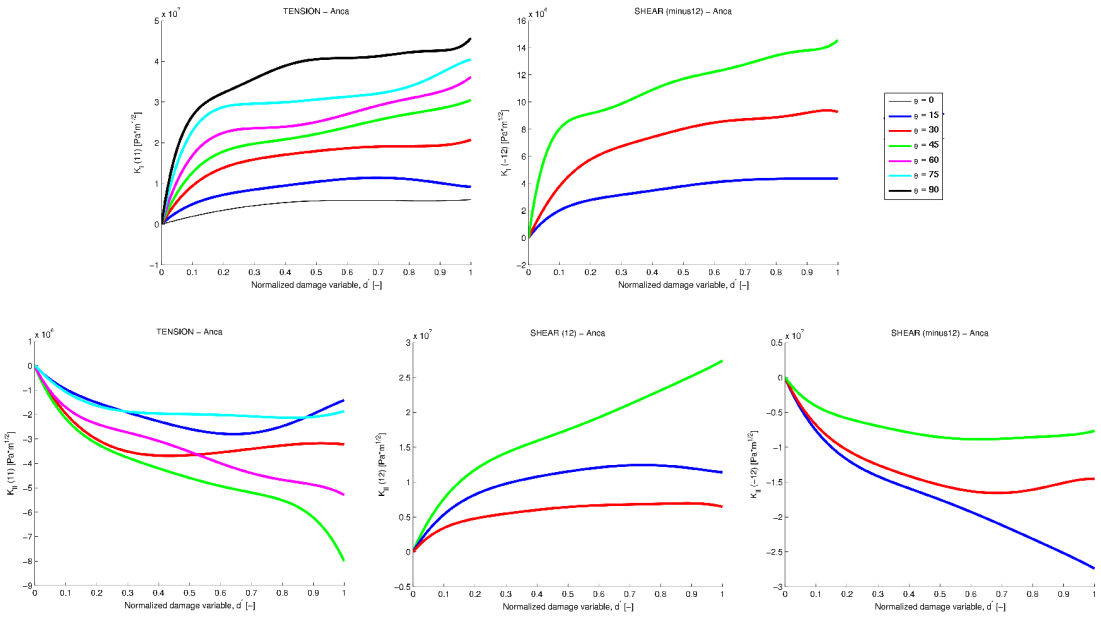

Figure 6.24: Evolution of the stress intensity factors K_I and K_{II} with respect to the damage variable d and the crack orientation θ for elementary modes of deformation: Opening conditions of the crack lips ($\mathbf{R}^+$ domain).

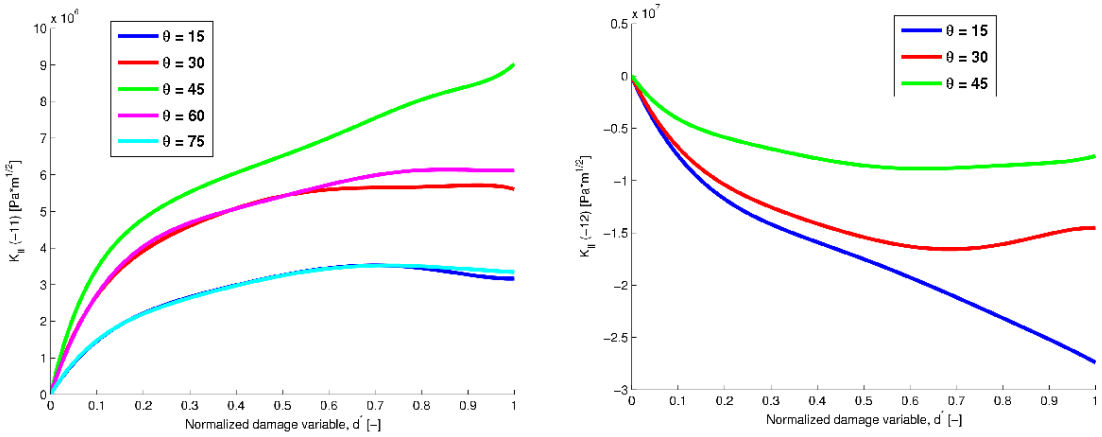

Figure 6.25: Evolution of the stress intensity factors K_{II} with respect to the damage variable d and the crack orientation θ for elementary modes of deformation: Contact conditions of the crack lips ($\mathbf{R}^-$ domain).

6.5.4 Mathematical formulation of the time-dependent model in particular case of rotating micro-cracks

Like in the previous time-dependent damage models, the evolution of the micro-crack length during propagation is described through a subcritical criterion also adapted from the Charles' law.

$$\frac{dl}{dt} = v_0 \left(\frac{K_I^\star}{K_0} \right)^n \tag{113}$$

Nevertheless, in this case, this criterion is used to describe the propagation of the kinked crack (Fig. 6.26 left), dl being the length of the branch and the corresponding stress intensity factor being indicated by the star upper index. K_0 is a particular stress intensity factor for which the velocity of the crack propagation is equal to v_0. K_0, v_0 and n are material parameters. $K_I^\star$ is the stress intensity factor for the tensile mode of rupture (Mode I) and depends on the stress state, on the internal length ε and on the geometry of the micro-cracks.

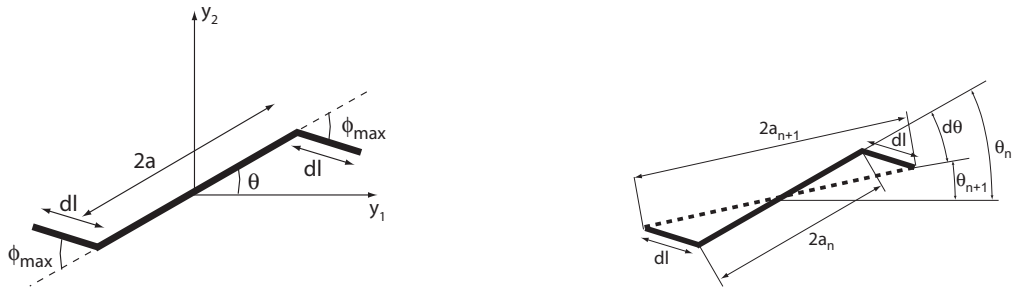

Figure 6.26: Left) Kinked crack. The out-of-plane crack growth propagates in the direction that maximize the energy release rate. Right) The kinked crack (solid line) with its equivalent replacement crack (dashed line) (images from [56])

The crack is assumed to propagate in the direction that maximizes the energy release rate. This criterion produces a kinking angle between the existing crack and the incrementally propagated crack (Fig. 6.26 left). This kinking angle can be expressed with the following function [131]:

$$\begin{aligned} \phi_{max} = \quad & sgn(K_{II})[0.70966\lambda'^3 - 0.097725sin^2(3.9174\lambda') \\ & -13.1588tanh(0.15199\lambda')] \end{aligned} \tag{114}$$

where sgn is the signum function and λ' is a mode mixity factor that combines the stress intensity factors of mode I, K_I, and mode II, K_{II}, of the straight crack :

$$\lambda' = \frac{|K_{II}|}{K_I + |K_{II}|} \tag{115}$$

At the level of the crack tips, the propagation of the kinked crack is governed in length and orientation by Eqs. (113) and (114), respectively.

In Section 6.5.3 stress intensity factors K_I and K_{II} for a straight micro-crack, as functions of the macroscopic deformations were determined using the displacement correlation method and comparison was made with the SIF determined with the path-independent integral procedure completely described in [56].

6.5.5 Stress intensity factors for kinked cracks

In what follows, we will express the intensity factors for kinks with those which were deduced for straight cracks (6.5.3).

In order to apply the subcritical criterion for the growth of micro-crack (Eq. 113), we consider the direction of crack propagation that maximize the energy release rate. This assumption implies that the crack produces a kinking angle as expressed by Eq. (114). Therefore, the mode I stress intensity factor included in the subcritical criterion is not the stress intensity factor of the straight crack K_I but $K_I^\star$ corresponding to the kinked crack.
If we assume that for short time intervals, the length of the crack propagation dl is small compared to the crack length ($dl << 2a$), then the relationship proposed by [95] can be used to expressed $K_I^\star$ and $K_{II}^\star$ (for the branches which appears) with respect to K_I and K_{II} (for the existing straight crack):

$$K_i^\star = F_{i,j}(\phi_{max}) K_j. \tag{116}$$

Here i and j take the values I and II and $F_{i,j}(\phi_{max})$ is a 2×2 matrix depending on the kinking angle ϕ_{max}. The main advantage of this expression is that it is universal, with respect to the geometry and the loading. The functions $F_{I,I}$, $F_{I,II}$, $F_{II,I}$ and $F_{II,II}$ are given with respect to the kinking angle through polynomials of order 20 by [95].

Many authors (e.g. Nemat-Nasser and Horii, 1982) have shown that the determination of the kinking angle through the maximum energy release rate gives essentially the same results than the condition of local symmetry which requires that the mode II stress intensity factor vanishes at the tip of the kinked extension. Therefore, we can neglect the mode II intensity factor ($K_{II}^\star = 0$).

6.5.6 Equivalent crack

After each determination of the direction (ϕ_{max}, Eq. 114) and of the length (dl, Eq. 113) of the out-of plane crack extension, the replacement of new formed kinked crack by an equivalent straight crack is necessary in order to compute the whole trajectory of the crack tips. If the obtained kinked crack would be kept, the determination of the subsequent crack extension would be imposible since the above theory using K_i is valid only in the case of smooth cracks.

There are several possible ways to to replace the kinked crack by an equivalent straight crack. For instance, [131] proposed to find, at each time step, a straight crack that is

thermodynamically equivalent to the kinked crack. [10] and [56] introduced an equivalent straight crack by joining the tips of the real branched crack. We adopted the criteria described by [56] for construction of the equivalent crack. A series of tests, at the macroscopic local level, both in tension and compression loading conditions have been run. We observed that in the case of the propagation of micro-cracks in pure mode II, micro-crack's rotating is too accelerate which diminuates the propagation. In order to overcome this inconvenience, some adjustments to the previous criteria are proposed in this thesis by the introduction of a parameter whose function should be to decrease micro-crack's rotation speed which would help in the increase of propagation. We will denote this parameter "Trajectory Corrector (TC)" and it will be introduced in the determination of the equivalent crack in the manner described in the following.

Geometrical relationships in a triangle are used to determine the equivalent crack. Chosen triangle is described by the lengths: where a_n and a_{n+1} are the half of the length of the straight crack at step n and $n+1$ and dl is the length of a branch (Fig. 6.26 Right). Law of Sines leads to:

$$\tan(d\theta) = \frac{\sin(\phi_{max})}{\frac{a_n}{dl} + \cos(\phi_{max})} \tag{117}$$

and for the updated crack length:

$$a_{n+1} = \frac{\sin(\phi_{max})}{\sin(d\theta)} dl \tag{118}$$

Assuming small time increments, equating $d\theta \simeq \tan(d\theta) \simeq \sin(d\theta)$ that result from Eqs (117) and (118) and using the up-scaling relation, the two last expressions can be transformed, at the limit, into differential equations:

$$\frac{dd}{dt} = \frac{2}{\varepsilon} \cos(\phi_{max}) \frac{dl}{dt} \tag{119}$$

If Mode I is active in the crack propagation, then

$$\frac{d\theta}{dt} = \frac{2}{\varepsilon d} \sin(\phi_{max}) \frac{dl}{dt} \tag{120}$$

else

$$\frac{d\theta}{dt} = \frac{2}{\varepsilon d} \sin(\phi_{max}) \frac{dl}{dt} \frac{1}{TC} \tag{121}$$

The three last equations show that the geometry of the equivalent micro-crack, in terms of length and orientation, depends on the propagation rate $\frac{dl}{dt}$ and the orientation ϕ_{max} of the kinked crack. These quantities are computed with respect to the stress intensity factor K_I and K_{II} of the equivalent straight micro-cracks, as shown previously. They depend on the macroscopic damage variables d and θ and on the macroscopic deformation $\mathbf{e_x}$. This establishes the homogenized damage model, based on mixed micro-crack propagation, in an implicit form. We remark the presence of the microstructural length parameter ε in the damage equations (119 - 121).

We introduce the factor TC in order to try to give a solution for the rapid acceleration of crack rotation under compressive conditions. Without this factor, our time-dependent

damage model predicts an evolution of micro-crack rotation to accentuate compared to the experimentally observed behaviour. The problem is not completely solved by the use of TC and more investigations are necessary. Nevertheless, in the following test we try to determine this parameter in the case of uniaxial compressive macroscopic local level test. Constant strain rate loading conditions in vertical direction are imposed.

The purpose of the first test is to find TC in the case of a micro-crack initially oriented at 45° and having an initial normalized length of 0.2. The criteria we use for the choice of TC is that the micro-crack crosses completely the unit cell and align to the vertical direction. The first value which satisfy this criteria is chosen.

Figure 6.27 shows the results of five uniaxial compressive tests with different values of TC. A vertical constant strain rate $\dot{e}_{x22} = 1e-8s^{-1}$ is imposed. It is observed that, for TC smaller than 8 the criteria is not satisfied, the cell not being crossed by the micro-crack. Figure 6.27 a) corresponds to the case when the criteria described by [56] for construction of the equivalent crack is used.

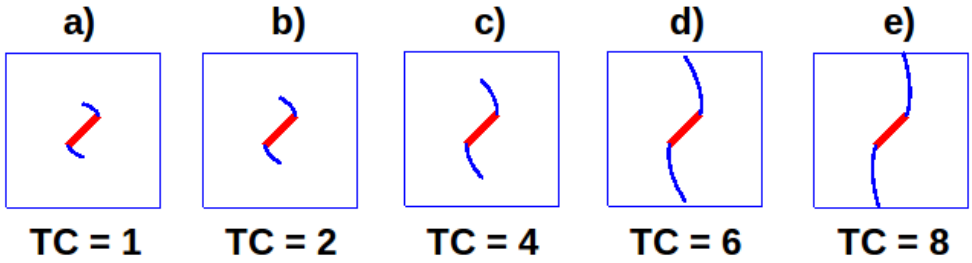

Figure 6.27: Influence of TC on a micro-crack behaviour under constant strain rate loading conditions ($\dot{e}_{x22} = 1e-8s^{-1}$): matching procedure in the case of a micro-crack having $\theta_0 = 45°$ and $d_0^* = 0.2$.

In figure 6.28 influence of initial micro-crack length is presented, the conclusion that can be drawn is that the Trajectory Corrector's value decrease with the increase of the initial length. The same vertical constant strain rate as for the previous tests is imposed ($\dot{e}_{x22} = 1e-8s^{-1}$).

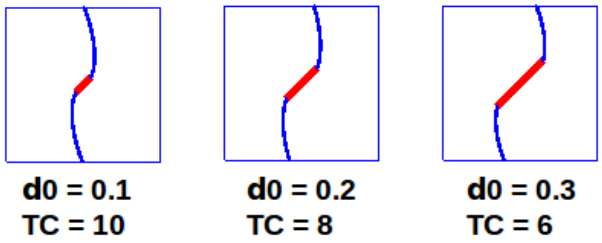

Figure 6.28: Influence of initial orientation on matching TC value: bigger the initial normalized length, smaller TC is observed.

Previous tests considered micro-crack orientation of 45° with respect to the x-axis. The new series of tests concentrates on the influence of the initial orientation on the micro-crack behaviour. Tests have been run also in the case of micro-cracks initially oriented

at 5°, 15°, 30°, 60° and 75° with respect to the x-axis. An increase of TC with the orientation, which is more severe when initial micro-crack tends to verticality, has been observed. Then tests which considered micro-crack orientation in the interval $[90°, 180°]$ were run. As expected, symmetry with the interval $[0°, 90°]$ was encountered. Figure 6.29 presents the six groups of micro-crack orientation denoted from a) to f). For each group, initial micro-crack orientation and matched TC is given.

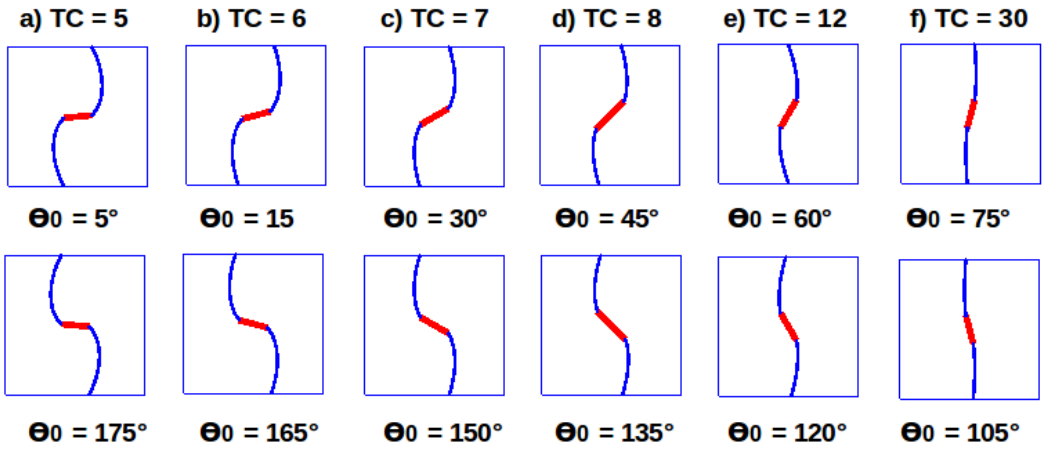

Figure 6.29: Influence of initial orientation on matching TC value. For initial orientation from the interval [0°,90°], increase in orientation value leads to increase in TC. Symmetry was observed for initial orientation from second quandrant with respect to the first quadrant.

One question arose: How the imposed strain rate affects the calibration procedure? Three values were considered: $\dot{e}_{x22} = 1e-7s^{-1}$, $\dot{e}_{x22} = 1e-8s^{-1}$ and $\dot{e}_{x22} = 1e-9s^{-1}$. Figure 6.30 shows the evolution of the normalized length and orientation of the micro-crack along the tests. It has been observed that the value of TC does not change with the strain rate (TC = 8 in all the three tests).

Final step in the matching procedure should be a linear interpolation between TC corresponding to consecutive values of θ_0 leading to a unique value of this parameter for each orientation angle in the interval [0°,180°].

To summarize, the geomechanical problem to be solved can be defined in terms of the "homogenized equilibrium equation" (Eq. 26) and "the damage law" as given below:

$$\frac{\partial}{\partial x_j}(\Sigma_{ij}(d,\theta,\mathbf{u}^{(0)})) = 0,$$

where

$$\Sigma_{ij}(d,\theta,\mathbf{u}^{(0)})) = C_{ijkl}(d,\theta)e_{xkl}(\mathbf{u}^{(0)}),$$

$$\frac{dd}{dt} = \frac{2}{\varepsilon}\cos(\phi_{max})v_0\left(\frac{K_I^\star}{K_0}\right)^n$$

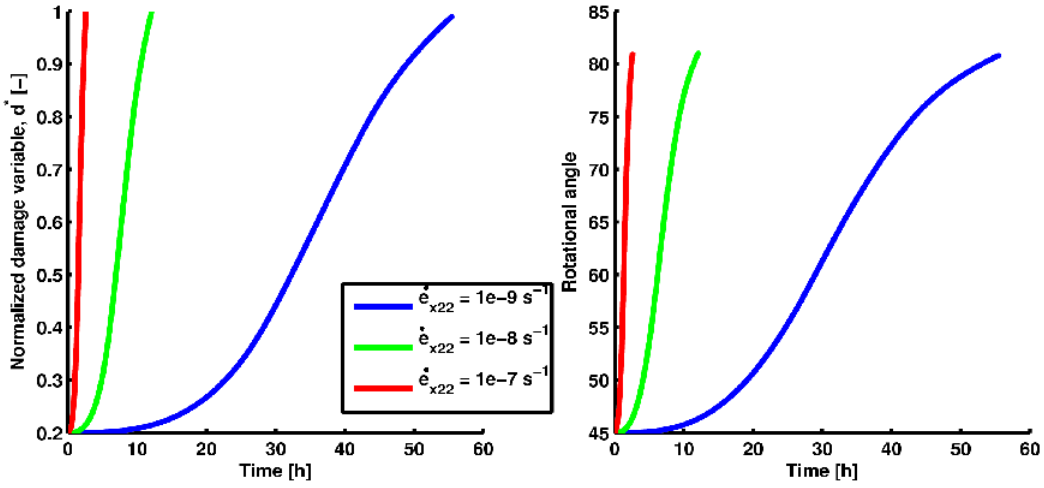

Figure 6.30: No influence of the applied strain rate on the matched TC.

$$\frac{d\theta}{dt} = \frac{2}{\varepsilon d}\sin(\phi_{max})v_0\left(\frac{K_I^\star}{K_0}\right)^n \frac{1}{TC}$$

where TC = 1 in tension case.

$K^\star_{I,II}$ at the tips of the branch can be found using Leblong polynomials:

$$K_i^\star = F_{i,j}(\phi_{max})K_j.$$

where

$$K_{I,II} = \pm\sqrt{(}\varepsilon)(e_{x11}K_{I,II}(\xi_\pm^{11}) + e_{x22}K_{I,II}(\xi_\pm^{22}) + e_{x12}K_{I,II}(\xi_\pm^{12})).$$

and

$$\phi_{max} = sgn(K_{II})[0.70966\lambda'^3 - 0.097725sin^2(3.9174\lambda') - 13.1588tanh(0.15199\lambda')]$$

where sgn is the signum function and λ' is a mode mixity factor that combines the stress intensity factors of mode I, K_I, and mode II, K_{II}, of the straight crack :

$$\lambda' = \frac{|K_{II}|}{K_I + |K_{II}|}.$$

6.5.7 Numerical integration scheme

In order to study the macroscopic response, we analyze the problem by the governing equations (113) and (114) at crack tip level, the differential equations (119) and (120 - 121)) linking the micro-crack level to the macroscopic one and the homogenized law (24) at macroscopic level. A simple procedure to follow is ilustrated in Figure 6.31

At each time step $n+1$ the input quantities are given by the previous crack lenght d_n and orientation θ_n and the current deformation tensor $e_x(n+1)$. The first step to be

made is to check the crack state. According to the state (tension (+) or compression (-)) the stress intensity factors $K_I, II(d_n, \theta_n, state)$ are called.
The second step is the determination of the direction (ϕ_{max}, Eq. 114) of the propagation. Using ϕ_{max} and $K_I, II(d_n, \theta_n, state)$ we compute the stress intensity factors at the branches' tips $K^*_{I,II}(n+1)$.
The third main step is to compute the length of the branches dl so, implicit, of the propagation rate dl/dt which will be used to update the damage and orientation of the micro-crack at the current step (d_{n+1}, θ_{n+1}).

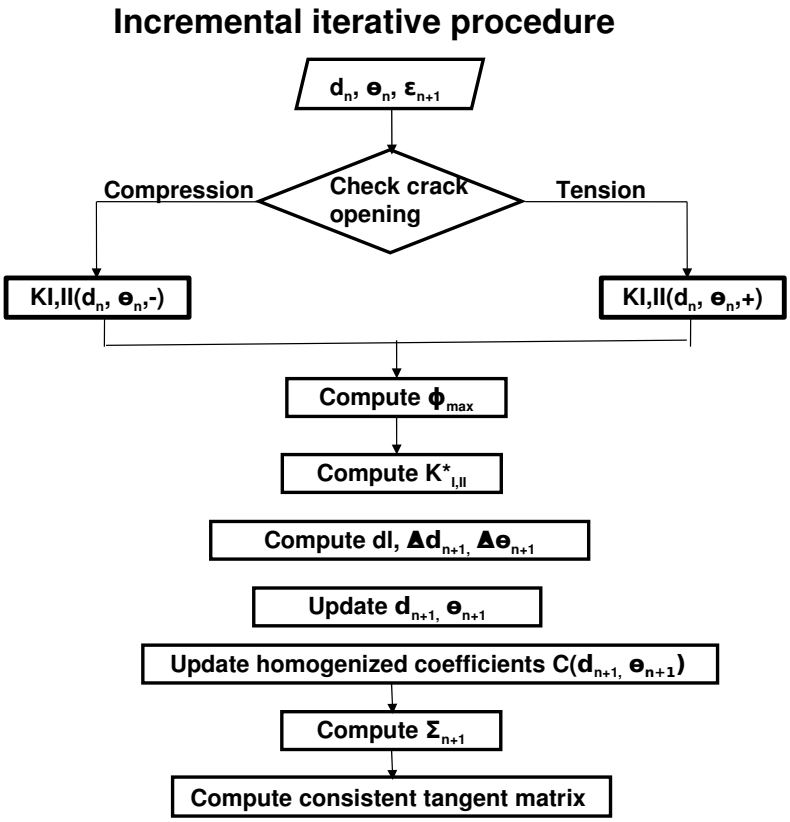

Figure 6.31: Numerical integration: Incremental iterative procedure

The time-dependent behavior of materials can be underlined through different laboratory tests (e.g. quasi-static loading tests, creep or relaxation tests). The response of materials observed during quasi-static compression tests is generally affected by the axial strain rate $\dot{e}_x$. Higher is the strain rate (i.e. faster is the loading) and higher is the strength. When $\dot{e}_x$ is sufficiently low, the micro-cracking has enough time to develop inducing a decrease of the material strength. Under the condition of creep tests (i.e. keeping a constant stress level), the failure is no more governed by the maximal stress that the material may sustain but rather by the time needed for the micro-cracks to propagate under subcritical conditions. Also, upon a relaxation test, obtained by keeping a constant strain level, the micro-crack may propagate until failure of the material, even if the loading is not evolving in time. The higher the strain level, the faster the failure.

According to the considered tests, the loading is stress- and/or strain- controlled in the vertical and/or horizontal directions. Plane-strain condition is considered in the third direction.

Material parameters are the following: $E = 2GPa$, $\nu = 0.3$, $K_0 = 0.6MPa.m^{\frac{1}{2}}$, $v0 = 1e-3\frac{m}{s}$. Charles' law exponent is $n = 4$ and the length of the elementary cell $\varepsilon = 1e-4m$. For the computations, initial normalized length $d_0^* = 0.1$ and orientation $\theta = 45°$ were considered.

Algorithm for consistent tangent

Analitical computation of the consistent tangent for the time-dependent damage model including kinking micro-cracks is not a simple task. Figure 6.32 tries to give some indications to simplify this process. Three levels are considered. Level 0 contains only the terms which enter directly in the formulation of the consistent tangent. Since current normalized length and orientation for a micro-crack are known, the homogenized coefficients and their derivatives with respect to d and θ can be directly employed in the computation of the consistent tangent matrix. The rest of the terms belonging to Level 0, ($\frac{\partial \Delta d}{\partial \Delta \varepsilon_k}$ and $\frac{\partial \Delta \theta}{\partial \Delta \varepsilon_k}$), require separate computations which are briefly schematized at Level 1. Eq. 113-116 and 119-120 give the ingredients which allow computation of their values.

The most difficult to compute is $\frac{\partial K_I^\star}{\partial \Delta \varepsilon_k}$ which is a key term in the computation of the consistent tangent. Therefore, Level 2 is entirely dedicated to the necessary terms in deduction process which starts from Eq. 116 by connecting $K_{I,II}^\star$ (stress intensity factors at the tips of the branches) with $K_{I,II}$ (SIF at the tips of the previous straight crack) using the polynomials of Leblond $F_{ij}(\phi_{max})$ ([95]).

6.5.8 Local macroscopic behavior

Loading at constant strain rate.

At the local macroscopic level, the first simulation is a uniaxial tension loading test. A constant vertical strain rate is imposed and the horizontal direction is free of stress. Influence of the strain rate, of the exponent present in Charles' law and of the internal length of the material, ε, is presented in Figures 6.33 to 6.35. Figure 6.33 shows that the developed model is able to reproduce the effect of strain rate on the obtained failure stress. Under low strain rate, the effect of time becomes predominant and the failure appears for a lower strain level than in the case of faster loading. Figure 6.34 presents the evolution of the micro-cracks in the unit cell. Initial micro-crack has a normalized damage length of 0.1 and it is orientated at 45° with respect to the horizontal axis. At the beginning of the loading, under weak strain level, the damage variable d and the orientation of the crack θ remain almost constant. As a consequence, the gradient of the stress-strain curve does not change during the first part of the loading. Then, when the strain level becomes sufficiently high, the combined effect of high $K_I^\star$ and time makes that the damage increases in the material. As the damage increases, the equivalent crack is rotating and we observe a rapid change in the gradient. At the end of the loading, the equivalent cracks tends to be perpendicular to the direction of the principal tensile strain. Nevertheless, the final crack is not perpendicular to the applied tensile stress. This fact can be explained by

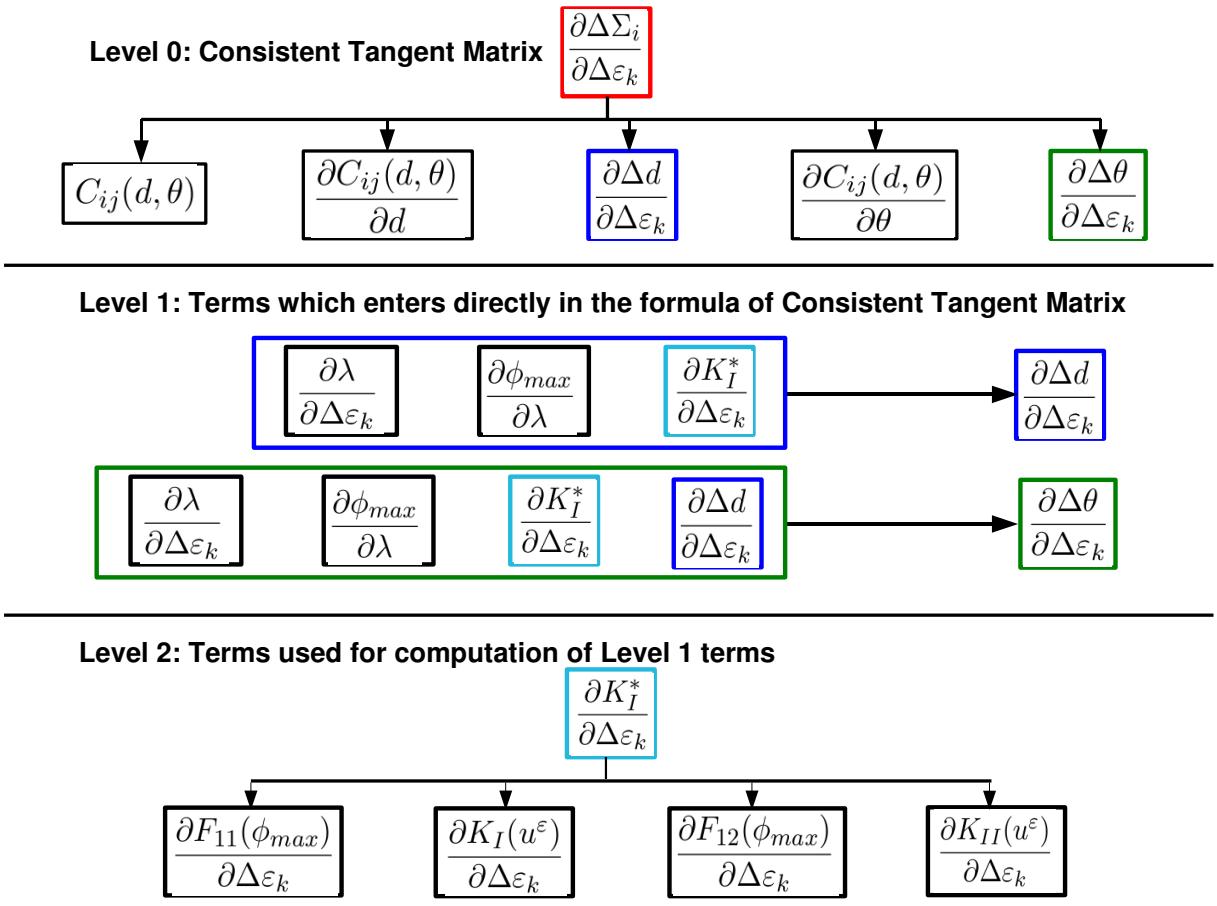

Figure 6.32: Consistent Tangent Matrix for Kinked cracks model

the anisotropic response of the material induced by the oriented crack, which leads to a shearing of the periodic cells, therefore, the principal strain rotates with respect to the principal stress.

Figure 6.35 shows the effect of two main parameters, the subcritical exponent and the microstructural length, on the response of the material under a tension test at constant strain rate. When the stress intensity factor $K_I^\star$ is lower than the referential stress intensity factor K_0, an increase of the sub-critical exponent decreases the rate of crack propagation and postpones the failure of the material, as observed in Figure 6.35a. For a same loading level, K_I and K_{II} increases with the internal length ε (Eqs. 104-105), inducing a faster failure of the structure (Figure 6.35b). In others words, the finer is the micro-structure, the more resistant is the material.

Remark: if in these tests Charles' law exponent would have been chosen $n = 2$, then the internal length ε would have vanished, therefore no size effect would have been encountered.

Figures 6.37 - 6.38 present the results of biaxial tests at constant strain rate in tension and in compression. Figure 6.37 shows the evolution of vertical stress with respect to the applied vertical strain. The vertical and horizontal strains are both in tension. A

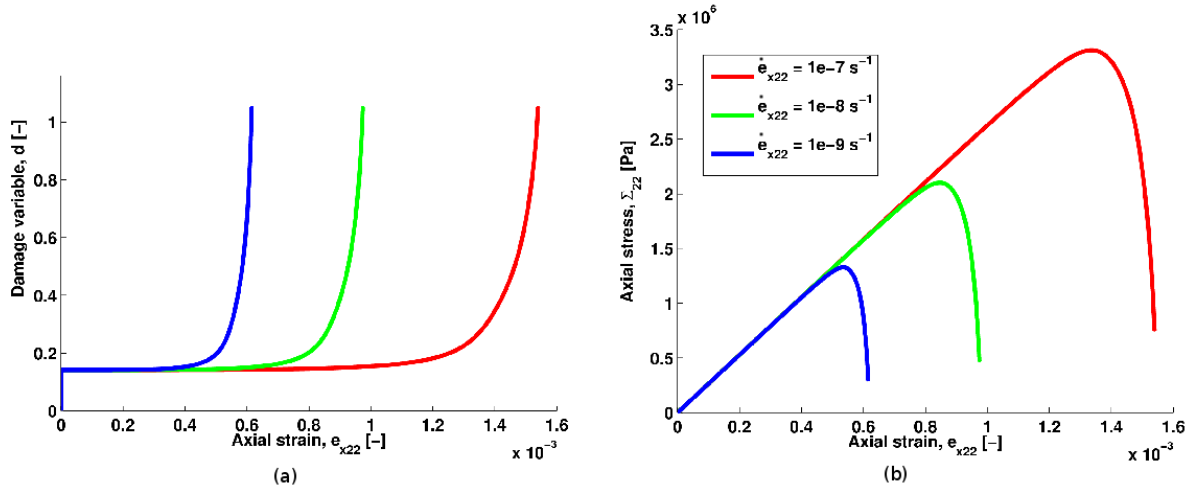

Figure 6.33: Axial tension tests at various constant strain rate $\dot{e}_{x22}$. The strength increases when the strain rate increases.

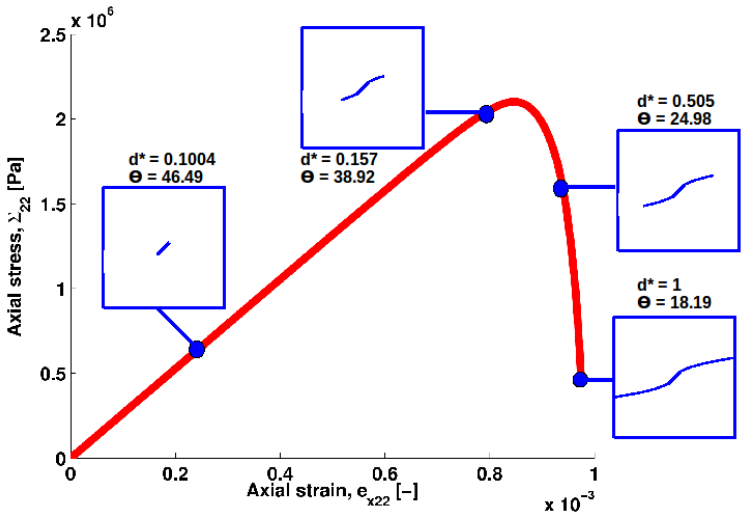

Figure 6.34: Axial tension test at a constant strain rate $\dot{e}_{x22} = 1.10^{-8}s^{-1}$. Evolution of the micro-crack in the periodic cell.

constant ratio between both strains is kept all along the test. $\dot{e}_{x11}$ induces a rotation of the equivalent crack toward the vertical direction while $\dot{e}_{x22}$ would tends to orient it toward the horizontal one. The final tendency of the crack orientation is given by the most powerful strain rate. If no horizontal strain is imposed ($\dot{e}_{x11} = 0$) the amount of crack rotation is maximum (cell number 5). If, on the contrary, $\dot{e}_{x11} = \dot{e}_{x22}$ induces that the micro-crack propagates without rotation.

Figure 6.38 shows, for the first time, that TC factor works well in the replacement of a kinked crack by an equivalent straight one. The evolution of vertical stress with respect to the applied vertical strain along a compressive biaxial test at constant strain rate is shown. A constant ratio between both strains is kept all along the test. In the end of the

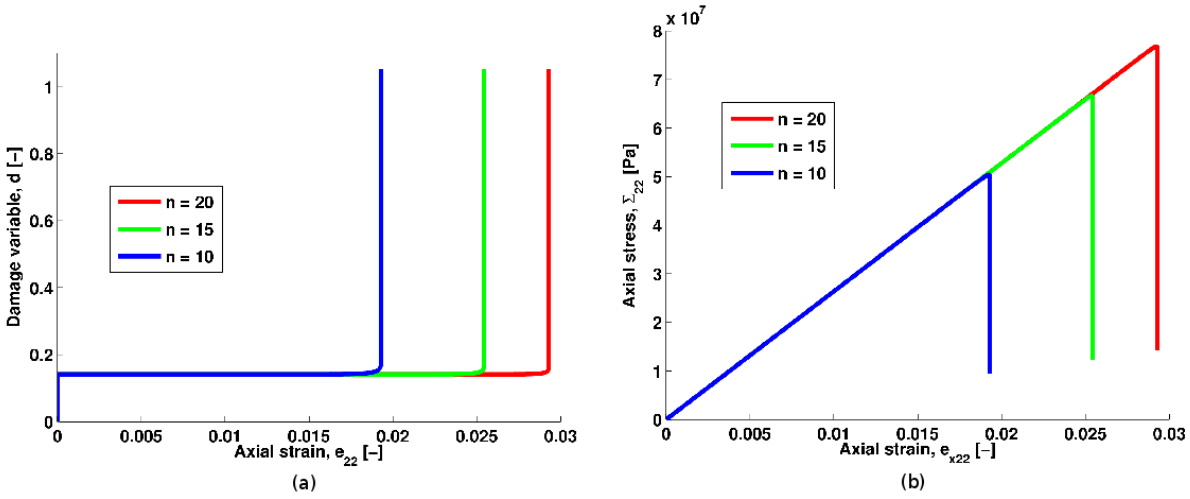

Figure 6.35: Axial tension test at a constant strain rate $\dot{e}_{x22} = 1.10^{-7}s^{-1}$. Effect of the variation of the sub-critical exponent: (a) - damage and (b) - stress - strain curves.

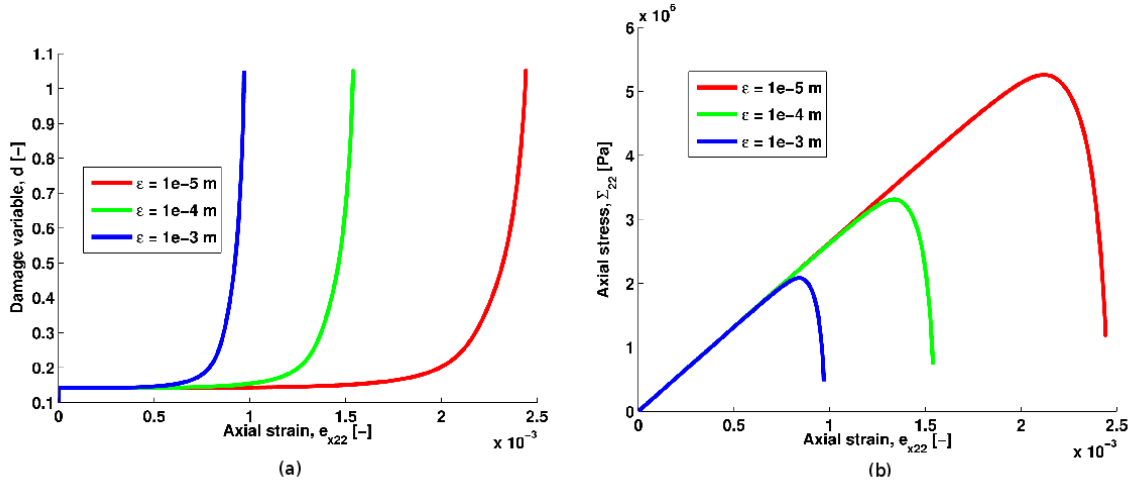

Figure 6.36: Axial tension test at a constant strain rate $\dot{e}_{x22} = 1.10^{-7}s^{-1}$. Effect of the variation of the internal length: (a) - damage and (b) - stress - strain curves.

test coalescence of micro-cracks is reached. In the limit case, when $e_{x11} = e_{x22}$, the initial crack being oriented at 45° with respect to both loading directions, $K_I = K_{II} = 0$ under the initial configuration and the micro-cracks do not propagate. As for the tension test, the damage increase induces degradation of the material rigidity but the softening zone is very small. Bigger the influence of the horizontal strain, lower the softening zone.

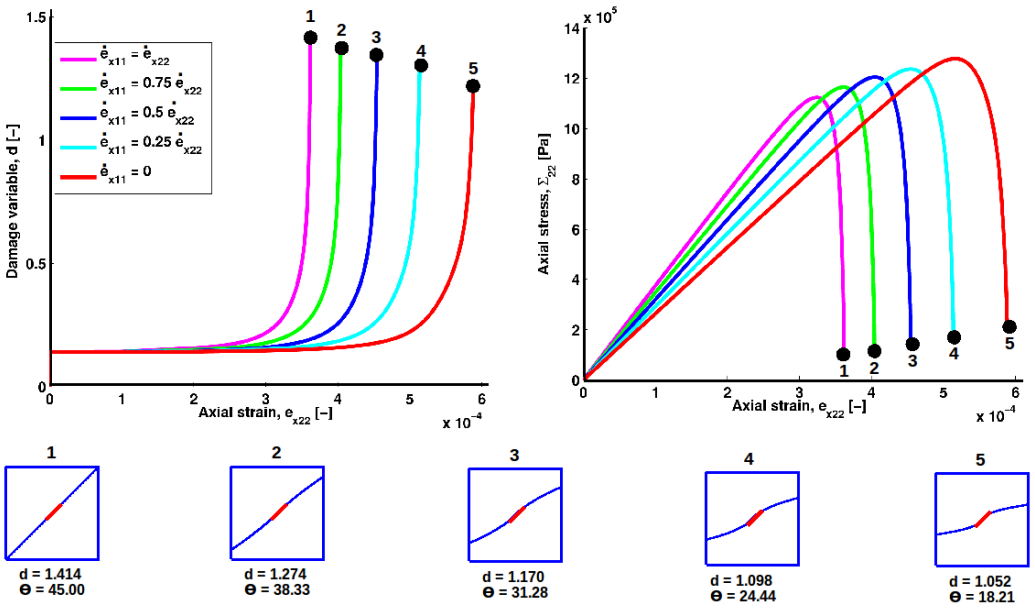

Figure 6.37: Biaxial test at constant strain rate ($\dot{e}_{x22} = 1.10^{-8}s^{-1}$), e_{x22} and e_{x11} in tension with a constant ratio between both strain ($\dot{e}_{x22} \geq \dot{e}_{x11}$).

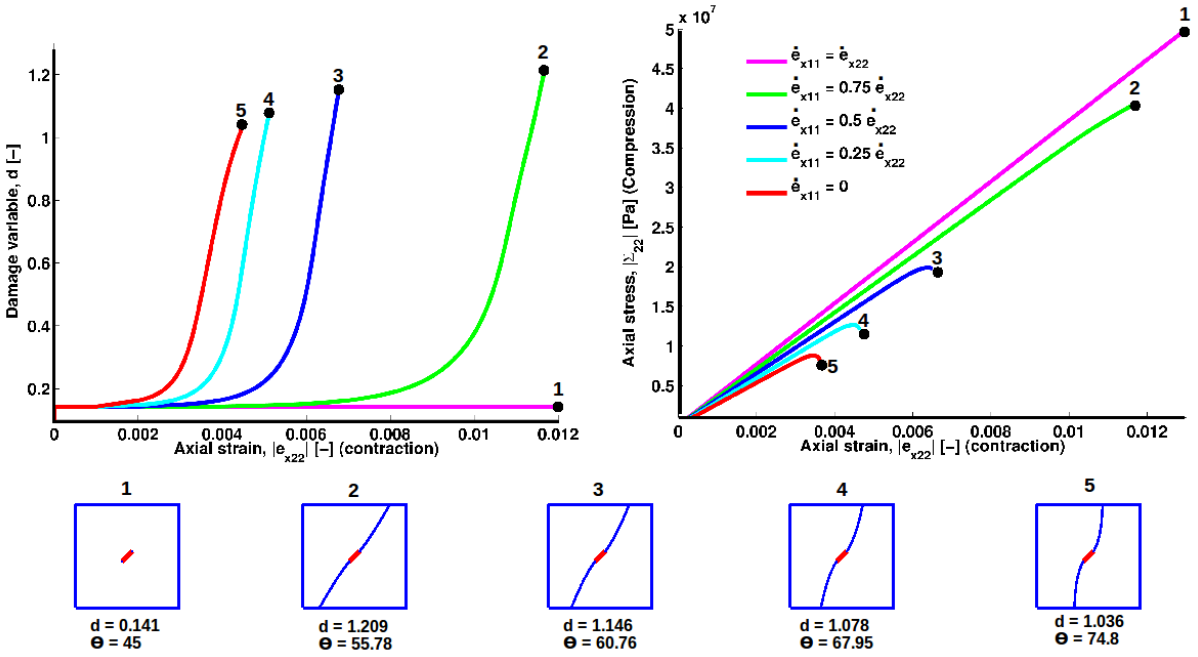

Figure 6.38: Biaxial test at constant strain rate ($\dot{e}_{x22} = 1.10^{-8}s^{-1}$), e_{x22} and e_{x11} in compression with a constant ratio between both strain and $|e_{x22}| \geq |e_{x11}|$.

Relaxation tests.

Applying a constant axial strain, the relaxation test aims at investigating the time-dependent response of material. Under a constant loading, the sub-critical micro-crack growth produces a progressive decrease of the rigidity as long as the damage state increases. As a consequence, the stresses are gradually relaxing upon failure. Under a biaxial combined tensile/compressive constant strain field ($e_{x22} = -0.0035$ (compression) and $e_{x11} = 0.0035$ (tension)), Figure 6.39 shows the evolution of horizontal and vertical stresses with time. In parallel, the evolution with time of the ratio between horizontal and vertical stress is shown. As long as the crack propagate, the direction of the equivalent crack tends toward vertical. As a consequence, the crack lips being under opening condition, the horizontal rigidity becomes much lower than vertical one. So, the ratio between horizontal and vertical stresses evolves in accordance with the relative lost of horizontal rigidity with respect to vertical one.

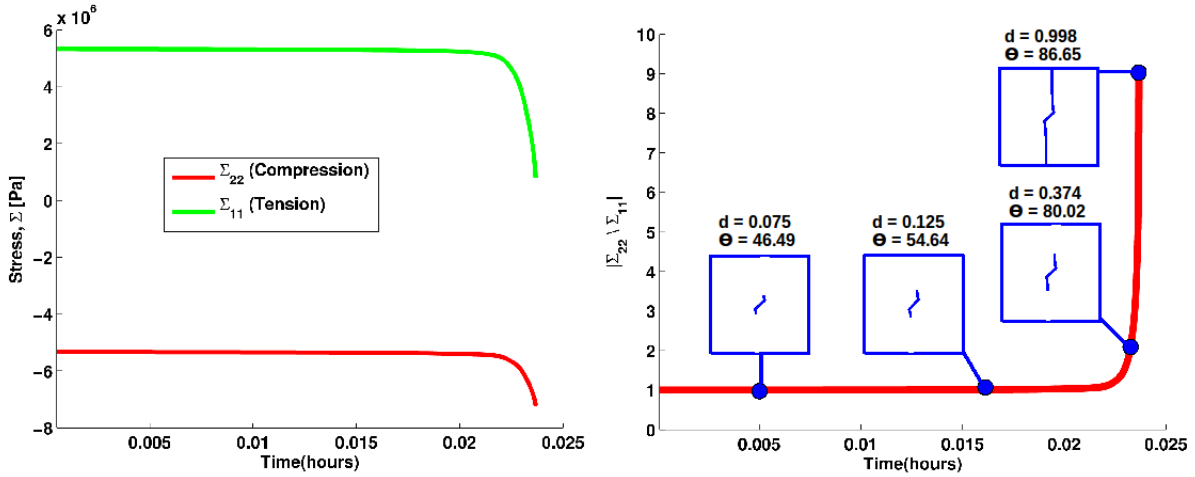

Figure 6.39: Relaxation test under biaxial conditions. $e_{x22} = -0.0035$ (compression) and $e_{x11} = 0.0035$ (tension). Evolution with time of the horizontal and vertical stresses (a) and of the ratio of anisotropy, defined as the absolute value of the stress ratio (b).

Creep tests.

Figure 6.40 shows the creep strain predicted by the model under a biaxial combined tensile/compressive constant stress field ($\Sigma_{22} = -50MPa$ (compression) and $\Sigma_{11} = 50MPa$ (tension)). After an instantaneous strain response corresponding to the short-term behavior of the material, the time effect makes damage variable increase and micro-cracks rotate. During the first part of the test, the damage evolution is slow. However, the rate of damage is amplifying with time. Indeed, under constant stress field, as long as the damage increases, the strain field increases which enhances the stress intensity factor at the crack tips. Consequently, the higher the damage, the higher the strain and the higher the rate of propagation of micro-cracks. The same comments as for the relaxation case can be done about the anisotropic response of the material.

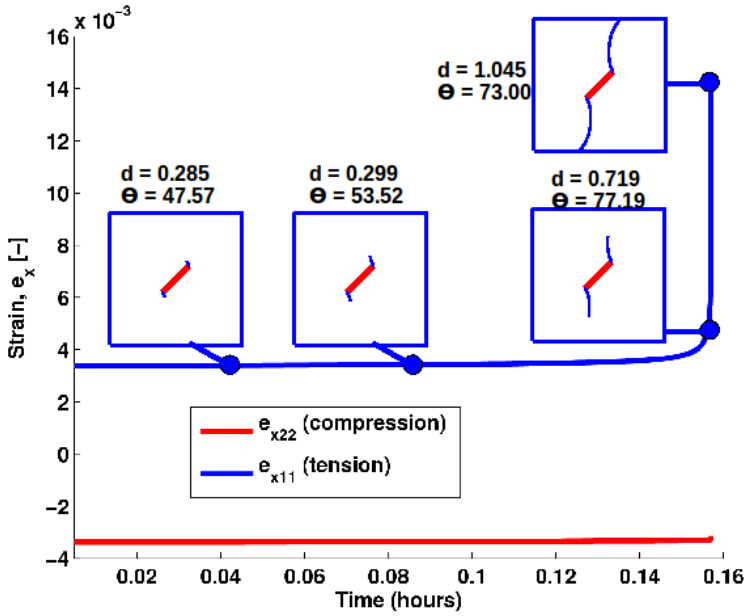

Figure 6.40: Creep test under biaxial conditions. Evolution of the horizontal and vertical strain with time.

6.5.9 Global macroscopic behavior

In the following results obtained from the same type of test (applied tensile displacement) as in the previous sections, will be presented. We remind that the previous sections were dedicated to rate dependent damage models based either on linear coefficients or on the propagation in a fixed direction. The geometry and boundary conditions are shown in the upper left part of Figure 6.1. Two topics are approached: first a discussion on the results obtained using a 1275 elements regular mesh is done and second, mesh independency is proven also with this rate-dependent damage model.

In this section a complex damage model is developed in which not only a criteria for the damage propagation is given, but also an orientation criteria is introduced. If the simplified damage models did not take into account the microscopic information, this is not the case anymore. On the contrary, the microscopic mechanism from which the damage law is deduced is the most important part of this model. Therefore, new variables must be introduced (initial orientation θ_0, microscopic length ε, Charles' law exponent n). In order to keep the comparison between the three damage models developed in this chapter, we considered Charles' law exponent $n = 2$ which will make the internal parameter to vanish. Test with bigger values of n have been done, but the behavior was the same. It is true that a quantifying equivalence cannot be made, since for bigger values of the Charles law exponent the internal parameter does not dissapear and, as we could see in subsection dedicated to the local behavior, size dependence appears.

In the next macroscopic simulations (see Chapter 7) higher values can be taken in order to add realism to simulations. Microscopic length ($\varepsilon = 0.1$ mm) has a very small value because the procedure of the separation of scales is valid if and only if the microscopic variable is small compared to the macroscopic variable. In the test a small specimen 100 mm x 50 mm is considered. Initially we considered a distribution of small vertical cracks. Since the length of the micro-cracks was small (normalized initial damage $d_0 = 0.01$ equivalent to 1% of a unit cell), the initial orientation θ_0 do not have too much importance. However, since the chosen simulations requests, initial orientation is vertical (90°).

Figures 6.41 - 6.42 show the evolution of the micro-cracks in terms of length, orientation and strains for four time steps which are represented by red disks on the global horizontal stress vs time curve (Fig. 6.41). The first remark is that the rotation of the micro-cracks induce a delay in damage propagation if the response from the actual test and those from the previous tests run with the simplified damage models are compared. In this case, the specimen is completely crossed by the macroscopic fracture after around 16500 s, meanwhile in previous cases, the same phenomena was taking place at about 15000 s.

Figures 6.42 shows all the details of the specimen evolution during the loading process. Upper part of the figure presents damage and orientation evolution and the lower part add the strain maps. The full process of breaking is considered, from the time $t_1 = 15955$ s when the localization zone appears, to $t_4 = 16487$ s when the macroscopic fracture is fully developed. Orientation evolution maps (upper, right part of the figure) offer precious information on the damage mechanism, such as:

- in the damaged zone, the micro-cracks rotation is minimum (green color on the rotations maps has a range of 88° - 92°), which proves that our model correctly predict the evolution of the damage. Since the direction of the load is horizontal, the

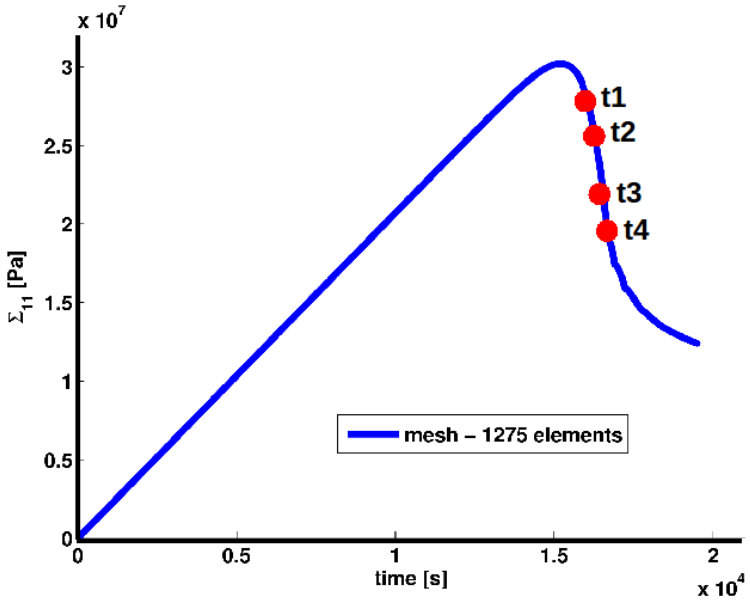

Figure 6.41: Damage evolution (left) and changes in the micro-craks orientation for four time steps.

most important response is given by the vertical cracks (which have the maximum opening in this boundary conditions);

- micro-cracks rotations are symmetrical to the vertical damaged zone. On the upper left part of each orientation representation (blue zone) the micro-craks turn clock-wise and on the right part (red zone) micro-cracks turn anticlock-wise (geometrical) with the same amount. In the bottom part, situation is similar but reversed.

Another important aspect is that contrary to simplified models previously presented in this thesis, the damaged zone has more than one element per line and strain localization precisely follows the damage localization. Localization process is even more visible in the bottom part of Figure 6.42 since the horizontal and shear strain maps are presented. Indeed, at the last time step $t_4 = 16487$ s, we got the maximum value of the horizontal strain along the damaged zone, and the minimum value in the rest of the specimen (the darkest blue represents the minimum value and it is obviously that outside the damaged zone, horizontal strain decrease from t_1, where a lighter blue is observed, to t_4).

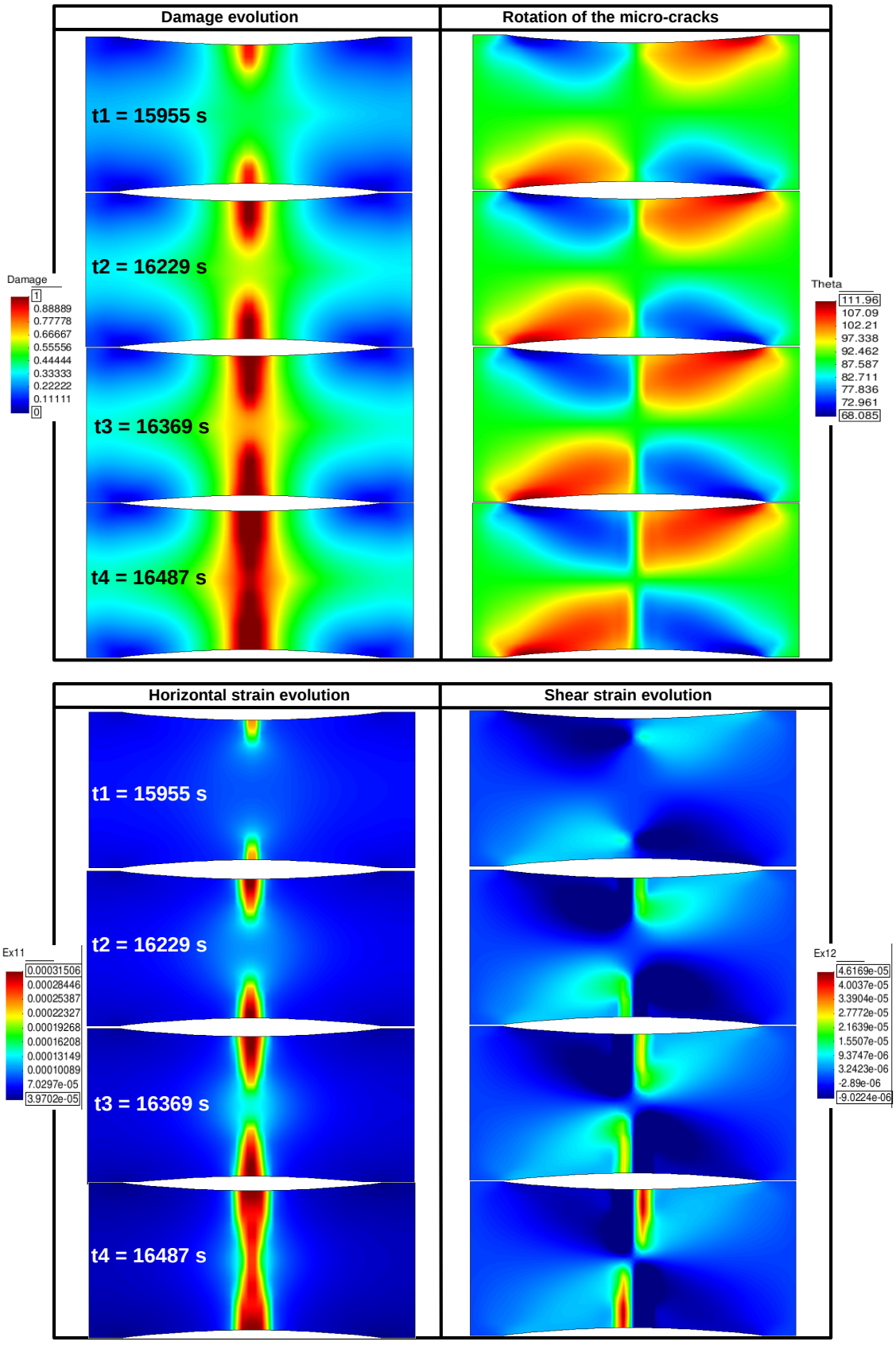

Figure 6.42: Strain evolution for four time steps. On the left of the figure horizontal strain localization perfectly following damage localization in Figure is shown. On the right part of the figure shear strain is presented.

Mesh independency

As for the previous damage models, the second discussion is on the mesh independency of the model. We have run tests with all the three meshes shown in Figure 6.1 containing 1108, 1275, and, respectively, 5050 elements. The computation were run with 4 Gauss points/element.
The corresponding global horizontal stress - time curves are over-posed, as can be seen in Figure 6.43.

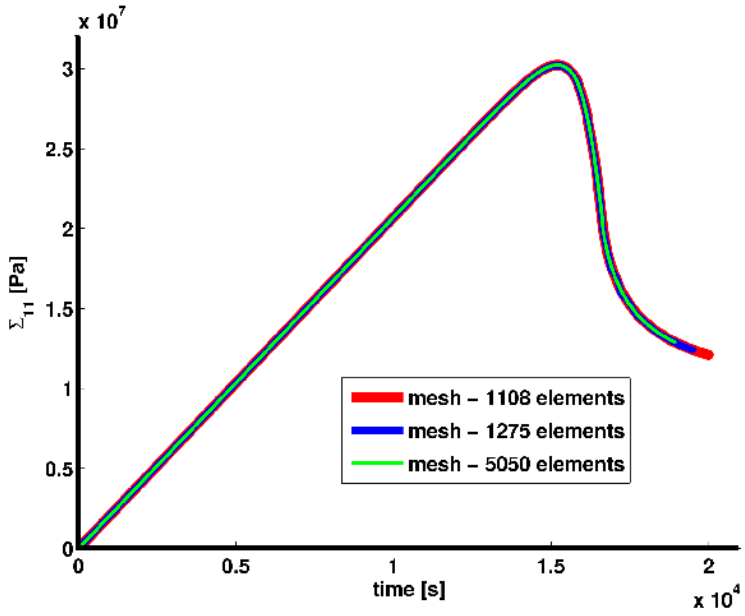

Figure 6.43: Global horizontal stress vs time curves obtained with the time dependent rotating micro-cracks damage law. In red, the global curve from a simulation test with 1108 elements. Blue correspond to the test using a mesh of 1275 elements previously fully presented. Finally, green color represents results from the test with 5050 elements mesh. The superposing of these three curves proves mesh independency.

For a complete proof of mesh independency, Figure 6.44 shows a comparison between damage distributions maps (up) and horizontal strain distribution (down) for tests run with the three considered meshes. It is obvious that at approximately the same time, the specimen is at the same stage of degradation of the elastic properties. No distinction can be made between the three sets of results, the size and shape of the localized zone are identical.

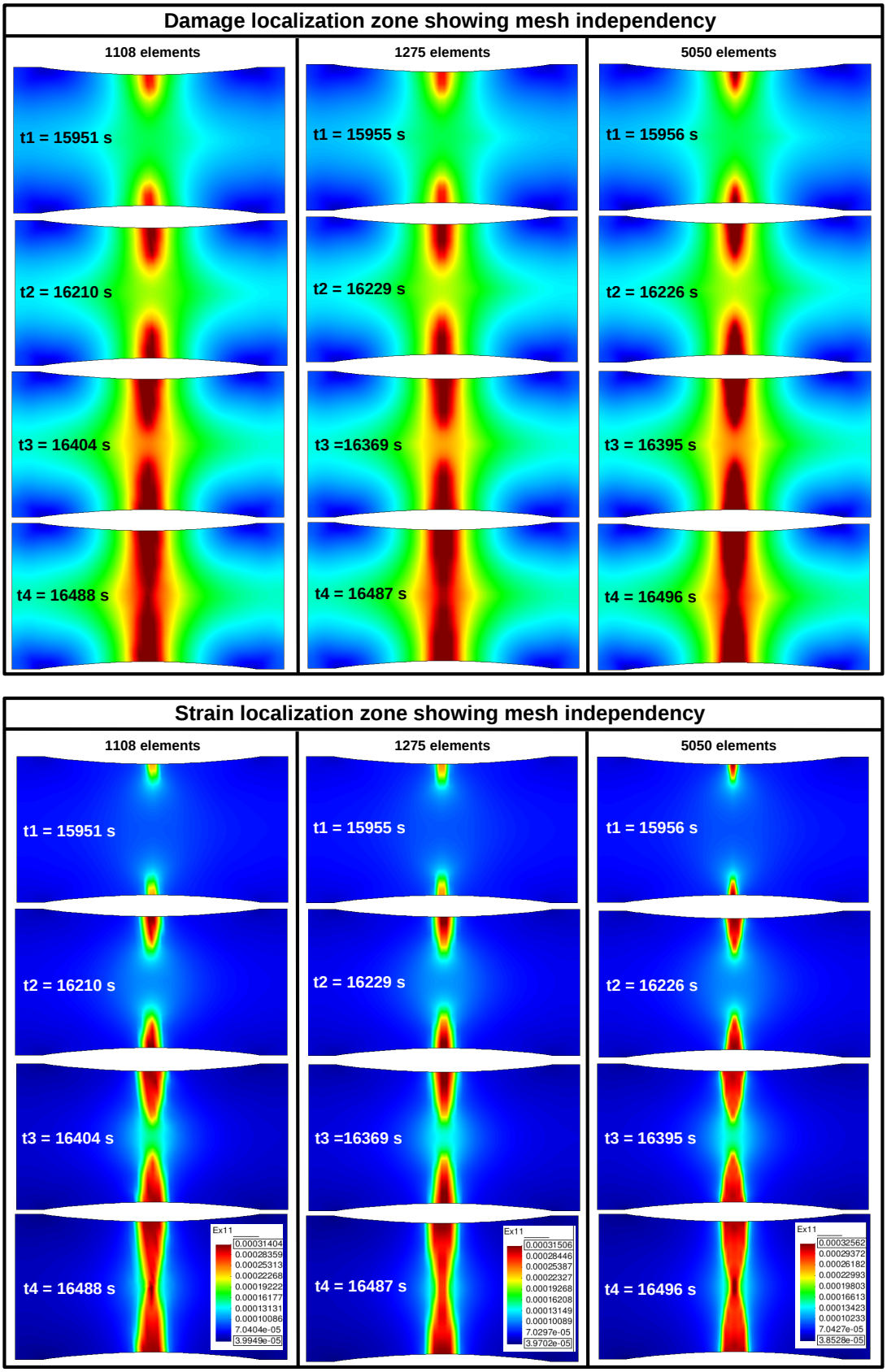

Figure 6.44: Comparison of the damage distributions maps (up) and horizontal strain distribution (down) for tests run with the three considered meshes.

6.6 Summary

The main objective of this chapter was the full development of a complex time-dependent damage model capable to take into account not only the propagation of the crack but also the evolution of the orientation. To achieve this goal several steps have been followed: first, extensions to the mathematical formulation of the general model, including the modification of macroscopic equilibrium equations and the sub-critical propagation of cracks, was presented. Then implementation of the three time-dependent damage models have been be given. In the case of rotational micro-cracks damage model two subsubsections were underlined: first one, dedicated to the surface interpolation for different orientations of homogenized coefficients and the other addressed to the calculation of the stress intensity factors that are needed to quantify the sub-critical growth of cracks at the tips. A comparison of the three time-dependent damage models can be made due to the fact that at the global macroscopic level the same 2D test in uniaxial tension loading conditions has been run. The geometry, boundary conditions, meshes and parameters were given in the introduction of this chapter.

For each damage model two aspects were followed: - localization phenomena and capability of the model to prove mesh independency. In the case of the damage model with micro-crack propagation under a fixed orientation it was proved that the initial crack length plays a very important role, an increase in d_0 from 0.01 to 0.3 provoke almost doubling the size of the localization zone. The velocity entering Charles' law has also a influence, but it is small, almost insignificant, a change of 15% occurring in the size of the localization zone.

Here we give only the conclusion of the comparison of the three time dependent damage models. Figure 6.45 shows the global stress - time curves for the three tests run with a regular mesh of 1275 elements. It can be seen that the natural anisotropy, induced by the introduction of the micro-crack orientation in the damage models, is playing a very important role on the macroscopic response: blue and green curves corresponding to the propagation in a fixed direction model and, respectively, rotational micro-crack damage models shows a delay in the damage process and a sharpening in the softening zone. Moreover, if the two time-dependent damage models presents similitudes in the damage profiles (a diffuse zone with normalized damage value $d \approx 0.7$ and a localized center band), the complex damage model give more realistic results: there is only one damaged zone fully developed and the horizontal strain maps show a perfect concordance between the localization zones.

In the future 3D extensions of all this time-dependent damage models should be made. We already started using the simplified damage model with linear coefficients and with the propagation in one fixed direction model. In the case of this model as in the case of the time-independent quasi-brittle damage model in 3D (5.6), one squared plane crack was taken (see Fig. 5.24). In 2D the simulations required vertical crack, so in 3D vertical plane cracks will be considered. The most difficult to adapt will be the rotational micro-cracks damage models, since it deals with all the three fracture modes and surface interpolation it is not enough (double surface interpolation or volume interpolation will be needed for homogenized coefficients and for the stress intensity factors).

In the following we present the first results of a 3D simulation of the same uniaxial

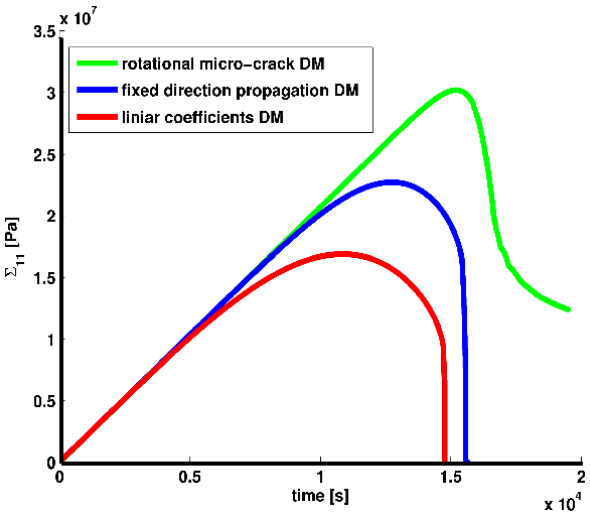

Figure 6.45: Comparison between time-dependent damage models: red - linear coefficients, blue - propagation in one fixed direction, green - rotational micro-cracks damage model.

displacement controller in tension test. The new geometry keep the 2D parameters but add a depth of 15 cm. A 4500 hexaedral elements with 8 Gauss points mesh is used for the computations. Figure 6.46 shows damage and strain in the solicitation direction evolution during the loading process. On three stages we observed the beginning of the localization process in the central zone of the specimen, just like in the 2D case.

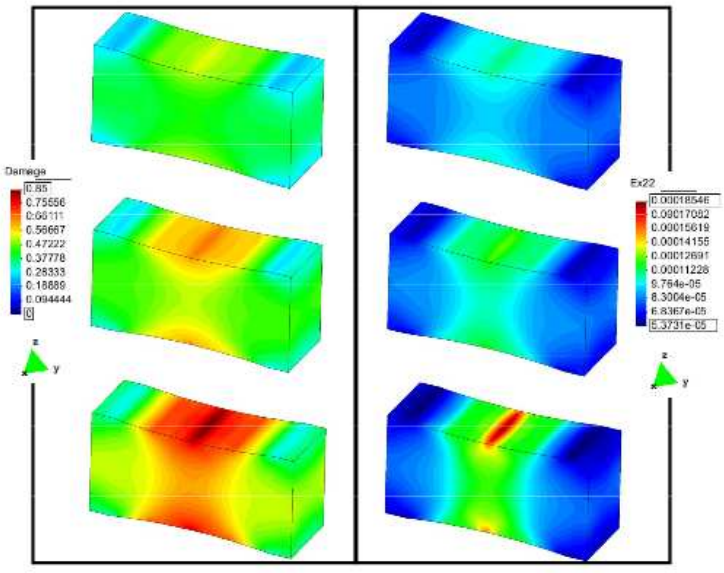

Figure 6.46: Damage and strain evolution in the case of time-dependent damage model using linear coefficients, without rotation of cracks.

7 Macroscopic simulations - examples

Contents

7.1 Introduction

Using the time dependent damage model including rotational micro-cracks, three types of simulations, corresponding to three scales (laboratory, tunnel and reservoir scales), will be presented in this chapter. Specific aspects of the homogenization procedure will be given in each test.

A specific two notched geometry is used in a uniaxial compression laboratory test in the first part of the chapter. For this test the main objective is to begin a procedure for calibration of the damage model through the study of the influence of different parameters entering the evolution law. Simulation results are compared to ones obtained experimentally in [113]. Next, a simple simulation of a tunnel excavation will be made, with the influence of the initial micro-crack orientation on fracture zone orientations being discussed.

At the reservoir scale, oil production/CO_2 injection processes will be represented through the simulation of an overburden of a reservoir under displacement imposed subsidence conditions. The specificity of this numerical application is the modeling of microseismic events and changes in seismic properties including anisotropy.

7.2 Laboratory level tests on notched specimen

In this section, simulations at the laboratory scale are carried out. The main objective is to explore some of the parameters of the time-dependent rotating micro-crack damage model by comparison with experiment results.

The same material model as used in the preceding chapters (E = 2 GPa and ν = 0.3) is considered, to maintain continuity with the previous examples. This, however, means that the comparisons with experimental data are qualitative. Both tension and compression tests will be simulated.

The "matching" procedure will consider:

- verification of the choice of initial orientation of micro-crack distribution;
- for a fixed orientation (best orientation "fitting" experimental results), influence of Trajectory Corrector parameter will be studied;
- after establishing good values for orientation and TC, influence of Charles' law v_0 will be considered;
- in the end of the simulation, mesh independence will be proved.

7.2.1 Background

Nguyen ([113]) carried out an experimental study on the Neapolitan Tuff (a soft rock; E = 2.1 GPa, ν = 0.25) using a particular geometry involving two large, offset, rounded notches (called "Meuwissen-type" by [113]); see Figure 7.1. The reason this geometry was chosen is that the shape favors shear strain localization under uniaxial compression. Figure 7.2 shows typical global stress-strain responses for these tests for different angular offsets between the notches.

The test denoted Tf-tm-45-03 (for a specimen with the angle between notches of 45°) was run under compressive conditions with imposed axial displacement velocity of 0.5 mm/min (equivalent to a nominal deformation velocity of $5e^{-4}$/min. Nucleation and growth of discontinuities in kinematic fields (displacement, strain) on the specimen surface were characterized using Digital Image Correlation.

The maximum shear strain is defined as:

$$\varepsilon_{max} = \sqrt{\left(\frac{\varepsilon_x - \varepsilon_y}{2}\right)^2 + \varepsilon_{xy}^2}, \tag{122}$$

where are the ε_x, ε_y and ε_{xy} strain components.

Figure 7.3 shows maximum shear strain maps corresponding to the times 1-7 represented with red circles on the global stress-strain curve. Strain localization appears early and developes to fracture later in the test between the two notches (Photos: 4-5, 5-6, 6-7).

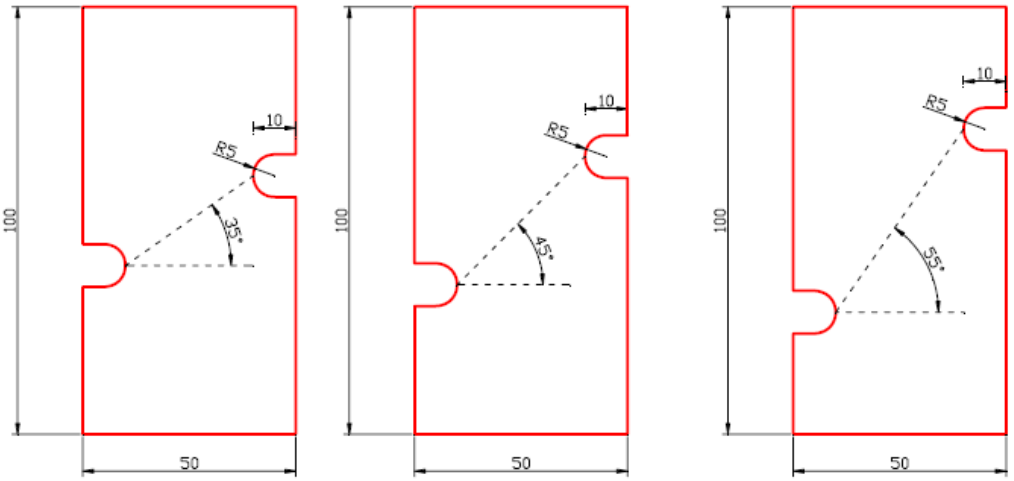

Figure 7.1: Meuwissen-type for Neapolitan Tuff specimen configurations (image from [113].

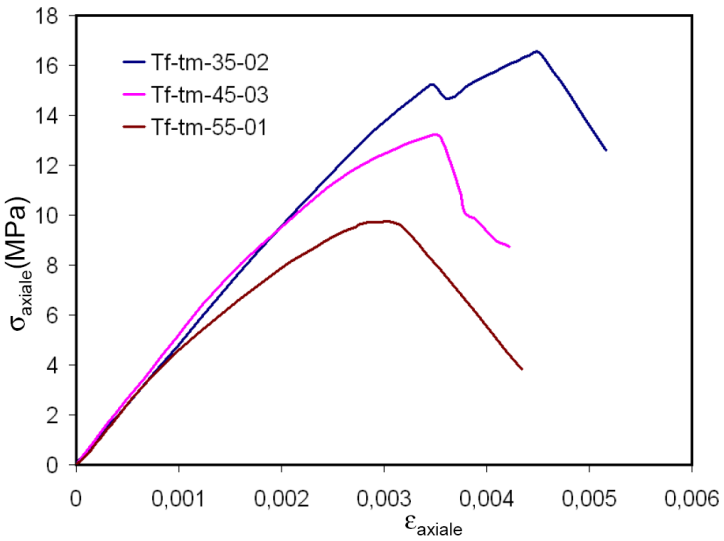

Figure 7.2: Axial stress vs. axial strain curves for three tests:Tf-tm-35-02 (angle between notches 35°), Tf-tm-45-03 (angle between notches 45°) and Tf-tm-55-01 (angle between notches 55°) (image from [113]).

7.2.2 Modeling concepts

One of the objectives is to see if the model developed in the preceding chapters can simulate damage and strain localization, micro-crack evolution and coalescence leading to macroscopic fracture. A second objective represents also the first step of parametrical matching procedure of our time dependent rotating micro-crack damage model.

In simulations, 2D representations of the Meuwissen-type geometry of dimensions 5 cm

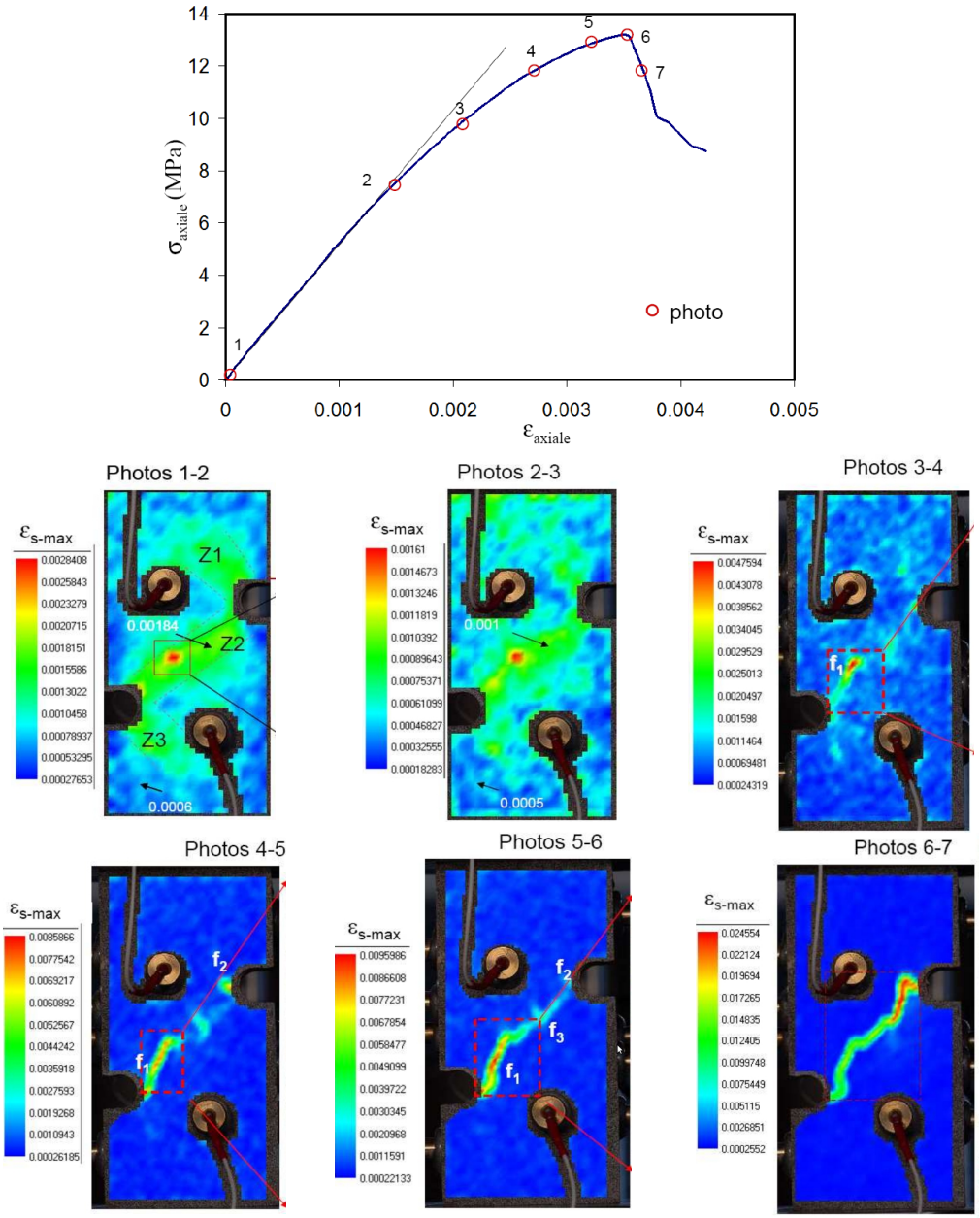

Figure 7.3: Six maximum shear strain maps obtained with DIC corresponding to the times 1-7 represented with red circles on the global stress-strain curve (images from [113])

.

x 10 cm are taken. The angle between notches is 45° and each notch is described by a half circle of radius of 5 mm situated at a distance of 5 mm from the vertical edge. Parameters used in Charles' law are $n = 2$, $K_0 = 2.5e5Pa\sqrt{(m)}$. We consider a compressive vertical displacement and in all cases a distribution of micro-cracks with the normalized length 0.1 and initial orientation $\theta_0 = 135°$. A study of the influence of v_0 and of Trajectory Corrector is made.

We need to mention that this is the first macroscopic test with compressive loading

run in this thesis. In the previous chapter where the time dependent damage models were developed, in the case of kinked cracks damage model, for the compression case a new parameter called "Trajectory Corrector (TC)" was introduced. The reason was that if the crack is in compressive state , therefore it propagates in pure Mode II, it turns too fast and it does not have the time to fully propagate.

7.2.3 Compressive loading tests - results and discussions

To verify the choice of model parameters, experimentally observed behavior in a test should be matching our modeling. Two steps have been done:

- verification of the choice of the initial orientation of micro-cracks: simulations have been run for eight discrete values between $[0° - 180°]$ with an increment of 22.5°. Figure 7.4 shows the damage evolution maps at an advanced time of the computations.

  In all the cases, four damage localization zones can be found, two at each side of each notch. Two zones tend to the exterior top and, respectively, bottom boundaries and two form between the two notches. In the last part of the tests, those two interior zones unify somewhere at the center of the specimen. In the case of vertical or horizontal micro-cracks, the damaged zones have completely opposite directions, meanwhile for the group 67.5° - 157.5°, interior damaged zones tend to be parallel instead of unifying. Only the group of 45° - 135° showed that the interior damage localization zones advance through the same point, somewhere in the middle of the geometry. It will be later shown that strain localization is in direct link with damage localization having approximately the same path (in Figure 7.8), therefore preliminary numerically obtained results from simulation with $\theta_0 = 135°$ might be compared, up to a certain point, to experimental ones (see Figure 7.3).

- verification of the choice of TC: for an initial micro-crack orientation of 135°, a test has been run without the use of the "trajectory corrector" factor TC (equivalent to TC = 1). The behavior seen at the local macroscopic scale (see Section 6.5) was also discovered at the global scale: micro-cracks turned too fast before having time to propagate. Figure 7.5 shows damage, orientation and strain maps at the end of the simulation. On the left part it can be seen that damage increased from the initial value $d_0^* = 0.1$ to $d^* \approx 0.177$, which is insignificant, meanwhile the micro-cracks changed their orientation drastically, the angle θ decreasing from 135° to 60° in a very short time.

  Simulations have been carried out for several different values of TC. Figure 7.6 shows the global vertical stress vs time curves from four simulations with different TC. There are two key aspects of this figure:
  - the bigger TC, the faster the micro-crack propagation and coalescence, which leads to a lower stress peak;
  - the bigger TC implies more pronounced softening in the global stress vs time curves.

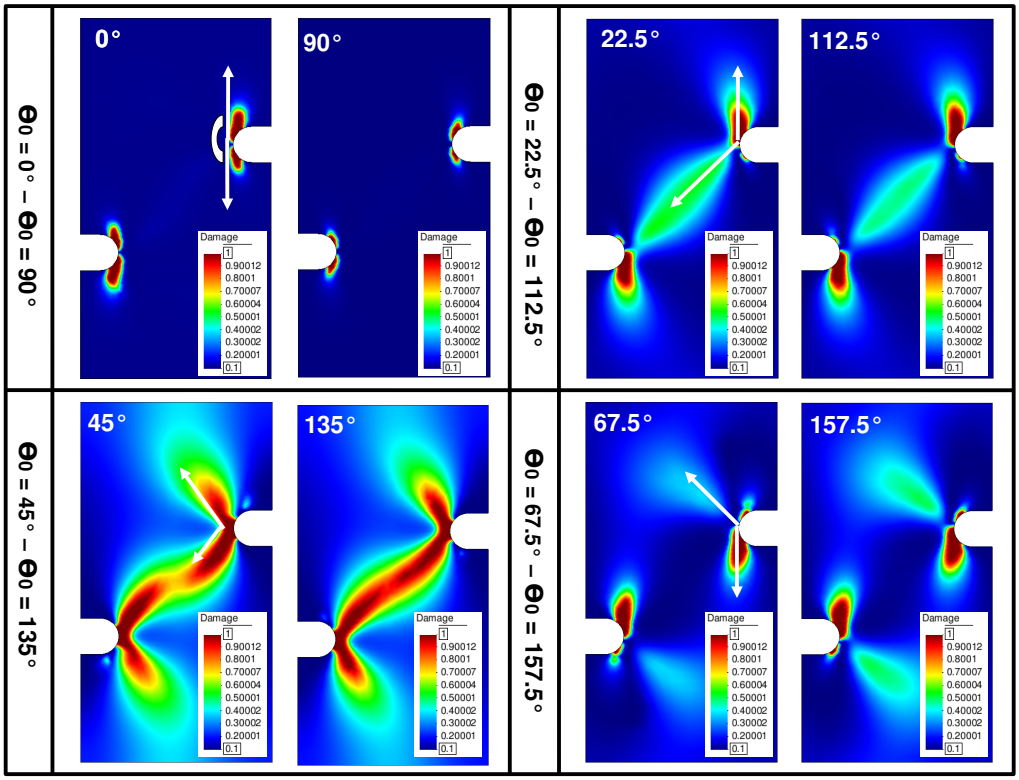

Figure 7.4: Influence of θ_0 on localization zone: four group of symmetries with respect to the vertical axis. Only the group 45° - 135° product results comparable to experimental ones

Figure 7.7 (top) shows damage and damage-orientations maps at the same time T_1. As expected, the bigger TC, the smaller the micro-crack rotation (only $\approx 5°$ for TC = 110, compared to $\approx 25°$ for TC = 20), but at the same time, the propagation is more advanced, for this time. more advanced stage of the propagation. Nevertheless it should be noticed that the four localization zones appear, no matter the value of TC, which indicates that the geometry of the strain (and damage) localisation is largely independent of TC and depends mostly on the initial micro-crack orientation.

Figure 7.7 (bottom) shows damage and damage-orientations maps at the end of each simulation. Two conclusions can be drawn here:

- even if the four damage localization zones appear in each simulation, the angle between external and internal damaged zones varies with TC. In the figure, the angle of the external zone is measured from the center of the notch with respect to x-axis. The bigger TC, the bigger the inclination of the external band and the smaller the angle between the internal and external zones. If we look at Photos 1-2, 2-3 and 3-4 from Figure 7.3 showing experimental strain localization zones obtained by [113], this angle is around 90°. There can be found a resemblance between numerical results obtained with TC = 110 and experiments.
- one observation is that smaller TC implies a bigger width of the localization

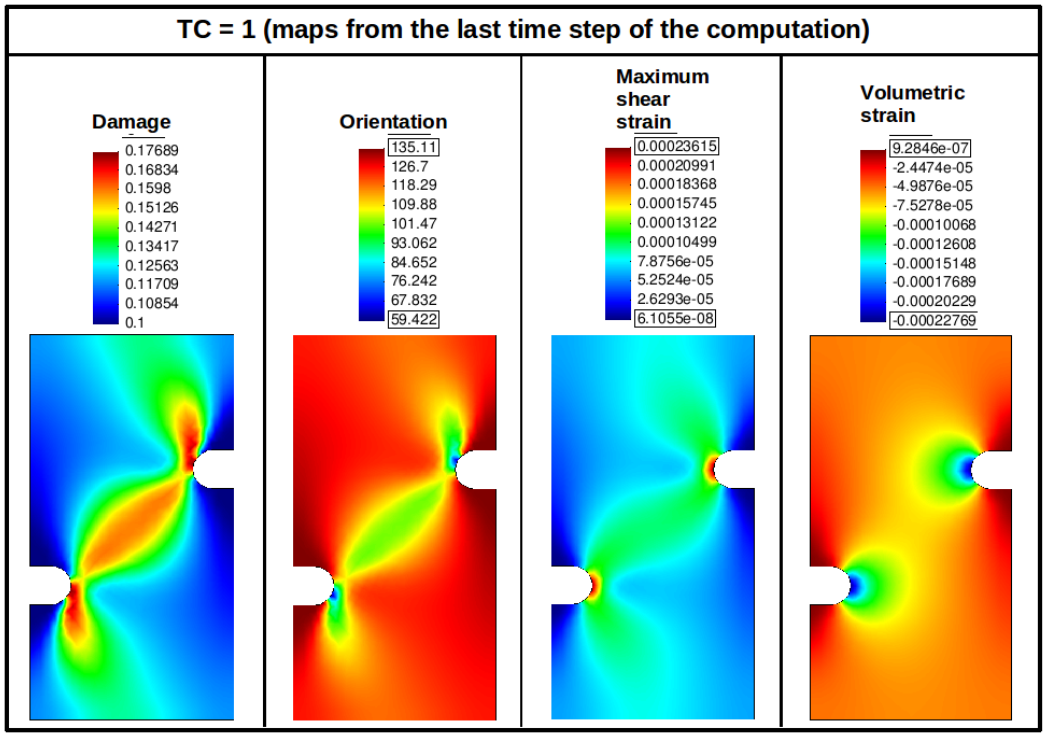

Figure 7.5: TC=1; maps from the last step of the computations: from left to right, normalized damage, orientation and volumetric, respectively maximum shear strain. Increase in the damage is insignificant, meanwhile a big change in orientation angle is seen. Strain localization process begins quite early.

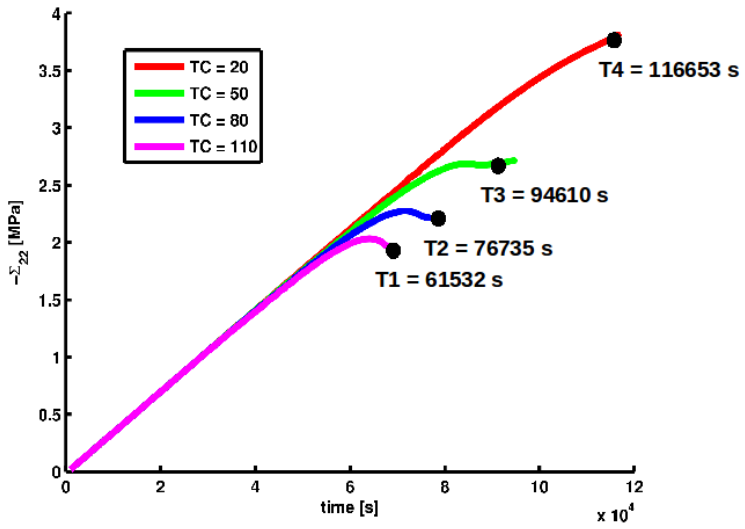

Figure 7.6: TC influence on the localization zones: - vertical stress vs. time curves for four values of TC. Black circles indicates the four time steps corresponding to the end of the simulation.

zones as can be seen from Figures 7.7 when looking the localization zones between the two notches. It is not an absolute statement since we have no experimental comparison to make. However, it is needed to be further investigated, either with the same test, either using other geometries and boundary conditions.

All the observations of the simulation on Meuwissen-type geometries run to the conclusion that the parameters which provide the best match to the experimental observations are $\theta_0 = 135°$ and TC = 110. Figures 7.9 and 7.8 provide more complete results for the simulation using these parameters.

Figure 7.8 shows maps for the damage and orientations of the micro-cracks, on the top part, and strain maps on the bottom part, for five time steps, marked with red circles on the blue curve from Figure 7.9 representing global vertical stress vs time.

Figure 7.9 shows global vertical stress vs time corresponding to our simulation. Five time steps are marked with red circles on the blue curve. t_1 is taken in a zone where begins the separation of the global curve from the linear trend (green line). The next three time steps are before the peak, the fourth one being the closest to peak. t_5 represents the post-peak behavior. It can be seen that before peak, the band of intense localised shear strain is only about a third of its final length.

Concerning the micro-crack orientations, it can be seen that in the localization zone, the micro-cracks tend to rotate towards the vertical direction, i.e. the angle is decreasing, which corresponds to the behavior of cracks in experiments.

It is well known that in a compression tests, cracks tends to align parallel to the maximum solicitation direction. Our simulation is a uniaxial compression test vertically loaded, therefore the micro-cracks tend to rotate towards the vertical direction, which is totally the case of our results.

The reason for choosing this special geometry was to be able to observe experimentally localization of shear strain in a uniaxial compression tests. The bottom part of Figure 7.8 shows that our model is also able to simulate the strain localization, which coincides with the localized damage zones. Volumetric strain values maps give another indication of the correctness of our results since, around the notches the values start to decrease in time due to the compressive state as the damage propagates.

In the previous chapter, when the time dependent damage models were introduced, discussion on mesh independence and on the independence of the localization zone's width with respect to the speed v_0 entering Charles' law took place. For the time dependent damage model which considers propagation in one fixed direction it was shown that strain localization zone does not depend on the mesh, meanwhile, very small variation of the localization zone with v_0 was encountered. In the case of kinked-cracks model, only mesh independence was proved.

To prove mesh independence three irregular meshes have been considered (827, 1778 and 2589 elements). Figure 7.10 shows on the left the global curves of the simulations which are over-posed. On the right of the figure, damage maps at the time $t = 6.78e4s$ are shown which prove that the size of the damaged zone does not change with mesh.

Figure 7.11 (a) shows the global stress vs time curves which indicates that smaller values of v_0 produce delay in the damage propagation. In figure 7.11 (b) damage and maximum shear strain maps are presented for four values of v_0 showing that there are no visible effects on the localization band width with the variation of velocity.

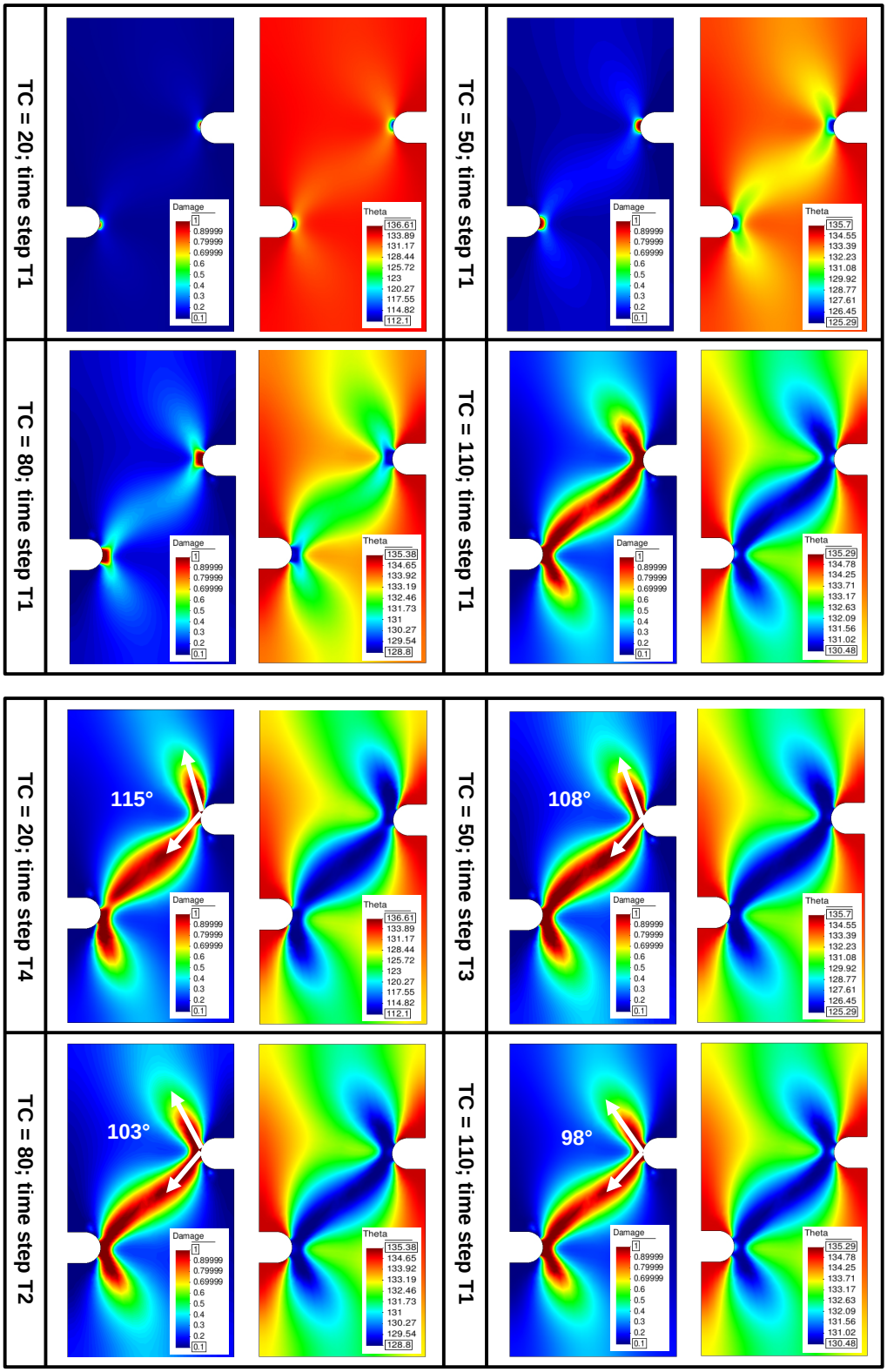

Figure 7.7: TC influence on the localization zones: (top) - damage and orientation maps at the same time, T_1. Bigger TC, more significant damage localization process; (bottom) - damage and orientation maps at times, T_1 - T_4. TC influences the angle between the damage localization zones.

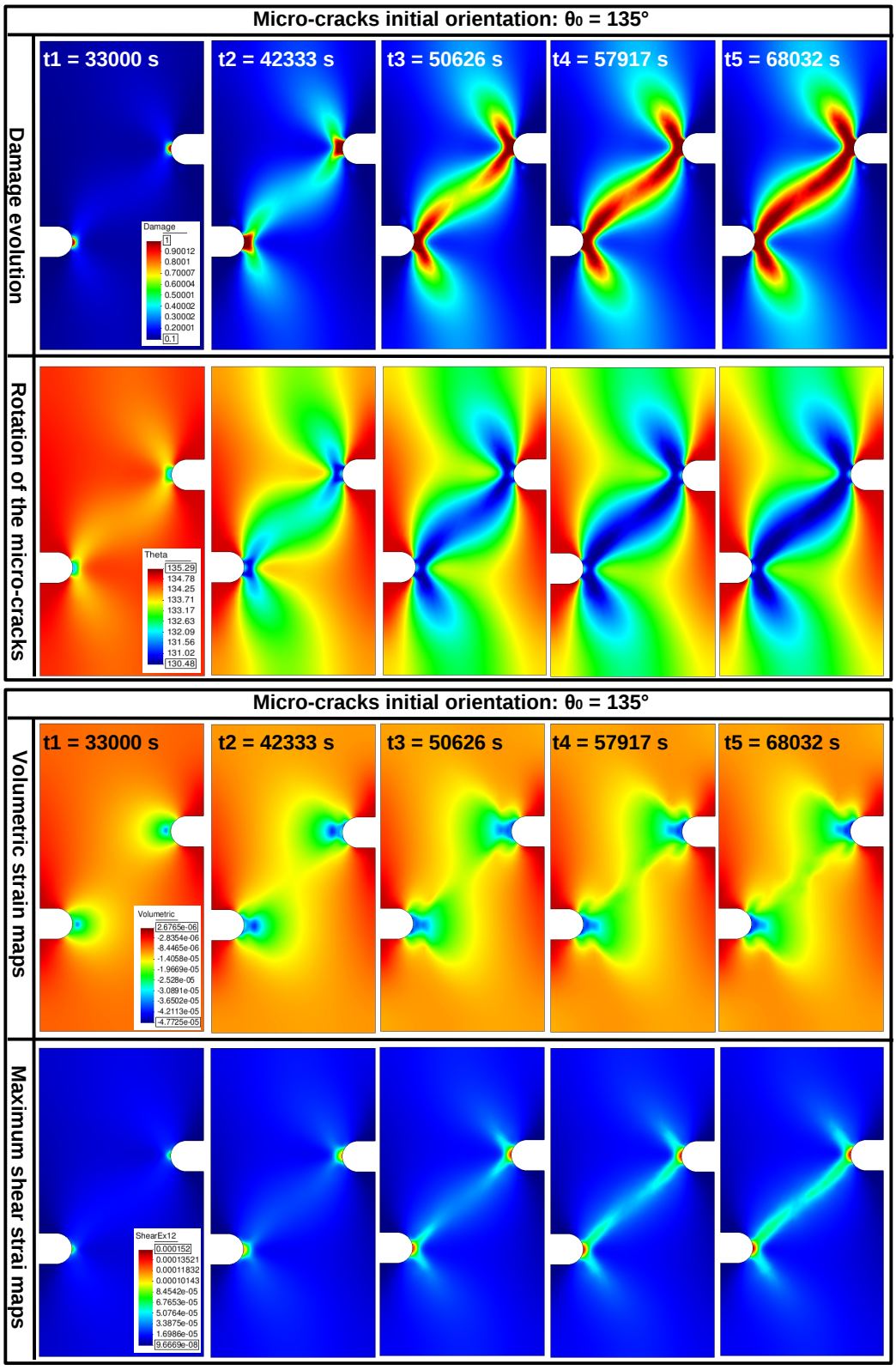

Figure 7.8: Damage, orientation and strain evolution in time. Five maps corresponding to five time steps (red circles on the blue curve from previous figure) for each considered parameter. Localization process is presented in terms of band development (increase in length of the micro-cracks belonging to the localization zone) and trajectory (to the center of the specimen).

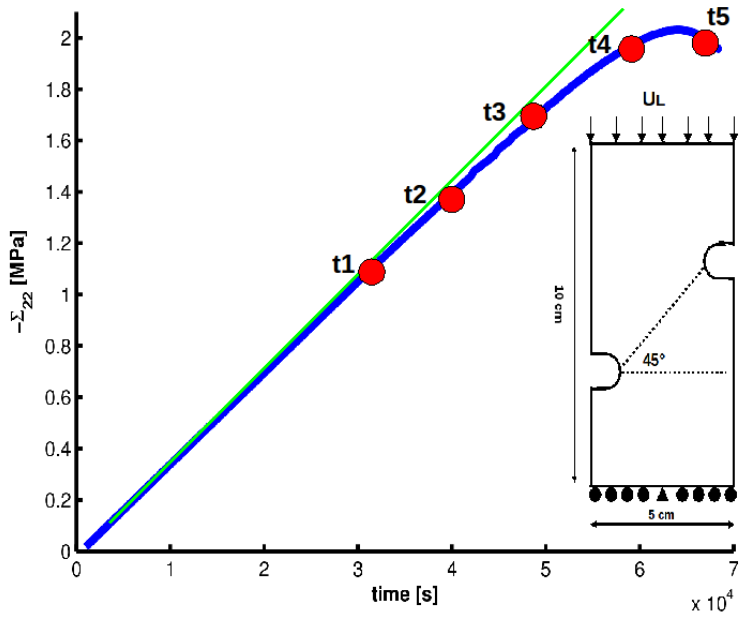

Figure 7.9: Vertical stress vs time global curve. Five time steps are marked with red circles and the linear trend is evidentiated by the green line.

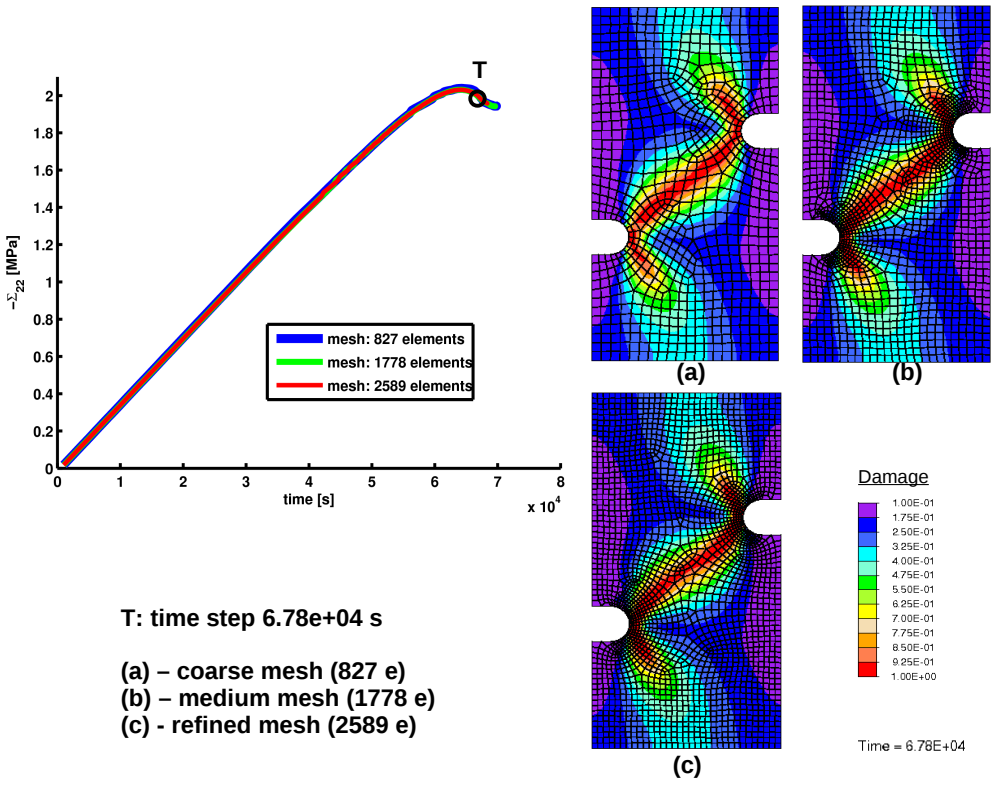

Figure 7.10: Mesh independence - tests on Meuwissen-type geometry

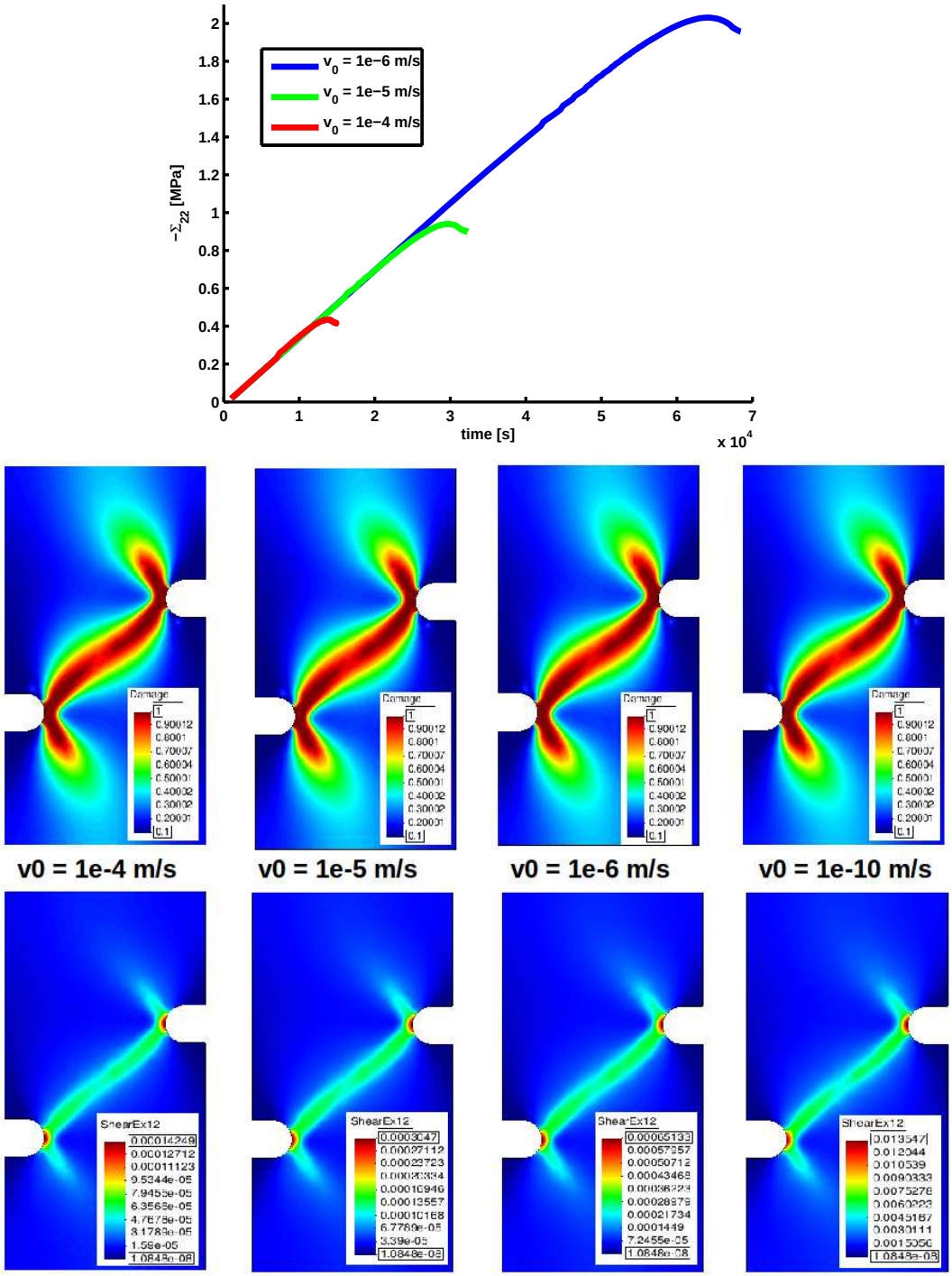

Figure 7.11: Influence of v_0: on the left, stress vs time curves proving that bigger v_0 induce smaller time effects; on the right, damage (up) and maximum shear strain (down) distribution at the end of simulations for four values of v_0. Localization zone is very little influenced.

7.2.4 Tensile loading tests - results and discussions

In this section several tests in tensile loading condition are described. Two objective are followed: the influence of the size of the notches and the influnce of initial micro-crack orientation on damage and strain localization processes. New geometry considered is also 5 cm x 10 cm Meuwissen-type shape, but each notch is described by a half circle of radius of 2 mm situated at a distance of 2 mm from the vertical edge. Vertical projection of the distance between the center of the two notches remains unchanged compared to the previous geometry. Short comparison between results obtained from simulations run with both geometries is given.

Parameters used in Charles' law are the same as in compressive loading case previously described. We consider a tensile vertical displacement applied on the top of the geometry. At the initial phase, micro-cracks are horizontally aligned and their normalized length is 0.1.

In the following figures, damage localization phenomena is captured. Figure 7.12 shows the global axial stress vs. time curve. With red circles, five time steps are designed. t_1 corresponds to the moment when the stress reaches its peak. t_5 is the time when the damage localization zone is fully developed. Corresponding to t_1 - t_5, five pairs of results are presented. On the left of each pair, damage map is shown. Four main zones of damage localization (two for each notch) appear as for the case of compression test previously presented in this section. Apart of the main zones, another two thiner bands develope.

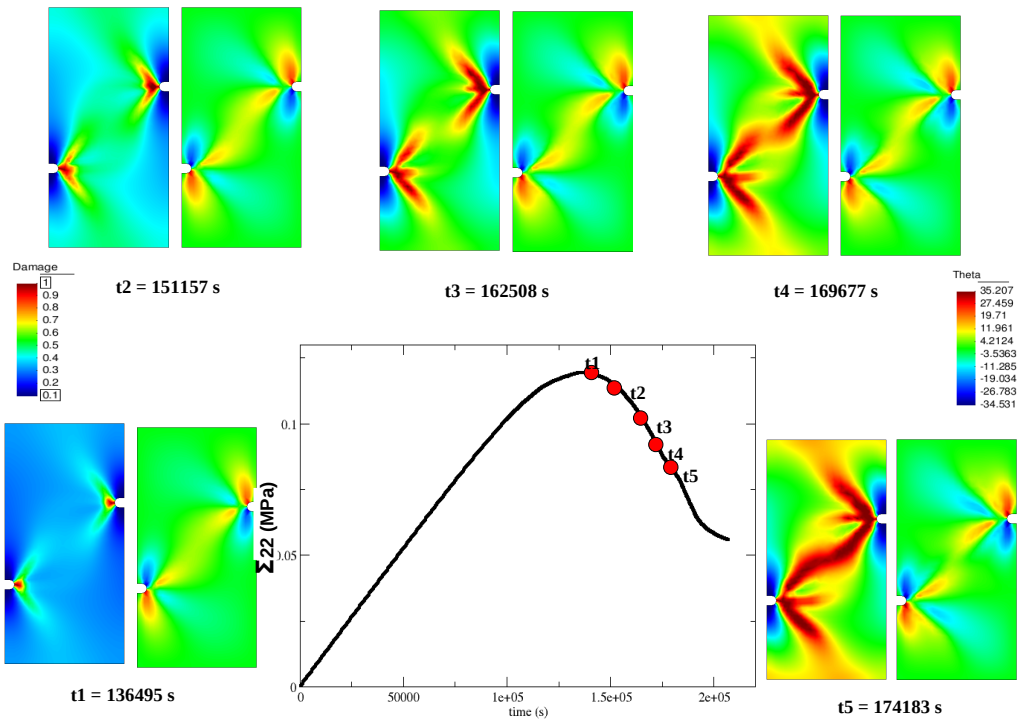

Figure 7.12: Damage localization phenomena captured at five time steps. t_1 - t_5 are represented with red circles on the global vertical stress vs. time curve.

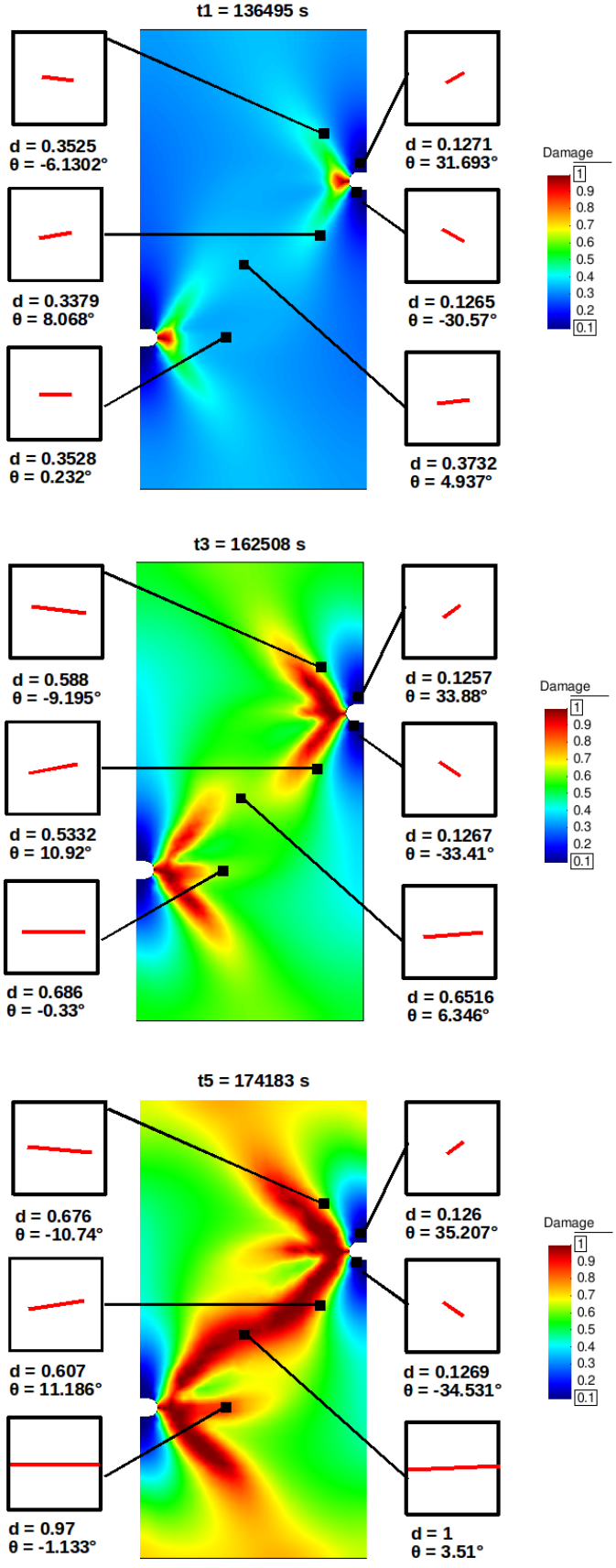

Figure 7.13: Evolution of six micro-cracks lengths and orientations during three time steps.

Figures 7.13 - 7.14 present the change in micro-cracks orientation during the simulation. Figure 7.13 shows the orientation of six specific micro-cracks at three time steps (among the five shown in figure 7.12). Two micro-cracks have been chosen from a zone of the specimen where the kinking mechanism is the most pronounced (right part of each specimen). It can be seen that there are not signifiant changes in micro-cracks lengths (normalized damage parameter increases from 0.1 to 0.127). The rest of micro-cracks is chosen from the damage localization zones (two corresponding to the top notch, one at the intersection between interior localization zones and one from the thiner band which starts from the bottom notch). Rotation of those micro-cracks is slower, but the increase in their lengths is important.

Figure 7.13 showed only the final orientation of each micro-crack which was obtained by the unification between the branches tips. Figure 7.14 will show the full micro-crack kinking process for several micro-cracks covering the geometry. With red color, the initial horizontal micro-crack is represented. The trajectory of the branches along the simulation process is drawn with black.

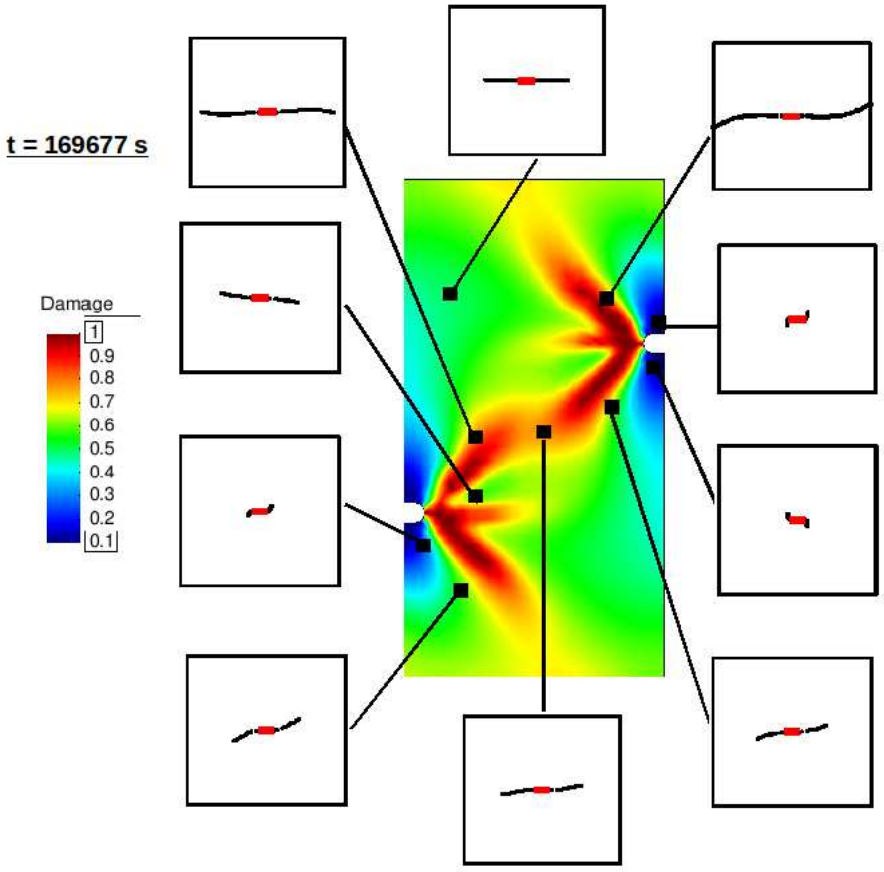

Figure 7.14: Kinking process fully represented for ten micro-cracks: initial micro-crack normalized length is 0.1.

Figure 7.15 shows maximum shear strain maps for the five time steps marked with red circles on the blue curve from Figure 7.12 representing global vertical stress vs time. It is proven that our model is also able to simulate the strain localization, which coincides

with the six localized damage zones.

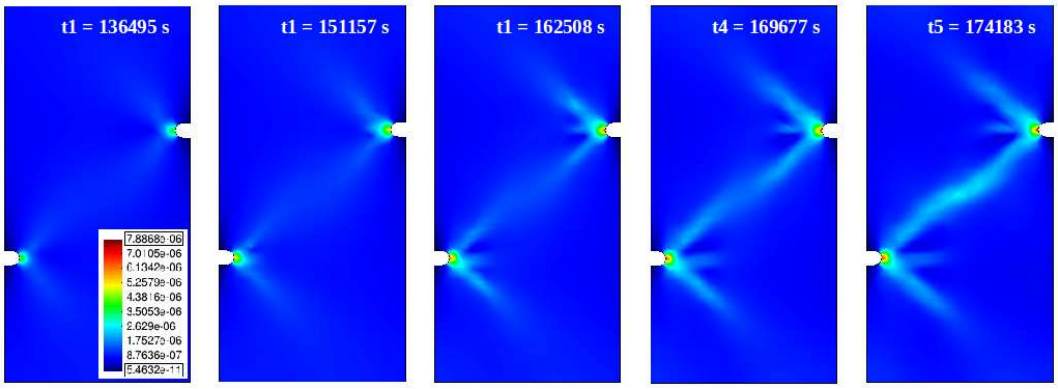

Figure 7.15: Maximum shear strain maps for five time steps along the simulation.

Figure 7.16 show a comparison between the previously obtained results and the new results from simulation run using micro-crack distribution with normalized lenght 0.3. On the left part of the figure, damage maps are presented. It can be seen that the size of the localization zone tends to increase with the increas in the initial micro-crack length. Moreover, exterior localization zones tend to unify with the thiner zones. On the right part of the figure, orientation maps are shown. The main conclusion is that the maximum inclination angle decrease with the increase of the initial length. If in the case of the previous simulations, θ increases from 0° to 35°, when initial micro-crack length is 0.3, the rotation angle decrease with about 6°.

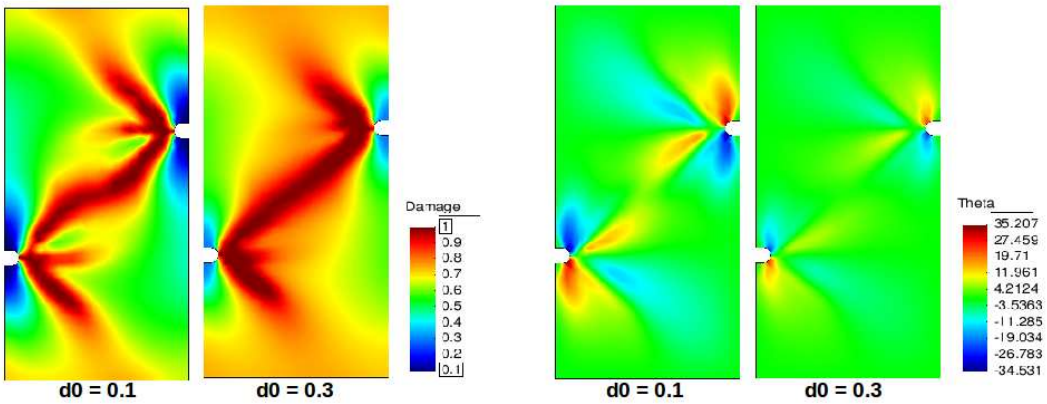

Figure 7.16:

As for the previous simulations Figure 7.17 shows the full micro-crack kinking process for several micro-cracks covering the geometry. With red color, the initial horizontal micro-crack is represented. The trajectory of the branches along the simulation process is drawn with black. The decrease in rotational angle, with respect to previous tests is obvious.

One objective of this section is to see what is the influence of the size of the notches on the damage localization process. Figure 7.18 presents damage and micro-crack ori-

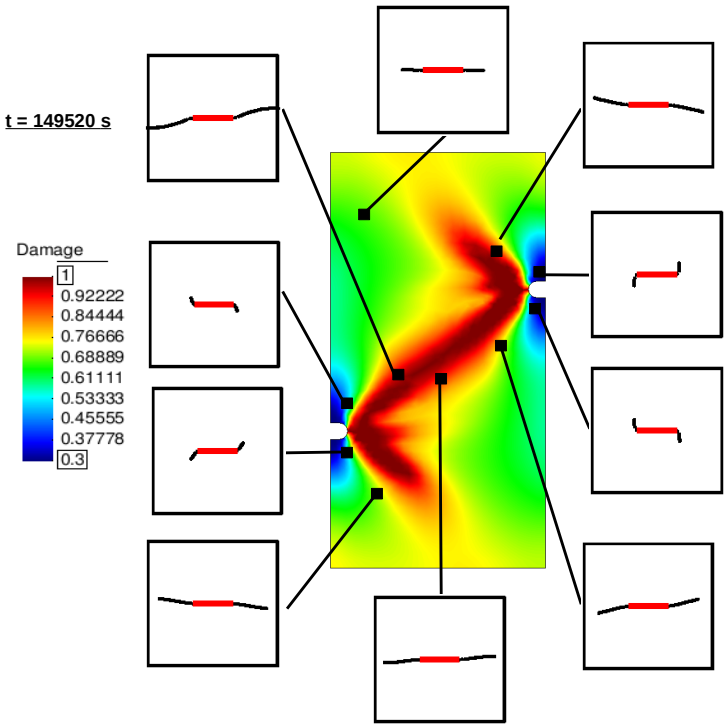

Figure 7.17: Kinking process fully represented for ten micro-cracks: initial micro-crack normalized length is 0.3.

entation maps obtained from simulations with two types of notches: with a radius of 5 mm (previously used in the case of compresion tests) and with a radius of 2 mm (used in tension tests presented in this section). Both 0.1 and 0.3 were considered as initial normalized lenght of the distribution of micro-cracks. In both cases, the geometry containing large notches has a bigger effect on the damage localization zone. The central part presents damage concentration zones, in the rest of those geometries, damage increase is insignificant. The minus of large notches is that the size of the localization zone in the vicinity of each notch is bigger.

7.2.5 Summary

A case study in which comparisons may be made with real experimental data for a relativly simple example was carried out. The main objective was to explore some of the parameters of the time-dependent including rotating micro-cracks damage model. This goal was achieved in several steps: first, the choice of initial orientation of micro-crack distribution was studied, then influence of TC and v_0 on the localization zone was shown. Furthermore, we have been able to show that the model is capable of reproducing, albet qualtitatively, the exprimental results, including strain localisation phenomena. In the end, some aspects of the model at the macro-scale, such as mesh independence, was verified.

In the case of tension tests, influence of the notch radius on the damage localization

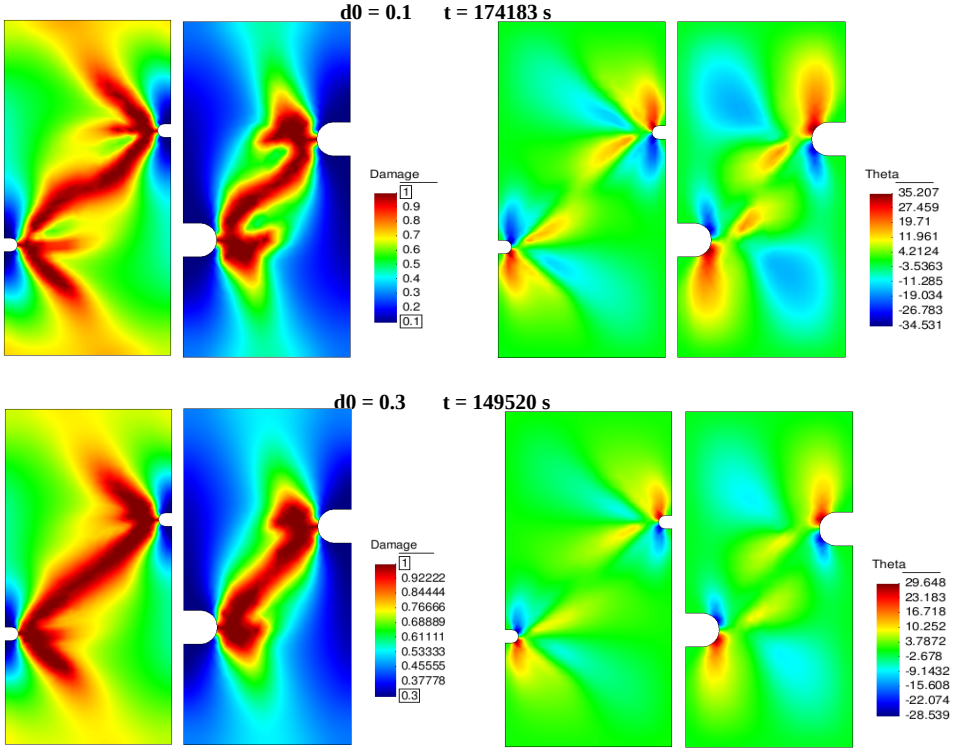

Figure 7.18:

zone was studied. New geometry containing smaller notches was considered and several tests were run with different initial damage parameter. Localization phenomena was studied from the perspective of evolution of micro-cracks in terms of length and propagation trajectory. Micro-cracks kinking mechanism was presented in arbitrary parts of the specimens.

7.3 Simulation of a tunnel gallery

7.3.1 Background

In the previous section we considered a laboratory-scale simulation of damage evolution. In the next two sections of this chapter we move to a larger-scale, to model real engineering problems. The first example of is a 2D simulation of a tunnel gallery excavation e.g. for radioactive waste disposal. Plane strain assumptions are considered in the third direction.

Aside from the simulation of the tunnel gallery excavation this section also explore the influence of length and orientation of the initial distribution of micro-cracks. Moreover, localization phenomena are investigated.

However, this is the first attempt to apply our time-dependent damage models in simulation of real engineering problems. More elaborated analysis of tunnel excavation can be found, for instance, in the work of Callari et al. ([23], [24]) where shallow tunnels in saturated soils were investigated.

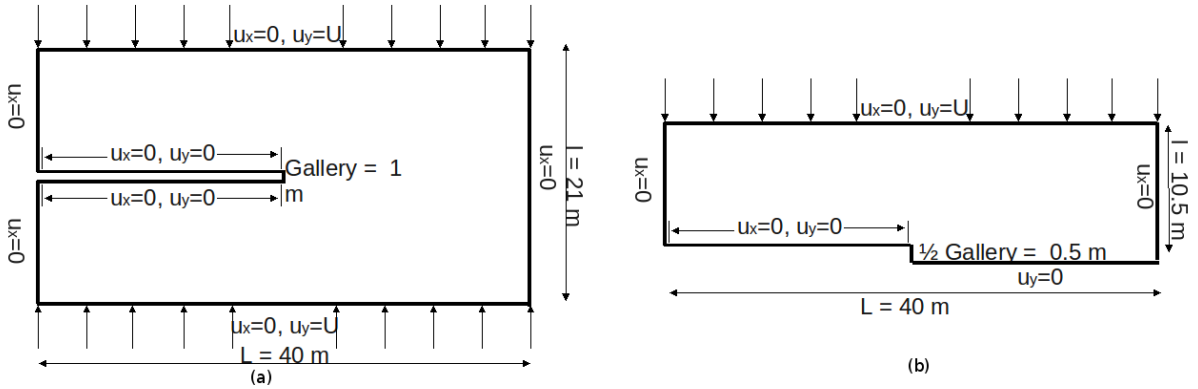

Figure 7.19: Geometry and boundary conditions for the problem of the gallery excavation: (a) full geometry used in the simplified model; (b) $\frac{1}{2}$ of the geometry plus additional symmetry conditions.

Digging underground galleries leads to the damage of the rocks around the excavated area. In-situ observations show that damage localizes in the form of inclined parallel plans symmetrical with respect to the horizontal plane crossing the gallery at the middle and having V-shaped paths pointing to the origin of the macro-fracture. These V-shaped markings are called "chevrons".

Through this first simulation our purpose is to numerically reproduce this behavior. We consider a structure already excavated with the length L = 40 m and width l = 21 m (figure 7.19), where the gallery has a diameter of 1 m. We consider a non-structured mesh that is more refined around the front of the gallery, with 1129 4-nodes quadrilateral elements and 4 Gauss points used for computations (figure 7.20).

In our first attempt, to this geometry we apply displacement boundary conditions:

- displacements on exterior boundaries in order to solicit the structure in vertical compression and to block displacements in the horizontal direction.

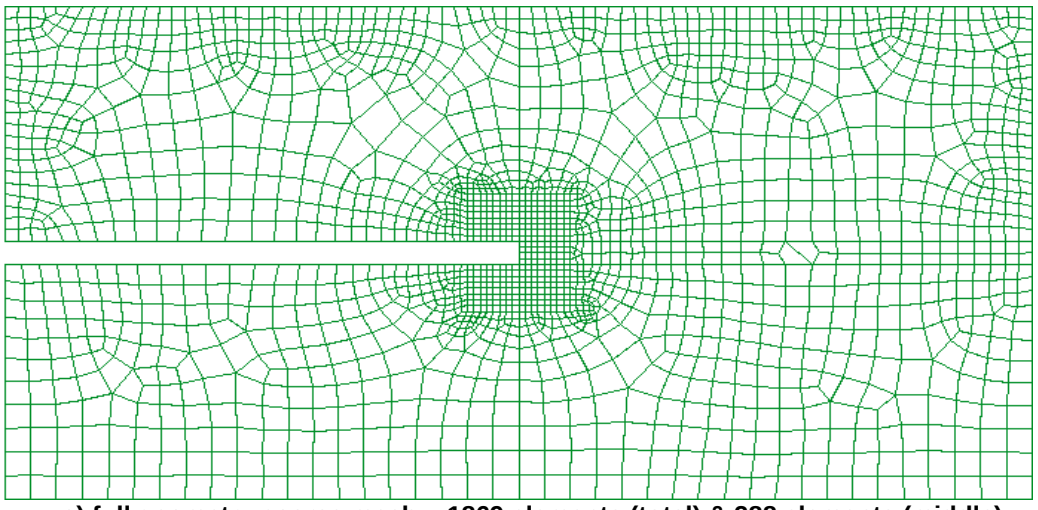

Figure 7.20: Meshes used in simulations: full geometry (top) and $\frac{1}{2}$ geometry (bottom).

- to simulate the support of the gallery, the displacements of interior boundaries of the excavation are blocked in both directions.

It is necessary to be mentioned that this is not the usual procedure. More realistic procedure, as, for instance, release of stress BC at the cavity boundaries, can be found for instance in [23].
The parameters taken into account in the simulation are the following:

- Parameters for the Charles law: $K_0 = 4.47e5Pa\ m^{\frac{1}{2}}$, $v_0 = 1e-3\ m/s$, $n = 2$.
- Elastic parameters: Young modulus = 2 GPa, Poisson ratio $\nu = 0.3$.
- Loading velocity: 1e-7 m/s.

7.3.2 Simulation of a tunnel gallery using rotational micro-cracks time dependent damage model

In this part we show the results of the simulation using an enriched damage model which takes into account micro-structural informations as well as the micro-cracks orientations or different behavior in tensile/compressive conditions (see section 6.5).

Figure 7.21 represents the distribution of the damage variable d corresponding to the same time step, on the full geometry (a) and on the half-geometry (b). In consequence simulations can be carried out more efficiently using the half-geometry without any loss of information or bias. In this example, micro-cracks initially were horizontal and their normalized length was 0.05. We see damage is more concentrated on the gallery ends and the appearance of orientated damaged zones. The obtained solution resembles the in-situ observations (see for instance the work of Bernier et. al ([14], [15])) and thus seems to be appropriate for simulating the real case.

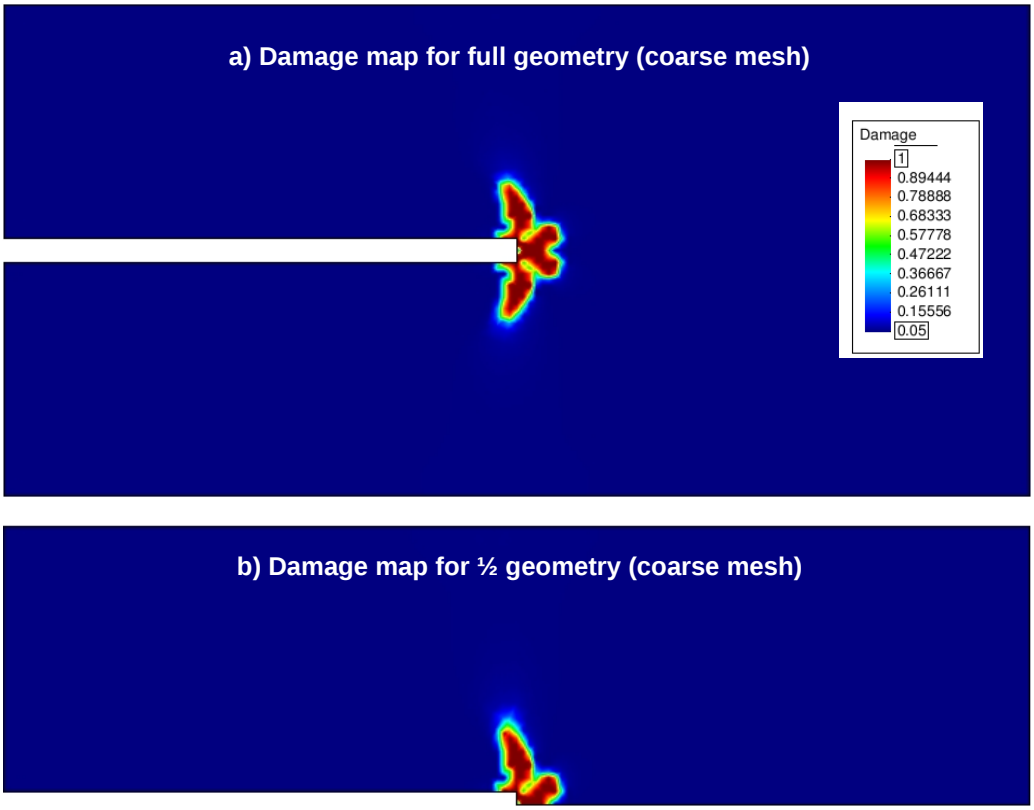

Figure 7.21: Damage distribution over the full geometry (a) and comparison with half-geometry (b).

In the following, a comparison between results obtained starting from different initial micro-cracks orientations or lengths will be presented to investigate how this might influence the final damage distribution.

Influence of the initial orientation of micro-cracks on the size and shape of the damaged zone

The behavior of a micro-crack under a given load depends on its initial length and orientation. In the following, a study of this influence will be done. Four families of micro-cracks with different inclinations with respect to abscissa of the micro-scopic coordinate system: (0°,15°,30°, 45°) were considered. (Figure 7.22). The influence of these four

families of micro-cracks is studied in the particular problem of the gallery excavation. The simulation parameters are the same as above, plus internal length of the micro-structure ε = 1e-4 m.

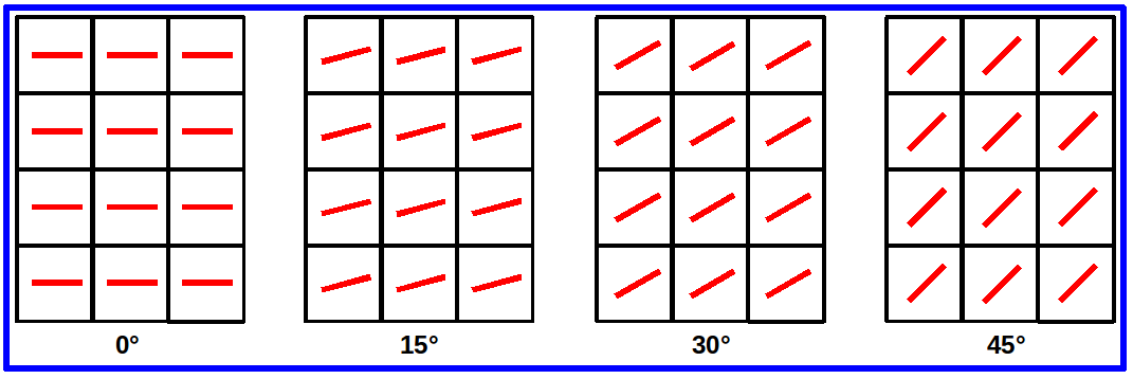

Figure 7.22: Family of micro-cracks into the specimen: from left to right 0°,15°,30°,45°.

Figure 7.23 presents damage localization from the numerical tests run with the different initial orientations for the micro-cracks. For a full understanding of the results, the discussion must be done simultaneously with Figure 7.24. Four time steps have been selected to show the appearance and propagation of the damaged zone. Here we focus on the central part of the geometry ($\approx$ 25 % of the full figure). The damage localization phenomena are clear, but, an interesting results is that the orientation of the damaged zone is dictated by the initial orientation of the micro-cracks. In the bottom part of Figure 7.24 the approximate angle of each damage localization zone is indicated. It is obvious that there is a strong dependence on the initial orientation of micro-cracks. If at the beginning of the test we consider a family of micro-cracks oriented at 45°, the most damaged elements are in an inclined zone which makes an angle of 130° with the abscissa of the macro-scopic coordinates system. Meanwhile, the decrease in the initial micro-crack orientation induces a decrease in the angle of the damaged zone.

Another important aspect presented by the two figures is that the increase of the initial micro-crack orientation induces also the activation of damage propagation outside the localized damage zone. For $\theta_0 = 0°$ and $\theta_0 = 15°$ the localization phenomena is very strong (left half of both figures), but, for $\theta_0 = 0°$ we observe another important damage zone in front of the tunnel, which increases more slowly than the main one.

Compared to the extremely localized damage (and orientation) observed for low initial micro-crack orientations, simulations with $\theta_0 = 30°$ and 45° show a decrease in the localization mechanism at the same time as the activation of the damage propagation outside the damaged zone. This complex aspect is fully explained in Figure 7.24 by the range of values of the actual configuration of micro-crack orientations, which shows that the damage mechanism has two distinct phases:

- first the rotation of each micro-crack is more important than the damage propagation;
- the second phase, involves an increase in the propagation at the same time as a slow rotation.

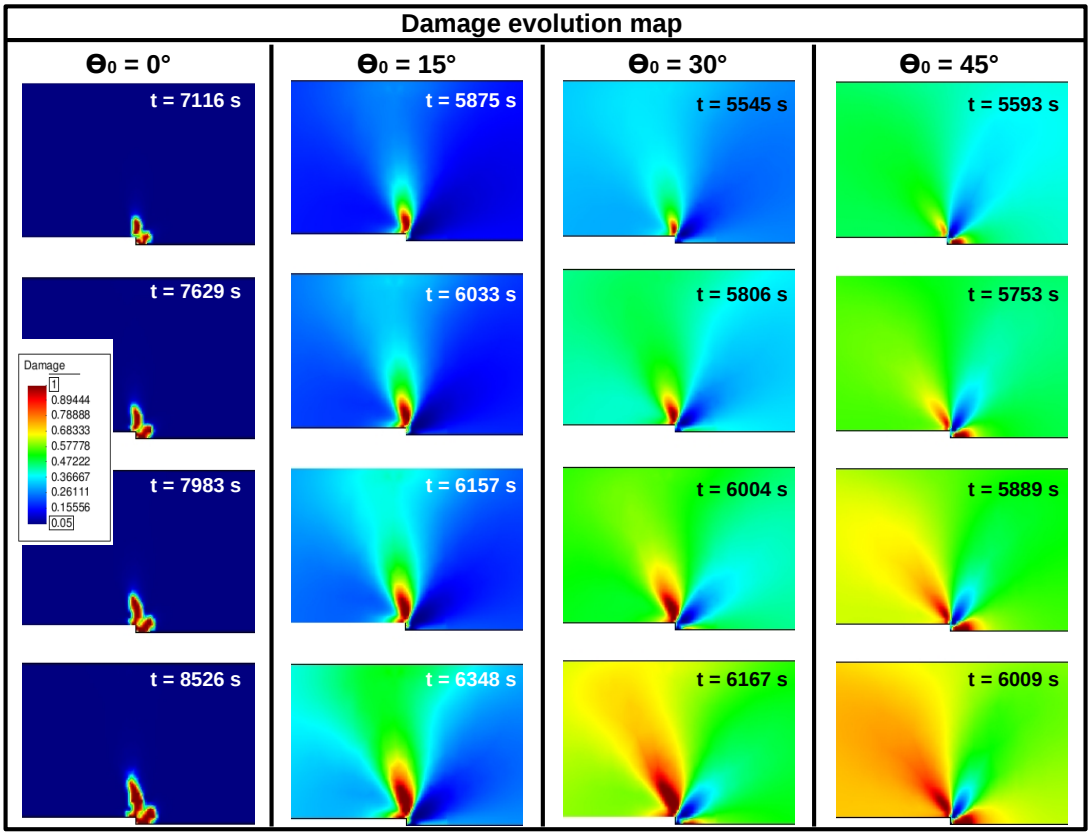

Figure 7.23: Damage evolution map for several tests. Influence of the initial orientation of a family of micro-cracks.

The value θ reached in the localization mechanism depends on the initial orientation and, as will be shown later, also on the initial length of micro-cracks. For the family of horizontal micro-cracks, θ is situated in a range of $[0° \ , \ 38.5°]$, but for the family of inclined micro-cracks this range decreases $5°$ $[45° \ , \ 51°]$ (right part of Figure 7.24).

Figure 7.25 shows the evolution of the maximum shear strain in time. The same time steps were taken into account as for the evolution of d and θ. All sets of maps show that the localization of the deformation process occurs. The high values of the shear strain inside the localized damage zone indicates that, even even if we have just mode I micro-cracking at the small scale, the model produces a shear-localisation phenomenon.

Figure 7.26 shows the pertinence of the numerically obtained results with respect to those obtained in real laboratory tests. One tomographic image of a horizontal CT slice extracted from the 3D images of a specimen is presented (all the details of the experiment are found in [99]). Two open cracks can be seen on the specimen edges. The interesting part from this image is that if we zoom the bottom part of the specimen, the macro-crack found there is formed not from continuous micro-cracks coalescing, but from families of "en-echelon cracks", which are defined as offset, parallel micro-cracks oriented obliquely to the band that they form as an ensemble.

In Figure 7.27 results from the numerical simulation of a gallery excavation, at an advanced time step (last step presented in Figure 7.23, where initial micro-cracks were

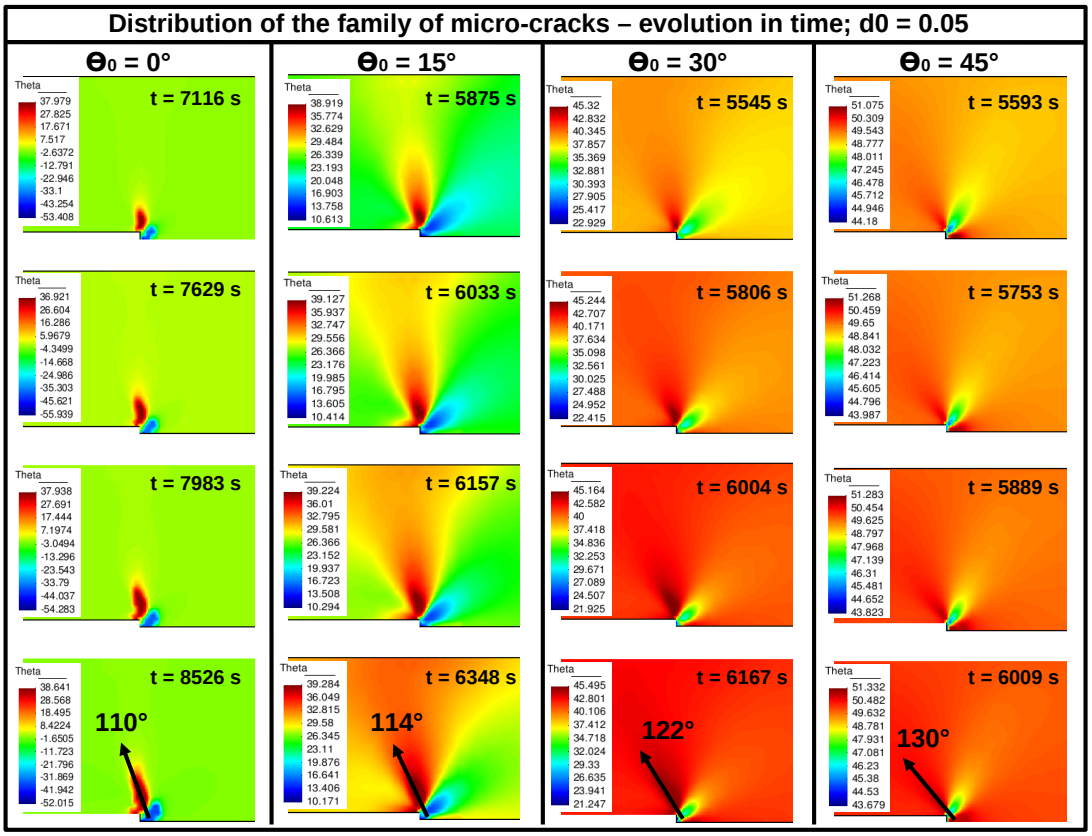

Figure 7.24: Orientation of the micro-cracks evolution map for several tests. Influence of the initial orientation of a family of micro-cracks

horizontal of normalized length $d = 0.05$), is presented. The obtained damaged zone has an angle of 110°, but the families which compose the damaged zone (shown in white rectangles) contain micro-cracks at approximately 37°.

Comparison of the damage evolution inside and outside the localization zone

Figure 7.28 presents the evolution of the normalized damage parameter d^* as well as the orientation parameter θ for a series of five elements far from the gallery to focus on the localization mechanism, three of them from within the localized damaged zone, the fourth exactly at the border and the fifth outside. In figure 7.28 (a) the damage distribution is considered and in (b) with black dots the five elements are localized. Figure 7.28 presents the evolution of the damage parameter (c) and the orientation parameter (d). Up to about 6000 s represents the pre-localization stage: damage in all elements is slowly increasing and the rotation of micro-cracks is almost inexistent. Between 6000 s and 8000 s, the micro-cracks rapidly change orientations which directly implies a rapid increase in the propagation of the damage until the maximum value is obtained. It is obviously that

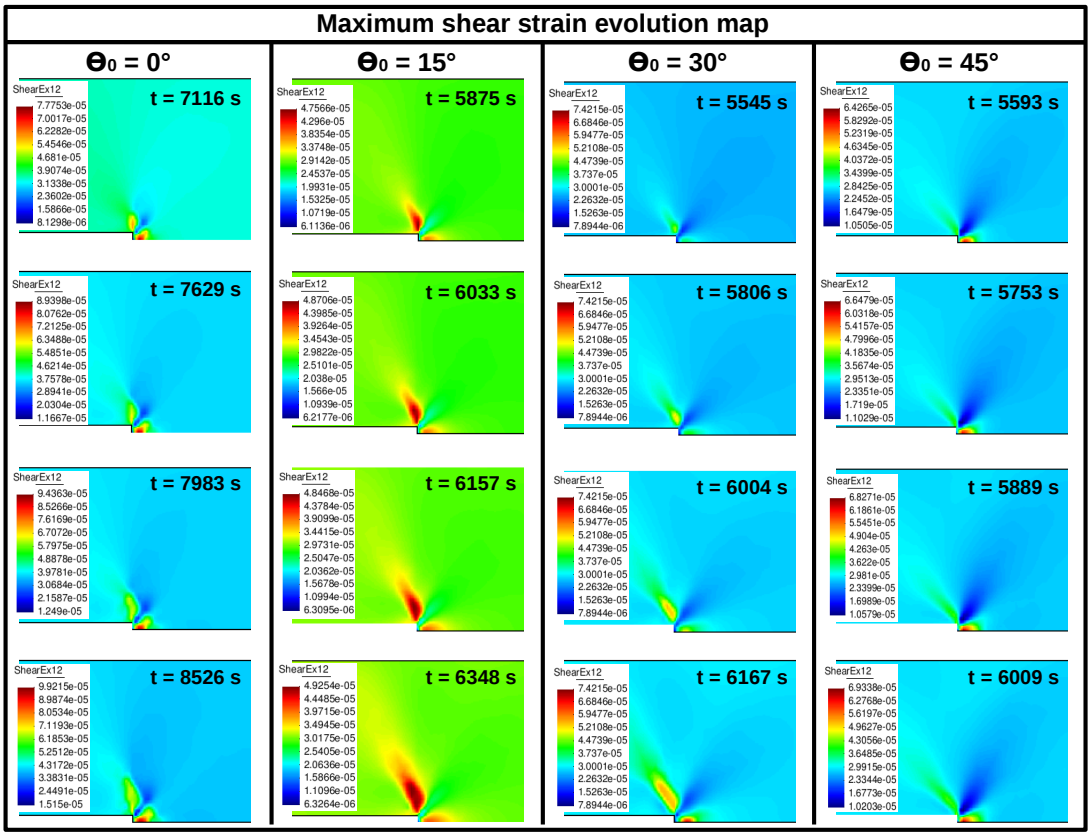

Figure 7.25: Evolution maps for shear strain for the four initial orientation of micro-cracks

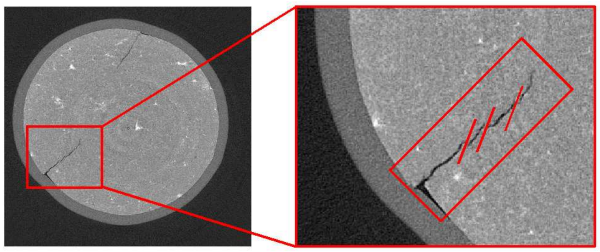

Figure 7.26: Examples of macro-cracks from experiments ([99]).

at the beginning of the localization mechanism, only two elements were a part of this zone (977 and 985). Later, (between 8000 s and 9000 s) the size of the zone increased with loading including also element 993. Normalized damage variable increased up to the maximum value ($d^* = 1$) and micro-cracks final orientation angle is about 37°. Elements 932 and 1001, which lie outside the localization zone, did not change much, although there is a slight change in orientation for the element from the border.

Influence of the initial length of micro-cracks, for a fixed orientation, on the size and shape of the damaged zone

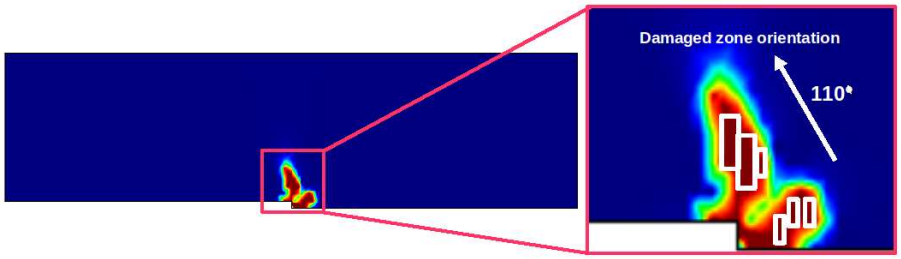

Figure 7.27: Examples of macro-cracks from numerical test. One macro-crack is formed of series of micro-cracks.

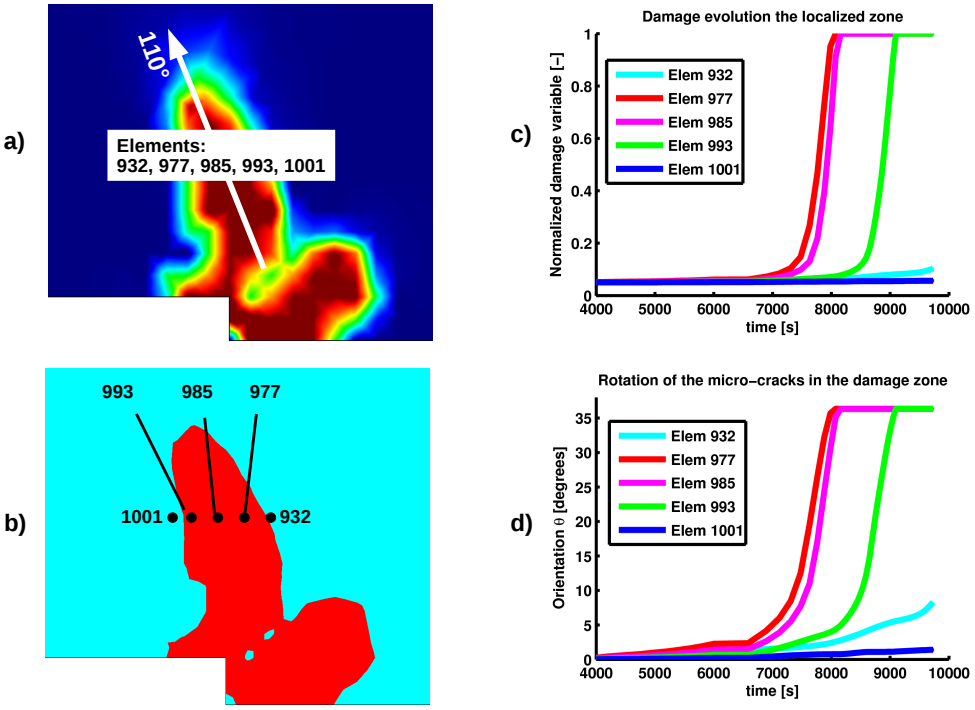

Figure 7.28: Evolution of the orientation inside the localized damaged zone: a) damage distribution at an advanced time step; b) identification of the elements - with red, damage localization zone and with black dots, the five elements considered; c) and d) micro-cracks evolution in time - normalized length and rotation angle.

In the following, the influence of the initial damage parameter is presented in Figure 7.29. The orientation of the damaged zone decreases with the increase of the initial length of the micro-cracks. This aspect can be fully explained by comparison between the maximum angle of the micro-cracks inside the localized damaged zone. For $d_0 = 0.05$ we reach $\theta_{damagedzone} = 38.6°$, but for $d_0 = 0.1$ the rotational angle cannot pass $\theta_{DamageZone} = 28.8°$, as well as for $d_0 = 0.3$ where $\theta_{DamageZone} = 14.2°$. By increasing the initial length of the micro-cracks, the model is too constrained and we reduce the time during which

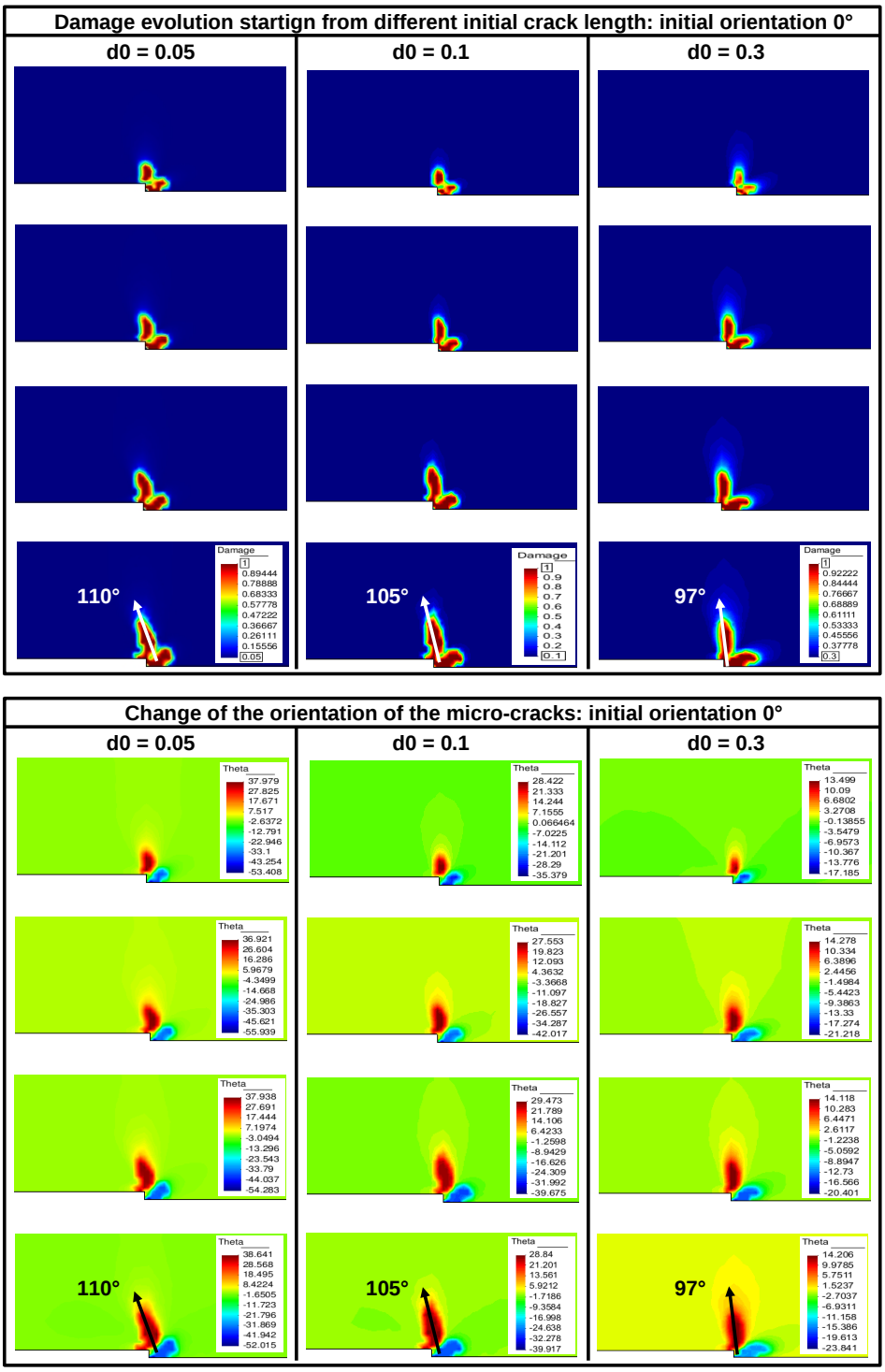

Figure 7.29: Change of the orientation of the micro-cracks: dependence of the initial damage

the cracks can rotate. Therefore the micro-cracks develop without reaching the maximum rotation and, since there is a direct connection between the angle of the damaged zone and the angle of the micro-cracks inside (as previously presented with the help of Figures 7.23

and 7.24), the direction of the damaged zone is also influenced. In conclusion, in order not to influence the response of the simulation, small initial micro-cracks are needed.

7.3.3 Summary

In this section a simple 2D simulation of a tunnel excavation whose final destination is radioactive waste disposal was presented. The first objective was to present the ability of the model to simulate real-scale problems and phenomena The second objective was to study the influence of length and orientation of the initial distribution of micro-cracks on the localization zone. Simulation was carried out with the time dependent including rotating micro-cracks damage model and the following conclusions can be presented:

- orientation of the damaged zone is dictated by the initial orientation of micro-crack distribution - smaller values of θ_0 leads to small angle of the damaged zone and by initial micro-cracks length - smaller d_0^* implies bigger angle of the orientation;
- final orientation of micro-cracks included in the damaged zone is first influenced by the initial orientation of micro-cracks and, second, for a fixed initial orientation of the distribution, is influenced by the initial length of the distribution.

Simulations with the time-dependent rotating micro-crack model provides localization sructures that reflect in-situ observations around excavated tunnels. To demonstrate the need for the rotating microcracks to simulate real examples such as this, simulations were also caried out using a simplified damage model where the damage evolution law is deduced, through the homogenization by asymptotic developments technique, but with the homogenized coefficients replaced by a linear model of normalized damage variable d^*. In this case anisotropy is not considered and the information of the microstructure is lost. Moreover it does not make the difference between the opening/closing states of micro-cracks.

The results from one such simulation are presented in Figure 7.30 with the evolution of the normalized damage variable d^* and corresponding vertical strain during the loading for different time steps. We observe that, for a smaller time step (t = 2105 s), damage and strain are concentrated around the gallery front. Meanwhile, during the loading, the damage evolves along the tunnel. No oriented band which can be interpreted as "chevron"-type fracture occurs. This suggests that such a simple model can not be used to simulate the real situation. Therefore a modelling approach that can account for crack orientation and rotation is needed. Moreover distiction between the state of the crack (opened or closed) is obligatory.

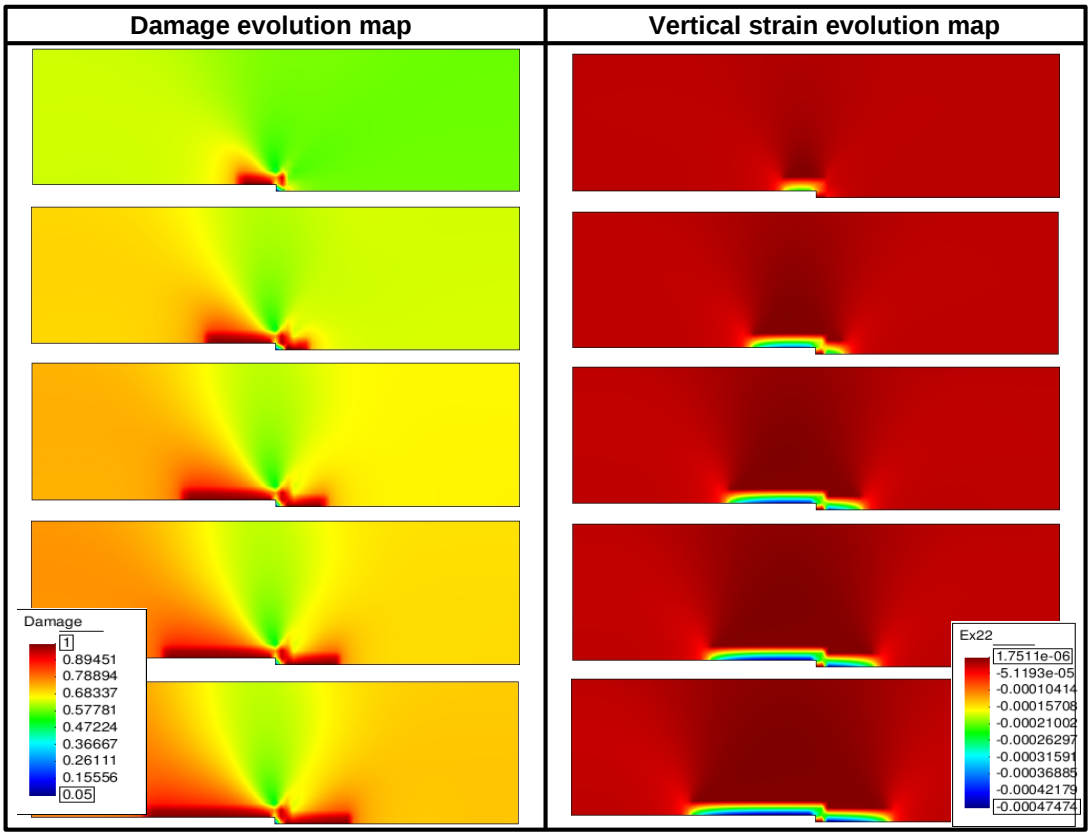

Figure 7.30: Evolution of the normalized damage variable d^* (left) and corresponding vertical strain (right) during the loading process.

7.4 Simulations of an overburden surrounding a subsurface geologic reservoir

7.4.1 Background

The probably best-known example of rock mechanical effects on reservoir scale behavior is reservoir compaction and associated surface subsidence. This phenomenon can have consequences on production of fluids (e.g., hydrocarbons or water) or injection of CO_2 for storage, by changing permeabilities in a reservoir or by damaging the overburden with possible leakage from the reservoir or causing issues for well-bore stability.

When oil or gas is produced from a subsurface reservoir, fluid pressure will generally decline. Reduced pore pressure in the reservoir rock will increase the effective stress and thereby cause the rock itself to shrink, and thus the reservoir will compact. Reservoir compaction may then in turn cause subsidence at the surface as sketched in Figure 7.31.

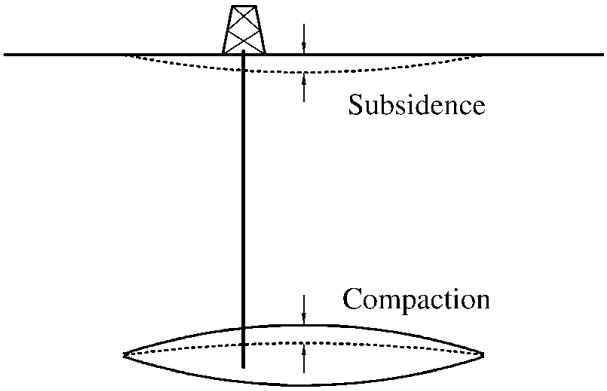

Figure 7.31: Compaction and subsidence (image from [55])

In a similar way, injection of CO_2 into a subsurfae geologic reservoir can increase pore pressure and so cause expansion that might damage the overburden seal. Since often CO_2 is injected into depleted hydrocarbon reservoirs the process of production, and associated damage, can have implications for subsequent CO_2 injection.

7.4.2 Modeling

In the following, we will present the results of a first simulation at the scale of an oil reservoir using time dependent damage model with rotational micro-cracks. The aim is to model the deformation and damage evolution in the overburden of a subsurface reservoir associated with fluid injection or extraction. In addition we wish to model the evolution in seismic properties and micro-seismic emissions associated with the deformation that might be indicators of damage processes measurable through geophysical techniques.

Figure 7.32 shows the overburden geometry and boundary conditions as well as the mesh and an overview of the parameters used in a simulation of the oil production that

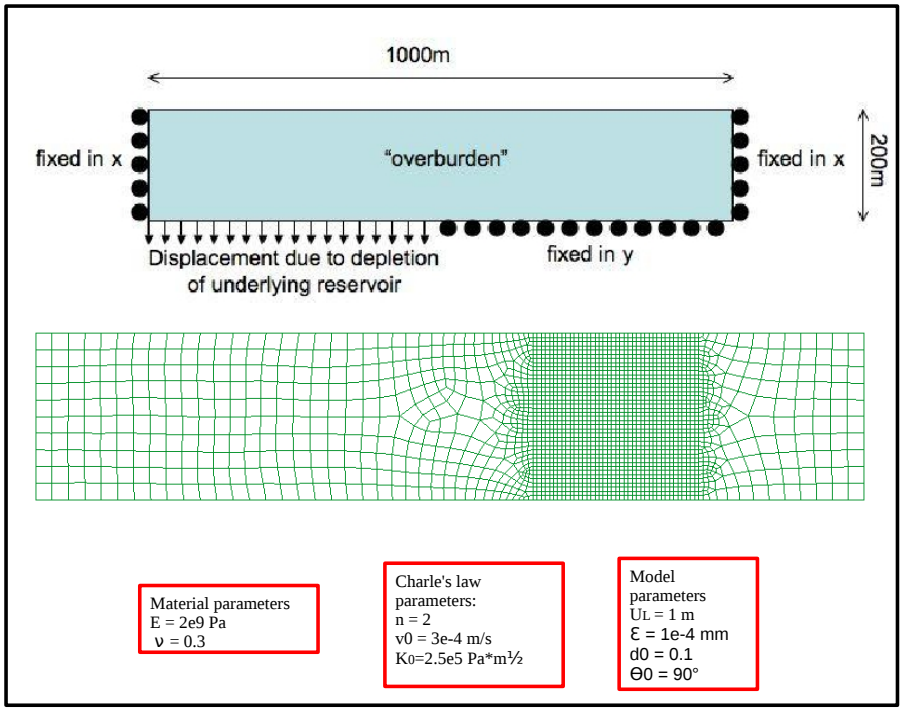

Figure 7.32: Geometry and boundary conditions of an overburden surrounding a subsurface geologic reservoir

might preceed CO_2 injection. We considered the overburden represented by a rectangle of 1 km long and 200 m width. Those measurements are realistic and they were taken with respect to the observation from [92] in the case of Valhall oil field in the North Sea. In the Valhall case, data indicates that most of the deformation occurs close to the reservoir within the first 100-200 m TVD (acronym for "true vertical depth" in the oil and gas domain) of the top of the reservoir.

Boundary conditions imposed are the following:

- A fixed corner has been considered in order to avoid the rigid body movements (right bottom corner);
- On a length of 300 m at the base of the model, representing the top of the (non-producing part of the) reservoir, the displacement is blocked in the vertical direction;
- Displacement is blocked in the horizontal direction for both lateral sides;
- A displacement of 1 m is imposed on the rest of 700 meters of the bottom boundary; imposed displacement is used in order to simulate depletion of the underlying reservoir.

As in the previous simulations, the parameters taken into account in the simulation are the following:

- Parameters for the Charles law: $K_0 = 2.5e5Pa\ m^{\frac{1}{2}}$, $v_0 = 3e-4\ m/s$, $n = 2$.

- Elastic parameters: Young modulus E = 2 GPa, Poisson ratio $\nu = 0.3$.

In the simulation, a locally periodical distribution of vertical micro-cracks ($\theta_0 = 90°$) of initial normalized length 0.1 is considered. Due to the nature of sub-surfaces stress generally being most compressional in the vertical direction, any existing open cracks are likely to be vertical.

7.4.3 Results - damage evolution

Figure 7.33 shows the first stress invariant (its values are the same regardless of the orientation of the coordinate system chosen) obtained from the simulation. Its formula is given by:

$$\Sigma_{invariant} = \Sigma_x + \Sigma_y, \tag{123}$$

where Σ_x and Σ_y represents stresses in horizontal and vertical direction.

With black dots, 4 different time steps are denoted, t_1 being the time close to the peak and t_4 at the end of our simulation. These will be analysed in more details in the following.

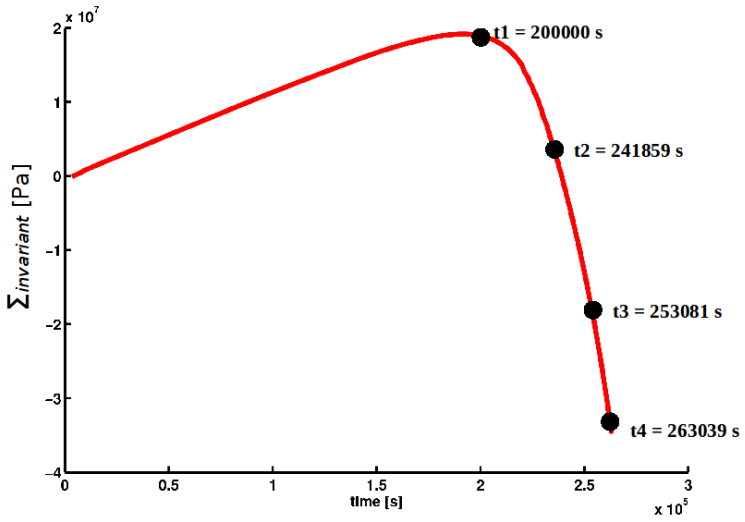

Figure 7.33: Global volumetric stress vs time curve obtained during the loading.

Figure 7.34 represents the damage evolution maps at four time steps.

It can be seen that damage initiates and propagates in the zone around the transition from fixed to free elements on the lower edge where the stress concentration is the highest. The zoomed images show that most damaged zone is exactly at the level of the bottom boundary and, then, is decreasing progressively with the advancement at the interior. It is very clear that in the majority of the overburden the micro-cracks did not evolved too much, neither in terms of length, nor in term of changing orientations, as it can be seen in the bottom part of Figure 7.34. Green color represents an orientation of 90° which coincides with the initial orientation of micro-cracks distribution and the changes are

insignificant elsewhere except the damaged zone. In this zone (100 m $\times$ 100 m) blue color represents micro-cracks which turned clock-wise for about 50° degrees and increased their normalized length from the initial one of 0.1 to $\approx$ 0.85.

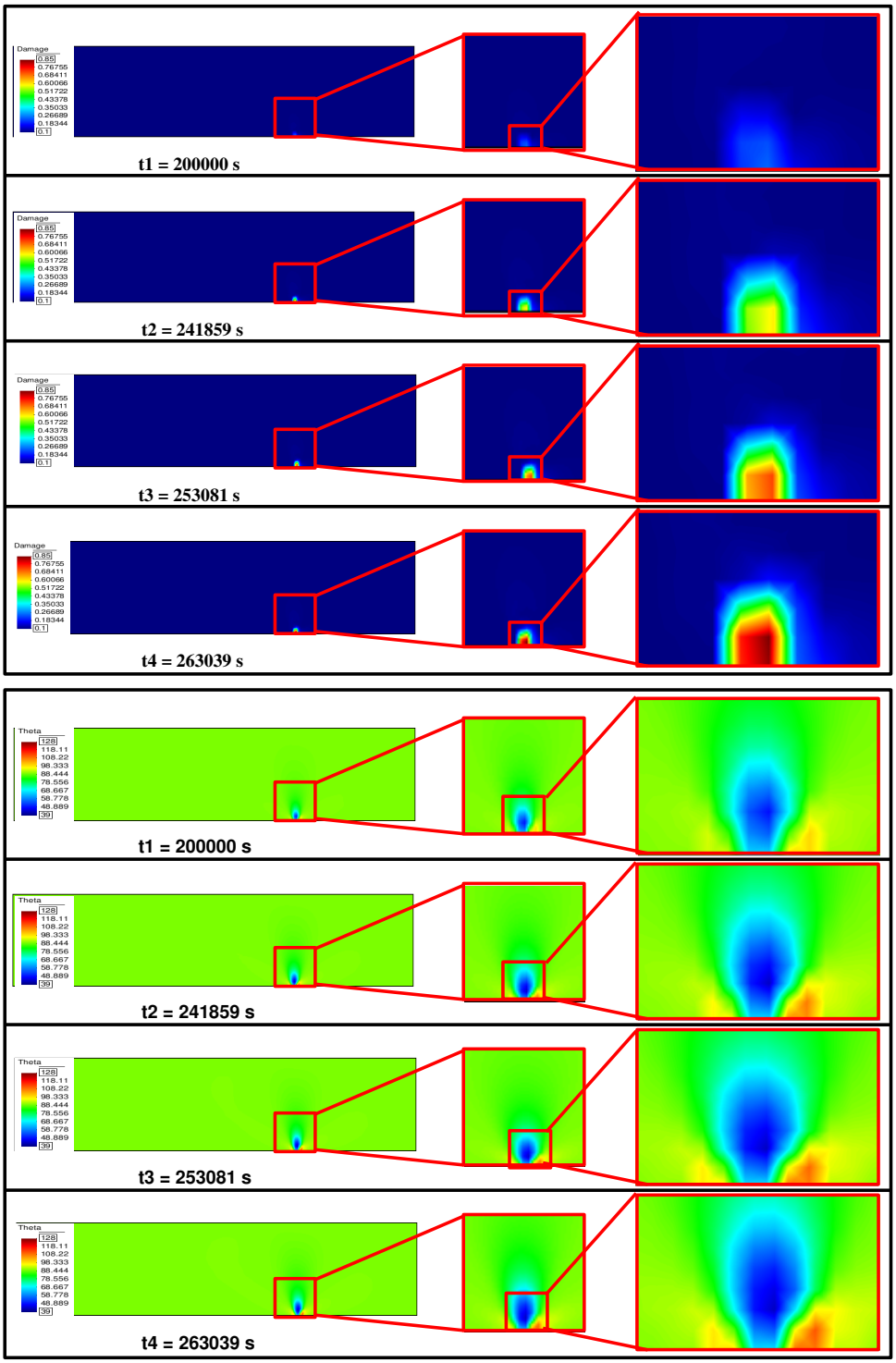

Figure 7.34: Length and orientation evolution maps of micro-cracks during the loading

In Figure 7.35 the evolution of six micro-cracks is followed. Among the chosen cracks, those corresponding to elements 21 and 61 had the bigges change in rotational angle with respect to x-axis. The reason is given by their localization right in the center of the most solicited zone in the entire geometry. On the right part, elements 23 and 63 were chosen from the zone where we have the influence of blocking vertical direction displacement and, on the left part, the set of elements, 19 and 59, from the "flexible" part of the overburden. It can be observed that the first mentioned set of micro-cracks (from the moving part of the overburden) are the least affected in both length and orientation changes. It can be seen that they turned anti-clock wise at about 12 degrees, but their length increase very little. On the "more fixed" part, the crack turned in the same way, but both length and orientation were more pronounced. With a blue thin line we followed the trajectory of each crack during the loading process. In the most solicited part, very clear wing-type cracks formed. Half of the evolution process is dedicated to the rotation of the cracks. In the end, the rotation is slowed, the orientation angle θ tends to a stable value and the crack propagates in that direction.

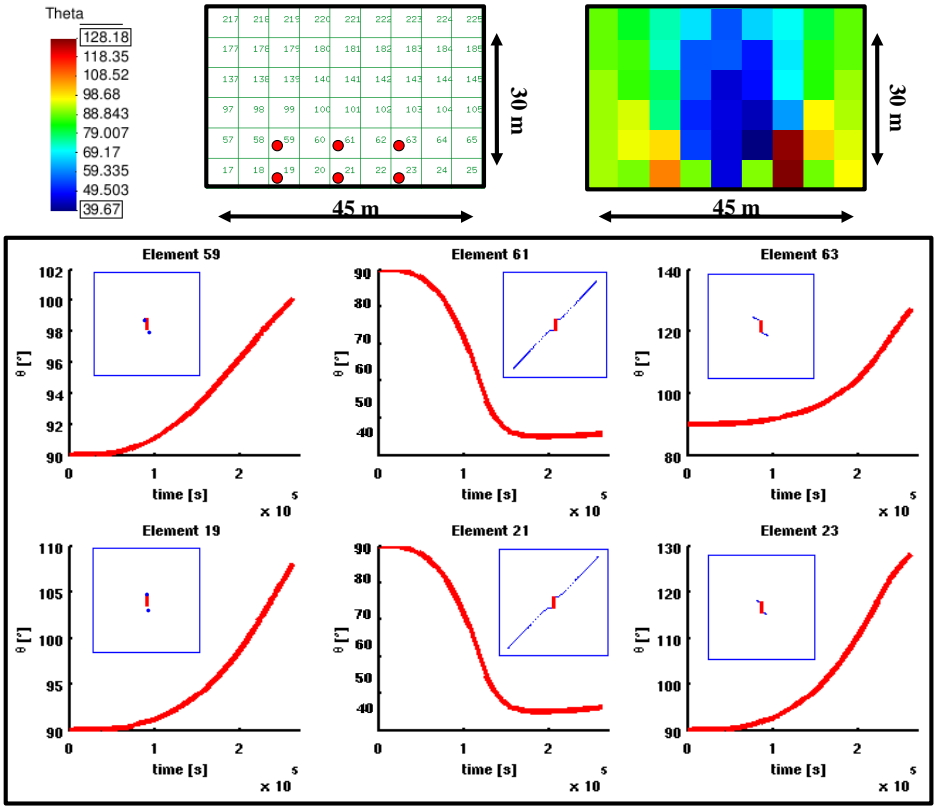

Figure 7.35: Evolution of micro-crack orientation for six elements in the neighborhood of the damaged zone

Figure 7.36 show on the one hand that the volumetric and maximum shear strain zones coincide with the damaged paths, but, the more important is that the cracking mechanism is identified. It is clear from the maps of maximum shear zone that shear strain localisation mechanisms occurs, but the micro-cracking remains mode I (details will

be given with respect to Figure 7.37). Strain values are given accordingly to continuum mechanics convention, so negative values found in the representation of volumetric strain corresponds to a more deformed zone due to damage evolution.

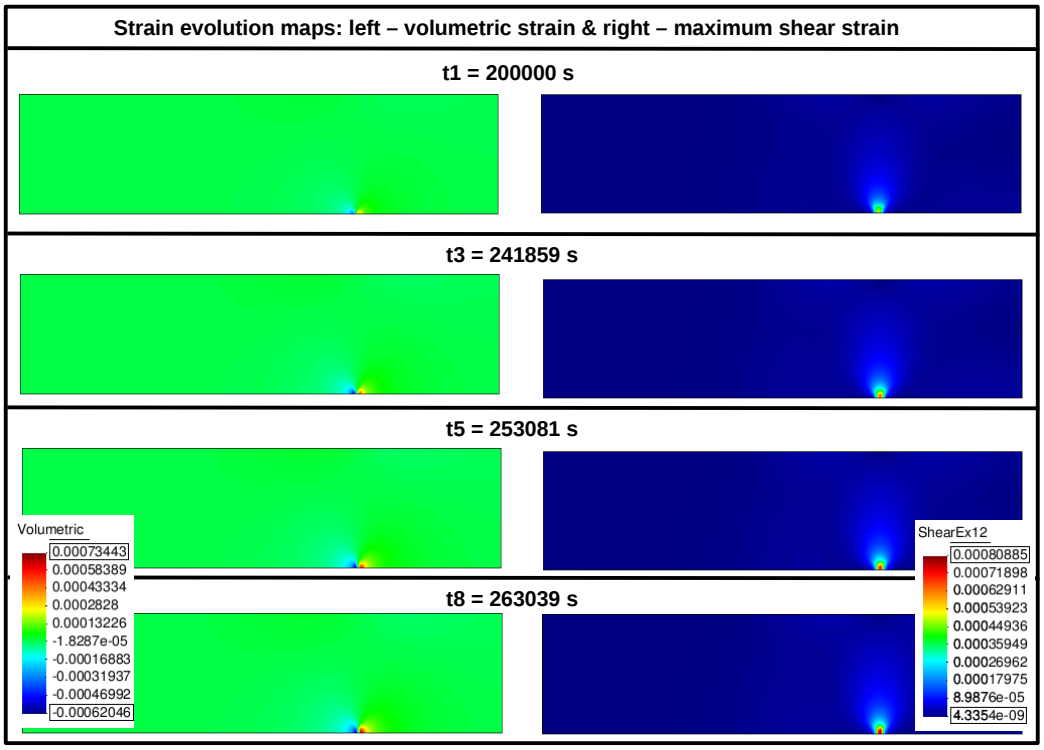

Figure 7.36: Volumetric strain (left) and maximum shear strain (right) evolutions maps.

Our time dependent damage model including rotating micro-cracks are able to distinguish between closed and opened cracks. Figure 7.37 clearly show the evolution of cracks states under the loading. Two zones are identified: a zone of closing cracks (light yellow) and one where cracks opens with the loading (light cyan). At the beginning of the simulations all micro-cracks were considered opened, but during the deformation of the overburden under the imposed displacement, on the left part, far from the most stressed zone, the cracks start to close and the consequence was a decrease in the damage propagation increments as well as a stabilization of the orientation. On the contrary, on the stressed zone, propagation and rotation of the cracks was accelerated and the opening mechanism start to be more and more visible. In the future, in order to have a better characterization of the geomechanical properties of the overburden, we should take into account partially closed cracks.

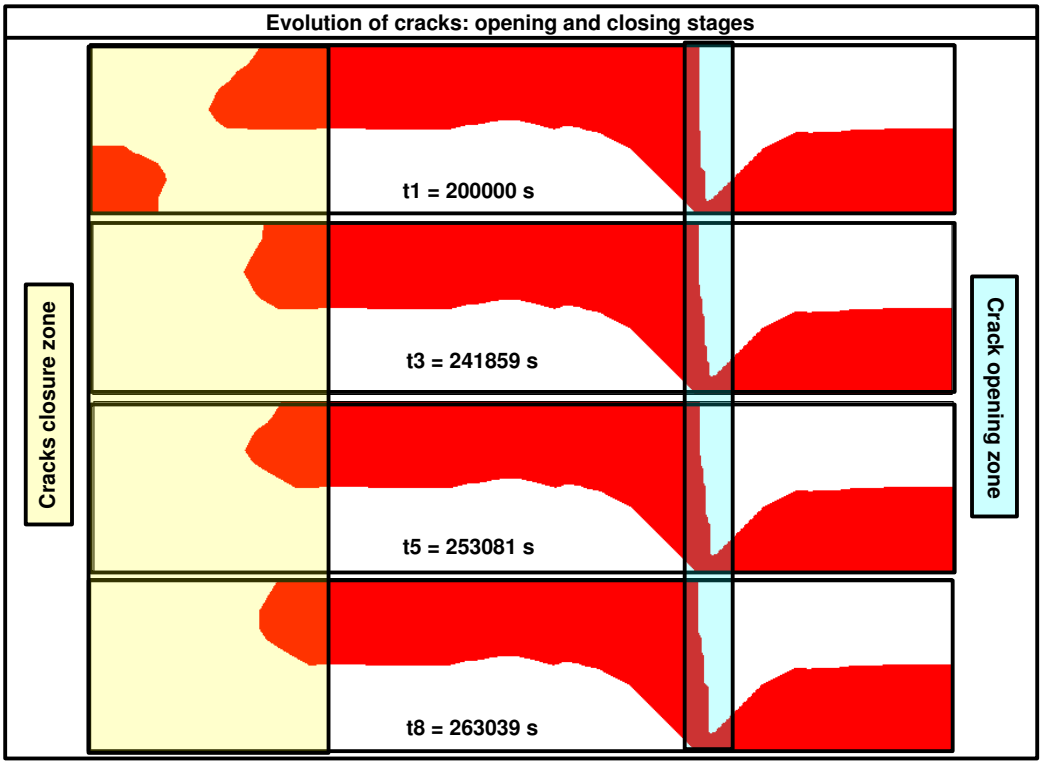

Figure 7.37: Evolution of the state of the cracks distribution: a zone of closing cracks (light yellow) and one where cracks opens with the loading (light cyan). With red, opened cracks are represented, meanwhile the white color describes closed micro-cracks. In the area which is neither blue nor yellow, micro-crack state do not change (opened cracks stay open, and closed ones stay closed).

7.4.4 Results - seismic property evolution and micro-seismic prediction

Seismic velocity changes and anisotropy evolution due to damage

Damage is one of the causes of changes in seismic properties around producing hydrocarbon reservoirs (including aspects of seismic anisotropy and time shifts) and of micro-seismic emissions, therefore exploitation of both is of significant interest in monitoring reservoir behavior during production of hydrocarbons or sequestration of CO_2. The model proposed in this thesis is capable of modeling the degradation of elastic moduli due to the micro-crack evolution and an explicit quantification of the acoustic emission energy associated with damage therefore our model has the potential to make a bridge between monitoring and modeling.

Orientations of the micro-cracks induce anisotropy such that the physical properties of the featured medium vary with the direction in which they are measured. Seismic anisotropy is, therefore, the variation in seismic velocity with direction. A major advantage of characterizing seismic anisotropy is its link to production processes in the oil domain since preferential orientation of the micro-cracks distributions can produce anisotropy in rock permeability.

In the case of an homogeneous elastic isotropic material, propagation velocities of waves are constant and depend on material characteristics. In reality most sedimentary rocks are anisotropic (the rock stiffness is directional dependent). As mentioned before, the orientation of micro-cracks induces an effective elastic anisotropy in a medium so the elastic properties at a point vary with direction. Therefore wave propagation will be slower perpendicular to the fracturing than parallel.

A general description of seismic wave propagation velocities in anisotropic media can be provided by our model. However, for simplicity, just the anisotropy of the P-waves will be considered based on the difference of velocities of vertically and horizontally propagating overly sample P-waves:

$$v_{Ph} = \left(\frac{C_{11}}{\rho}\right)^{\frac{1}{2}}, \qquad v_{Pv} = \left(\frac{C_{22}}{\rho}\right)^{\frac{1}{2}}, \tag{124}$$

where C_{ij} is the elastic tensor for an anisotropic medium using Voigt notation (C_{11} reprezenting horizontal homogenized coefficient and C_{22} being the vertical one) and ρ is the density of the medium.

Thomsen ([140]) simplified the description of anisotropy considering transversely isotropic rocks with weak anisotropy. His description is relevant for oilfield rocks and the data available in field situations, and has become widely applied. Thomsen introduced a new set of parameters: ε_{Th}, γ_{Th} and δ_{Th}. ε_{Th} can be interpreted as the P-wave anisotropy and γ_{Th} as the S-wave anisotropy. In the 2D case only ε_{Th} make sense and its modified formula reduces to:

$$\varepsilon_{Th}^{2D} = \frac{C_{22} - C_{11}}{2C_{11}} \tag{125}$$

Figure 7.38 shows normalized P-wave velocity evolution for the overburden model. We denoted by v_{Ph0} and v_{Pv0} horizontal and vertical P-wave velocity at the beginning of simulation. Our case of vertical micro-cracks confirm this since velocity of horizontal

P-wave (i.e. perpendicular to micro-cracks) increases up to a value bigger than in the case of vertical P-wave. Dark blue represents the lowest value of the velocities and it corresponds to areas of closed micro-cracks. The propagation of these cracks is quasi-inexistent, therefore little variation in the velocity is seen. Lighter blue represents the areas with opened cracks which are still evolving with time. Naturally, it is more visible for horizontal P-wave and the magnitude of changes is about 10 %. As expected, the highest values of the normalized P-wave velocities are in the damaged zone (changes of about 50 %).

Bottom part of Figure 7.38 shows the velocities of P-waves for six elements: 21 and 61 located in the heart of the damaged zone, elements 23 and 63 on the right part, from the zone where we have the influence of the bottom boundary condition of blocking vertical direction displacement and 19 and 59 from the "moving" part of the overburden. Blue corresponds to horizontal P-wave velocity and, red, to vertical P-wave velocity. The most solicited part of the model shows the biggest increase in normalized P-wave velocities. In this region the two curves tend to the same values since the micro-cracks orientation changed from 90° to 45° orientation which acts as a symmetry center for the two P-waves. Elements 23 and 63 shows a less important increase in P-wave velocities. Again, elements from the flexible part of the overburden show the least important activity (as in the previous cases where evolution of damage and orientation was presented).

Figure 7.39 show the evolution of the P-wave anisotropy. It can be seen that the most significant variations are localized around the most damaged area and away from this the anisotropy variations are quite small. In the bottom of the figure, the same particular discussion on six elements is presented. Minima or maxima of the anisotropy evolution correspond to the peak in the stress curve. It is clear that the most important evolution is found in the most damaged elements (21 and 61). Therefore, whilst our model allows the prediction of seismic anisotropy that may be compared to data measurements, but, in this specific case, it is not expected that seismic anisotropy measurements would help to detect the deformation. At least not if just comparing vertical and horizontal velocities - one would have to perhaps analyse the full anisotropy of the system and find the principal directions of the anisotropy and thus the maximum differences.

Acoustic emissions

In our simulation we can make an assumption that micro-seismic emissions are related to the fracture energy, which is defined by:

$$G_f = \frac{K_I^{*2} + {K_{II}^*}^2}{E'} \tag{126}$$

where K_I^* and K_{II}^* are the stress intensity factors at the branches tips and depends on the crack orientation and length. Using this definition, for any time step we can determine the locations and magnitude of micro-seismic emissions or calculate cumulative events over the duration of a simulation, either locally in the model or globally.

Figure 7.40 shows the global micro-seismic emmision energy for all the time steps in the overburden simulation. A double-scale graph first stress invariant and acoustic events is presented which highlights that the maximum microseismic activity coincides with the peak of the volumetric stress. The five fracture energy evolution maps from the bottom of the figure indicate that this activity is mostly concentrated around the hinge zone at the

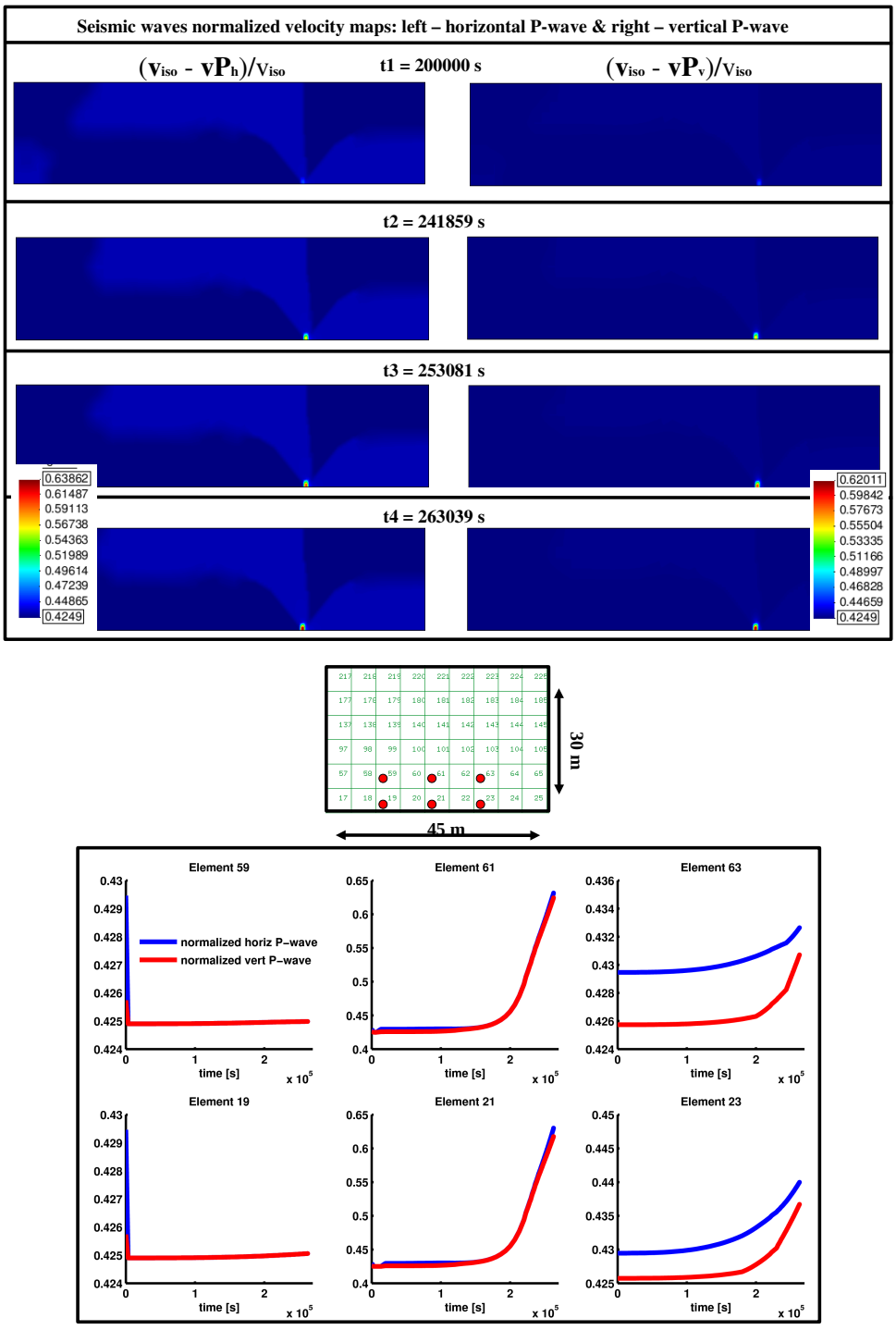

Figure 7.38: Normalized P-waves velocity: horizontal and vertical normalized velocity maps for four time steps (top); evolution of horizontal and vertical normalized velocity for six elements in the neighborhood of the damaged zone (bottom).

transition from fixed to free elements at the bottom of the model. Emissions elsewhere are of insignificant ampitude.

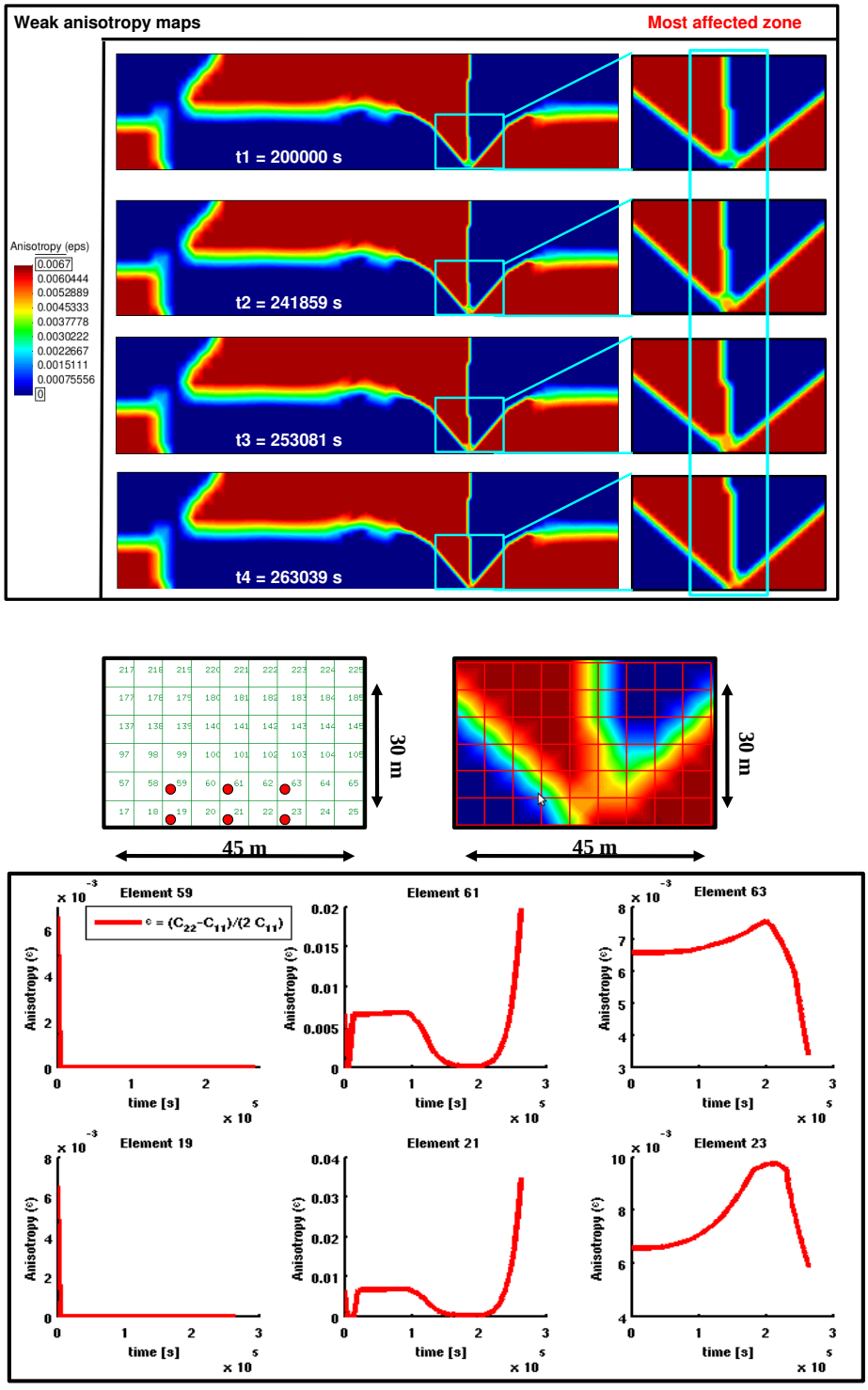

Figure 7.39: Weak Anisotropy of P-waves: (top) Anisotropy maps at four time steps. The most active evolution is in correspondence to the crack opening zone from Figure 7.37; (bottom) Evolution of the anisotropy for six elements in the vicinity of the damage zone - depends on the crack changes in length and orientation.

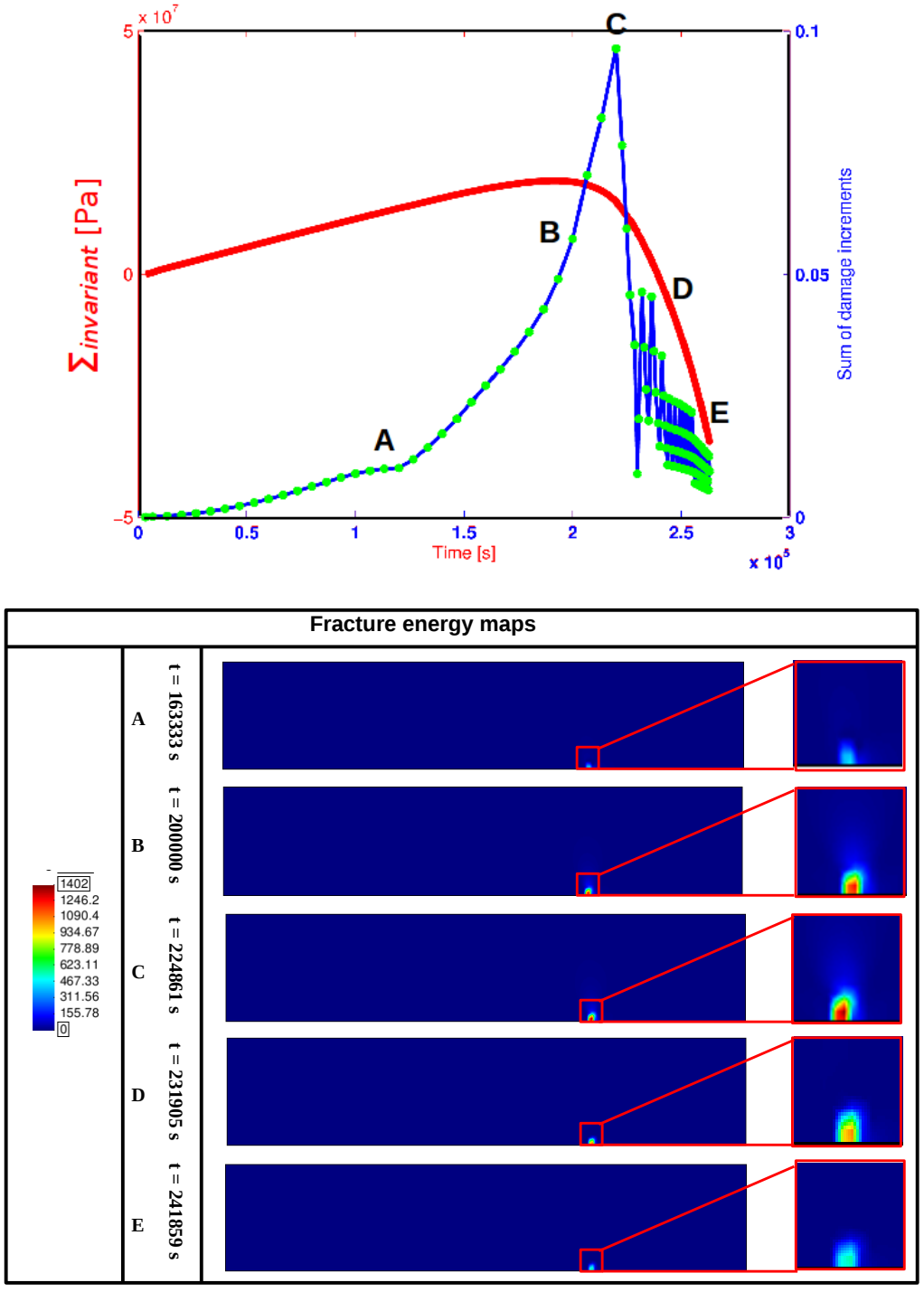

Figure 7.40: Monitoring of Acoustic Emission events: (top) We describe an event as the sum of overall damage increments from one time steps to another. It can be seen that the maximum AE event is right immediately the peak values of the first stress invariant (red curve); (bottom) Fracture energy maps in correlation with the AE events: the third representation in the middle of the image prove that the maximum energy release due to fracture also occurs after peak.

7.4.5 Summary

The aim of this section was at presenting results of a first simulation at the scale of an oil reservoir using time dependent damage model with rotating micro-cracks. Several points were followed. First, damage evolution (damage, orientation, deformation, micro-cracks opening/closing state) in the overburden of a subsurface reservoir associated with fluid injection or extraction was presented.

A locally periodic distribution of vertical micro-cracks of normalized length 0.1 has been considered at the beginning of the simulation. It was shown that damage initiates and propagates in the zone around the transition from fixed to free elements on the lower edge where the stress concentration is the highest. In the major part of the overburden the micro-cracks did not evolved too much, neither in terms of length, nor in term of changing orientations. In the damage localization zone micro-cracks turned clock-wise for about 50° degrees and increased their normalized length from the initial one to ≈ 0.85.

Evolution of the state of the distribution of micro-cracks was also presented. Three major zones have been identified: a zone of closing cracks, a zone of opening of the previously closed crack and a zone where no change occurs in the micro-crack state.

In the second part, evolution in seismic properties and micro-seismic emissions associated with damage was modeled. Our results indicate that predicted changes in velocities are easily detectable compared to the anisotropy changes, which exists, but are less evident.

This simulation represents just an attempt to model real-scale simulations, but it was clear that our model is able to output the degradation of elastic properties and the development of elastic anisotropy. Furthermore, since the evolution of the micro-crack damage is based on an energy dissipation approach such that the energy release with damage evolution, acoustic emission energy of micro-seismic events can also be modeled.

8 Conclusions and perspectives

8.1 General conclusions

The key phrase of the Introduction is: *Links are required between the geophysical monitoring techniques and the geomechanical simulations!* Indeed, to assure the success of a project development, no matter if in civil engineering domain (tunnels, foundations ...), in geological storage of radioactive waste or CO_2 or oil production field, two aspects are equally important:

- modeling of inelasticity and failure in geomaterials;
- monitoring of the actual process in play.

This thesis project was concentrated on the development of modeling of damage evolution and its links to monitoring techniques involving elastic waves. This integration of geophysics and geomechanics approaches targeted two key researches:

- microscopic and macroscopic processes governing rock behavior and the evolution of the constitutive properties;
- the connection between "geomechanical" and "geophysical" properties of rocks and associated phenomena plus their modeling.

The objective of this thesis was the development of macroscopic damage evolution laws based only on an explicit description of the micro-scale level which can be successfully employed to describe long term damage behavior of storage places. Homogenization (change-of-scale procedure) was the key aspect of the considered approach. Asymptotic developments of displacement and stress fields combined with micro-crack propagation energy analysis were considered.

A summary was given at the end of each chapter in order to underline the most significant results, therefore in this part the main contributions to the chosen topic brought by this thesis are described:

- Chapter 4 - represent a short review of the multi-scale damage modeling method. The starting basis to attain the objective of this thesis are the results given in [17] (only straight micro-cracks with four possible orientations were considered and only brittle type damage model was developed).
- Chapter 5 - was dedicated to the first extensions made in the framework of time independent damage models. First, microscopic level was enriched by the description of wing type micro-cracking mechanism. A damage evolution law for micro-cracks emerging from pores was also given. In both cases, brittle type damage law was used to characterize macroscopic behavior. However, since experimental observations indicate that rocks show a more gradual fracture behavior, quasi-brittle type-damage models were implemented, at the beginning in 2D and then extended at the 3D case. Notions such "Fracture Process Zone", "R-curve", "instability of the crack propagation", "snap-back behavior" appeared for the first time. Difficulties at the global level were encountered, therefore, a new class of damage models was conceived.

- Chapter 6 - quintessence of this thesis, was dedicated to time-dependent damage laws. It was one way of solving the snap-back problem we encountered using time independent damage models and to enlarge the field of applications of the model to time-dependent effects. Based on Charles' law propagation criterion, three models have been developed. Implementation process went from simple to complex modeling situations. At the beginning, linear coefficients have been used. The damage model which resulted was mostly for theoretical purposes (verification of the correctness of the implementation, for instance). The disadvantage was that the information from the micro-structure was partially lost and intrinsic anisotropy completely absent. Therefore, a second model, less constraining, was needed. A fixed direction for the micro-cracks propagation criterion was considered. Homogenized coefficients previously computed in the frame of the up-scaling procedure were used instead of linear coefficients and intrinsic anisotropy due to preference of the orientation was naturally captured.

  We did not forget that the aim of the thesis is to simulate real processes, therefore propagation in a fixed direction was not enough. It was the time for a criterion regarding crack propagation direction to be introduced. Propagation and trajectory of micro-cracks were controlled by the stress intensity factors, so, before introducing the damage law, a short section is dedicated to $K_{I,II}$. From energy-based we passed to stress intensity factors based damage models. Moreover kinked crack were considered, but since the homogenization techniques was developed in the case of straight micro-cracks, after each time step, the obtained kinked crack was replaced with a straight one following specific rules.

- Chapter 7 - Time depending damage model including kinked micro-cracks simulations were made at three levels: laboratory, tunnel and reservoir scales. Different aspects of this modeling were underlined at each level. At the laboratory scale, a specific two notched geometry loaded in a uniaxial compression was given in the first part of the Chapter in order to give a "qualitative calibration" (test results being compared, from qualitative and not quantitative point of view, to the ones experimentally obtained in [113]. Then, a simple simulation of a tunnel excavation was made, influence of the initial micro-cracks orientation on fracture zones orientations being discussed. At the reservoir scale, oil production/CO_2 injection process was represented through the simulation of an overburden surrounding a reservoir under displacement imposed conditions, the specificity of this numerical application being given by the modeling of micro-sismic events.

Our objective was attended: a two-scale damage model where the macroscopic behavior is totally described by the micro-scopic analysis (macroscopic time dependent damage law is fully deduced on the base of homogenized coefficients and stress intensity factors computed at the microscopic level) and which consider all the possibilities considering micro-cracks evolving both in length and in orientation (between $[0°, 180°]$) the consequence being the possibility of modeling micro-sismic events so linking "geophysics" and "geomechanics".

8.2 Perspectives

The thesis objective was to establish links between "geomechanics" and "geophysics" and it was attended. Developed damage models were able to describe degradation of elastic properties and the development of elastic anisotropy. Furthermore, acoustic emission energy of micro-seismic events can be considered since it is linked with the energy release with damage evolution and the evolution of the micro-crack damage is based on an energy dissipation approach.

But it was only a starting point. Future work is necessary to assess the accuracy of the modeling. Several directions can be considered:

- At the level of the unit cell, several improuvments can be done: consideration of other types of micro-cracks (por-type, curvilinear micro- cracks ...), integration of frictional compressive conditions for the type of micro-cracks already discussed (straight, wing-type, kinked micro-cracks), inclusion of fluid effects ....

- Considering the crack propagation, the time independent damage models can be improved. It is true that we encountered difficulties for the quasi-brittle type damage models, but, there are possible solutions to be investigated without chosing a new class of damage models (for instance other formulations for resistence curves should be considered, in order to start from a certain minimum threshold and not from zero as used).

- The 3D case it was just begun. Only one crack orientation was discussed. All the topics for the two 2D case discussed in this thesis should be implemented in 3D (opening/closing conditions, energy-based and/or stress intensity factors based crack propagation criterion ...).

- Implementation of the dynamics equations and damage evolution and comparison with quasi-static results.

- Further investigation in the compressive case of the kinking crack damage model should be done. We observed that the crack turns too fast the consequence being incapability of micro-cracks to propagate to failure. One solution was given, but the problem needs to be further investigated.

- Application of approach to model experimental results. For that, developments of effects of fluid pressure and saturation variations (including effects of gas replacing liquid) are necessary.

- Addition of intrinsic anisotropy (in matrix elastic properties and damage evolution parameters). The model is able to have a fully anisotropic background medium, thus in the future, intrinsic anisotropy (due, for example, to crystal alignments) can be considered.

- Modeling of medium containing fracture and sliding faults. The investigation of models of production/injection in order to assess the associated issues should continue, either using simple models like those already presented, as well as more elaborate models such as a fluid pressurised fault propagating into the overburden.

Moreover, partially closed cracks should be taken into account. Last but not least, modeling of a reservoir rock, not only the seal rupture, and linking to monitoring data is necessary.

9 Résumé français / French Summary

9.1 Introduction générale

L'objectif de cette thèse est de développer des lois d'évolution macroscopiques d'endommagement à partir des descriptions explicites de la rupture à l'échelle microscopique en vue de la modélisation du comportement des roches.

L'approche adoptée est basée sur l'homogénéisation par développements asymptotiques et sur la description énergétique de la propagation des microfissures, qui permettent l'obtention des lois d'endommagement et conduisent à une quantification explicite de l'énergie dissipée lors de la micro-fissuration. Les modèles obtenus sont capables de prédire la dégradation des modules d'élasticité en raison de l'évolution des microfissures. Cette représentation permet de modéliser la propagation des ondes dans un milieu à endommagement évolutif.

Deux types de modèles d'endommagement seront proposés: indépendants de temps et dépendants de temps. Les modèles indépendants de temps décrivent l'évolution progressive quasi-fragile de la micro-fissuration. Dans les modèles dépendants de temps, l'évolution des microfissures est décrite à travers un critère sous-critique et la propagation mixte, par branchement. En utilisant le modèle dépendant de temps, des simulations seront faites à trois niveaux: du laboratoire, du tunnel et du réservoir.

La structure de la thèse est la suivante:

- Chapitre 4 - présente le cadre de la modélisation double-échelle ainsi que les développements précedents.

- Chapitre 5 - est dédié aux développements concernant les modèles indépendants de temps. Nous introduisons d'abord le modèle d'endommagement pour les microfissures branchées (de type "wing"), ensuite nous décrivons les microfissures se propagéant à partir des micro-pores, et, finalement nous développons des modèles d'endommagement quasi-fragiles en 2D et 3D.

- Chapitre 6 - introduit les modèles d'endommagement dépendant du temps. Trois modèles basés sur une loi de propagation de type Charles sont développés. Dans un premièr temps nous allons modéliser la propagation des microfissures en utilisant des coefficients linéairs. Ensuite, nous allons considérer que les microfissures se propagent dans une direction fixe a priori définie. Dans le cadre de ce modèle, des coefficients homogénéisés seront utilisés. Le troisième modèle prend en compte non seulement la vitesse de propagation des microfissures, mais aussi la direction de la propagation. La propagation des microfissures et la trajectoire seront controlés par les facteurs d'intensité des contraintes (SIF). Des microfissures branchées seront considérées.

- Chapitre 7 est dédié aux simulations sur trois niveaux (laboratoire, gallerie soutérraine et réservoir) en utilisant le modèle d'endommagement avec des microfissures branchées. La spécificité du test simulé à l'échelle du réservoir est la modélisation des événements micro-sismiques et des changements dans les propriétes sismiques en incluant aussi l'anisotropie.

La thèse finit avec une section dédiée aux conclusions et aux perspectives.

9.2 Cadre de modélisation double-échelle

Dascalu et collaborateurs ([36], [37], [38], [39], [17], [56]) ont proposé une nouvelle procédure pour obtenir des modèles micro-mécaniques d'endommagement en utilisant le changement d'échelle - une combination entre l'homogénéisation périodique basée sur des développements asymptotiques (e.g., Bakhvalov et Panasenko ([7])) et l'analyse de l'énergie due à la micro-fissuration. Les lois d'évolution d'endommagement sont complètement déduites par l'homogénéisation à partir d'une description énergétique sur une cellule de périodicité de taille finie, sans utiliser aucune hypothèse phenomenologique. Dans les équations macroscopiques d'évolution de l'endommagement, la longueur normalisée des microfissures apparît comme variable d'endommagement et la taille de la cellule comme paramètre de longueur interne du matériau. La présence de cette longueur interne dans la loi résultante d'endommagement conduit, de façon naturelle, à la prédiction des effets de taille.

Nous considérons que le milieu est élastique isotrope contenant une distribution localement périodique de microfissures. Chaque fissure est considérée droite, de longueur $2a$ et d'angle d'orientation θ par rapport à la direction x_1 (abscisse du système considéré à l'échelle macroscopique). La longueur $2a$ et l'orientation θ peuvent être différents en différents points macroscopiques. La variable d'endommagement d, qui peut varier entre 0 (pour le matériau sain) et $1/[\max(|\cos(\theta)|;|\sin(\theta)|)]$ (pour une cellule complètement traversée par la microfissure), est définie comme le rapport entre la longueur de la fissure $2a$ et la distance entre les centres des microfissures voisines ε:

$$d = \frac{2a}{\varepsilon}. \tag{127}$$

La variable ε représente aussi la taille d'une cellule de périodicité (Fig. 9.1).

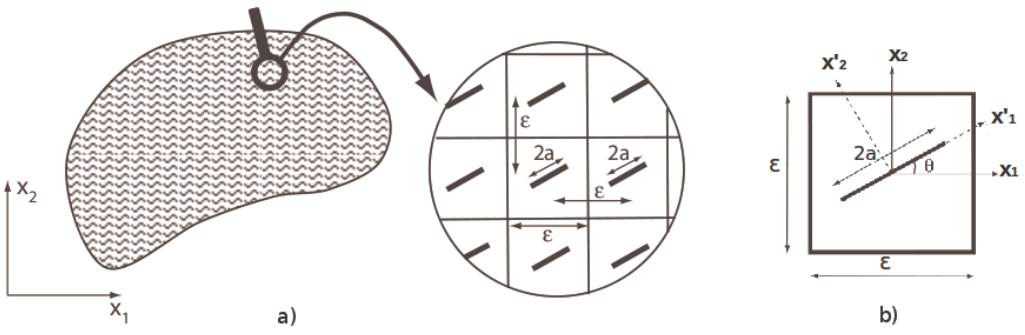

Figure 9.1: Milieu fissuré avec une microstructure locale périodique.

9.2.1 Le problème initial

Dans la partie solide $\mathcal{B}_s = \mathcal{B}\backslash\mathcal{C}$, ou $\mathcal{B}$ est le corps et $\mathcal{C}$ l'ensemble de toutes les microfissures dans $\mathcal{B}$, les équations d'équilibre sont

$$\frac{\partial \sigma_{ij}^{\varepsilon}}{\partial x_j} = 0, \qquad \text{dans} \quad \mathcal{B}_s \tag{128}$$

et les relations constitutives de l'élasticité linéaire anisotrope sont:

$$\boldsymbol{\sigma}_{ij}^{\varepsilon} = a_{ijkl} e_{xkl}(\mathbf{u}^{\varepsilon}), \tag{129}$$

oú a_{ijkl} est le tenseur d'élasticité, $\sigma_{ij}^{\varepsilon}$ est le tenseur des contraintes et $\mathbf{u}^{\varepsilon}$ le champs de déplacement à partir duquel le tenseur des déformations est calculé par rapport aux variables x_i :

$$e_{xij}(\mathbf{u}^{\varepsilon}) = \frac{1}{2}\left(\frac{\partial u_i^{\varepsilon}}{\partial x_j^{\varepsilon}} + \frac{\partial u_j^{\varepsilon}}{\partial x_i^{\varepsilon}}\right). \tag{130}$$

On suppose que les bords de la fissure sont soit libres de contrainte si la fissure est ouverte soit en contact unilatéral sans frottement si la fissure est fermée. Ces deux solutions sont exprimées par les deux jeux de formules

$$\boldsymbol{\sigma}^{\varepsilon}\mathbf{N} = 0 \;\; ; \;\; [\mathbf{u}^{\varepsilon} \cdot \mathbf{N}] > 0 \tag{131}$$

$$[\boldsymbol{\sigma}^{\varepsilon}\mathbf{N}] = 0 \; ; \; \mathbf{N} \cdot \boldsymbol{\sigma}^{\varepsilon}\mathbf{N} < 0 \; ; \; \mathbf{T} \cdot \boldsymbol{\sigma}^{\varepsilon}\mathbf{N} = 0 \; ; \; [\mathbf{u}^{\varepsilon} \cdot \mathbf{N}] = 0 \tag{132}$$

oú $\mathbf{N}$ est le vecteur normal unitaire, $\mathbf{T}$ le vecteur tangent unitaire à la fissure et $[\,\cdot\,]$ le saut à travers les lèvres de la fissures. On suppose que chaque microfissure est caractérisée en totalité par une des deux conditions (131) et (132). Le fait que chaque microfissure soit complètement ouverte ou fermée est une hypothèse raisonnble pour de petites longueurs de fissures. Le passage d'un état à l'autre sera décrit ultérieurement, au niveau des solutions homogénéisées.

9.2.2 Changement d'échelle et coefficients effectifs

La microstructure locale périodique est construite à partir d'une cellule unitaire Y contenant une microfissure (fig. 9.2). La fissure fait un angle θ par rapport à l'axe y_1. La cellule unitaire subit une transformation homothétique de paramètre ε pour obtenir la période physique du matériau εY (Fig. 9.2).

On suppose que cette longueur est assez petite par rapport aux dimensions du milieu, de sorte qu'on puisse distinguer deux variables d'espace physique, macro et microscopique. Dans ce cadre, les deux échelles distinctes sont représentées par les variables $\mathbf{x}$ (variables macroscopiques) et $\mathbf{y} = \mathbf{x}/\varepsilon$ (variables microscopiques) ([127],[96]).

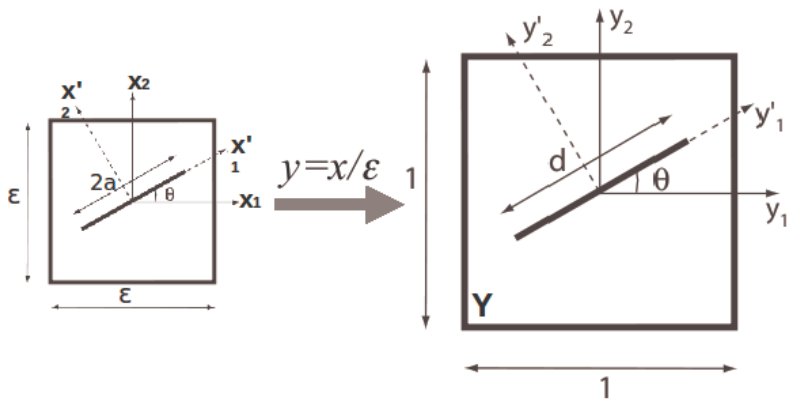

Figure 9.2: Procédure de changement d'échelle

La cellule unitaire Y contient la fissure CY et $Y_s = Y \backslash CY$ est la partie solide. Suivant la méthode d'homogénéisation basée sur le développement asymptotiques (e.g. [13],[127]), on cherche l'expansion de $\mathbf{u}^\varepsilon$ sous la forme :

$$\mathbf{u}^\varepsilon(\mathbf{x}, t) = \mathbf{u}^{(0)}(\mathbf{x}, \mathbf{y}, t) + \varepsilon \mathbf{u}^{(1)}(\mathbf{x}, \mathbf{y}, t) + \varepsilon^2 \mathbf{u}^{(2)}(\mathbf{x}, \mathbf{y}, t) + \ldots, \tag{133}$$

Il peut être prouvé que $\mathbf{u}^{(0)} = \mathbf{u}^{(0)}(\mathbf{x}, t)$ est indépendant de $\mathbf{y}$, représentant un vrai champ de déplacement macroscopique.

On peut aussi démontrer que le correcteur de premier ordre $\mathbf{u}^{(1)}$ peut s'exprimer:

$$\mathbf{u}_\pm^{(1)} = \xi_\pm^{pq} e_{xpq}(\mathbf{u}^{(0)}) \tag{134}$$

où $\xi_\pm^{pq}$ sont les fonctions caractéristiques représentant des modes de déformation élémentaires de la cellule unitaire. A partir des fonctions caractéristiques, les coefficients homogénéisés C_{ijkl}, dépendent de l'état d'endommagement du matériau (i.e. d et θ) et des propriétés mécaniques de la matrice solide, peuvent être calculés. La présence de microfissures induit une anisotropie dans le comportement effectif. Nous avons déterminé pour chaque régime: C_{1111}, C_{2222}, C_{1122}, C_{1212}, C_{1112}, C_{2212}. Pour des différentes valeurs de d et θ, chaque de ces 12 coefficients (6 en traction et 6 en compression) est obtenu par interpolation polynomiale. Ces coefficients, obtenus pour une matrice isotrope caractérisée par le module de Young $E = 2GPa$ et Poisson ratio $\nu = 0.3$, sont présentés dans Fig. 9.3.

9.2.3 Modèles d'endommagement

En suivant les développements des travaux récents: [37], [38], [39], [56], nous obtenons des modèles d'endommagement à partir d'une formulation énergétique de la micro-fissuration. Ces modèles dépendent de la loi de propagation considérée (fragile, quasi-fragile, sous-critique) et des conditions sur les lèvres des microfissures (contact sans frottement).

Dans le cas d'un milieu contenant des microfissures non-frottantes, le problème macroscopique obtenu est le suivant:

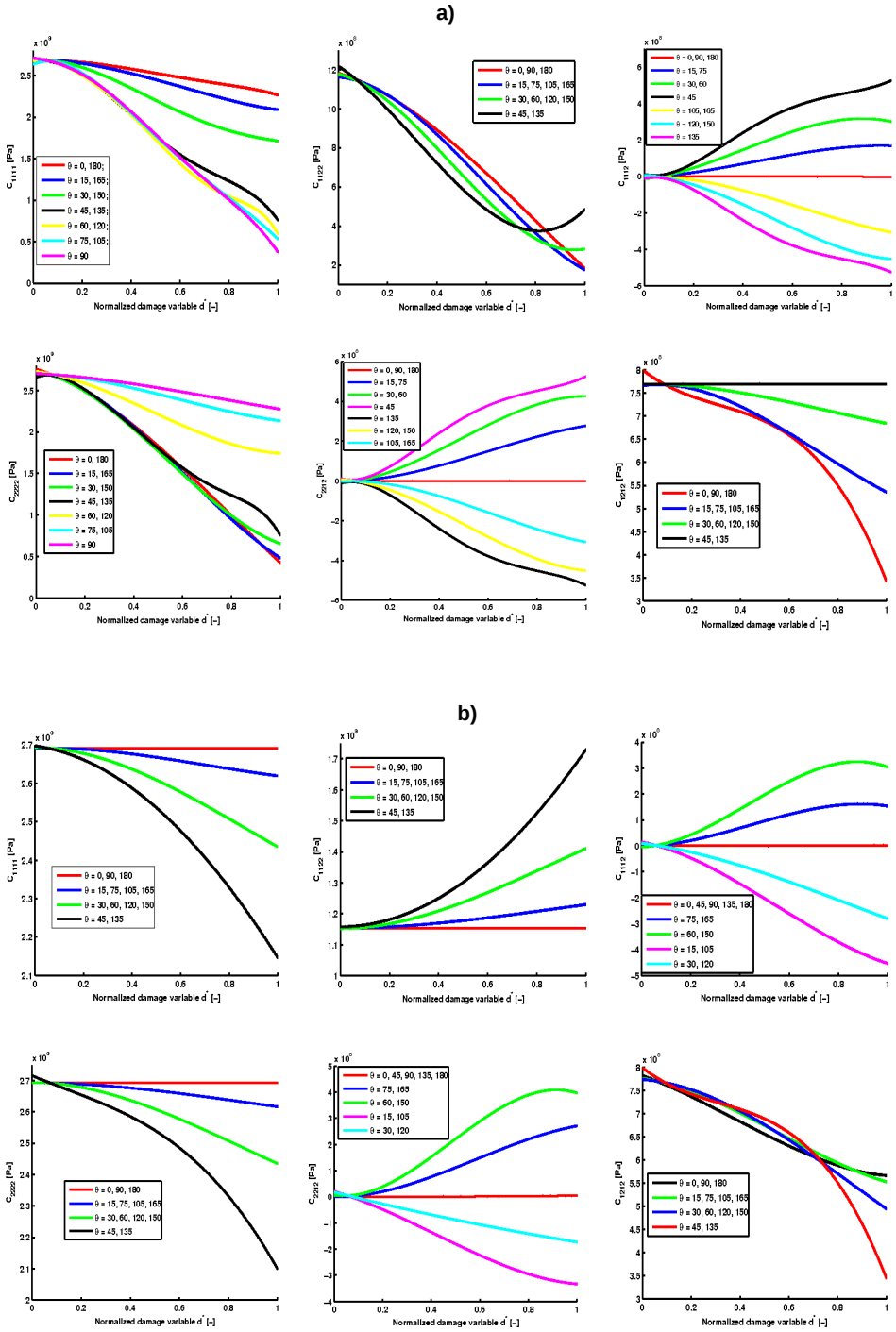

Figure 9.3: Evolution des coefficients homogénéises par rapport à la variable d'endommagement d et à l'orientation de la microfissure θ: (en haut) En traction; (en bas) En compression.

- equation d'équilibre homogénéisée

$$\frac{\partial}{\partial x_j}(C_{ijkl}e_{xkl}(\mathbf{u}^{(0)})) = 0, \tag{135}$$

- Lois d'endommagement (de type Kuhn - Tucker)

$$\begin{aligned}\frac{dd}{dt} \geq 0, \qquad -\frac{1}{2}\frac{dC_{ijkl}(d)}{dd}e_{xkl}(\mathbf{u}^{(0)})e_{xij}(\mathbf{u}^{(0)}) \leq \frac{G_f}{\varepsilon},\\ \left(\frac{1}{2}\frac{dC_{ijkl}(d)}{dd}e_{xkl}(\mathbf{u}^{(0)})e_{xij}(\mathbf{u}^{(0)}) + \frac{G_f}{\varepsilon}\right)\dot{d} = 0.\end{aligned} \tag{136}$$

dans l'equation (136) G_f représente l'énergie critique de rupture, qui peut être donnée par une fonction constitutive.

Nous allons décrire, dans ce qui suit, des cas plus complexes, en prenant en compte le changement d'orientation des microfissures.

9.3 Modèles indépendants du temps

Ce chapitre est dédié aux modèls d'endommagement indépendents du temps. Nous avons etudié deux lois de fissuration: fragile et quasi-fragile pour des microfissures droites et des processus de microfissuration en mode mixte (de type wing).

9.3.1 Le comportement fragile

Si dans l'equation d'évolution de l'endommagement,

$$\left(\frac{1}{2}\frac{dC_{ijkl}(d)}{dd}e_{xkl}(\mathbf{u}^{(0)})e_{xij}(\mathbf{u}^{(0)}) + \frac{\mathcal{G}^{\varepsilon}}{\varepsilon}\right)\dot{d} = 0, \tag{137}$$

nous considérons $G^{\varepsilon} = G_{cr}$, nous nous trouvons dans le cas d'un endommagement fragile. Ce cas a été étudié par Dascalu et al. [37].

Dans la première étape, nous calculons les fonctions caractéristiques qui représentent les modes élémentaires de déformation de la cellule unitaire ([37]). Ces fonctions caractéristiques ont été calculées, dans le cas de traction et de compression, en utilisant le logiciel FEAP ([136]) avec des éléments iso-paramétriques triangulaires á trois noeuds et une condition de périodicité implémenté par la méthode des Multiplicateurs de Lagrange.

Pour les simulations numériques nous avons utilisé un matériau élastique isotrope: module de Young E = 2 GPa et Poisson's ratio $\nu = 0.3$. L'énergie critique pour la rupture G_{cr} est considérée égale à 100 $\frac{J}{m^2}$ et la longueur de la cellule élémentaire ε = 1e-5 m.

Figure 9.4 montre des modes élémentaires de déformation d'une cellule unitaire contenant une microfissure verticale.

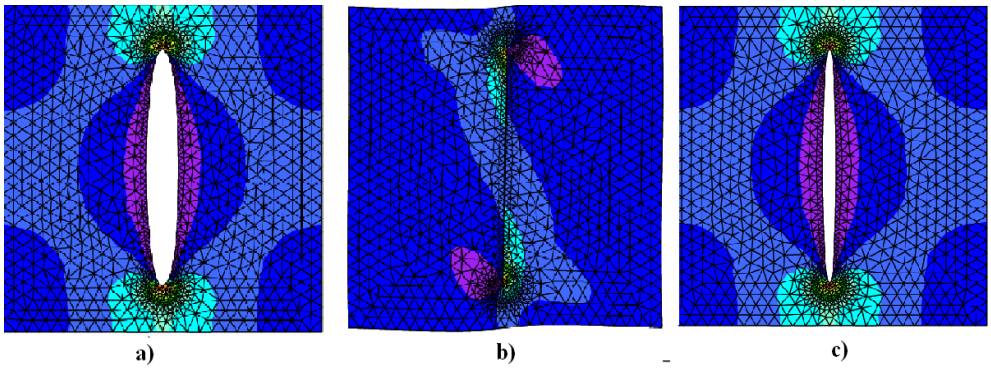

Figure 9.4: Modes élémentaires de déformation de la cellule periodique.

9.3.2 Le comportement quasi-fragile

Le modèle antérieur est convenable pour des matériaux fragiles, mais les observations expérimentales indiquent que les roches présentent un endommagement graduel, i.e. une

réponse quasi-fragile.

Dans cette partie nous décrivons un modèle alterntif dans lequel la résistance du matériau augmente avec la propagation de la fissure. Ce genre de comportement apparaît comme une conséquence du développement d'une zone de micro-fissuration aux extrémités de la fissure.

La courbe qui décrit la variation de G avec d, est définie dans la littérature comme R-curve (courbe de résistance) qui présente un modèle équivalent pour la description d'une zone de micro-fissuration de taille c_f autour des éxtremitées.

La courbe de résistance qu'on considère dans la loi d'évolution de l'endommagement est $G^{\varepsilon}(d) = \frac{G_{cr}2d}{cf}$. Les paramètres de matériau sont les mêmes: $E = 2GPa$, $\nu = 0.3$, G_{cr} = $100\frac{J}{m^2}$ et la taille de la cellule ε = 1e-5 m.

Dans le cas fragile on passe directement d'une phase initiale non endommgée à une phase complètement endommgée. Dans le cas quasi-fragile on a des valeurs de rigidité qui décroissent de façon continue dues au développement progressif de la zone de micro-fissuration, si bien que l'on obtient un d mximum. Pour une zone de micro-fissuration complètement développée, d, le paramètre d'endommagement, doit être égal à 1. On arrive à cette valeur dés qu'on utilise une phase charge - décharge complète dans le contrôle de la déformation macroscopique. La conséquence de ce cycle complet de charge - décharge est un comportement de snap-back. On charge jusqu'un plateu critique ou une valeur maximale de d est obtenue et après on continue avec la procédure de décharge qui a pour effet de développer la zone de micro-fissuration jusqu'a ce qu'un niveau maximum d'endommagement soit atteint. On peut observer ce comportement sur (Fig. 9.5).

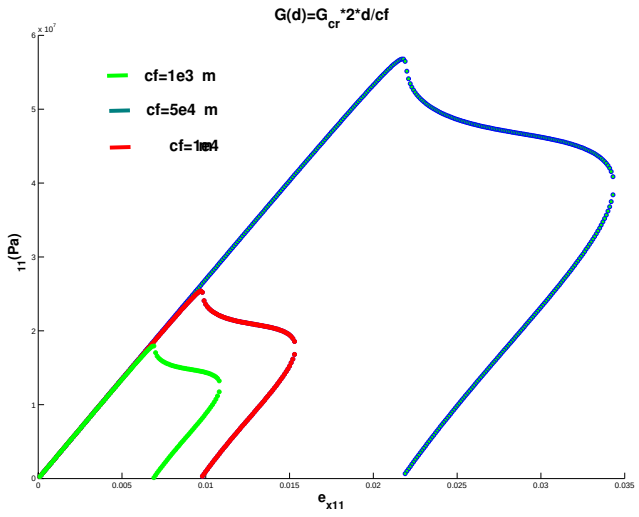

Figure 9.5: La courbe contrainte - déformation pour le cas quasi-fragile: l'initiation de l'endommagement pour différent c_f

Dans la Figure 9.5 nous présentons les courbes contrainte - déformation pour 3 valeurs différentes du paramètre c_f. On peut voir que le moment d'initiation de la fissure augmente si c_f décroît. Cette situation s'explique par l'augmentation du gradient de $G^{\varepsilon}(d)$, qui conduit à une valeur plus grande de G pour un d plus petit et pour une valeur petite de c_f.

Dans un processus de rupture, en général on peut identifier trois étapes: (I) initiation; (II) la propagation stable; (III) la propagation instable vers la rupture complète. Avec notre modèle, après l'initiation, nous pouvons retrouver les deux phases de la propagation en utilisant un critère de stabilité (Eq. 72):

On peut voir clairement dans la Figure 9.6 les deux étapes de propagation: bleu quand la fissure apparaît et commence à se propager de manière satble et sur la partie snap-back (rouge) on observe la propagation instable jusqu'au niveau maxime de l'endommagement.

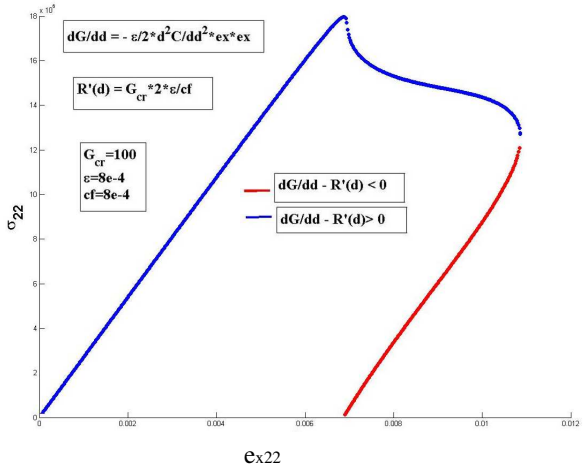

Figure 9.6: Instabilité pour le cas quasi-fragil avec snap-back (bleu pour propagation stable, rouge pour instable)

Extensions de ce modèle ont été faites pour le cas 3D (Section 5.6).

9.3.3 Fissures de type wing

Dans cette section nous présentons une procédure alternative qui nous donne un meilleur modèle pour le cas de fracture en compression dans les roches. Nous considérons un modèle représentant une fissure inclinée avec des branches ("wings") pour lequel nous avons construit un modèle équivalent. Le modèle de la micro-fissure inclinée, montré dans Fig. 9.7, consiste d'un défaut initial de longueur $2a$ et de 2 branches verticales (dans la direction du chargement principal σ_{11}). Le modèle équivalent a une force concentrée P, qui se projette selon la composante normale par rapport à une fissure verticale. On admet l'hypothèse que la longueur de contact ne varie pas en fonction de cisaillement.

Sur la base d'un critère de type Mohr-Coulomb, la contrainte de cisaillement τ_s appliquée sur les surfaces inclinés du modèle présenté dans la Figure 9.7 est réduite par la présence du frottement (μ), et on peut l'évaluer en utilisant la relation suivante:

$$\tau_s = (\sigma_{11} - \sigma_{22})\frac{sin(2\phi)}{2} - \mu(\sigma_{11}\cos^2(\phi) + \sigma_{22}\sin^2(\phi)). \tag{138}$$

oú ϕ est l'angle de la fissure inclinée initiale. La force appliquée dans ce modèle équivalent prend en compte la contrainte de cisaillement décrite ci-dessus.

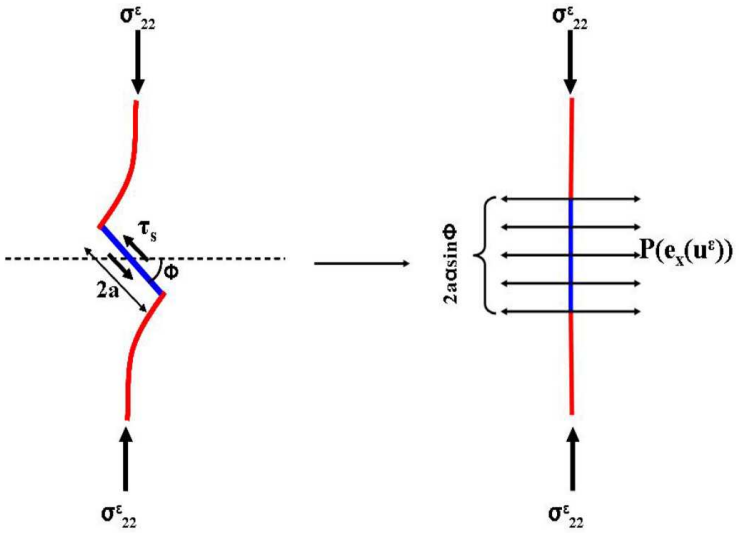

Figure 9.7: Le modèle de micro-fissuration sous compression: (gauche) la fissure glissante; (droite) le modèle équivlent

Le cisaillement induit des zones de traction en tête de la fissure. Ceci a pour effet la propagation en Mode I. Pour l'implémentation numérique on a utilisé $\mu = 0.3$, $\phi = 45°$ et les constantes de matériau $E =$ 2e9 GPa et $\nu = 0.1$.

Dans le cas de compression (avec une fissure droite oú de type wing), la loi de développement de l'endommagement a une nouvelle formule qui inclut aussi des intégrales de saut à travers les lèvres de la fissure. En traction ces intégrales sont nules à cause de la symmétrie des mouvements: un point situé sur la lèvre gauche bouge d'une distance equivlente que le point correspondant sur la lèvre droite, mais dans la direction opposée.

En utilisant l'implémentation numérique pour le modèle initial (les cas: fragil et quasi-fragil), quelques tests de base ont été simulé pour vérifier les résultats du modèle avec des microfissures de type "wing". Le plus important est montré dans la Figure 9.8 oú, comme on obsèrve avec une fissure droite, l'énergie critique (i.e. l'énergie nécessaire pour l'initiation de l'endommagement) est soulignée par la relation Hall-Petch entre l'effet d'échelle et la contrainte maximale ("yield").

9.3.4 Conclusions partielles

Ce chapitre a été dédié aux modèles indépendant du temps. Des lois de propagations fragile ont été utilisés dans le cas de microfissures de type "wing" ou pour les microfissures se propageant a partir des pores. Des lois d'endommagement quasi-fragiles ont été dévéloppés en 2D et en 3D. Dans ces cas, le phénomen de "snap-back" est apparu. Des effets d'échelle ont été présentés dans tous les modèles discutés.

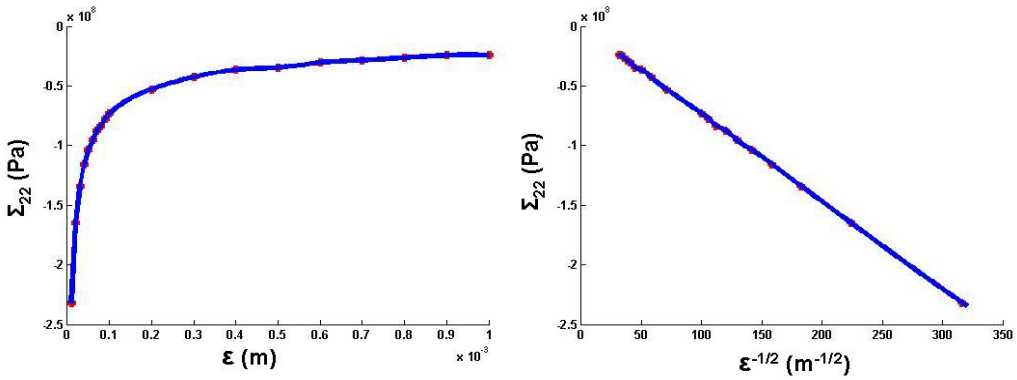

Figure 9.8:) Effet d'échelle - dépendence de la contrainte critique Σ_{22} du paramètre ε; b) L'effet Hall-Petch

9.4 Modèles dépendants du temps

Nous présentons dans cette partie le modèle d'endommagement obtenu par homogénéisation à partir d'une loi de propagation sous-critique des microfissures. Ce modèle va être employé pour la description de l'endommagement à des échelles courtes ou longues de temps, par un choix approprié des paramètres du modèle (temps caractéristique). Dans cette première section nous considérons le cas de la propagation en mode I, décrite par une loi de type Charles [30],[126]:

$$\frac{dl}{dt} = \frac{c_f}{\tau_0}(\frac{K_I}{K_0})^n \tag{139}$$

où $l = 2a$ est la longueur des fissures et K_0 est une valeur limite pour le facteur d'intensité des contraintes K_I. Nous suivons Salganik et l. [126] pour l'introduction de la longueur d'une zone d'élaboration de l'endommagement c_f et pour le temps caractéristique τ_0 dans la loi de Charles. On considère l'exposant sous-critique égal 2. En utilisant la relation entre les SIF et le taux de restitution d'énergie on obtient, pour l'energie critique de la rupture:

$$G_f = (\frac{\varepsilon G_c \tau_0}{c_f})\dot{d}; \qquad G_c = \frac{{K_0}^2}{E'}; \qquad E' = \frac{E}{1-\nu^2} \tag{140}$$

En employant la méthode d'homogénéisation basée sur des développements asymptotiques (voir [37], [38], [39], [56]) nous obtenons la loi d'endommagement sous la forme:

$$\frac{dd}{dt}(\frac{1}{2}\frac{dC_{ijkl}}{dd}e_{xkl}(u^{(0)})e_{xij}(u^{(0)}) + \frac{{K_0}^2\tau_0}{cfE'}\frac{dd}{dt}) = 0. \tag{141}$$

9.4.1 Modèle d'endommagement enrichi: branchement des microfissures

La rupture au niveau microscopique est, en général, une rupture en mode mixte. Le modèle décrit précédemment est limité car il ne faut pas seulement prendre en compte la longueur de la fissure, mais aussi l'orientation de la propagation. Nous présentons dans ce qui suit une extension du modèle, basée sur la propagation des microfissures en mode mixte. Les détails de cette modélisation se trouvent dans [56]. On suppose que l'évolution des fissures se fait par branchement (tangente discontinue) et que les branches se propagent en mode I, toujours d'après la loi de type Chrles :

$$\frac{dl}{dt} = v_0 \left(\frac{K_I^\star}{K_0}\right)^n \tag{142}$$

Dans cette formule on introduit $v_0 = \frac{cf}{\tau_0}$ une vitesse de référence, n est le coefficient sous-critique et $K_I^\star$ représente le facteur d'intensité des contrainte en mode I. Ce critère est utilisé pour décrire la propagation de la fissure branchée. K_0 est une valeur particulière

du facteur d'intensité des contraintes pour laquelle la vitesse de propagation de la fissure est v_0. K_0, v_0 et n sont les paramètres de matériau. $K_I^\star$ depend de l'état de contrainte, de la longueur interne ε et de la geometrie de la micro-fissure.
On suppose que la fissure se propage dans la direction qui maximise le taux de restitution d'énergie. Ce critère prédit un angle de branchement entre la fissure initiale et le branchement incrémental. Cet angle est exprimé en utilisant les equations 114 - 115 (voir [131]). Au niveau de pointes de la fissure, la propagation de la fissure branchée est régie par les equations (113) et 114). Nous avons donc besoin de déterminer K_I et K_{II} pour la fissure droite et $K_I^\star$ pour la fissure branchée.

Coefficients d'intensité des contraintes

I) Fissures droites

L'élasticité linéaire conduit à des points singuliers en contrainte en pointe de fissure ([146]). La distribution de contraintes est donnée par Eq. 98 ou les coordonnés polaires r et φ sont centrées sur la pointe de fissure. Il est evident qu'en pointe de fissure, la contrainte est gouvernée par une singularité $1/\sqrt{r}$. Les coefficients d'intensité des contraintes K_I, K_{II} et K_{III} représentent une mesure de l'intensité de la contrainte à proximité de la pointe de fissure. Les modèles multi-échelles d'endommagement présentés, partent de l'hypothèse d'un milieu isotrope élastique contenant une distribution locale périodique des microfissures de longueur $2a$ et d'orientation θ par rapport à la diréction x_1 (abscisse du système de coordonné macroscopique). Dans le problème macroscopique, nous devons exprimer les termes $K_{I,II}(\mathbf{u}^\varepsilon)$. La procédure de changement d'échelle nous permet d'exprimer K_I et K_{II} dans le problème macroscopique:

$$K_I(\mathbf{u}^\varepsilon) = \sqrt{\varepsilon} K_I(\mathbf{u}^{(1)}) \tag{143}$$

$$K_{II}(\mathbf{u}^\varepsilon) = \sqrt{\varepsilon} K_{II}(\mathbf{u}^{(1)}) \tag{144}$$

Cependant pour tout champ macroscopique $[e_{x11}\ e_{x22}\ e_{x12}]$, les SIF résultants sont déterminés par superposition des SIF des modes élémentaires de déformation:

$$K_{I,II}(\mathbf{u}^{(1)}) = \pm(e_{x11}K_{I,II}(\xi_\pm^{11}) + e_{x22}K_{I,II}(\xi_\pm^{22}) + e_{x12}K_{I,II}(\xi_\pm^{12})), \qquad \text{in } \mathbf{R}^\pm \tag{145}$$

La distinction entre les SIF pour l'ouverture et la fermeture des microfissures est donnée par l'orientation d'un vecteur de type "force" dans le membre de droite par rapport à l'axe de la fissure [36].

En conclusion, pour obtenir les SIF dans le problème macroscopique, il est nécessire de définir les SIF $K_{I,II}$ des modes de déformation élémentaire.

Si l'on considère un mode de rupture simple (K_I oú K_{II} est nul), le SIF non nul peut être déduit du taux de restitution d'énergie en pointe de fissure $\mathcal{G}^\varepsilon$ (en déformation plane):

$$\mathcal{G}^{\varepsilon} = \frac{1-\nu^2}{E}[K_I^2 + K_{II}^2] \tag{146}$$

En se basant sur l'équilibre énergétique d'une cellule périodique comportant des microfissures évolutives, à trajectoires rectilignes, et sans frottement entre les lèvres de la fissure, l'expression, de l'équilibre énergétique, suivante est déduite [37], et exprimée en terme de solution omogénéisée $\mathbf{u}^{(0)}$ permetatnt de déterminer le taux de restitution d'énergie $\mathcal{G}\varepsilon$ pour une structure locale périodique.

$$\frac{dd}{dt}\left(\frac{1}{2}\frac{\partial C_{ijkl}(d,\theta)}{\partial d}e_{xkl}(\mathbf{u}^{(0)})e_{xij}(\mathbf{u}^{(0)}) + \frac{\mathcal{G}^{\varepsilon}}{\varepsilon}\right) = 0 \tag{147}$$

Le premier terme entre paraenthèses est l'opposé du taux de restitution d'énergie d'endommagement. Pour un endommagement évolutif, la relation précédente montre que le paramètre de la micro-structure ε établit le lien entre l'énergie de surface dissipée pendant la propagation des microfissures, et l'énergie par unité de volume $\mathcal{G}^{\varepsilon}$.

Dans le cas oú un mode de rupture mixte est considéré, les SIF de chaque mode ne peuvent pas être déterminés à partir du taux de restitution d'énergie, un autre procédé doit être utilisé. Nous utilisons une méthode basée sur des calculs numérique à l'échelle locale en pointe de fissure, *méthode de corrélation en déplacements*, utilisant des informations à faible distance de la pointe de fissure oú la contrainte est singulière. Le principe est d'extraire les SIF d'une analyse par éléments finis d'un solide fissuré.

Puisque les contraintes et les déplacements au voisinage de la pointe sont complètement déterminés, on peut les superposer à la solution asymptotique pour calculer les coefficients d'intensité des contraintes. Si la faible distance est mesurée entre la pointe de la fissure et le noeud voisin, les champs de déplacement devient:

$$u_1(r,\pi) = -\sqrt{\frac{r}{2\pi}}\frac{4K_{II}}{E'}, \tag{148}$$

$$u_2(r,\pi) = \sqrt{\frac{r}{2\pi}}\frac{4K_I}{E'}. \tag{149}$$

avec $E' = \frac{E}{1-\nu^2}$ en déformation plane. u_1 et u_2 représentent les déplacements normal et tangentiel du noeud à proximité de la pointe de la fissure dans le système de coordonnées de la fissure. Dans un calcul d' éléments finis, le champs de déplacement est obtenue par rapport au système de coordonnées global, une formule de passage prenant en considération l'orientation de la fissure θ est alors nécessaire pour connecter les champs de déplacement u_1 et u_2 :

$$u_1(r,\pi) = \cos\theta u_x + \sin\theta u_y u_2(r,\pi) = -\sin\theta u_x + \cos\theta u_y \tag{150}$$

Une étude sur la dépendance du maillge a été réalisée.

Les coefficients K_I et K_{II} sont calculés pour un grand nombre des longueurs d et d'orientations θ de la fissure et pour les trois modes de déformation ($\xi_{\pm}^{11}$, $\xi_{\pm}^{22}$ et $\xi_{\pm}^{12}$) dans les deux régimes (ouverture (+) ou fermeture (-)). Ensuite, on obtient par interpolation des expressions polynomiales pour $K_I(d^\star, \theta)$ et $K_{II}(d^\star, \theta)$. L'évolution de ces coefficients en fonction de la variable d'endommagement normalisée $d^\star$, pour différentes orientations θ, est présentée dans les figures 6.24 et 6.25. Dans le deuxième cas, pour les fissures en contact, $K_I = 0$ pour tous les modes de chargement de la cellule unitaire. Les calculs ont été faits en utilisant le code d'éléments finis [32].

II) Fissures branchées

Après avoir calculé les coefficients d'intensité pour des microfissures droites, nous allons exprimer les coefficients des fissures branchées en fonction de ceux pour les fissures droites.

La trajectoire des branches est régie par le critère sous-critique (Eq. 113) et celui de la direction de propagation qui maximise le taux de restitution d'énergie. Cette condition implique que la fissure ne se propage pas dans son plan, mais à un angle de branchement donné par l'Eq. (114). Les coefficients K_I et $K_I I$ correspondent à la fissure droite initiale, tandis que $K_I^\star$ est celui de la fissure branchée. Pour des petits incréments de propagation, quand la longueur de la nouvelle fissure dl est petite par rapport a la longueur de la fissure initiale ($dl << a$), nous pouvons employer la relation proposée par [95] pour exprimer $K_\alpha^\star$ par rapport a K_β

$$K_\alpha^\star = F_{\alpha,\beta}(\phi_{max}) K_\beta \tag{151}$$

oú α et β prends les valeurs I et II et $F_{\alpha\beta}(\phi_{max})$ est une matrice 2×2 dépendante de l'angle ϕ_{max}. L'avantage principal de cette expression est son universalité par rapport à la géométrie ou le chargement. Les paramètres géométriques et mécaniques sont inclus dans K_β. $F_{I,I}$, $F_{I,II}$, $F_{II,I}$ et $F_{II,II}$ sont de polynomes de degrés 20 dépendants de l'angle de branchement [95].

Plusieurs auteurs (e.g. Nemat-Nasser and Horii, 1982) ont montré que la détermination de l'angle de branchement en utilisant le maximum du taux de restitution d'énergie donne les mêmes résultats que le critère de symmétrie locale, c'est à dire $K_{II}^\star = 0$.

La fissure équivalente

La détermination de la direction ϕ_{max}, par l'equation (114) et de la longueur dl, à partir d' Eq. (113), permet d'effectuer un incrément de propagation. Pour aller plus loin, en utilisant le même algorithme, nous avons besoin d'une (nouvelle) fissure initiale droite.

Après chaque incrément du temps, la fissure avec ses branchements sera remplacée par une fissure droite équivlente. Il existe différentes possibilités de définir la fissure équivlente, par exemple celle proposée par [131] qui porte sur une équivalence thermodynmique (énergétique). [10] introduit une fissure droite équivalente qui relie les pointes des branchements. Nous adoptons la dernière solution (Fig. 9.9).

L'orientation et la longueur de la fissure équivalente est déterminée à chaque pas de temps (Figure 9.9). La géométrie de la fissure équivalente, en termes de longueur et

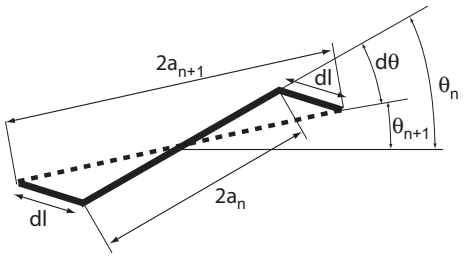

Figure 9.9: Construction de la fissure équivalente

orientation, dépends du taux de propagation $\frac{dl}{dt}$ et de l'orientation ϕ_{max} de la fissure branchée. Ces quantités sont calculées en fonction des coefficients d'intensité K_I et K_{II}, comme il a été montré antérieurement. Ils dépendent des variables d'endommagement macroscopique d et θ et de la déformation macroscopique $\mathbf{e_x}$. La combinaison de ces relations établit le modèle complet d'endommagement, basé sur la propagation en mode mixte des fissures. On remrque la présence de la longueur microscopique ε dans les équations d'endommagement (119-120).

Schéma d'intégration numérique

Pour le modèle d'endommagement présenté dans la section précédente, nous donnons ici quelques détails sur l'algorithme d'intégration numérique.
Le schéma d'intégration dans un point de Gauss du maillage EF au niveau macro est donné dans la Fig. 9.10. Au pas de temps $n+1$, nous avons en entrée les quantités correspondant à la fissure antérieure: d_n et θ_n ainsi que le tenseur de déformation courent ε_{n+1}.
Après la vérification du régime de la nouvelle fissure - fermeture (-) ou ouverture (+) - on calcule les facteurs d'intensité correspondant $K_{I,II}(d_n, \theta_n)$.
Ensuite, on détermine la direction de branchement (ϕ_{max}) par l'équation (114). En utilisnt ϕ_{max} et $K_{I,II}(d_n, \theta_n)$ on calcule le coefficient d'intensité de la fissure branchée $K^{\star}_{I,n+1}$.
Finalement, on calcule l'incrément des branches dl et la nouvelle longueur et orientation de la fissure au pas de temps courrent (d_{n+1}, θ_{n+1}).
Cette solution pour l'endommagement nous permet d'actualiser les coefficients effectifs, de calculer les contraintes et la matrice tangente cohérente.

Résultats numériques: comportement local

Chargement à vitesse de déformation constante

Les figures 6.33 a 6.35 montrent la réponse d'un matériau soumis a une traction uniaxiale. Les paramètres du matériau sont les suivants: $E = 2GPa$, $\nu = 0.3$, $K_0 = 0.6MPa.m^{\frac{1}{2}}$, $v_0 = 10^{-3}m/s$. L'exposant sous-critique, dans la loi de Charles, est $n = 4$ et la taille de la cellule élémentaire $\varepsilon = 1e-4$. L'endommagement initial est $d_0 = 0.1$ et l'orientation initiale $\theta = 45°$.
La figure 6.33 présente l'effet du taux de déformation sur la réponse du matériau pour un

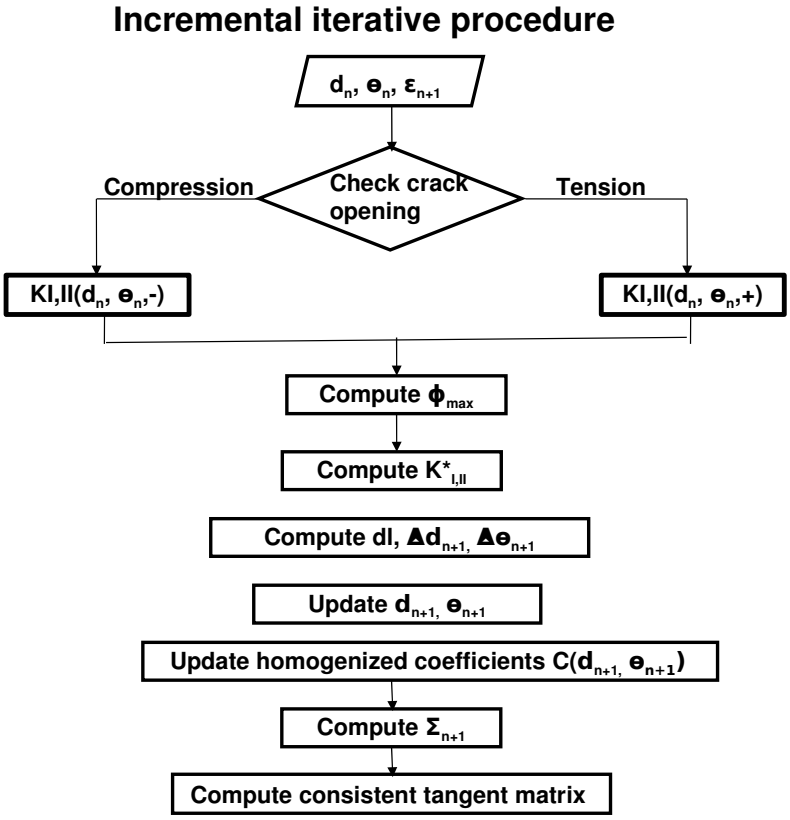

Figure 9.10: Schéma d'intégration numérique du comportement homogénéisé.

essai de traction uniaxiale en déformation e_{x22} imposée. L'effet de la vitesse de déformation sur la résistance du matériau est clairement visible. Ainsi, plus la sollicitation est rapide, plus le matériau est résistant.
La figure 6.34 illustre la réponse du matériau soumis à une traction uniaxiale avec une fissure initiale orientée à 45° par rapport à la direction de chargement. Un taux de déformation verticale constante de $1.10^{-8}s^{-1}$ est imposé, tandis que la contrainte horizontle et de cisaillement sont nulles. Au début du chargement, à fible niveau de déformation, le facteur d'intensité en mode I aux extrémités des fissures est faible. Par conséquent, le taux de propagation sous-critique de la fissure est quasi-nul. La variable d'endommagement et l'orientation de la fissure restent constantes. La rigidité est peu modifiée dans la première partie du test de traction et le comportement est linéaire. Ensuite, quand le niveau de déformation devient suffisamment élevé, le facteur díntensité élevé induit une augmentation de l'endommagement du matériau au cours du temps. La fissure se propage avec un angle de branchement, ce qui induit une rotation de la fissure équivalente accompagnée d'une perte de rigidité du matériau. On observe une tendance d'orientation vers la direction horizontale, mais la déformation de cisaillement contre-balance cette tendance au cours de la propagation. L'orientation horizontale peut être atteinte en imposant des déformations (et non des contraintes) de cisaillement nulles aux cellules de périodicité.
Dans la figure 6.35), l'effet de l'exposant sous-critique est montré. Quand le facteur

d'intensité $K_I^\star$ est plus petit que le facteur de référence K_0, l'augmentation de l'exposant implique la décroissance du taux de propagation des fissures et retarde l'endommagement du matériau.

Le comportement du matériau dépend de l'espacement entre les fissures, ε, qui est un paramètre du matériau. Cet effet d'échelle est mis en évidence dans la figure 6.35 b). La résistance du matériau augmente lorsque l'espacement entre les microfissures diminue.

Les deux figures qui suivent, 6.37 et 6.38, présentent des résultats de simulation des testes biaxiaux à taux de déformation imposée constant.

La figure 6.37 montre les courbes contraint-déformation lors d'un essai biaxial en traction, à vitesse de chargement constante. Un rapport constant entre les déformations horizontale et verticale est mintenu tout au long du test. La traction horizontale e_{x11} induit une rotation de la fissure vers la verticale, tandis que la traction verticale e_{x22} tend à orienter la fissure vers l'horizontale. La déformation e_{x22} étant supérieur à e_{x11}, la fissure se tourne vers la direction horizontale. Quand $e_{x11} = 0$, la rotation de la fissure est maximale. Par contre, lorsque $e_{x11} = e_{x22}$, la fissure se propage sans rotation.

La figure 6.38 montre l'évolution de la contrainte verticale en fonction de la déformation verticale appliquée au cours d'un essai de compression biaxiale. La vitesse de chargement reste constante. Un rapport constant entre la compression horizontale et verticale est maintenu tout au long du test. Les fissures se propagent et tournent jusqu'a atteindre une position où les facteurs d'intensité s'annulent à la pointe de la fissure. La longueur et l'orientation de la fissure finale dépendent de la position initiale et des conditions de chargement, dans notre cas, du rapport entre les déformations dans les deux directions. Plus ce rapport est proche de l'unité moins la fissure tourne. Dans le cas limite, lorsque $e_{x11} = e_{x22}$, la fissure initiale ne se propage pas car elle est déjà orientée dans la direction produisant l'annulation des facteurs d'intensité.

Résultats numériques: comportement global

Calcul de la matrice tangente cohérente

Le calcul anlytique de la matrice tangente pour le modèle avec rotation de microfissures est décrit sur l'algorithme dans la figure 9.11.
Nous considérons les développement analytiques sur 3 niveaux, le niveau 0 contient les termes impliqués directement dans l'expression de la matrice tangente. Sur la configuration actuelle nous connaissons l'endommagement d et l'orientation θ ce qui nous permet de calculer les coefficients homogénéisés et leur dérivés par rapport à d et θ.
Les termes restant ($\frac{\partial \Delta d}{\partial \Delta \varepsilon_k}$ et $\frac{\partial \Delta \theta}{\partial \Delta \varepsilon_k}$) nécessitent des développements supplémentaires brièvement décrits au niveau 1. Ces termes sont obtenus en calculant 113-116 et 119-120.

L'étape la plus complexe est le calcul décrit au niveau 2 du terme $\frac{\partial K_I^\star}{\partial \Delta \varepsilon_k}$ obtenue via l'équation 116 avec $K_{I,II}^\star$ (les facteurs d'intensité des contraintes aux extrémités des branches), $K_{I,II}$ (le SIF aux extrémités de la précédente fissure droite) et les polynomes de Leblond $F_{ij}(\phi_{max})$ ([95]).

Test en traction uniaxiale

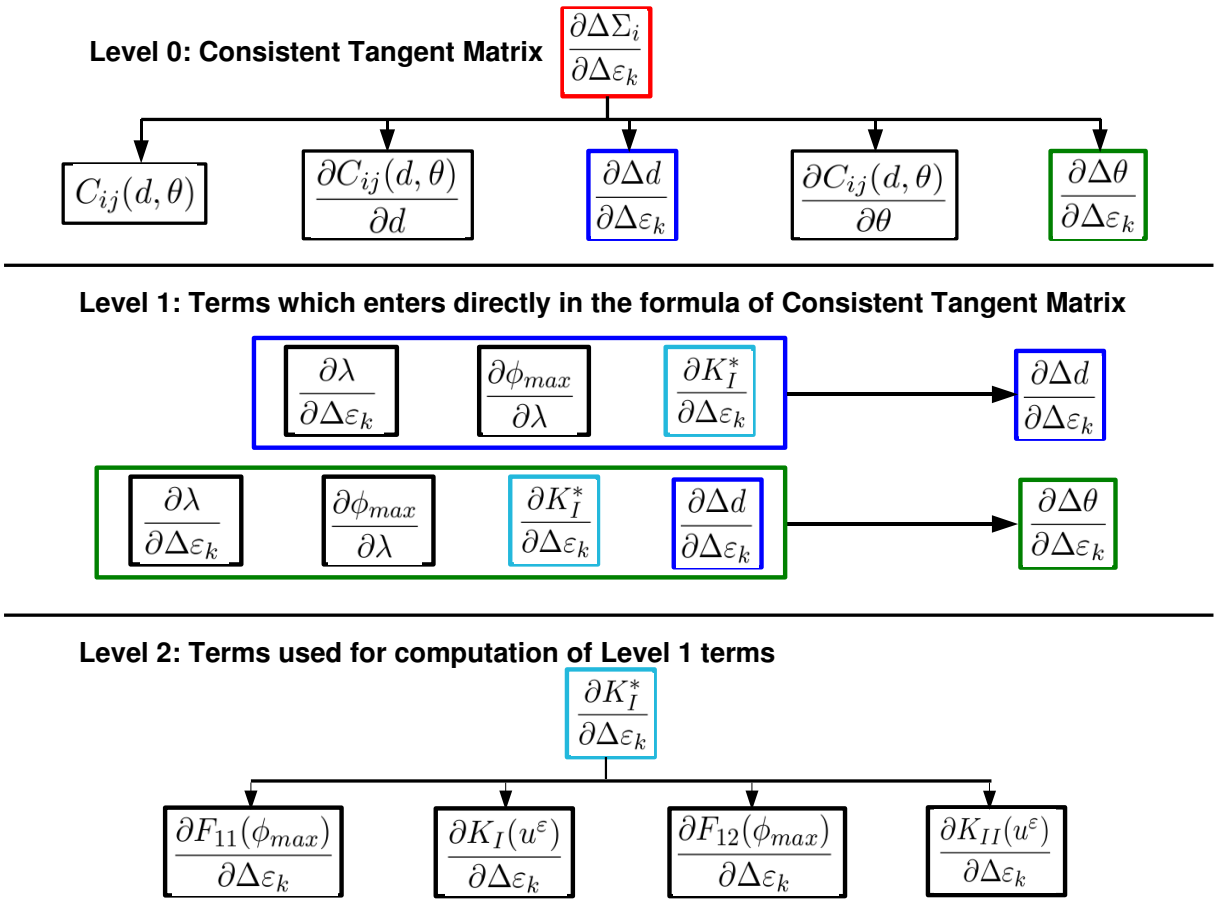

Figure 9.11: La matrice tangente cohérente pour les modèle avec des microfissures branchées

Nous effectuons une première simulation avec le modèle enrichi, un test en traction uniaxial. L'échantillon et les conditions aux limites utilisées sont décrites dans la figure 6.1. Nous utilisons pour cette simulation un maillage a 1250 éléments qudrilatéraux à 4 points de Gauss.
Les paramètres considérés pour le modèle sont les suivants:

- paramètres de la loi de Charles: $K_0 = 4.47Pa\ m^{\frac{1}{2}}$, $v_0 = 1e-3\ m/s$, $n = 2$.
- paramètres élastiques: Module de Young $E = 2GPa$, Coefficient de Poisson $\nu = 0.3$.

Sur la figure 9.12 nous représentons l'évolution de l'endommagement et de l'orientation des microfissures au cours du processus de chargement et sur la figure 9.13 l'évolution des déformations horizontale et de cisaillement au cours du processus de chargement. Les simulations ont été réalisées pour une orientation initiale des microfissures de 90° et une longueur initiale $d = 0.01$. Sur ces 2 figures, 4 étapes de chargement sont considérés. On observe la formation progressive d'une bande localisée dans la zone centrale de l'échantillon. Cette formation est clairement visible sur les distributions d'endommagement et de déformation horizontale au cours de l'avancement du chargement. La figure 9.12 nous montre également une rotation progressive des microfissures (initialement orientées de 90°) qui

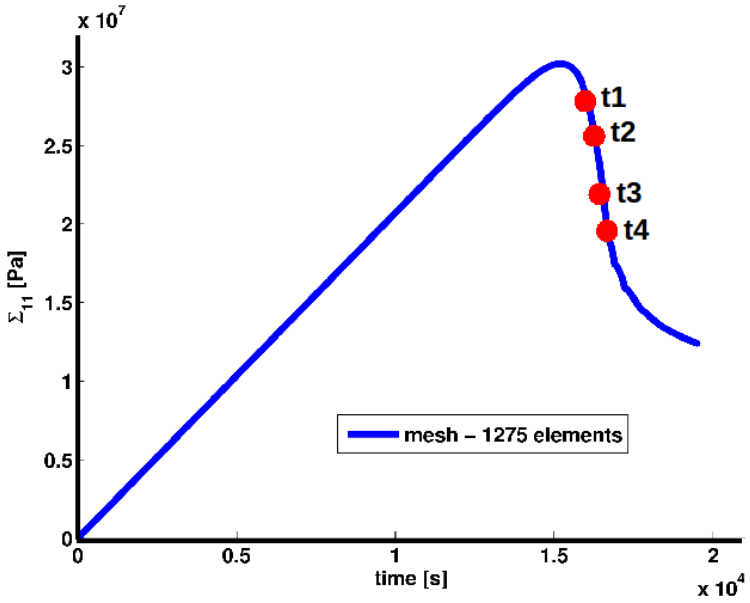

Figure 9.12: Evolution de l'endommagement et orientation des microfissures.

évoluent avec la formation de la bande. La distribution d'orientation des microfissures reste symétrique par rapport au centre de l'échantillon au cours du processus de chargement.

9.4.2 Conclusions partielles

Implémentation des trois modèles d'endommagement dépendent du temps a été réalisé dans ce chapitre. Le modèle le plus complex, dans lequel nous donons des critères pour les orientation de microfissures, a été présenté. De plus, une discution a été faite pour les facteurs d'intensité des contraintes dans le cas des fissures droites et dans le cas des fissures branchées.

Une comparaison entre les trois modèls dévéloppés a été faite en soulignant l'importance de controller pas seulement la vitesse de propagation, mais aussi la trajectoire des microfissures. Dans tous les cas, l'indépendence du maillage a été provée.

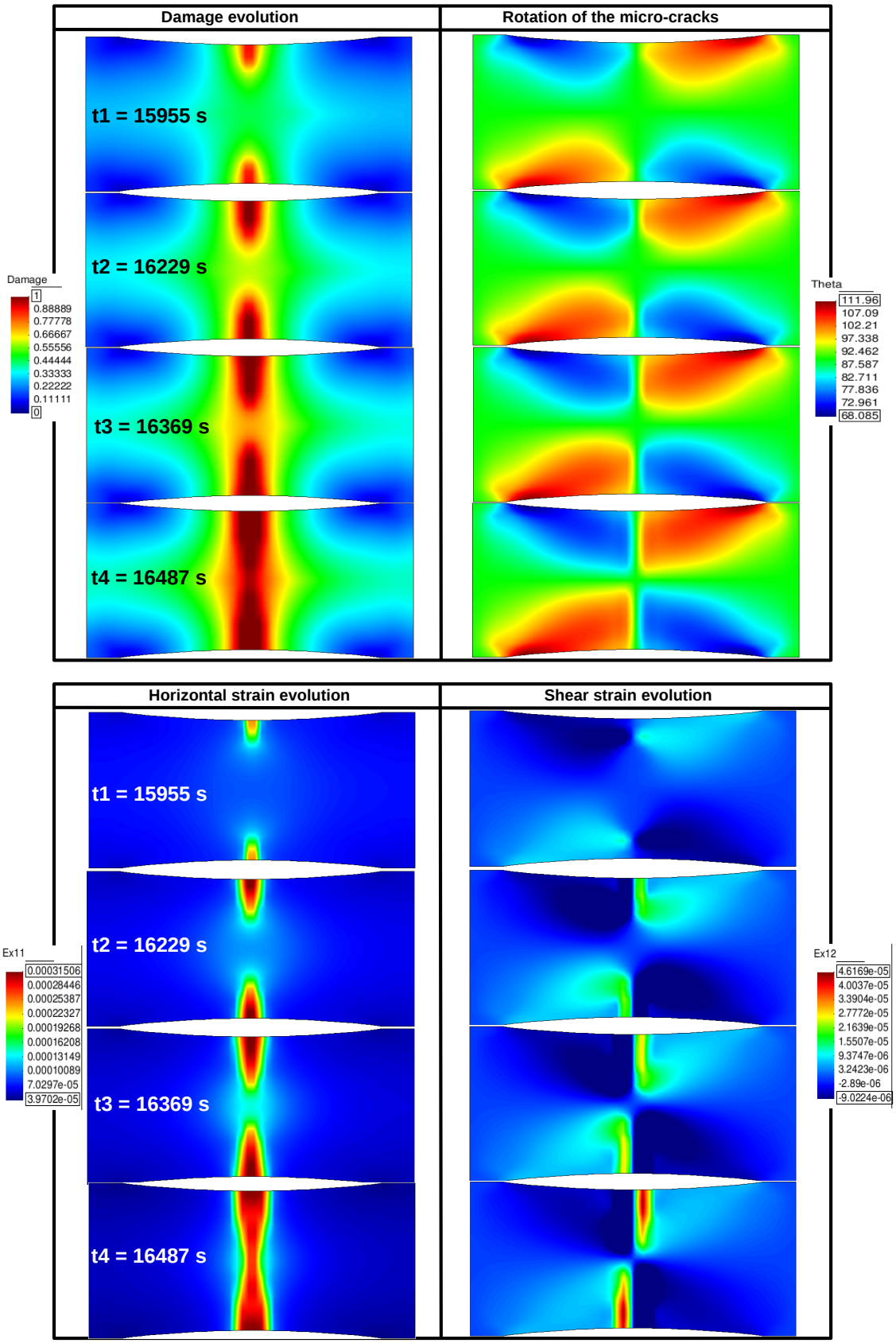

Figure 9.13: Evolution de la déformation horizontale et de la déformation de cisaillement.

9.5 Applications

A l'aide du modèle d'endommagement avec rotation des microfissures précédemment décrit, nous avons rélisé trois tests à différent échelles. Au niveau du laboratoire, une geometrie de type Meuwissen avec deux entailles a été utilisé. Puis, en 2D une galerie souterraine dans le but d'observer l'endommagement de la roche environnante, notamment par la formation des plans de rupture orienté par la direction de creusement, a été faite. Finalement, la simulation de la phase de production/injection du CO_2 dans un réservoir a été discutée. Aspects specifiques de la procedure d'homogénéisation ont été donné dans chaque test (i.e. pour le test au niveau du labortoire, nous vons étudié le comportement de différent paramètres appartenant a la lois d'évolution d'endommagement et nous vons compré nos résultats numeriques avec les résultats expérimentaux trouvé dans [113]; la spécificité du test simulé a l'échelle du reservoir est la modélisation des événiments micro-sismiques et des changements dans les propriétes sismiques en incluant aussi l'anisotropie).

9.6 Conclusions

L'objectif de cette thèse a été le dévéloppement des lois macroscopiques d'évolution de l'endommagement basés exclusivement sur la description de la micro-structure. L'homogénéisation (le changement d'échelle) a été l'aspect clé dans notre approche. Nous avons considèré les dévéloppements asymptotiques des champs de contraintes et de déplacement ainsi que l'analyse de l'énérgie avec la propagation de la micro-fissure.

Un résumé a été donné à la fin de chaque chapitre. Dans cette partie nous donnons les conclusions générales:

Au début de la thèse nous avons décrit la modélisation multi-échelle de l'endommagement que nous avons utilisé et dévéloppé dans les chapitres suivants.

Une partie de la thèse a été dédié aux modèles d'endommagement indépendants du temps. Nous avons commencé par les microfissures branchés et les microfissures dans le milieau poreux. Des modèles d'endommagement specifiques ont été développé. Ensuite, des modèles d'endommagement quasi-fragile en 2D et 3D ont été décrite.

Le Chapitre 6 - la quintessence de cette thèse, a été dédié aux lois d'endommagement dependents du temps. Trois modèles basés sur une loi de propagation de type Charles ont été dévéloppé. Dans un premier temps nous avons modélisé la propagation de microfissures en utilisant des coefficients linèairs. Ensuite, nous avons considéré que les microfissures se propagent dans une direction fixe a priori definie. Dans le cadre de ce modèle, des coefficients homogénéisés, ont été utilisés. Ainsi, l'anisotropie intrinséque due à l'orientation de la micro-fissure, a été naturallement capturée. Le troisième modèle que nous avons proposé dans cette thèse, prend en compte non seulement la vitesse de propagation de microfissures, mais aussi la direction de la propagation. La propagation et la trajectoire des microfissures ont été controllés par les facteurs d'intensité des contraintes (SIF). C'est pour cette raison que nous avons introduit une section dédiée aux SIF. Des microfissures branchées ont été considérés.

La dernière partie a été dédiée aux applications. Nous avons présenté trois types de

simulations, en utilisnt le modèle avec des fissures branchées: au niveau du laboratoire, au niveau d'excavation d'une gallerie et aux niveau d'un reservoire de petrol. Différent aspects de la modèlisation ont été donée a chaque niveau. A l'échelle de laboratoire, des tests uniaxiau ont été effectués en traction et en compression sur un echantillon avec deux entailles. Nos résultats ont été comparés de point de vu qualitatif avec les résultats expérimentaux obtenus par [113].

A l'aide du modèle d'endommagement avec de microfissures branchées, précédemment décrit, nous avons modélisé en 2D une galerie souterraine dans le but d'observer l'endommagement de la roche environnante, notamment par la formation des plans de rupture orientés par la direction de creusement.

A l'échelle du reservoire, nous avons simulé les processus de production du petrol ou d'injection du CO_2 en imposant des conditions de déplacement sur les frontières exterieures d'un souscouche entourant un reservoire de petrol. La specificité de ce test a été la modélisation des événements micro-sismiques.

9.7 Perspectives

Plusieurs directions de developpement sont possibles.

Au niveau de la cellule unitaire d'autres formes des microfissures peuvent être considéré (i.e des courbes au lieu des microfissures droites). De plus, l'intégration des conditions de frottement sur les lèvres de la microfissures où des conditions de couplage hydro-mecanique doivent être considérés.

Les modèles indépendents du temps peuvent être approfondis. D'autres formulations pour la courbe de résistence doivent être étudiés. De plus, le cas quasi-fragile en 3D présenté dans cette thèse a été juste le debut. Tous les developpements faites pour le cas 2D doivent être faites pour 3D (conditions d'ouverture ou férmeture des microfissures, des crit́eres de propagation basés soit sur le bilan de l'énérgie, soit sur les SIF ...).

Une autre direction peut être l'implémentation des équations dynamiques pour la modélisation de l'évolution de l'endommagement et la comparaison avec les résultats quasi-statiques.

D'autres solutions pour les microfissures branchée dans le cas de compression sont necessaires. Nous avons observé que les microfissures changent d'orientations trop rapidement sans se propager de façon évidente.

L'application de notre approche dans la modélisation des résultats expérimentaux doit être plus soutenue.

La modélisation des milieux contenant des macro-fracturés ainsi que l'invéstigation des modèles de production/injection doit continuer soit en utilisant des modèlas symples comme celui qui été présenté dans cette thèse, soit avec des modèles complexes.

References

[1] Alonso-Marroquin, F., Hermann, H.J. and Vardoulakis, I. Micromechanical aspects of soil plasticity: an investigation using discrete model of polygonal particles. Int. Symp. on continuous and discontinuous modeling of cohesive-frictional materials, Stuttgart, 2004.

[2] Anderson, O., Grew, P. Stress corrosion theory of crack propagation with applications to geophysics. Reviews of Geophysics and Space Physics, 1977, 15, 77-104.

[3] Andrieux, S., Bamberger, Y. Marigo, J.J. Un modéle de materiau microfissure pour les roches et les betons. Journal de Mecanique Theorique et Appliquee, 1986, 5, 471-513.

[4] Atkinson, B., Meredith, P. The theory of subcritical crack growth with applications to minerals and rocks. In Fracture Mechanics of Rocks, 1987, 111-166. Academic Press Inc.

[5] Auriault, J. L. et Sanchez-Palencia, E. Etude du comportement macroscopique d'un milieu poreux saturé déformable, J. Mécanique, 1977, vol. 16, pp. 575-603.

[6] Auriault J.-L. Mechanique des Milieux Poreaux Satures Deformables, Cours de 3eme cycle MMGE Grenoble, 1986, 1-71.

[7] Bakhvalov, N., Panasenko, G. Homogenisation: Averaging Processes in Periodic Media. Kluwer Academic Publisher Group, Dordrecht, 1989.

[8] Barenblatt, G.I. The mathematical theory of equilibrium cracks in brittle materials. Adv. Appl. Mech.,1962, vol. 7,55-129.

[9] Barkved, O. I., Kristiansen, T. and Fjaer, E. The 4D seismic response of a compacting reservoir - examples from the Valhall field, Norway: 75th Annual International Meeting, SEG, Expanded Abstracts, 2005, 2508-2511.

[10] Baud, P., Reuschle, T. A theoretical approach to the propagation of interacting cracks. Geophys. J. Int., 1997 130, 460-468.

[11] Bazant, Z. P. and Planas, J. Fracture and Size Effect in Concrete and Other Quasibrittle Materials, CRC Press, 1997, Boca Raton, FL.

[12] Bazant, Z. P. Scaling of quasi-brittle fracture: asymptotic analysis, Int. J. Fracture, 1997, vol. 83, pp. 19-40.

[13] Benssousan, A., Lions, J.L. and Papanicolaou, G. Asymptotic Analysis for Periodic Structures, North-Holland, Amsterdam, 1978.

[14] Bastiaens, W. and Bernier, F. (2006). 25 years of underground engineering in a plastic clay formation: the HADES underground research laboratory. In Geotechnical aspects of underground construction in soft ground (eds K. J. Bakker, A. Bezuijen, W. Broere and E. A. Kwast), pp. 795–801. London: Taylor and Francis.

[15] Bernier, F., Li, X.-L. and Bastiaens, W. Twenty-five years' geotechnical observation and testing in the Tertiary Boom Clay formation, Géotechnique 57, 2007, No. 2, 229–237.

[16] Bigoni, D., Loret, B. Effects of elastic anisotropy on strain localization andflutter instability in plastic solids. J. Mech. Phys. Solids, 1999, 47, 7, 1409-1436.

[17] Bilbie, G. Modélisation multi-échelle de l'endommagement et de la rupture dans les milieux (quasi-) fragiles, PhD Thesis, Université Joseph Fourier, Grenoble, 2007.

[18] Bobet A., Einstein, H. Numerical modeling of fracture coalescence in a model rock material. Int. J. Fracture, 1998, 92, 3, 221-252.

[19] Bobet, A. The initiation of secondary cracks in compression. Engin. Fracture Mech, 2000, vol. 66, 2, 187-219.

[20] Brace, W.F., Bombolakis, E.G. A note on brittle crack growth in compression. J. Geophys. Res., 1963, 68, 3709-3713.

[21] Caiazzo, A.A., Constanzo, F. On the constitutive relations of materials with evolving microstructure due to microcracking. Int. J. Solids Struct., 2000, 37, 3375-3398.

[22] Caillerie, D., Dascalu, C. One-dimensional localization solutions for time-dependent damage (to appear), 2011.

[23] Callari C. Coupled numerical analysis of strain localization induced by shallow tunnels in saturated soils, Computers and Geotechnics, 2004, vol. 31, 3, 193-207.

[24] Callari C., Casini S. Three-dimensional analysis of shallow tunnels in saturated soft ground, Fifth Int. Symp. TC28 "Geotechnical Aspects of Underground Construction in Soft Ground", Amsterdam, 2005, Balkema, 495-501.

[25] Calvetti, F., Viggiani, G. and Tamagnini, C. Micromechanical inspection of constitutive modelling. Constitutive modelling and analysis of boundary value problems in Geotechnical Engineering, Benevento, 2003, 187-216.

[26] Carol, I., Rizzi, E., Willam, K. On the formulation of anisotropic elastic degradation. I:Theory based on a pseudo-logarithmic damage tensor rate. Int. J. Solid Struct., 2001, 38, 491-518.

[27] Chaboche, J.-L. Sur l'utilisation des variables d'état interne pour la description de la viscoplasticité cyclique avec endommagement. In Problèmes Non Linéaires de Mécanique, Symposium Franco-Polonais de Rhéologie et Mécanique, 1977, 137-159.

[28] Chaboche, J.L. Damage induced anisotropy: On the difficulties associated with the active/passive unilateral condition. Int. J. Damage Mech., 1992, 1, 148-171.

[29] Charalampidou, E. M., Hall, S. A., Stanchits, S., Lewis, H., Viggiani, G. Characterization of shear and compaction bands in a porous sandstone deformed under triaxial compression, Tectonophysics, 10.1016/j.tecto.2010.09.032

[30] Charles, R. Dynamic fatigue of glass. J. Appl. Phys., 1958, 29, 1657-1662.

[31] Christensen, R. M. and Lo, K. H.Solutions for effective shear properties in three phase sphere and cylinder models. J. Mech. Phys. Solids, 1979, 27, 315 - 330.

[32] COMSOL AB. COMSOL Multiphysics Users Guide, 2006 Version 3.3 Documentation.

[33] Conil, N., Djeran-Maigre, I., Cabrillac, R., and Su, K. Poroplastic damage model for claystones. Applied Clay Science, 2004, 26, Issue 1-4, 473-487.

[34] Cotterell, B., Rice, J.R. Slightly curved or kinked cracks. Int. J. of Fract., 2007, 16, 155-180.

[35] Dartois, S., Nadot-Martin, C., Halm, D., Dragon, A., Fanget, A. Discrete damage modelling of highly-filled composites via a direct multiscale "morphological approach", Journal of Multiscale Modelling, 2009, 1, 347-368.

[36] Dascalu, C., Bilbie, G. A multiscale approach to damage configurational forces. Int. J. of Fract., 2007, 147, 285-293.

[37] Dascalu, C., Bilbie, G., Agiasofitou, E.K. Damage and size effect in elastic solids: A homogenization approach. Int. J. Solid Struct., 2008, 45, 409-430.

[38] Dascalu, C. A two-scale damage model with material length. C.R. Mecanique, 2009, 337, 645-652.

[39] Dascalu, C., François B. and Keita O. A two-scale model for subcritical damage propagation. Int. J. Solids Structures, 2010, 47, 493-502.

[40] De Sanctis, F. Studio dei meccanismi di rottura fragile nel tufo Napoletano. ThÃ¨se de Doctorat. UniversitÃ di Napoli Federico II, Napoli, Italy, 2005.

[41] Deude, V., Dormieux, L., Kondo, D., Maghous, S. Micromechanical approach to nonlinear poroelasticity: application to cracked rocks. Journal of engineering mechanics, 2002, 848-855.

[42] Diederichs, M.S., Kaiser, P.K. and Eberhardt, E. Damage initiation and propagation in hard rock during tunnelling and the influence of near-face stress rotation. Int. J. Rck Mech. & Mining Sci., 2004, 41, 5, 785-812.

[43] Dormieux, L. and Kondo, D., (2005). Poroelasticity and damage theory for saturated cracked media, Applied Micromechanics of Porous Materials, CISM Lecture Notes, Springer-Verlag, 2005, 480, 153-186.

[44] Dormieux, L., Kondo, D., Ulm, F.-J. A micromechanical analysis of damage propagation in fluid-saturated cracked media, Comptes rendus. Mecanique ISSN 1631-0721, 2006, 334, 7, 440-446.

[45] Dormieux, L., Kondo, D., Ulm, F.-J. Microporomechanics, John Wiley & Sons, Inc., 2006.

[46] Dragon, A., Mroz, Z. A continuum model for plastic-brittle behaviour of rock and concrete. Int. J. Eng. Sci.,1979, 17, 121-137.

[47] Dugdale D.S. Yielding of steel sheets containing slits. J. Mech. Phys. Solids., 1960, 8, 2, 100-104.

[48] Eshelby, J. D. The determination of the field of an ellipsoidal inclusion and related problems. Proc. R. Soc. Lond A, 1957, 241, 376 - 396.

[49] Espinosa, H.D. and Zavattieri, P.D. A grain level model for the study of failure initiation and evolution in polycrystalline brittle materials. Part I: Theory and numerical implementation. Mech. Mat., 2003, 35, 3-6, 333-364.

[50] Falls, S. and Young, R. P. Acoustic emission and ultrasonic-velocity methods used to characterise the excavation disturbance associated with deep tunnels in hard rock. Tectonophysics,1998, 289, 1-3, 1-15.

[51] Fanella, D., Krajcinovic, D. A micromechanical model for concrete in compression. Eng. Fract. Mech., 1988, 29, 49-66.

[52] Fedorov, F. I. Theory of elastic waves in crystals. Plenum Press, 1968.

[53] Feyel, F., Chaboche, J.L.FE2 multiscale approach for modelling the elastoviscoplastic behaviour of long fibre SiC/Ti composite materials. Computer Methods in Applied Mechanics and Engineering, 2000, 183, 3-4, 309-330.

[54] Fielding, E. J., R. G. Blom, and R. M. Goldstein. Rapid subsidence over oil fields measured by SAR interferometry: Geophysical Research Letters, 1998, 25, 3215-3218.

[55] Fjaer, E., Holt, R.M., Horsrud, P., Raaen, A.M. and Risnes, R. Petroleum Related Rock Mechanics, Second edition, Elsevier, 2008, 53.

[56] François, B., Dascalu, C. A two-scale time-dependent damage model based on non-planar growth of micro-cracks. Journal of the Mechanics and Physics of Solids, 2010, 58, 11, 1928-1946.

[57] Freund, L.B. Dynamic Fracture Mechanics, Cambridge University Press, 2004.

[58] Frey, J. Modélisation multi-échelle de l'endommagement hydromécanique des roches argileuses. PhD Thesis, Université de Grenoble, 2010.

[59] Fortin, J., Stanchits, S., Dresen, G., Guéguen, Y. Acoustic emission and velocities associated with the formation of compaction bands in sandstone. J. Geophys. Res., 2006, 111, B10203.

[60] Gajo, A., Bigoni, D., and Muir Wood, D. Multiple shear band development and related instabilities in granular materials J. Mech. Phys. Solids, 2004, 52, 12, 2683-2724.

[61] Gambin, B. and Telega, J.J. Effective properties of elastic solids with randomly distributed microcracks. Mechanics Research Communications, 2000, 27 (6), 697-706.

[62] Garagash, D. and Detournay, E. Plane-strain propagation of a fluid-driven fracture: Small toughness solution. ASME J. Appl. Mech., 2005, 72, 916-928.

[63] Gdoutos, E.E. Fracture Mechanics: An Introduction. Kluwer, Dordrecht,1993

[64] Ghosh S., Lee, K., and Moorthy, S. Multiple scale analysis of heterogeneous elastic structures using homogenisation theory and Voronoi cell finite element method. Int. J. Solids Structures, 1995, 32(1):27 - 62.

[65] Ghosh S., Lee, K., and Moorthy, S. Two scale analysis of heterogeneous elastic-plastic materials with asymptotic homogenization and Voronoi cell finite element model. Computer Methods in Applied Mechanics and Engineering, 1996, 132, 63-116.

[66] Grechka, V., Vasconselos, I. and Kachanov, M. The influence of crack shapes on the effective elasticity of fractured rocks. Geophysics, 2006, 71 (5), D153 - D160.

[67] Griffith, A. The phenomena of rupture and flow in solids. Phil. Trans. Roy. Soc. London CCXXI-A, 1920, 163-198.

[68] Guedes, J. M. and Kikuchi, N. Preprocessing and postprocessing for materials based on the homogenization method with adaptive finite element methods. Comput. Methods Appl. Mech. Engrg., 1990, 83, 143 - 198.

[69] Guery, A. Contributions Ã la modélisation micromécanique du comportement non linéaire de l'argilite du callovao- oxfordien, Thése de doctorat, Laboratoire de mecanique de Lille, 2007.

[70] Hall, S. A. Rock fracture characterisation and seismic anisotropy: application to ocean bottom seismic data. PhD thesis, Univeristy of Leeds, 2000.

[71] Hall, S. A., J-M. Kendall and O. I. Barkved, Fractured reservoir characterisation using P-wave AVOA anaylsis of 3D OBC data, The Leading Edge, 21, 777-781, 2002.

[72] Hall, S. A. and J-M. Kendall. Fracture characterisation at Valhall: Application of P-wave AVOA analysis to a 3D ocean-bottom data set, Geophysics, 2003, 68, 1150-1160.

[73] Hall, S.A. A methodology for 7D warping and deformation monitoring using time-lapse seismic data. Geophysics, 2006, 71, O21-O31.

[74] Hall, S.A. When geophysics met geomechanics: Imaging of geomechanical properties and processes using elastic waves, in Mechanics of Natural Solids, Kolymbas, D. and Viggiani, G. (Eds.), VIII, Springer, 2009, 147-175.

[75] Hardy H.R. Acoustic emission/Microseismic activity, volume 1: Principles, Techniques and geotechnical applications, A.A. Balkema, 2003.

[76] Hill, R. A self-consistent mechanics of composite materials. J. Mech. Phys. Solids,1965, 13, 213 - 222.

[77] Hillerborg, A., Modeer, M., Petersson, P.E. Analysis of crack formation and crack growth inconcrete by means of fracture mechanics and finite elements. Cem. Conc. Res., 1976, 6, 6, 773-782.

[78] Hoek, E. and Bienawski, Z. T. Brittle fracture propagation in rocks under compression. J. Fracture Mech., 1965, 1, 137-155.

[79] Horii, H., Nemat-Nasser, S. Brittle fracture in compression: splitting, faulting, and brittle-ductile transition. Philos. Trans. R. Soc. (London), Series A, 1986, 319, 337-374.

[80] Horii, H., Nemat-Nasser, S. Compression - induced microcrack growth in brittle solids: axial splitting and shear failure. J. Geophys. Res., 1985, 90, 3105-3125.

[81] Hosseini, M. Etude expérimentale du comportement hydro-mécanique d'une roche poreuse en relation avec les problemes d'excavation. These de Doctorat. Université Joseph Fourier, Grenoble, 2005.

[82] Huang, J.F., Chen, G.L., Zhao, Y.H., Wang, R. An experimental study of the strain field development prior to failure of a marble plate under compression. Tectonophysics, 1990, 175, 1-3, 283-290.

[83] Huang, C., Subhash, G., Vitton, S. J. A dynamic damage growth model for uniaxial compressive response of rock aggregates, Mechanics of Materials, 2002, 34, 267-277.

[84] Huang, C., Subhash, G. Influence of lateral confinement on dynamic damage evolution during uniaxial compressive response of brittle solids, Journal of the Mechanics and Physics of Solids, 2003, 51, 1089-1105.

[85] Hudson, J., A. The excitation and propagation of elastic waves. Cambridge University Press, 1980a.

[86] Inglis C. E. Stress in a plate due to the presence of crack and sharp corners. Transaction of the Royal Institution of Naval Architecture, 1913, 55, 219-241.

[87] Ingraffea A.R., Heuze F.E. Finite element models for rock fracture mechanics. Int. J. Num. Analys. Method. Geomech., 1980, 4, 1, 25-68.

[88] Irwin G.R. Fracture dynamics. In: Fracturing of Metals. Amer. Soc. For Metals, 1948, 147-166.

[89] Irwin G.R. Analysis of stresses and strains near the ends of a crack traversing a plate. J. Appl. Mech.,1957, 24, 361-364.

[90] Kachanov, L.M. Time of the rupture process under creep conditions. Isv. Akad. Nauk. SSR. Otd Tekh. Nauk., 1958, 8, 26-31.

[91] Kienzler, R., Herrmann, G. Mechanics in material space with applications to defect and fracture mechanics. Springer-Verlag, Berlin Heidelberg, 2000.

[92] Kristiansen, T. Geomechanical Characterization of the Overburden above the Compacting Chalk Reservoir at Valhall, SPE/ISRM Eurock, Trondheim, Norway, 1998, 193-202.

[93] Kristiansen,T., G., Barkved, O., Pattilo, P., D., Use of Passive Seismic Monitoring in Well and Casing Design in the Compacting and Subsiding Valhall Field, North, SPE 65134, 2000.

[94] Lajtai E.Z. Brittle fracture in compression. Int. J. Fracture, 1974, 10, 4, 525-561.

[95] Leblond, J.B. Crack paths in three-dimensional elastic solids. I: two-term expansion of the stress intensity factors - application to crack path stability in hydraulic fracturing. Int. J. Solids Struct., 1999, 36, 79-103.

[96] Leguillon, D., Sanchez-Palencia, E. On the behavior of a cracked elastic body with (or without) friction. J. Mech. Theor. Appl., 1982, 1, 195-209.

[97] Lemaitre, J., Chaboche, J.L. Aspect phénoménologiques de la rupture par endommagement. Journal de Mécanique Appliquée, 1978, 2, 317-365.

[98] Lene, F., Damage constitutive relations for composite materials. Engineering Fracture Mechanics, 1986, 25, 713-728.

[99] Lenoir, N., Bornert, M., Desrues, J., Bésuelle, P., Viggiani, G. Volumetric Digital Image Correlation Applied to X-ray Microtomography Images from Triaxial Compression Tests on Argillaceous Rock, Strain, 2007, 43, 3, 193-205.

[100] Li Y-P., Chen L-Z., Wang Y-H. Experimental research on pre-cracked marble under compression. Int. J. Solids. Struc., 2005, 42, 9-10, 2505-2516.

[101] Liner, C. A column on the history and culture of geophysics. The Leading Edge, 2010, 29, 02, 146-147.

[102] Lydzba, D. and Shao, J.F. Study of poroelasticity material coefficients as response of microstructure, Mech. Cohes-Frict. Mater., 2000, vol 5, 149-171.

[103] Meglis, I.L., Chow, T., Martin, C.D., Young, R.P. Assessing in situ microcrack damage using ultrasonic velocity tomography. International Journal of Rock Mechanics and Mining Sciences, 2005, 42, 1, 25-34.

[104] Meuwissen, M.H.H., Oomens, C.W.J., Baaijens, F.P.T., Petterson, R., Janssen, J.D. Determination of the elasto-plastic properties of aluminium using a mixed numerical-experimental method. J. Material Proc. Tech., 1998, 75, 1-3, 204-211.

[105] Miehe, C., Schroder, J., Schotte, J. Computation homogenization analysis in finite plasticity. Simulation of texture developement in polycrystalline materials. Computer Methods in Applied Mechanics and Engineering, 1996, 171, 387-418.

[106] Miura, K., Okui, Y., Horii, H. Micromechanics-based prediction of creep failure of hard rock for long-term safety of high-level radioactive waste disposal system. Mechanics of Materials, 2003, 35, 587-601.

[107] Mori, T., and Tanaka, K. Average stress in the matrix and average elastic energy of materials with misfitting inclusions. Acta. Metall., 1973, 21, 571 - 574.

[108] Murakami, Y., Aoki, S. Stress Intensity Factors Handbook, Pergamon, Oxford, New York, 1987.

[109] Nasseri, M.H.B., Mohanty, B., Young, R.P. Fracture toughness measurements and acoustic emission activity in brittle rocks. Pure appl. geophys., 2006, 163, 5-6, 917-945.

[110] Nemat-Nasser, S., Horii, H. Micro-Mechanics: Overall Properties of Heterogeneous Materials, Amsterdam, North-Holland, 1993.

[111] Nemat-Nasser, S., Deng, H. Strain-rate effect on brittle failure in compression. Acta Metall. Mater., 1994, 42, 1013-1024.

[112] Nemat-Nasser, S. and Hori, M. Micromechanics: Overall Properties of Heterogeneous Materials, Elsevier, Amsterdam-Lausanne-New York, 1999.

[113] Nguyen T. L. Endommagement localisé dans les roches tendres. Experimentation par mesure du champs. PhD Thesis, Université de Grenoble, Grenoble, 2011.

[114] Niandou, H., Shao, J.F., Henry, J.P. and Fourmaintraux D. Laboratory investigation of the mechanical behaviour of Tournemire shale. Int. J. Rock Mech. & Min. Sci., 1997, 34, Issue 1, 3-16.

[115] Nitka, M. Multi-scale modelling of granular media. PhD Thesis, Université de Grenoble, Grenoble, 2010.

[116] Oden, J.T., Vemaganti, K., Moes, N., Hierarchical modeling of heterogeneous media. Computer Methods in Applied Mechanics and Engineering, 1998, 172, 3-25.

[117] Operchalska, B., Multiscale modelling of subcritical damage in rocks, Master Thesis, MEMS, Université Joseph Fourier - Grenoble INP, 2008.

[118] Ozdemir, I., Brekelmans, W.A.M., Geers, M.G.D. FE2 computational homogenization for thermo-mechanical analysis of heterogeneous solids, Computer Methods in Applied Mechanics and Engineering, 2008, 198 (3-4), 602-613.

[119] Paliwal, B., Ramesh, K.T. An interacting micro-crack damage model for failure of brittle materials under compression, Journal of the Mechanics and Physics of Solids, 2008, 56, 3, 896-923.

[120] Park C.H., Bobet A. Crack coalescence in specimens with open and closed flaws: A comparison. Int. J. Rock Mech. Min. Sci., 2009, 46, 5, 819-829.

[121] Pénse, V., Kondo, D., Dormieux, L. Micromechanical analysis of anisotropic damage in brittle materials. J. Engrg. Mech., 2002, 128, 889-897.

[122] Pietruszczak, S., Lydzba, D. and Shao, J.F., Modelling of inherent anisotropy in sedimentary rocks. Int. J. Solids Struct., 2002, 39, 3, 637-648.

[123] Prat, P.C., Bazant, Z.P. Tangential stiffness of elastic materials with systems of growing or closing cracks. J. Mech. Phys. Solids, 45, 611-636, 1997.

[124] Renaud V. Contribution á l'etude d'un modele de mesofissuration: application au comportement d'un gres, Doctoral These de l'Université Lille I, 1998.

[125] Sagong, M., Bobet, A. Coalescence of multiple flaws in a rock-model material in uniaxial compression. Int. J. Rock. Mech. Min. Sci., 2002, 39, 2, 229-241.

[126] Salganik, R.L., Repoport, L., Gotlib, V.A. Effect of structure on environmentally assisted subcritical crack growth in brittle materials, Int. J. Fracture, 1997, 87, 21-46.

[127] Sanchez-Palencia, E. Non-homogeneous Media and Vibration Theory, Lecture Notes in Physics, 1980, 127, Springer, Berlin.

[128] Sevostianov, I. and Kachanov, M., On the elastic compliances of irregularly shaped cracks, Int. J. Fracture, 2002, 114, 245 - 257.

[129] Shen, B., Stephanson, O., Einstein, H., Ghahreman, B., (1995). Coalescence of fracture under shear stresses in experiments. J. Geohys. Res., 1995, 100, B4, 5975-5990.

[130] Simone, A. and Sluys, L.J. The use of displacement discontinuities in a rate-dependent medium, Computer Methods in Applied Mechanics and Engineering, 2004, 193 (27-29):3015-3033.

[131] Schütte, H., Bruhns, O.T. On a geometrically nonlinear damage model based on a multiplicative decomposition of the deformation gradient and the propagation of microcracks. J. Mech. Phys. Solids, 2002, 50, 827-853.

[132] Sleipner Carbon Dioxide Sequestration Project
http://www.statoil.com/en/TechnologyInnovation/NewEnergy/Co2Management/Pages/SleipnerVest.aspx

[133] Stanchits, S., Fortin, J., Gueguen, Y., Dresen, G. Initiation and Propagation of Compaction Bands in Dry and Wet Bentheim Sandstone. Pure. Appl. Geophys., 2009, 166, 5-7, 843-868.

[134] Suquet, P.M. Local and global aspects in the mathematical theory of plasticity. In: Plasticity Today: Modelling A. Sawczuk and G. Bianchi, Editors, Methods and Applications AMD-Vol. 212/MD-Vol. 62, Elsevier Science Publishers, London, 1985, 279-310.

[135] Tada, H., Paris, P.C., Irwin, G.R. The Stress Analysis of Cracks Handbook. ASME Press, New York, 2008.

[136] Taylor R. L. FEAP User manual, Berkeley, USA, 2008.

[137] Teanby, N., J-M. Kendall, R. H. Jones and O. I. Barkved. Stress-induced temporal variations in seismic anisotropy observed in microseismic data, Geophys. J. Int., 2004, 156, 459-466.

[138] Terada, K. and Kikuchi, N. Nonlinear homogenization method for practical applications. In Ghosh, S. and Ostoja-Starzewski, M., editors, Computational Methods in Micromechanics, 1995, AMD-Vol. 212/MD-Vol. 62, 1 - 16, ASME.

[139] Terada, K., Kikuchi, N. A class of general algorithms for multiscale analyses of heterogeneous media. Comput. Methods Appl. Mech. Enrg., 2001, 190, 5427-5464.

[140] Thomsen, L. Weak elastic anisotropy. Geophysics, 1986, 51, 10, 1954-1966.

[141] Truesdell, C. A. and Toupin, R. A., The Classical Field Theories, Handbuch der Physik, 1960, vol. III-1, Springer-Verlag, Berlin, Germany.

[142] Van Gestel, J.-P., Kommedal J. H., Barkved, O. I., Mundal, I., Bakke, R., Best, K. D. Continuous seismic surveillance of Valhall Field. Special section. Permanent monitoring, smart oil fields and reservoir survaillance, 2008.

[143] Voyiadjis, G.Z., Park, T. The kinematics of damage for finite-strain elasto-plastic solids. Int. J. Eng., 1999, 37, 803-830.

[144] Weyburn Carbon Dioxide Sequestration Project
http://www.netl.doe.gov/publications/factsheets/project/Proj282.pdf

[145] Wiederhorn, S., Bolz, L. Stress corrosion and static fatigue of glass. Journal of the American Ceramic Society, 1970, 53, 543-548.

[146] Williams, M.L. On the stress distribution at the base of a stationary crack. J. Appl. Mech., 1957, 24, 109-144.

[147] Wong R.H.C., Chau K.T. Crack coalescence in a rock-like material containing two cracks. Int. J. Rock Mech. Min. Sci., 1998, 35, 2, 147-164.

[148] Wong L.N.Y., Einstein H.H. Crack Coalescence in Molded Gypsum and Carrara Marble: Part 1. Macroscopic observations and interpretation. Rock Mech. Rock Engin., 2008a, 42, 3, 475-511.

[149] Wong L.N.Y., Einstein H.H. Crack Coalescence in Molded Gypsum and Carrara Marble: Part 2 - Microscopic Observations and Interpretation. Rock. Mech. Rock. Engin., 2008b, 42, 3,513-545.

[150] Wong L.N.Y., Einstein H.H. Systematic evaluation of cracking behaviour in specimens containing single flaws under uniaxial compression. Int. J. Rock. Mech. Min. Sci.,2009, 46, 2, 239-249.

[151] Wong, R.H.C., Chau, K.T., Tang, C.A., Lin, P. Analysis of crack coalescence in rock-like materials containing three flaws - Part I: experimental approach. Int. J. Rock Mech. Min. Scie., 2001, 38, 7, 909-924.

[152] Zhang Z.X., Kou S.Q., Jiang L.G., Lindqvist P-A. Effects of loading rate on rock fracture: fracture characteristics and energy partitioning. Int. J. Rock. Mech. Min. Sci., 2000a, 37, 5, 745-762.

[153] Zhang X., Jeffrey R.G. and lanos E.M. On Plane-Strain Fluid-Driven Shear Fracture Propagation in Elastic Solids, Geophys. J. Int., 2005, 163, 419-430.

[154] Zhu, Q., Kondo, D., Shao, J.F., Pensee, V. Micromechanical modelling of anisotropic damage in brittle rocks and application. Int. J. Rock. Mech. Min. Sci., 2008, 45, 467-477.